

Novel Synthesis of Carbon Dots and 2D materials for optical and electrochemical applications

Thesis submitted by

Dipayan Roy

Doctor of Philosophy (Science)

School of Materials Science & Nanotechnology
Faculty of Interdisciplinary Studies, Law and Management
Jadavpur University
Kolkata, India

2023

CERTIFICATE FROM SUPERVISOR

This is to certify that the thesis entitled “*Novel Synthesis of Carbon Dots and 2D materials for optical and electrochemical applications*” submitted by Shri **Dipayan Roy** who got his name registered on **07.12.2020** for the award of Ph.D. (Materials Science and Nanotechnology) degree of Jadavpur University is absolutely based upon his own work under the supervision Dr. Sourav sarkar and that neither his thesis nor any part of the thesis has been submitted for any degree/diploma or any other academic award anywhere before.

1. Sourav Sarkar
7/11/23.
Signature of the Supervisor

Dr. Sourav Sarkar
Associate Professor
School of Materials Science & Nanotechnology
Jadavpur University
Kolkata - 700032

1. Title of the thesis:

Novel Synthesis of Carbon Dots and 2D materials for optical and electrochemical applications

2. Name, Designation & Institution of the Supervisor:

a) Dr. Sourav Sarkar
Associate Professor
School of Materials Science & Nanotechnology
Jadavpur University Kolkata-700032, India
e-mail: sourav.sarkar@jadavpuruniversity.in, souravsarkars@gmail.com

3. List of Publications

First authored

1. Site specific nitrogen incorporation in reduced graphene oxide using imidazole as a novel reducing agent for efficient oxygen reduction reaction and improved supercapacitive performance. **Dipayan Roy**, Sarkar Sarkar, Kaustav Bhattacharjee, Karamjyoti Panigrahi, Bikram K. Das, Kausik Sardar, Sourav Sarkar, and Kalyan K. Chattopadhyay. *Carbon*, **2020**, 166, pp.361-373.
2. Boron vacancy: a strategy to boost the oxygen reduction reaction of hexagonal boron nitride nanosheet in hBN–MoS₂ heterostructure. **Dipayan Roy**, Karamjyoti Panigrahi, Bikram K. Das, Uday K. Ghorui, Souvik Bhattacharjee, Madhupriya Samanta, Sourav Sarkar, and Kalyan K. Chattopadhyay. *Nanoscale Advances*, **2021**, 3, 16, 4739-4749.
3. Oxygen vacancy-induced band engineering and metal unsaturation in MoS₂–MoO₃ with spillover-based confined catalysis. **Dipayan Roy**, Bikram Kumar Das, S. Najes Riaz, Dimitra Das, Sourav Sarkar, Kalyan Kumar Chattopadhyay. *ACS Applied Energy Materials*, **2023**, 6, 9, 4892–4908.
4. Probing the emission dynamics in nitrogen-doped carbon dots by reversible capping with mercury (ii) through surface chemistry. **Dipayan Roy**, Antika Das, Rajarshi Roy, Dimitra Das, Bikram Kumar Das, Uttam Kumar Ghorai, Kalyan Kumar Chattopadhyay and Sourav Sarkar. *New Journal of Chemistry*, **2022**, 46(30), pp.14690-14702.

Collaborative publications

5. Morphology tuning of bismuth oxychloride nano-crystals by citric acid variation: Application in visible light-assisted dye degradation and hydrogen evolution by electrochemical method. Ratna Sarkar, **Dipayan Roy**, Dimitra Das, Subrata Sarkar, and Kalyan Kumar Chattopadhyay, *International Journal of Hydrogen Energy*, **2021**, 46(30), pp.16299-16308.
6. Zinc doping induced WS₂ accelerating the HER and ORR kinetics: A theoretical and Experimental Validation. Arnab Das, **Dipayan Roy**, Bikram Kumar Das, M.I. Ansari, Kalyan

Kumar Chattopadhyay and Sourav Sarkar. *Catalysis Today*, **2022**, 423, p.113921.

7. Exploring the interfacial behavior of SiNWs/Sulphur and Nitrogen-doped carbon dot based heterostructure for near-infrared photodetection application. S.N Riaz, **Dipayan Roy**, Souvik Bhattacharjee, Ankita Chandra, Kalyan Kumar Chattopadhyay and Sourav Sarkar **2023**. *Materials Letters*, p.134458.

8. Synthesis of Silicon Nanowire and Crystalline Carbon Quantum Dots heterostructure and Study of Photo response and Photoluminescence Property. Sourav Sarkar, Unmesha Ray, **Dipayan Roy**, Diptonil Banerjee, and Kalyan Kumar Chattopadhyay *Materials Letters*, **2021**. 303, p.130493.

9. Observation of polarization-dependent excitonic luminescence in few-layered WS₂ flakes. Rajarshi Roy, Sarthak Das, Nilesh Mazumder, **Dipayan Roy**, and Kalyan Kumar Chattopadhyay *Chemical Physics Letters*, **2021**. 781, p.139012.

10. Size-modulation of functionalized Fe₃O₄: Nanoscopic customization to devise resolute piezoelectric nanocomposites. Souvik Bhattacharjee, Nilesh Mazumder, Suvankar Mondal, Karamjyoti Panigrahi, Anibrata Banerjee, Dimitra Das, Saikat Sarkar, **Dipayan Roy**, and Kalyan Kumar Chattopadhyay *Dalton Transactions*, **2020**. 49(23), pp.7872-7890.

11. Resonant energy transfer in van der Waal stacked MoS₂ – functionalized graphene quantum dots composite with ab-initio validation. Rajarshi Roy, Ranjit Thapa, Shibsankar Biswas, Subhajit Saha, Uttam Kumar Ghorai, Dipayan Sen, E Mathan Kumar, Gundam Sandeep Kumar, Nilesh Mazumder, **Dipayan Roy**, and Kalyan Kumar Chattopadhyay, *Nanoscale*, **2018**, 10(35), pp.16822-16829.

This thesis is based on the above-mentioned published works (1-4)

4. List of Patents: Communicated

Dedicated to my Parents and Wife

Acknowledgment

I find myself extremely privileged to have the opportunity to thank many people who have helped me in various stages of my research work throughout the last few years. First of all, my foremost deepest gratitude to my supervisor Prof. Kalyan Kumar Chattopadhyay and Dr. Sourav Sarkar for giving me opportunity to work in this group. The scientific guidance in the fields of materials chemistry, physics and nanotechnology encourages independent and insightful research.

I would also like to thank my seniors Dr. Subhajit Saha, Dr. Kaustav Bhattacharjee, Dr. Uttam Kumar Ghorai, and Dr. Rajarshi Roy motivated me to grow manuscript-writing skills and in-depth knowledge. Their passion for research and problem-solving motivates me not only a good researcher but also a good human. I would like to take this opportunity to thank all the graduate (M.Sc. and M. Tech) students who are working in this lab. I especially would like to mention the names of S.N Riaz, and Manas Thakur, who are working now as research scholars for their cooperation. I shall forever remain highly obliged to my close collaborators Karamjyoti Panigrahi, Bikram Kumar Das, Dimitra Das, Anibrata Banerjee, and Arnab Das for their constant help in various research aspects.

I appreciatively acknowledge all my other lab members Suvankar, Souvik, Tufan, Saikat, Subhasish, Kaushik Chanda, Kaushik Sardar, Shabarni, and Ratna for providing a homely atmosphere in our lab. I must thank Dr. Chandan Kumar Ghosh, and Dr. Mahua Ghosh Chaudhuri of School of Materials Science & Nanotechnology, Jadavpur University for their supportive role during my Ph.D. journey. I have experienced a healthy atmosphere in our lab and institution for research work.

I also wish to acknowledge the Science & Engineering Research Board (SERB), a statutory body of Department of Science & Technology (DST), Government of India (File No. EEQ/2018/001127) for providing financial support in my early career of research work. Also, I would like to thank University Grand Commission (UGC), Government of India (Ref No. 191620010342), for funding me to continue my research work.

Over and above, I profess my deepest regard to my dearest parents and wife. Their inspiration, blessings, and caring are the biggest inspirations of my life.

School of Materials Science & Nanotechnology
Jadavpur University
Kolkata-700032
India
Dipayan Roy

“Statement of Originality”

I **Dipayan Roy** registered on **07.12.2020** do hereby declare that this thesis entitled *“Novel Synthesis of Carbon Dots and 2D materials for optical and electrochemical applications”* contains literature survey and original research work done by the undersigned candidate as part of Doctoral studies.

All information in this thesis have been obtained and presented in accordance with existing academic rules and ethical conduct. I declare that, as required by these rules and conduct, I have fully cited and referred all materials and results that are not original to this work.

I also declare that I have checked this thesis as per the “Policy on Anti Plagiarism, Jadavpur University, 2019”, and the level of similarity as checked by iThenticate software is 6%.

Signature of Candidate: *Dipayan Roy*

Date: *07.11.2023*

Certified by

Supervisor(s): *Soumya Sarkar*

(Signature with
date, seal) *7/11/23.*

Dr. Soumya Sarkar
Associate Professor
School of Materials Science & Nanotechnology
Jadavpur University
Kolkata - 700032

I.

CONTENTS

CHAPTER 1: General Introduction	1-32
1.1. Material Science and Nanotechnology	01
1.1.1. Nanomaterials and nanotechnology	01
1.1.2. Classifications of nanomaterials	02
1.1.3. Properties of nanomaterials	05
1.1.3.1. Physical Property	05
1.1.3.2. Chemical Property	07
1.1.4. Structural and electronic properties of 2D materials	09
1.1.4.1. Non-metal based 2D materials	09
1.1.4.2. Transition metals dichalcogenides (TMDs)	10
1.2. Electrochemistry and fundamentals of energy conversion and storage	12
1.2.1. Green Energy and electrochemistry on energy storage	12
1.2.2. Fundamental on Batteries	13
1.2.3. Supercapacitor as energy storage device	15
1.2.4. Oxygen reduction reaction and fuel cells	19
1.2.5. Water splitting reaction	22
1.3. Fluorescence-based quantum dots and sensing	24
1.3.1. Type of Fluorophores and Optical property of Nanomaterials	25
1.3.2. Type of sensors and mathematical tools	27
1.3.2.1. PL quenching	27
1.3.2.1. Electrochemical quenching	27
1.4. Aims and Objectives	28
1.5. References	29
CHAPTER 2: Review of the past work	33-58
2.1. Synthesis of 2D materials	33
2.1.1. CVD based synthesis	34
2.1.2. Wet Chemical synthesis	35
2.1.3. Exfoliation based synthesis	36
2.2. Synthesis of carbon quantum dots	37
2.3. Previous work on Oxygen reduction reaction	38
2.4. Oxygen reduction reaction with 2D materials	39
2.5. Previous work on supercapacitive performances	42
2.6. Hydrogen evolution reaction (HER) with Nobel and Non- Nobel metals	44
2.7. Hydrogen evolution reaction (HER) with 2D materials	46
2.8. Metal Sensing based applications	48
2.9. References:	49
CHAPTER 3: Experimental techniques	59-72
3.1. X-ray Diffraction (XRD) and Rietveld Analysis	59
3.2. High Resolution Transmission Electron Microscope (HRTEM)	61
3.3. Raman spectroscopy	62

3.4. Fourier-transform infrared spectroscopy (FTIR) -----	63
3.5. UV-Vis and Photoluminescence Spectroscopy -----	64
3.6. Field Emission Scanning Electron Microscope (FESEM) -----	66
3.7. X-ray and ultra-violet photoelectron spectroscopy (XPS & UPS) -----	67
3.8. Brunauer-Emmett-Teller (BET) analysis -----	69
3.9. Electrochemical Characterization -----	70
3.10. References -----	72

CHAPTER 4: Site-specific nitrogen incorporation in reduced graphene oxide using imidazole as a novel reducing agent for efficient oxygen reduction reaction and improved supercapacitive performance -----73-105

Abstract -----	73
4.1. Introduction -----	74
4.2. Experimental Section -----	76
4.2.1. Materials -----	76
4.2.2. Preparation of Graphene Oxide (GO) -----	76
4.2.3. Preparation of Nitrogen functionalized reduced Graphene Oxide (NrGO) -	77
4.2.4. Preparation of reduced Graphene Oxide (rGO) -----	77
4.2.5. Characterization -----	78
4.2.6. Electrochemical Measurement -----	78
4.2.7. Theoretical Methods -----	79
4.3. Results and Discussion -----	80
4.3.1. Phase Purity, Atomic percentage and Morphology analyses -----	80
4.3.2. ORR results and analysis -----	87
4.3.3. Active sites and DFT analyses in ORR mechanism -----	95
4.3.4. Capacitive performance and analysis -----	97
4.4. Conclusion -----	102
4.5. References -----	102

CHAPTER 5: Boron Vacancy: A strategy to boost the Oxygen Reduction Reaction of Hexagonal Boron Nitride Nanosheet in hBN-MoS₂ Heterostructure -----106-135

Abstract -----	106
5.1. Introduction -----	107
5.2. Experimental Section -----	108
5.2.1. Reagents and chemicals -----	108
5.2.2. Preparation of hBN Sheet -----	109
5.2.3. Preparation of hBN and MoS ₂ heterostructure (HBPS) -----	109
5.2.4. Preparation of MoS ₂ (MS) -----	109
5.2.5. Characterization -----	109
5.2.6. Theoretical methods -----	110
5.2.7. Electrochemical measurement -----	111
5.3. Results and Discussions -----	112
5.3.1. Phase purity, composition, structure, and morphological investigations --	112
5.3.2. Electrochemical (ORR) performance study -----	119
5.3.3. Active surface sites in ORR catalysis -----	124
5.3.4. Theoretical validation of electrochemical investigations -----	127
5.4. Conclusion -----	132

5.5. References	133
CHAPTER 6: Oxygen vacancy induced band engineering and metal unsaturation in MoS₂-MoO₃ with spillover based confined catalysis	136-184
Abstract	136
6.1. Introduction	137
6.2. Experimental Section	139
6.2.1. Reagents and chemicals	139
6.2.2. Preparation of oxygen vacancy induced MoS ₂ -MoO ₃ heterostructure	139
6.2.3. Preparation of 2H-MoS ₂ , MoS ₂ nanosheet (MoS ₂ Ns) and Quantum Dots.....	140
6.2.4. Characterization	140
6.2.5. Electrochemical Characterization	141
6.2.6. Calculation of turn over frequency (TOF)	142
6.2.7. Catalytic Reduction of PNP	143
6.2.8. Potassium Ferricyanide K ₃ [Fe(CN) ₆] reduction	144
6.2.9. Theoretical methods	145
6.3. Results and Discussion	146
6.3.1. Structural and Morphological analyses of different MoS ₂ based composites-	146
6.3.2. Band Engineering and surface activity	154
6.3.3. Acidic HER activity and catalytic mechanism	156
6.3.4. Alkaline HER activity and catalytic mechanism	165
6.3.5. Catalytic reduction of PNP and K ₃ [Fe(CN) ₆]	169
6.4. Conclusion	179
6.5. References	179
CHAPTER 7: Probing the emission dynamics in nitrogen doped carbon dots by reversible capping with mercury (II) through surface chemistry	185-220
Abstract	185
7.1. Introduction	186
7.2. Experimental Section	187
7.2.1. Reagents and chemicals	187
7.2.2. Synthesis of N-CQD	187
7.2.3. PLE and PL study of N-CQD with different metal ions	188
7.2.4. Characterization	189
7.2.5. Theoretical methods	189
7.3. Results and Discussion	190
7.3.1. Surface chemistry and optical properties of the functional N-CQDs	190
7.3.2. Photoluminescence quenching and binding of N-CQDs with metal ions ---	199
7.3.3. Sensing dynamics between N-CQDs and Hg ²⁺ ion	205
7.3.4. Static and dynamic quenching	208
7.3.5. Photoluminescence recovery	212
7.4. Conclusion	217
7.5. References	218
CHAPTER 8: Grand Conclusion and Future Scope	221-225
8.1. Research Outcomes	221
8.2. Future scope of the work	224

List of Abbreviations

AC
BE
BET
BJH
CB
CD
 C_{dl}
CNT
CPE
CQD
CV
CVD
DI
DFT
DMF
EDLC
EDS
EIS
ESCA
EXAFS
FESEM

FID
FRET
FTIR
FWHM
GC
GCE
GGA
GO
QD
HER
HRTEM

IFFT
K-L
LIB
LOD
LSV
MA
MWCNT
OER
ORR
PAW
PEMFC
PBE
Pc

Original phrase

Alternating current
Binding energy
Brunauer–Emmett–Teller
Barret-Joyner-Halenda
Conduction band
Charge discharge
Double-layer capacitance
Carbon nanotube
Constant phase element
Carbon quantum dots
Cyclic voltammetry
Chemical vapor deposition
Deionized
Density Functional theory
Dimethyl formamide
Electric double layer capacitor
Energy-dispersive X-ray, spectroscopy
Electrochemical impedance spectroscopy
Electrochemically active surface area
Extended X-ray absorption fine structure
Field emission scanning electron
microscopy
Flame ionization detector
Foster resonance energy transfer
Fourier-transform infrared spectroscopy
Full width half maxima
Glassy electrode
Glassy carbon electrode
Generalized gradient approximation
Graphene oxide
Graphene quantum dots
Hydrogen evolution reaction
High resolution transmission electron
microscopy
Inverse Fast Fourier transform
Koutecky-Levich
Lithium-ion batteries
Limit of detection
Linear sweep voltammetry
Mass activity
Multiwall carbon nanotube
Oxygen evolution reaction
Oxygen reduction reaction
Projector-augmented-wave
Proton exchange membrane fuel cell
Perdew-Burke-Ernzerhof
Pseudocapacitor

PL	Photoluminescence
PLE	Photoluminescence excitation
PNP	Para Nitro phenol
QY	Quantum yield
R_{CT}	Charge transfer resistance
RDE	rotating disk electrode
RDS	Rate determining step
RF	Roughness factor
RRDE	Rotating-ring disk electrode
RHE	Reversible hydrogen electrode
SAED	Selected area electron diffraction
SCs	Supercapacitors
SHE	Standard hydrogen electrode
TOF	Turnover frequency
VASP	Vienna Ab-initio Simulation
VBM	Valance band maxima
XANES	X-ray absorption near-edge spectroscopy
XPS	X-ray photoelectron spectroscopy
XRD	X-ray diffraction

Abstract

Index No: D-7/ISM/35/2020


To mitigate the energy crisis and environmental hazards by anthropogenic activities in modern world, highly durable and cost-effective nanotechnology must be developed. Electrochemical based nanotechnology and nanosensors provide efficient clean energy and environmentally friendly technologies for energy conversion, energy storage and sustainable development. In the energy storage system, water electrolysis involves oxygen and hydrogen evolution, providing energy storage in fuel cell economy. Fuel cells are commercial energy sources to produce electricity by chemical reactions at cathode and anode through oxygen reduction and hydrogen oxidation respectively. In recent times, energy storage technologies like capacitors, and batteries have attracted the scientific community for the development of smart devices. Considerable theoretical and experimental investigation is necessary to understand the catalytic mechanism for highly efficient and durable smart devices for commercial applications. In this regard, size and morphology dependent nanomaterials facilitate various chemical, optical sensor and electrochemical properties due to quantum confinement effect, surface plasmon resonance, high surface to volume ratio, packing fraction, chemical stability, mechanical strength and various catalytic sites. However, selective materials structure and band alignment for various sensing, energy conversion, energy storage applications, and correlation with device is essential to enhance the efficiency of the interfacial mechanism. The catalytic mechanism and reaction rate by nanomaterials is modified with particle size, surface area, preferred morphology, surface optimization, vacancies, defects, doping, functionalization, coating, and the formation of binary and ternary composites. Several research groups have implemented multiple synthetic parameters to improve energy-based applications. Two-dimensional (2D) materials have unique properties due to multiple band gap, layer thickness, porosity, surface area, edge active sites. Therefore, such efficacy can be achieved by suitable material design using diverse synthetic protocols. Indeed, the optical, electronic, and structural properties of 2D materials with reaction mechanisms in the domain of energy and sensing application require more fundamental insight. Carbon based materials like graphene, carbon nanotubes have emerged as potential applications in electric devices, drug delivery but lower mass production as well as understanding of the defect

formation and its functions are still unexplored. Besides, till now, transition metal dichalcogenides (TMDs) can serve as an electrode material where most of the TMDs are theoretically predicted. Secondly, it is difficult to enhance the conductivity of the basal plane of TMDs and rigorous synthetic techniques have been modulated using epitaxial growth, chemical vapour deposition (CVD), ion intercalation, exfoliation and high temperature annealing. Owing to developing better electrode and sensing material, synthetic procedures and internal mechanisms must be paid more attention. Aiming this, quantum dots and 2D material based heterostructure have been synthesized by controlling reaction parameters, additives, defects, porosity, surface area, and band alignment. The surface reactivity, surface area and porosity of graphene are enhanced with nitrogen functionalization by incorporating a reducing agent imidazole, a biomolecule under ambient temperature. The pyridinic, graphitic, pyrrolic and amine type functionalization on graphene (NrGO-90) increases defect density, defect length and interlayer distance, confirmed with different experimental protocols like Raman spectroscopy, X-ray diffraction (XRD) analysis. NrGO-90 exhibits four electron transfer processes for oxygen reduction reaction (ORR) in fuel cells. It is noticed, that at higher temperatures, the pyridinic and amine nitrogen are converted to graphitic nitrogen (for NrGO-400) as well as change in mesoporous nature, layer stacking and low defect density shrinks the ORR kinetics and capacitive performances. Theoretical analysis suggests favorable negative free energy pathways during ORR pathways at pyridinic and amine sites and validates our experimental analysis. The stand-alone ORR performances of NrGO-90 and NrGO-400 are determined from overpotential, onset potential Tafel slope, half wave potential, limiting current density and rate constant. The porous interlayer space and surface active sites for NrGO-90 also boost specific and volumetric capacitance of 287.5 F/g at 1 A/g current density and 880 mF/cm² at a scan rate of 2 mV/s respectively. Such dual efficacy of NrGO is covered with conventional reduced graphene oxide (catalytic inactive for ORR) and other metals with 2D porous heterostructures. A similar observation has been manifested for hexagonal boron nitride (hBN) which is catalytically inactive for electrochemical performances due to insulating in nature. A new strategy has been demonstrated by incorporating boron vacancy (~7%) on hBN basal plane which can enhance the conductivity for ORR reaction. Looking ahead, the hBN and MoS₂ heterostructure (HBPS) enhances the B-OH bond polarity due to charge transfer between two heterostructures. The long time ultrasonication stimulates to removal B-OH group and facilitates boron vacancy upto ~28%.

Control over the change in geometry of hBN sheet due to vacancy also lowers the band gap and enhances electrochemical active surface area (ESCA). The vacancy sites are favourable adsorbent of oxygen which is reduced to four OH^- ions and follows the ORR kinetics with four electron transfer process. Notably, theoretical analysis suggests boron vacancy mediated hBN sheet and hBN and MoS_2 heterostructure without boron vacancy follows two electron transfer processes and promotes hydrogen peroxide formation as a major product instead of OH^- ions. Regarding applications in water splitting and hydrogen evolution reaction (HER), platinum related noble metals and 2D heterostructures have been widely investigated whereas high cost, low durability and complex catalytic mechanisms need to be optimized. To reduce the basal plane inactivity of TMDs like MoS_2 , interlayer spacing and surface functionalization are necessary for facile charge transfer process. The catalytic limitation of MoS_2 has been overcome by formation of MoS_2 - MoO_3 heterostructures with oxygen vacancies. The in-situ preparation of MoS_2 - MoO_3 has multiple Mo oxidation states ($\text{Mo}^{4+/5+/6+}$) due to oxygen vacancies. The metal $\text{Mo}^{5+/6+}$ states are active sites for alkaline HER, ferrocyanide, and para nitrophenol (PNP) reduction. A series of experiments containing Mo^{4+} state (MoS_2 nanosheet, MoS_2 quantum dots, sulphur vacancy induced MoS_2) has been employed to compare the benchmark multiple activities of MoS_2 - MoO_3 . However, the $\text{Mo}^{5+/6+}$ states are inactive for acidic HER catalysis while adsorbed hydrogen spillover from oxygen (MoO_3) to sulphur site (1T MoS_2) triggers the acidic HER kinetics with lower overpotential at 114 mV/decade. The superior acidic and alkaline HER of MoS_2 - MoO_3 is determined in terms of lower overpotential, charge transfer resistance, Tafel slope and higher turnover frequency (TOF), ESCA. The surface sites are masked via integration with masking agent to correlate the activities of binding sites obtained from experimental as well as theoretical validation. The resulting synergistic performances can be employed as a hydrogen storage device for commercial applications. Upcoming challenges are to establish the sensing dynamics of environmental pollutants by low dimensional materials like quantum dots using optical based spectroscopy. The size and functional group dependent carbon/graphene quantum dots (CQD) show broadband excitation and emission which is deconvoluted with four/five individual peaks. The involvement of the surface functionalized groups (OH , epoxy, COOH , COO^- , NH_2) turns the CQD surface to negative zeta potential. The sensing with toxic pollutant Hg^{2+} involves ground state and excited state quenching via sp^2 carbon at basal plane, $(\text{COO}^-)_2\text{-Hg}^{2+}$, $\text{NH}_2\text{-Hg}^{2+}$ complex formation. The recovery of deconvoluted emission and excitation spectra are carried out with

ethylene diamine tetraacetic acid (EDTA) at different Hg^{2+} concentrations. The higher energy peak (π - π^*) has lower recovery percentage in terms of FWHM, peak intensity and area. Whether, the peak originates from n - π^* transitions (COOH , COO^- , NH_2) shows comparatively higher recovery than core state transitions. After recovery, positive surface changes to negative due to complexation of Hg^{2+} with EDTA. The study reveals the sensing mechanism and optical properties of CQD are mainly governed by surface states rather than core states.

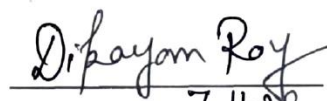
Keywords: NrGO, ORR, capacitance, hBN, DFT, Boron Vacancy, Tafel slope, Electron transfer, Band gap, MoS_2 - MoO_3 , oxygen vacancy, PNP reduction, band engineering, HER, hydrogen spillover, Nitrogen doped carbon quantum dots, photoluminescence, PL signals, Hg^{2+} , PL recovery


7.11.23.

Signature of the supervisor

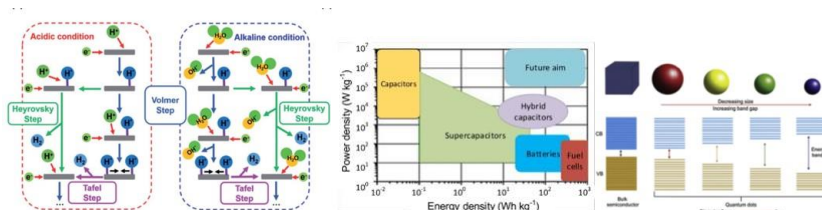
Dr. Sourav Sarkar

Associate Professor
School of Materials Science & Nanotechnology
Jadavpur University
Kolkata - 700032


7.11.23
Signature of the candidate

CHAPTER 1

Introduction



1.1. Material Science and Nanotechnology

1.1.1. Nanomaterials and nanotechnology

From the last decade, nanoscience and nanotechnology have a potential application in wide fields in fundamental science, biomedical, energy-based devices, sensing, optoelectronics devices, foods etc. Nanomaterials have few nanometre order sizes (1 nm to 100 nm) and various applications can be tuned depending on their surface energy, shape, sizes, and composition. The terms nanometre and nanotechnology were first coined by eminent scientists Richard Adolf Zsigmondy and Richard Feynman, who is known as the father of nanotechnology [1]. After 1980, the invention of various characterization tools scanning tunnelling microscopy (STM), atomic force microscopy (AFM) and other sophisticated characterization tools have been employed to investigate nanomaterials with better dimensions to obtain fundamental understandings [2]. Nowadays, nanotechnology is getting attention in all branches like physics, chemistry, biology, medicine, engineering and such correlation is important to develop the next generation materials and advanced technologies. Researchers and scientists have been fascinated to work in this field to minimize the cost and maximize the efficiency of nanomaterials. To poverty eradication, improve health, environment and, economy, United Nations (UN) has focused on sustainable development goals and how nanotechnology can fulfill the above goals [3]. In the environment and energy related applications, next-generation lithium (Li-Na)-ion batteries, fuel cells, polymers, CO₂ reduction, water waste management, green hydrogen production will help also

important in agriculture, food sector and mitigate the problems and promote sustainable developments [4]. Sustainable developments are nanotechnology help supply essential minerals in food to increase yield, and promote food packaging and environmental sensors [5].

1.1.2. Classifications of nanomaterials

Nanomaterials are classified on their dimension, origin, structure, and toxicity. The various types of nanomaterials have been illustrated in Figure 1.1.

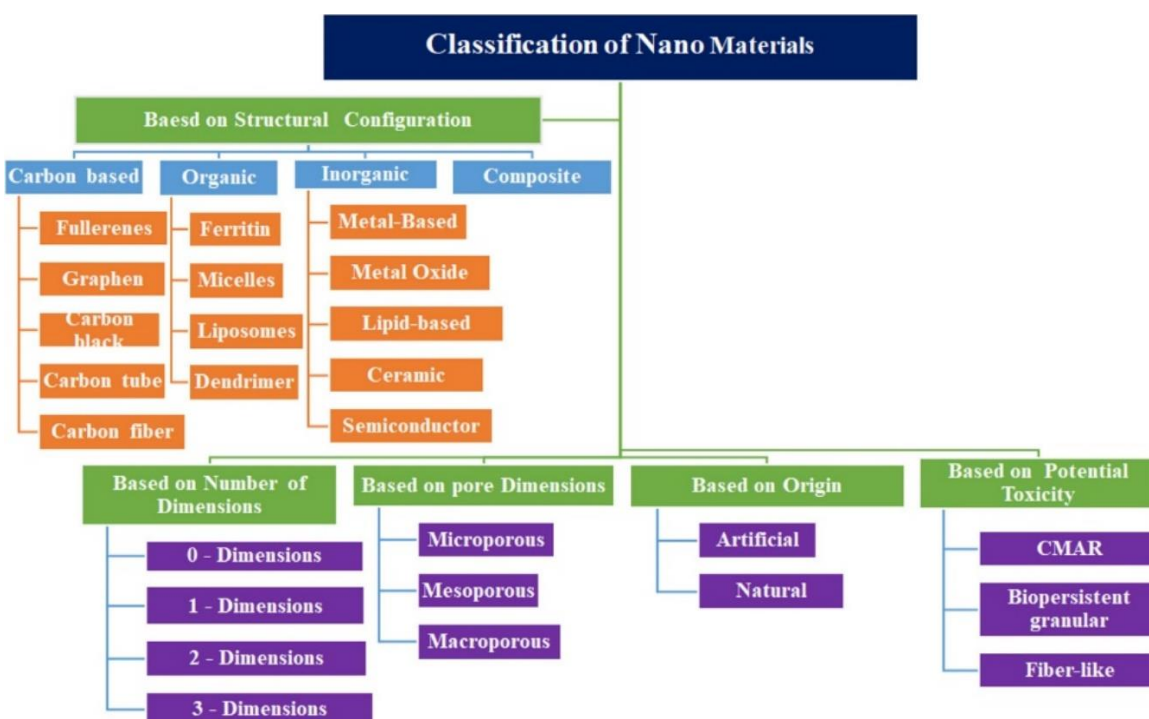


Figure 1.1: Classifications of nanomaterials. [7]

According to the particle dimensions, zero dimensional material (0 D) has three axes (-x,-y,-z) lies in nanoscale range (< 10 nm) (Figure 1.2). It can be crystalline, metallic, semiconducting, ceramic, amorphous and the property depends on the shape, size and quantum confinement effect. In one dimensional material (1 D), two axes lie in the nanoscale range and one axis lies outside the non-metric range (> 10 nm). Nanofibers, nanotubes, nanoribbons, and nanowires are some examples of 1D materials and they can be semiconducting, single or polycrystalline, metallic or ceramic in nature [6]. Two dimensional materials (2D) have two dimensions outside the nanoscale range. Nanosheets, nanotubes, fibres are two-dimensional materials whereas 3D materials have dimensions more than

100 nm. For 0 D system, the closed packed electrons are confined in 3D space due to all dimensions are being nanoscale range. In 1D materials, the density of states lies along the axis of the material. In contrast, the electrons are confined at the thickness and delocalized along the basal plane of the 2D nanosheet [7].

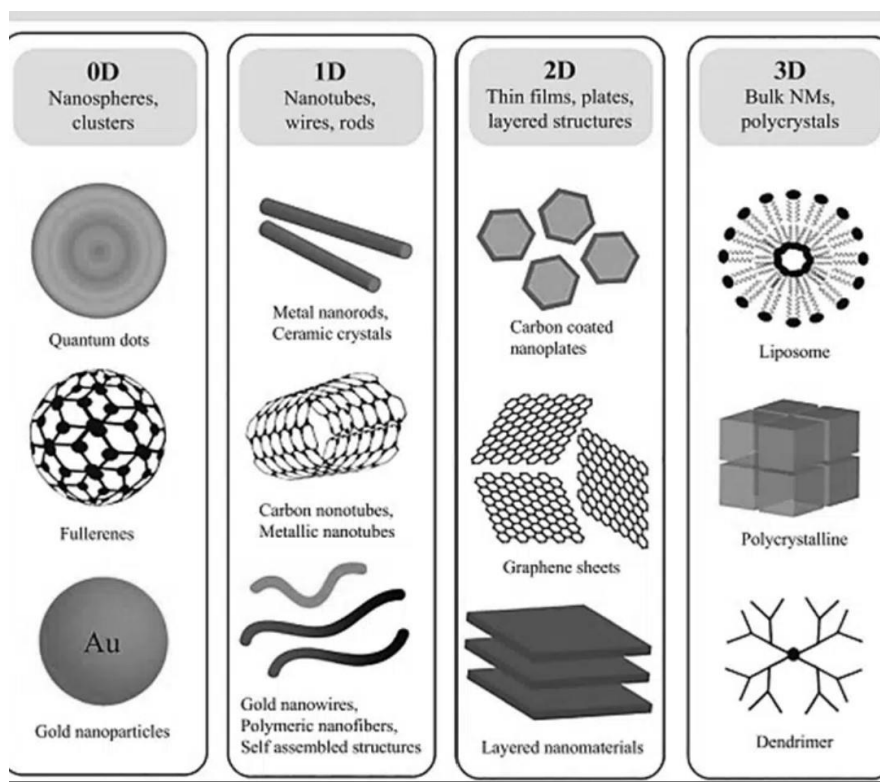


Figure 1.2: Classifications of nanomaterials based on particle dimensions. [8]

Apart from particle dimensions, the variation of pore diameters (micro porous, meso porous, macroporous) can distinguish the nanomaterials. The interaction between the nano material with guest molecule depends on pore diameter and diffusion process. If the particle size of the guest material is lower than pore diameter of the material, there will be more intramolecular interactions through diffusion process. Microporous materials have 2 nm pore diameter which has been utilized in membrane, water purifications. Mesoporous materials have large pore diameter between 2 nm to 50 nm which is used to adsorb various solid and vapor adsorption. Macroporous material has pore diameter above 50 nm which is mainly porous carbon materials, porous glasses. This type of nanomaterials mainly used for functional molecules and sensing

applications [9]. Based on potential toxicity, nanomaterials are classified into three categories i.e. fiber like nanoparticles, bio persistent granular nanoparticles and CMAR (Carcinogenic, Mutagenic, Asthma genic, Reproductive toxin) nanoparticles. Based on potential rigidity and work exposure limit the molecules are distinguished. The proposed work exposure limit of fiber like nanoparticles, bio persistent granular nanoparticles and CMAR lies within the range of 10^4 - 10^5 fibers/ m^3 , 2×10^7 particles/ m^3 and 4×10^7 particles/ m^3 respectively [10]. Structural based nanomaterials are divided into four groups. In organic based nanomaterial, non-toxic biodegradable nanoparticles, lysosomes, micelles are functionalized with long chains and used in various applications in the field of light harvesting, nano sensing and drug administration [11]. Inorganic metal based nanoparticles like Pd, Ni, Au, Ag, Fe, Ti have high surface-to-volume ratios and depending on the capping agent different morphologies can be obtained. Despite the formation of nanoparticles, the strong Van Der Waals interaction between the surfaces of nanoparticles leads to promoting aggregation where effect of ligand can minimize the self-aggregation. Different types of ligands like alkanethiols, alkane amines, carboxylic acids, tri-n-octyl phosphine oxide (TOPO), phosphonic acid are used to bind with metal nanoparticles depending on their binding affinity (HSAB principle), steric factors and position of frontiers orbitals of metals and ligands [12-16]. Due to wide band gap and surface functionalization, metal nanoparticles have served as a potential candidate in bioimaging, catalysts, antibacterial, electrical and optical properties. Metal oxide based nanomaterials like silicon dioxide (SiO_2), zinc oxide (ZnO), and aluminum oxide (Al_2O_3), ferric oxides (Fe_3O_4), tungsten oxide (WO_3) have brought attention due to low cost synthesis, variable band gaps, water splitting and outstanding (photo)-electrochemical stability [17-18]. Moreover, doped metal oxides and oxygen vacancy can enhance photo reactivity, oxygen evolution reactions and water splitting applications [19-20]. Nanostructured hematite (Fe_2O_3) has high surface area where elemental doping and surface passivation can enhance the electrical conductivity and photoactivity [21]. Perovskite based materials (ABO_4) and spinel structures (AB_2O_4) have been widely used in energy devices, photocatalysis and sensing applications due to variable band gaps and reactivity [22]. However, ceramic based solids like phosphides, chalcogenides, carbides, phosphates, carbonates have been synthesized due to variable applications in energy, drug delivery, dye degradation [23]. The mechanical, thermal and electrical properties of the nanomaterials are enhanced due to large scale

synthesis of composite and synergistic effect between two or more nanomaterials [24]. Carbon based materials like graphene, fullerene, carbon nanotube, carbon black have different morphology, dimensions and conductivity. Graphene is the sp^2 hybridized hexagonal network of carbon atoms in 2D surface whereas carbon nanotube is hollow cylindrical morphology with length few micrometers [26-27]. Fullerenes are spherical structures with diameters of 8.2 nm and 4-36 nm for single and multi-layer structures.

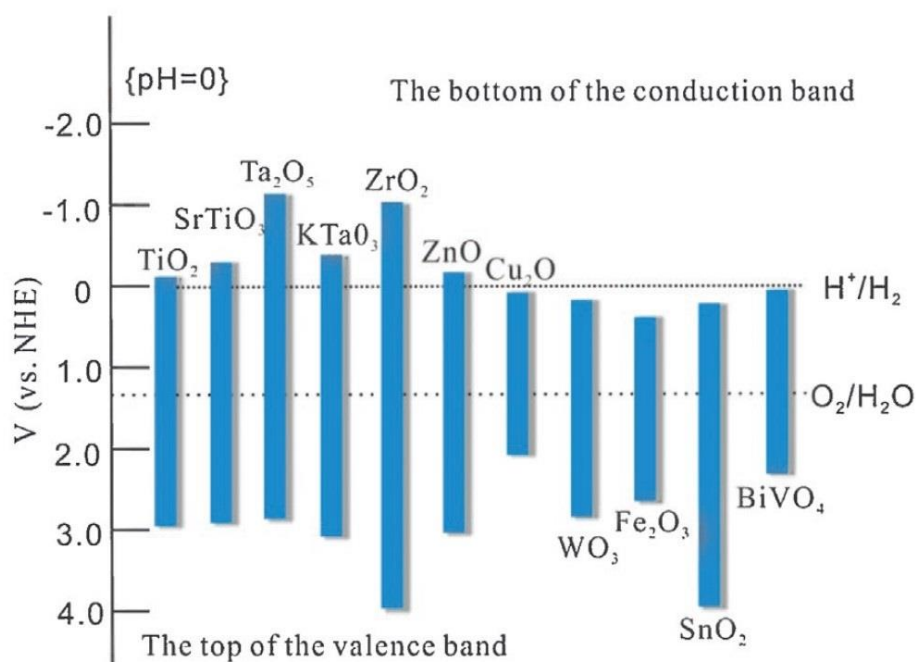


Figure 1.3: Classifications of nanomaterials based on band engineering [25].

1.1.3. Properties of nanomaterials

The structural, mechanical, chemical, optical, electrochemical, magnetic, surface properties of the nanomaterial depend on surface-to-volume ratio, number of atoms and molecules, surface charge and chemical purity.

1.1.3.1 Physical property

The size of the nanomaterials decreases with increasing the surface area and volume ratio. For

example, the surface area and volume of a spherical nanoparticle are $4\pi R^2$ and $\frac{4}{3}\pi R^3$ respectively. Therefore, the surface area and volume ratio can be represented as:

$$\frac{A}{V} = \frac{3}{R} \quad (1.1)$$

The increase in surface area enhances surface atoms and catalytic sites, beneficial for catalytic reactions. The melting point of the nanomaterial decreases with decrease in size due to high concentration of unbound or surface free atoms. The melting points of the nanomaterials are lower than bulk material and ionic compounds where electrostatic interaction between two different atoms increases the melting points. The transition temperature, curie temperature also decreases when bulk materials are reduced to nanometer size. The Ge nanowires with size 10-100 nm change their melting point to 650°C from 950°C in bulk form [28]. However, the mechanical strength is enhanced with decreasing size which is mainly due to lesser impurities and more perfections of the facets at the reactive sites. The hardness, internal strength and young modulus of nanomaterials increase with decreasing the grain size. For example, the σ bond along the axial line of carbon nanotube (CNT) improves the mechanical strength to 1 Tpa range [29]. Graphene is known as strong material due to high intrinsic strength of 42 N/m. The strength and stiffness of graphene remain unchanged after induced doping [30].

The optical properties are modified with the diameter of the nanoparticles. When the particle size is equal to de-Broglie wavelength, band gap increases due to quantum confinement effect (Figure 1.4). The energy levels become distinct and variable color changes occur between 2-10 nm particle sizes. However, the interaction of conduction band electrons with external electric field and coherent electronic oscillation on the surface of nanoparticle induces nonradiative excitations which are commonly known as surface plasmon resonance (SPR). For Au nanoparticles, the SPR occurs at 520 nm in aqueous solvent and the high intensity allows for bioimaging based applications [31]. The magnetic properties like giant magnetoresistance, tunneling magnetoresistance, and superparamagnetic behavior exist with decreasing the particle sizes of the nanomaterials. It has been observed that particle size less than 40 nm shows super para magnetism due to the existence of very low or single domain regions.

For larger particles, the multidomain region decreases the coercivity shown in Figure 1.5. In giant magnetoresistance, a conducting (nonmagnetic) layer is sandwiched between two ferromagnetic materials and the resistance is measured in presence of magnetic field.

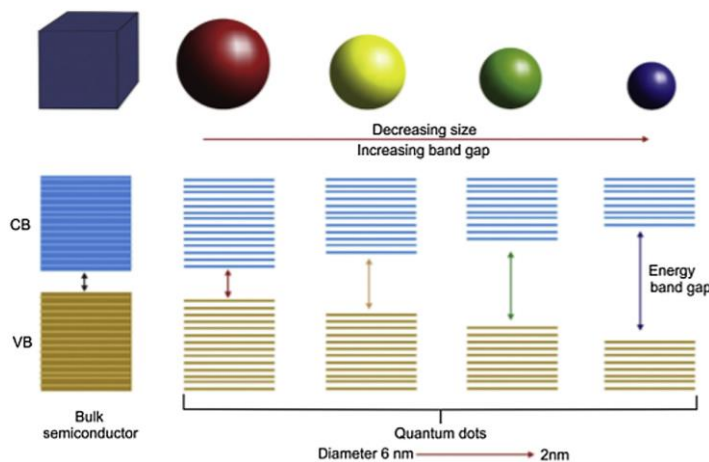


Figure 1.4: Quantum confinement effect of quantum dots.[32]

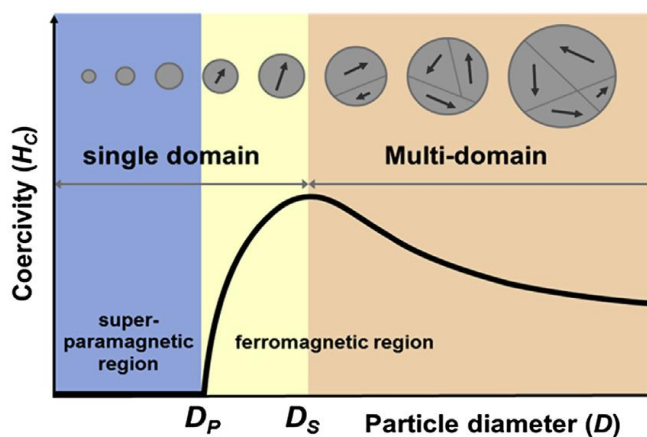


Figure 1.5: Correlation of coercivity with particle size. [33]

1.1.3.2. Chemical property

The solubility in different solvents is the essential parameter for nanomaterials where solubility increases with decreasing the particle size. The increase in solubility is also related to surface curvature (convex and concave) and chemical potential of the system. The chemical potential is dependent on the radius of curvature of the surface, surface energy, atomic volume and the relation is shown as: [34]

$$\Delta\mu = 2\gamma\frac{\Omega}{R} \quad (1.2)$$

Where $\Delta\mu$ is the chemical potential, γ is the surface energy, Ω is the atomic volume and R is the radius of curvature in spherical surface. From eq. 1.2, it is clearly shown the chemical potential is inversely proportional to radius of curvature. The convex surface has higher surface potential and lower R which increases the solubility of the particles. The stabilization of the particles also depends on surface energy, electrostatic and steric stabilization. The tight bounds of oppositely charged ions are attracted to the surface of the nanoparticles which is known as stern layer.

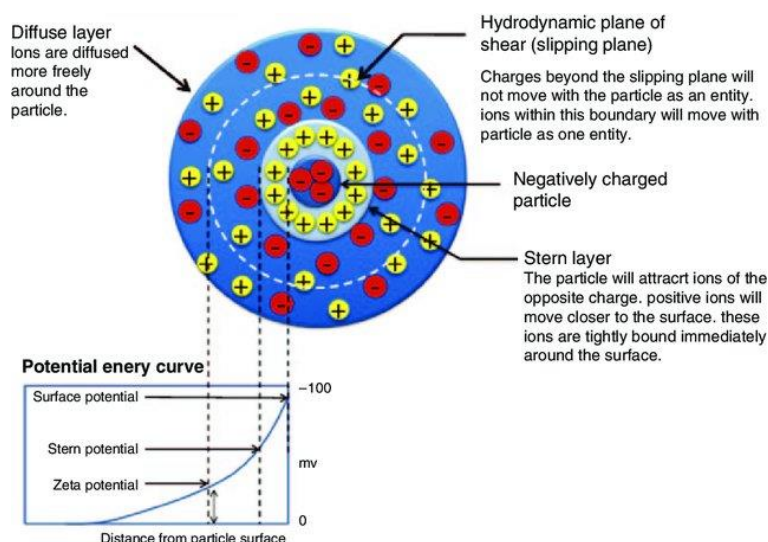


Figure 1.6: The electrical double layer, surface potential on the surface of a nanoparticle is based on the Gouy-Chapman-Stern model.[35]

Depending on the diffusion coefficient, the different charged ions are surrounded by stern layer. Finally, the diffuse layers are formed having free ions which are known as Gouy layer (Figure 1.6). When two particles will come closer, the double layers will overlap and create a repulsive force increasing the stability of particles in solvent. A potential barrier was established between the particles to reduce the agglomeration when the electrostatic repulsive force overcomes the van der Waals attractive forces. However, polymer based surface adsorption forms chemical bond with nanoparticles and enhance the stability due to steric effect. The solubility, zeta potential and

foreign particle interaction can be modified through surface functionalization. For carbon based materials, various covalent groups like carboxyl, hydroxyl, amines can change the zeta potential and allow to binding of small polymeric molecules [36]. Depending on the binding ability with polymers, the π - π and van der Waals stacking between the CNT molecules can be optimized and subsequently solubility and reactivity can be tuned. However, anchoring of protein on carbon based surfaces enhances protein-protein recognition and hydrogen bonding [37]. The reduction of size of nanomaterials also influences surface energy or surface tension. Surface energy depends on the broken bonds of the surface atoms and is represented as:[38]

$$\gamma = \frac{1}{2}N_b\epsilon\rho_A \quad (1.3)$$

. Where, γ is the surface energy, ρ_A is surface atomic density, N_b is number of broken bonds and ϵ is the bond strength. The chemical properties of the nanomaterials also change with the surface energy. The surface containing higher Miller indices has higher surface energy where as formation of larger particles due to Oswald ripening and strong chemical bonds reduce the surface energy of the nanoparticles [39].

1.1.4. Structural and electronic properties of 2D materials

1.1.4.1. Non metal based 2D materials

Graphene has been studied more extensively due to high surface area, conductivity, porosity, high mechanical strength and flexibility [40]. Graphene is sp^2 bonded network of carbon atoms and has zero band gap. The thickness of graphene is 0.35 nm and the carbon-carbon bond length is 0.142 nm. Graphene has flat surface which allows the different aromatic molecules for adsorption, doping and functionalization. The single layer is highly transparent and absorbs 2-3% of light. The optical properties change with layer number of graphene. The electronic and thermal conductivity of graphene is 10^6 S/m and 5×10^3 W/mK respectively. The valance and conduction band overlap at room temperature exhibits cone like structure which is known as Dirac point [41]. The delocalization of π electrons and overlap of bands are the origin of high conductivity of graphene. The doping induced defect with transition metals of graphene can lead to enhancing the magnetic properties of graphene. Different chemical route has been utilized to prepare graphene or reduced graphene oxide where oxygen functionalization like epoxy, hydroxyl, carboxylic groups are present at the basal plane and edge state of graphene. Nitrogen

and boron can lie in the same period of carbon which can replace carbon atoms by substantial doping through various thermal treatments and reducing agents. The incorporation of nitrogen leads to pyridinic, pyrrolic, graphitic, imide, amide, amines group which has potential applications in energy and optoelectronics field [42]. The boron doping can open the band gap of graphene due to different types of point defects [43]. Two dimensional hexagonal boron nitride (hBN) is analogous to graphene having sp^2 hybridized boron and nitrogen atoms alternately lie in hexagonal honeycomb lattice. The electrostatic force and van der Waals interaction between two adjacent layers are responsible for interlayer distance similar to graphite or multilayer graphene. The interlayer spacing is 0.33 nm which is almost analogous to graphene but hBN has higher band gap (5-6 eV) than graphene due to high asymmetry [44]. Due to high band gap, hBN is electrically inactive and used as an active layer in tunneling based devices. Two types of stacking such as AA/ and AB stacking have been observed in hBN but the most possible stacking depends on sonication and synthetic conditions. hBN is thermally stable and thermal expansion coefficients depend on the number of layers. The high temperature resistance and frictional characteristics make hBN a separator of metals to prevent aerial oxidation and corrosion. For example, the hBN is used as a coating agent to prevent nickel, cobalt, alloys, graphene due to high thermal stability (above 1100°C) [45]. The hBN is also beneficial as a protective layer on Cu surfaces in Li/hBN/Cu based batteries to reduce the suppression of Li based dendrites [46]. Golberg et al. have proposed the ejection of boron and nitrogen in hBN by C doping in graphene/hBN composites which opens up band gap of graphene and two electrical conductivity regimes have been created [47, 48]. Thus doping and functionalization of hBN can change, structural, electronic and catalytic properties.

1.1.4.2. Transition metal dichalcogenides (TMDs)

Transition metal dichalcogenides (TMDs) are layered materials having transition metals are sandwiched between two chalcogenides (triple layers) via weak van der Waals forces. The transition metal consists of group IV (Si, Ge, Sn), V (V, Nb, Ta), and VI (Cr, Mo, W) where chalcogenides are Sulphur (S), selenium (Se) and tellurium (Te). The crystal structure of bulk TMDs has three possible stacking structures; 1T, 2H and 3R structures. 1T phase is highly active with octahedral coordination and tetragonal geometry where 2H and 3R structures have

hexagonal and rhombohedral geometry respectively (Figure 1.7). Li intercalation promotes the phase transfer between 1T and 2H phases where the two phases exist with strain free interactions. Unlike pristine graphene, coulombic interaction becomes important for TMDs rather than van Der Waals interaction. Theoretical prediction suggests the indirect to direct band gap transition occurs when bulk TMDs are converted to single layer [49]. The direct band gap at k point remains unaltered which depends on the d orbital energy and is independent of layer thickness. The Γ point is related to p orbital of chalcogens and d_{z^2} of the transition metal which increases during Γ to k point transition. DFT calculation manifests Γ to Γ -K and K to Γ -K increases from bulk to single layer transition for MoSe_2 where K-K direct bandgap is same to a value of 1.34 eV [50]. To correlate the phenomenon experimentally, temperature dependent photoluminescence (PL) spectra were carried out for bulk and single layer TMDs where band gap increases for single layer structure [51]. The electronic band gap of various TMDs is tuned by doping with various adatoms (C,N,F,O,H etc.) [52]. It is shown the addition of hydrogen on the top surface of sulphur in MoS_2 is thermodynamically preferable and induces n type behavior. In other case, adsorption of nitrogen enhances the p type character [52,53]. The Nb and Ta doping in TMDs changes the semiconducting to metallic phase and opens up different electronic applications [54]. The compressive, tensile strain can modulate the band gap of the TMDs where d orbital of transition metals are strain dependent. The direct band gap of monolayer TMD can be shifted to indirect band gap when strain is applied in monolayer between 0.03 to 0.09.

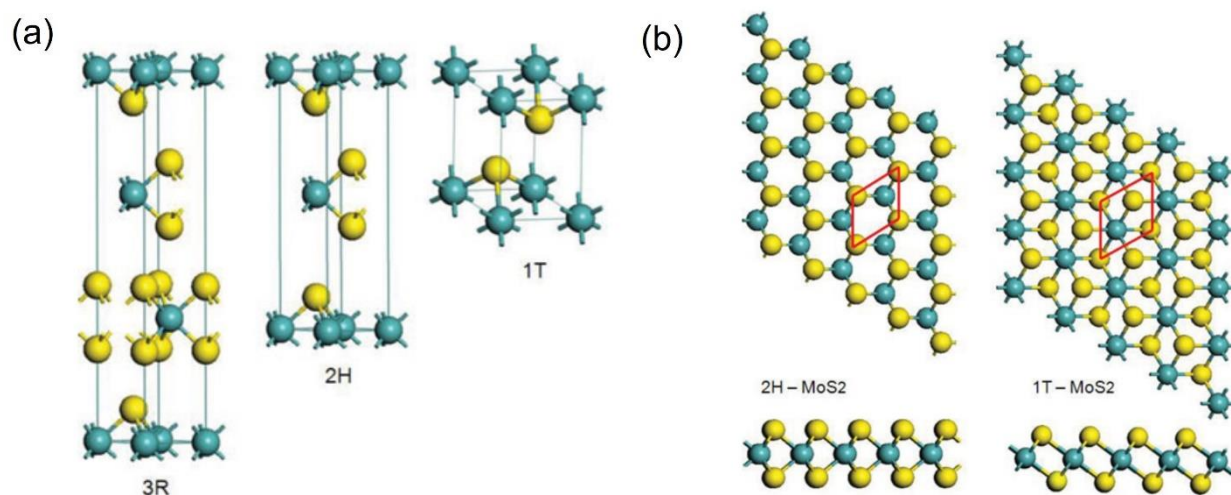


Figure 1.7: Unit cell and 1T, 2H and 3R MoS_2 . Mo: blue, S: yellow. [56].

When the strain is above 0.1, the dz^2 of metal is closer to Fermi level which leads to overlap of valance band and conduction band and metallic character increases [55]. Besides, layer structure, TMD nanotube can be established theoretically and experimentally as similar to carbon nanotube (CNT). Different types of morphologies like armchairs, zig-zag, chiral nanotubes can be constructed where chalcogen atoms have different charges at inner and outer walls [57]. Due to rolling effect, inner chalcogen atoms are compressed where outer atoms are strengthened leading to lower overlap between metal d orbital and p orbitals of chalcogens. Similarly, the band gap has been reduced from monolayer TMDs which is greater than the bulk counterpart [58].

1.2. Electrochemistry and fundamentals of energy conversion and storage

1.2.1. Green Energy and electrochemistry on energy storage

The consumption of fossil fuels produces almost 80% of energy consumption but the emission of greenhouse gas due to combustion of fossils enhances global warming. In 2019 UN climate summit, the primary goals of maximum nations are to zero emission of CO₂ and use clean and renewable energy are the main alternatives to reduce global warming [59]. Green energy is the electricity produced from renewable energy sources such as solar cells, biomass, wind energy, geothermal energy. Green energy can be used in daily life and industries due to zero pollution. Clean, sustainable energy production can reduce the air pollution and global warming with efficient energy-conversion storage systems. Electrochemical technology involves energy generation such as fuel cell, batteries, synthesis of chemicals, sensors, electrodialysis [60-62]. Environmental electrochemistry removes different poisonous impurities from gaseous mixtures, solids and liquids. Different types of electrodes like 2D, 3D, gas diffusion electrodes are utilized to separate gaseous compounds like chlorine (Cl₂), ammonia (NH₃) gas and oxidation of carbon monoxide, nitric acid [63]. Batteries and fuel cells involve controlled oxidation and reduction reactions of selective compounds electrochemically where scientists and researchers are now motivated to design different materials depending on size, reactivity, stability and morphology. Both configurations contain electropositive anode and electronegative cathode with a separator. Water electrolysis is the source of renewable hydrogen energy which becomes an alternative way for fossil fuel effectively. The two half cell reaction i.e. hydrogen evolution reaction (HER) and

oxygen evolution reaction (OER) occurs at cathode and anode respectively in water electrolysis. The large scale production of hydrogen and oxygen is essential and the large overpotential with sluggish kinetics rate requires selective materials. However, solar technologies like solar cells have been designed with various organic and inorganic films to mitigate the energy crisis in modern century. Energy and power density are the two crucial parameters for energy storage devices. Energy density is how much energy is stored per unit volume and power density is the energy stored per unit of time. A superior energy storage device has both high energy and power density. Battery, supercapacitor, capacitor, fuel cell are energy storage devices where battery, fuel cell have high energy density. Capacitor has low energy density but high power density whereas supercapacitor is the bridging materials between battery and capacitors (Figure 1.8).

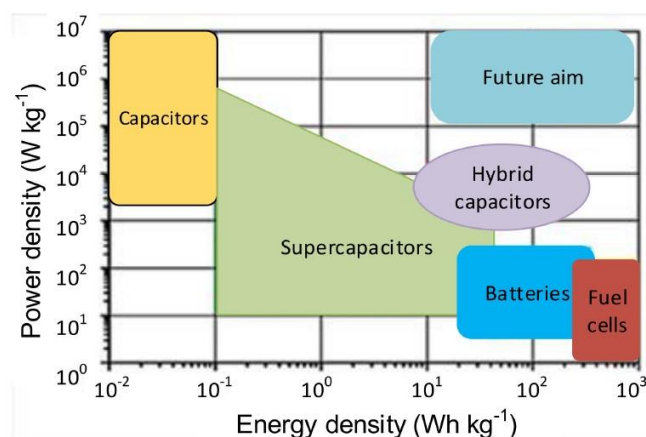


Figure 1.8: Correlation between energy devices. [64]

1.2.2. Fundamental on Batteries

Batteries are indirect forms of energy storage that can be preliminarily classified into two categories i.e. primary and secondary batteries. Primary batteries cannot be recharged whereas secondary batteries are rechargeable. Electrochemical Battery device converts chemical redox reactions to electrical energy and is composed of two electrodes, one separator or salt bridge. The salt bridge is used to prevent mixing and maintain electrical neutrality. The battery is fabricated by depositing electrolytes and electrodes on paper. The Au/Cu based paper batteries can supply voltage upto 3V with current range of $0.7 \mu\text{A}$ to $25 \mu\text{A}$ where the electrode is prepared on the thin paper by thermal evaporation [65]. The operating system of electrochemical battery is simple and produces power upto μW to mW range. In some cases, the electrode, electrolytes

are unstable, explosive and flammable which resists them as a potential candidate for environment friendly batteries. Biofuel energies have taken much attention due to conversion of biochemical energy to electricity through biocatalysts [66]. Instead of expensive noble metals, sugar, pyruvate, ethanol, microorganisms, and enzymes are used as a biocatalyst. Microbial fuel cell consists of cathode and anode separated by proton exchange membrane where H^+ ions can pass from anode to cathode. Enzymatic biofuel cells use enzymes that facilitate the electron generation between electrodes. Generally, glucose oxidase, laccase is used as a catalyst and Whatman filter paper is used as a substrate. For oxygen electroreduction, functionalized CNT is used as a ionic electrolyte to increase the stability of the biocatalyst [67]. Li-ion battery (LIB) is a promising candidate for battery applications due to its high energy and power density. The high reactivity and mobility of Li ion van easily move between the electrodes and separators. In LIB the cobalt oxide acts as a cathode and graphite layer is anode. During discharging, the Li^+ ion intercalates between the layer of the graphite to form LiC_6 and CoO_2 is reduced to $LiCoO_2$. [68]

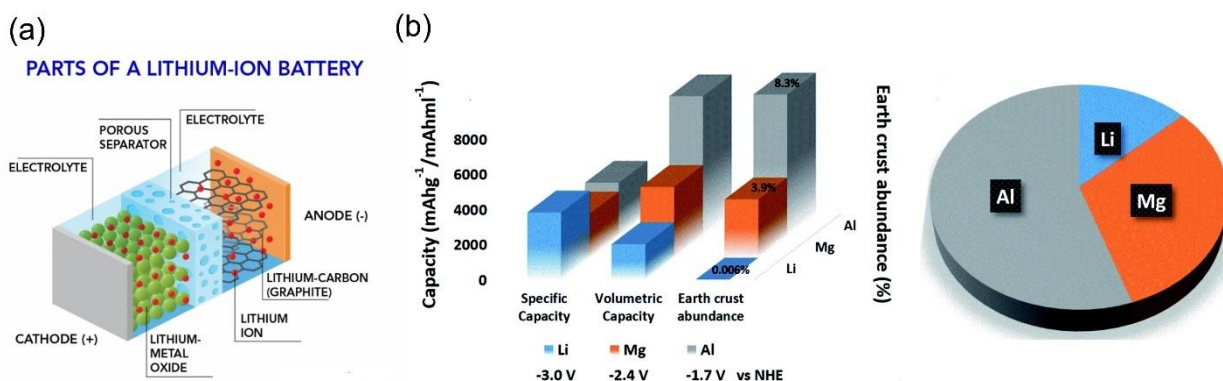
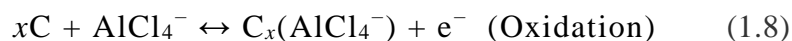
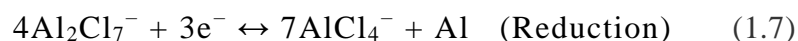


Figure 1.9: (a) Li ion battery configurations. (b) Performance of Li, Mg and Al battery.[69]

The four types of LIB batteries are cylindrical, prismatic, coin and pouch cells. The Shuttling effect of Li^+ ion produces heat and no dissipation of heat occurs during charging-discharging

effect. Due to high heat production, LIB batteries need safety. At high voltage and temperature, the solid electrolyte interface (SEI) undergoes decomposition and dendrite formation with Li-ion. Therefore, the oxygen evolution at the cathode results explosion and rupture of electrodes. Besides thermal runaway, mechanical and electrical abuse can cause damage to battery and undergo explosion. For safety assessments, several safety tests have been employed like overcharged tests, heating tests, short circuit tests, crush tests [70]. Recently, Mg and Al ion batteries are the alternatives to Li batteries due to low cost, environmentally friendly and low probability of dendrite formation [71]. In Al ion battery or Al ion dual battery (AIB or ADIB), the trivalent Al^{3+} has multiple charge transfer and high volumetric capacity (four times than Li battery) to $8046 \text{ mA h cm}^{-3}$. However, the theoretical energy density potential of AIB lies at a value of 1060 W h kg^{-1} which is higher than LIB based batteries (406 W h kg^{-1} limit). The reaction mechanism of ADIB at cathode and anode is shown as follows: [72]



The mechanism of AIDB is more complex where AlCl_4^- ions have dual roles in reaction mechanism. Magnesium ion battery (MIB) has similar configuration to Li battery having cathode, anode and current collector. For example, Mg is used as an anode and V_2O_5 layer as a cathode using $\text{PhMgCl-AlCl}_3/\text{THF}$ electrolyte. The chemical reaction between cathode and anode produces electricity as shown: [73]



Current research focuses on the development of low cost, environment friendly cathode materials, current collectors and investigation of side reactions during charging-discharging mechanism.

1.2.3. Supercapacitor as energy storage device

Supercapacitors (Sc) are employed as conventional energy storage devices with high power density, long charge-discharge cycle and moderate energy density. Depending on the charge storage mechanism, materials and energy density, Sc can be classified into three types i.e. pseudo capacitor, electrical double layer capacitance (EDLC) and hybrid capacitor (Figure 1.10). In pseudo capacitor (Pc), Faradic redox reaction occurs between electrode material and electrolyte.

The process is reversible and high charge storage system. The Faradic reaction (oxidation and reduction) depends on diffusion of ions, dopants, surface area, type of materials, multivalence states, conductivity and electrolytes [74].

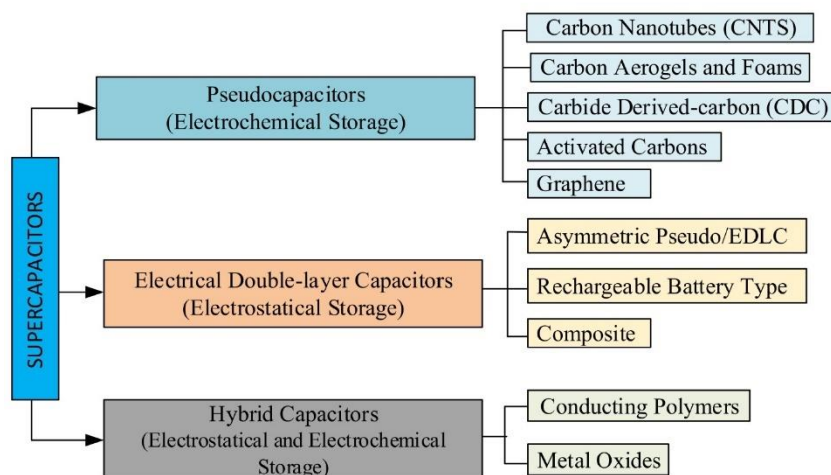


Figure 1.10: Different types of supercapacitors. [74]

The capacitance is much larger than EDLC type of capacitor. However, Pc suffers from long term cycling stability hinders its commercial applications and researchers are motivated to synthesize different redox active materials to enhance the supercapacitive performances and long term durability. EDLC type Sc is made of two electrodes, electrolyte and one separator. EDLC can store charges via electrostatic attraction between two opposite charges at the electrode-electrolyte interface. Therefore, an electrical double layer and electric fields arise at the electrode interface. The nonfaradic (no redox) charge storage in EDLC involves double layer theory which is based on Helmholtz, Gouy-Chapman and Stern model. According to this theory, at electrode-electrolyte interface, three zones have been established. The inner Helmholtz plane (IHP) consists of specific adsorbed ions, outer Helmholtz plane (OHP) is non-specific solvated ions and finally the diffuse layer contains different solvated and counter ions (Figure 1.11). For electrostatic capacitor, the fundamental equation is given as: [75]

$$C = \frac{\epsilon \times \epsilon_0 \times A}{d} \quad (1.11)$$

Where C is the capacitance, A is the surface area of the electrode, ϵ is the relative permittivity of the material, ϵ_0 is the vacuum permittivity and d is the distance of the electrodes. The relation

between entire double-layer (C_{dl}), diffusion layer (C_{diff}) and stern layer (C_H) are determined from Gouy-Chapman and Stern model as follows: [76]

$$\frac{1}{C_{dl}} = \frac{1}{C_{diff}} + \frac{1}{C_H} \quad (1.12)$$

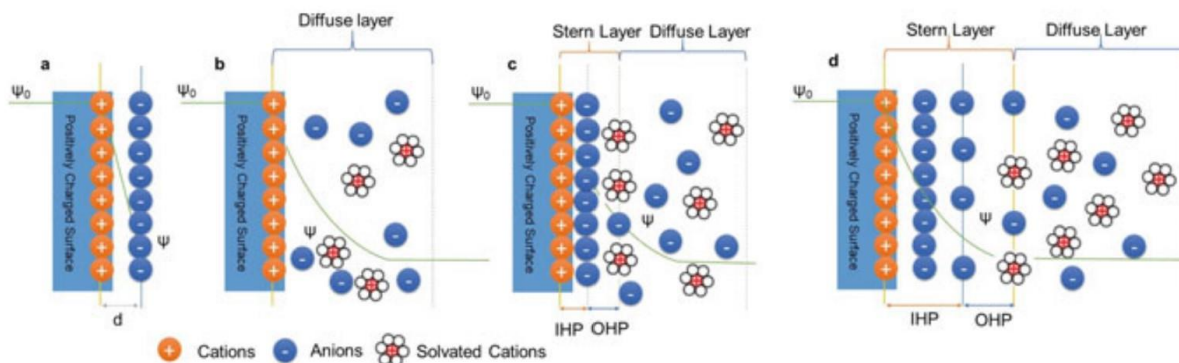


Figure 1.11: EDLC mechanism from Helmholtz, Gouy-Chapman and Stern model. [77]

The activation and adsorption of charges on the electrode surface depend on surface area of the material, conductivity and pore diameter. Carbon based sample acts as a EDLC type Sc due to high polarizability, larger window, thermal stability, various doping concentrations and morphologies like graphene, CNT.MWCNT, activated carbon and high conductivity. The energy density of EDLC type materials has higher energy density than Pc. Moreover, hybrid supercapacitor is utilized as a bridge between battery and capacitor due to high energy density and specific capacitance. Conducting polymers, metal oxides are treated as hybrid supercapacitor that possesses both pseudo and EDLC type behavior. The electrodes in Sc can be modified with same or different types of materials i.e., symmetric and asymmetric supercapacitors. Symmetric supercapacitor is mostly used due to low cost and easy fabrication process. In asymmetric supercapacitors, anode is made of carbon derivatives and cathode materials are mainly different polymers, metal oxides, ceramic materials etc.

For Sc measurement, cyclic voltammetry (CV), charge discharge (CD) and Electrochemical impedance spectroscopy (EIS) are studied in two or three electrode systems. For the three electrode system, Gravimetric capacitance or specific capacitance from CV and CD can be calculated as follows [78]:

$$\text{For CV} \quad C = \frac{\int_{V_1}^{V_2} I(V) \times dV}{m \times \Delta v \times \frac{dv}{dt}} \quad (1.13)$$

$$\text{For CD} \quad C = \frac{\Delta t}{m \times \Delta v} \quad (1.14)$$

$$\text{For Areal CV} \quad C = \frac{\int_{V_1}^{V_2} I(V) \times dV}{A \times \Delta v \times \frac{dv}{dt}}, \quad (1.15)$$

where, $\int_{V_1}^{V_2} I(V) \times dV$ is the current response during the cathodic and anodic scan, m is the mass (in gram), Δv is the potential window in volts, $\frac{dv}{dt}$ is the scan rate in mV/s, Δt is the discharged time without IR drop in a sec, A is the surface area of active material on the substrate. Specific capacitance was measured in F/g and areal capacitance in mF/cm².

The energy and power density has been calculated as

$$E = \frac{1}{2} \times C \times V^2 \quad (1.16)$$

$$\text{and} \quad P = \frac{E}{t} \quad (1.17)$$

Where E and P are energy and power density in Wh/kg and W/kg respectively.

For EIS measurement, the electric potential Ψ is a harmonic potential with time and is represented as: [79]

$$Z = \frac{\Psi}{j} e^{i\phi} = Z' + Z'' \quad (1.18)$$

Where Z' and Z'' are “real and imaginary impedance” respectively. The relation between impedance, capacitance (C) and frequency (f) per unit surface area is given by: [79]

$$C^{EIS} = \frac{-1}{2\pi f Z''} \quad (1.19)$$

The capacitance (C) is calculated from “RC” circuit model where C depends on applied frequency. The double layer form at the electrode-electrolyte surface is related to RC circuit which contains resistance and capacitance in series or double layer capacitance and diffuse capacitance in series (Figure 1.12). EIS data is fitted with this model to obtain double layer capacitance, resistance but the process is not universal. Nyquist plot of EDLC consists of three regions such as semicircle region (AB at high frequency), non-vertical region (BC) and vertical region (above C) (Figure 1.12). R_A and R_B correspond to bulk electrolyte, electrode and contact

area at the electrode-electrolyte interface. The difference between the two resistances (R_{AB}) denotes the charge transfer resistance. The non-vertical line BC manifests the diffusion layer where ion transport occurs from

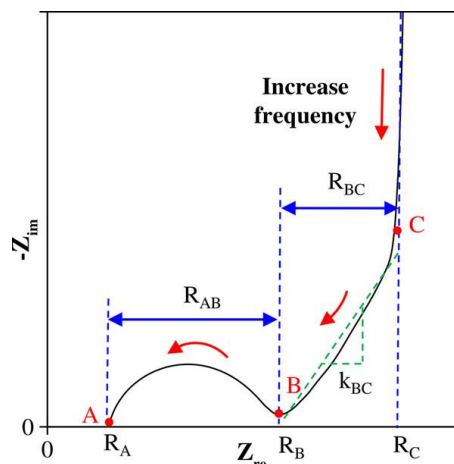
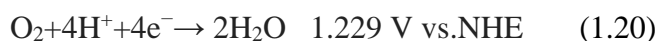


Figure 1.12: Nyquist plot for EDLC electrode. [80]

bulk to electrode interface and pores. At the point C, electrical double layer formed. However, there are practical limitations of RC models such as nonuniform concentration of electrolytes and diffusion of neglecting ions.

1.2.4. Oxygen reduction reaction and fuel cells

The restoration of renewable fossil fuels has an adequate effect on sustainable energy storage and clean environment. Recently, fuel cells have been alternative energy source for energy storage devices. The high power density and production of chemical energy in fuel cells are efficient for high power generation. Two types of fuel cells have been designed i.e. alkaline fuel cells and proton exchange membrane fuel cell (PEMFC). In fuel cell, hydrogen ion reduction (HOR) reaction occurs at anode and oxygen reduction reaction at cathode simultaneously [81]. The ORR process proceeds through two reaction pathways. The initially two electron transfer process forms hydrogen peroxide (H_2O_2) which after reduced to water via two electron transfer process. The overall four electron transfer process produces water in the final product. The reaction in PEMFC can be represented as follows: [83]



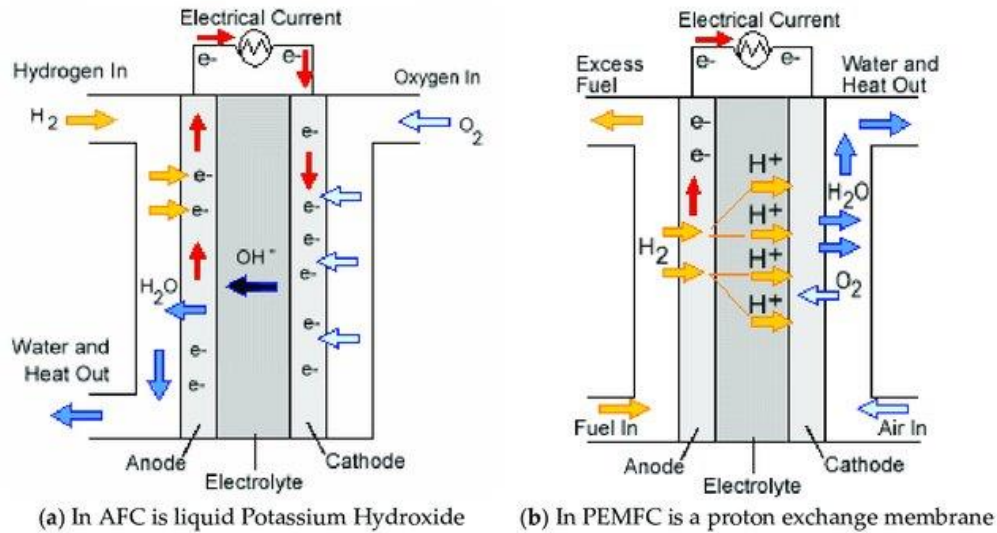
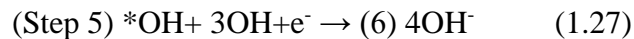
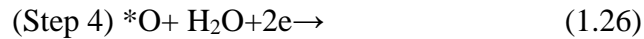
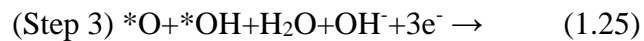
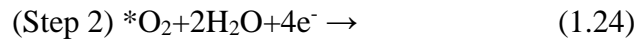
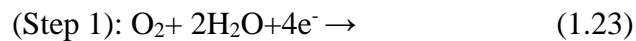
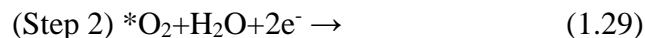
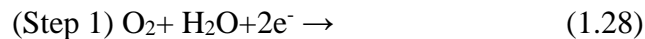


Figure 1.13: Alkaline and proton exchange membrane fuel cell. [82]

ORR in alkaline medium proceeds via either of the two following pathways, namely, the four electron pathway:



where * denotes chemisorption's site on the catalytic surface or via energetically less efficient two electron pathway:





However, the reaction rate becomes sluggish at cathode due to inactivity of the O-O double bond to dissociate and adsorb on the surface of the catalyst. The adsorption of O₂ on the catalytic surface and the intrinsic nature of the catalyst can influence the rate of the ORR kinetics. The binding ability of intermediate *OOH, *OH, O* with active sites of the catalyst predicts the rate determining step of the reaction. Generally, very strong or very weak adsorption sluggishes the reaction kinetics and the catalyst becomes less active to show facile catalytic performances. When, the binding constant of *OOH (O*+ OH*) is high after adsorption on surface, the process is slow and termed a rate determining step (RDS) [84]. In another case, if the binding of O₂ is weak, then protonation of oxygen and formation of *OOH will be the slow step i.e., rate determining step. However, the metal based d band energy near the adsorbent energy level promotes charge transfer and the high activation energy of the O-O bond breaking can be minimized. Thus, depending on exposed active sites, facile mass transfer ability, mobility, pore diameter of the catalysts such as platinum (Pt) and palladium (Pd) have been utilized for ORR catalysts [85]. Rotating disk electrode (RDE) and rotating ring-disk electrode (RRDE) techniques are used to study the oxygen reduction kinetics. In RDE, the rotation of flat disk electrode produces laminar flow near the electrode surface (cathode) which enhances the mass transfer rate. The electrochemical kinetics of oxygen reaction has been evaluated from the Koutecky-Levich (K-L) equation as follows [86].

$$\frac{1}{J} = \frac{1}{J_K} + \frac{1}{J_L} \quad (1.31)$$

$$\frac{1}{J} = \frac{1}{J_K} + \frac{1}{B\omega^{1/2}} \quad (1.32)$$

$$B = 0.21nFD^{2/3}C_0\nu^{-1/6} \quad (1.33)$$

$$J_K = nFKC_0 \quad (1.34)$$

Where J is the current density (mA/cm²), J_K and J_L are the kinetic and limiting-diffusion current density (mA/cm²), ω is the rotation speed of working electrode, n is the total electron transfer number for oxygen reduction, D is the diffusion coefficient of oxygen in 0.1 (M) KOH, F is the Faraday constant, C₀ is the bulk concentration of O₂, ν is the kinematic viscosity of the

electrolyte, K is the electron transfer rate constant. The plot between $1/J$ vs. $1/\omega$ results a linear characteristic curve which denotes first order reduction kinetics of oxygen. Electron transfer number (n) and electron transfer rate constant (K) can be evaluated from the slope and intercept respectively. The linear portion of the Tafel plot can be obtained by plotting the logarithm of kinetic current density vs. Potential applied in RHE as follows [87]:

$$\eta = a + b \log (J_k) \quad (1.35)$$

Where, η is over potential (V), a , and b are constant and Tafel slope respectively.

The percentage of peroxide generated within the intermediate and electron number are also calculated from RRDE tests following the Eqn:

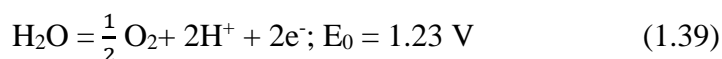
$$H_2O_2 (\%) = 200 * \frac{\frac{I_r}{N}}{\frac{I_r}{N} + I_d} \quad (1.36)$$

$$n = 4 * \frac{I_d}{\frac{I_r}{N} + I_d} \quad (1.37)$$

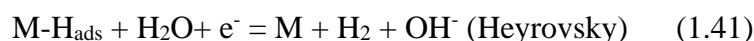
Where, I_d and I_r imply disk and ring current, current collection efficiency $N=0.42$.

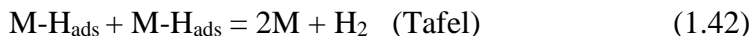
1.2.5. Water splitting reaction

To develop renewable, clean energy production and reduce fossil fuel combustion, hydrogen gas (H_2) can be an attractive fuel in modern technology. The electrolysis of water to produce hydrogen and oxygen can be an efficient strategy to replace fossil fuel combustion. In water splitting, hydrogen evolution (HER) occurs at cathode and oxygen evolution (OER) at anode where the OER process involves multistep reaction and requires higher activation energy. The overall reaction at cathode and anode is represented as: [88]



The HER kinetics depends on the reaction intermediate and the rate determining step. Three types of intermediates have been postulated in acidic and alkaline HER such as Volmer, Tafel and Heyrovsky mechanisms.





In Volmer- Heyrovsky mechanism, the surface-active sites are comparatively lower than Volmer-Tafel mechanism. The adsorption of hydrogen (H_{ads}) occurs on the active site in the primary step (rate determining step) in Volmer- Heyrovsky mechanism and further addition of another water molecule on H atom produces hydrogen gas and hydroxyl ion. On the other hand, Volmer-Tafel mechanism involves the adsorption of two hydrogens on the active sites where the distance between the active sites is much lower than the van Dar Waals radius of the dihydrogen (Figure 1.14). Experimentally, the mechanism is established from the Tafel slope analyses. In Volmer process, the Tafel slope lies within 120 mV/decade during H^+ adsorption desorption process. In Heyrovsky and Tafel mechanism, the Tafel slope is 40 mV/decade and 30 mV/decade respectively. The HER process can be determined from linear sweep voltammetry (LSV) where the efficiency of a HER catalyst can be predicted to measure the overpotential (η) at current density of 10 mA cm^{-2} . The rate of alkaline HER is slower than acidic HER due to dissociation barrier of H_2O molecule at the intermediate. In OER catalysis, the Tafel slope lies within 120 mV/ decade which is governed by hydroxyl ion adsorption (initial step). The lower Tafel slope at 40 mV/ decade indicates M-O_{ads} group is the key step i.e. rate determining step [90]. The different rate determining step involved in HER and OER kinetics depends on type of catalyst, temperature, electrolyte concentration.

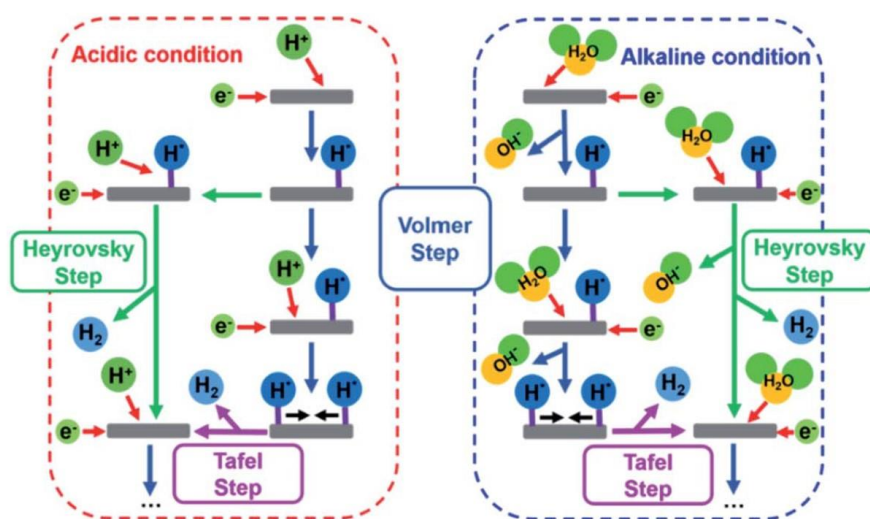


Figure 1.14: Acid and Alkaline HER mechanism. [89]

In oxygen evolution reaction, the intermediate $M-OH_{ads}$, $M-O_{ads}$, $M-OOH_{ads}$, $M-OO_{ads}$ predict the overall electrocatalytic activity (Figure 1.15). The OH group adsorption on the single or double active sites and formation energy of $M-OOH_{ads}$ plays an important role in OER kinetics which dissociates to form O_2 and water.

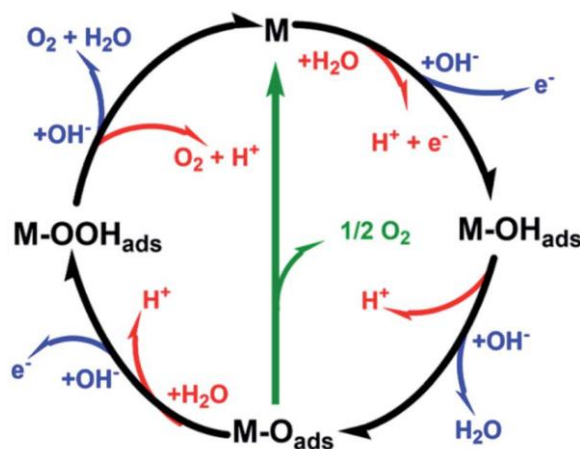


Figure 1.15: Acid and Alkaline OER mechanism (red and blue color corresponds to acidic and alkaline OER). [90]

1.3. Fluorescence-based quantum dots and sensing

Photoluminescence is the emission of the nonradiative transition (photon) during the relaxation process of particles from excited to ground state. The photoluminescence mechanism of the fluorophore can be explained simply from Jablonski diagram. In the first step, absorption of light by the fluorophore excites the molecule to higher electronic states (S_2 or S_1). Then the disintegration of the particle from S_2 to S_1 and finally emission from S_1 to S_0 occurs which is commonly known as fluorescence. In the excited state the fluorophore involves different vibrational relaxation through internal conversion and intersystem crossing. The intersystem crossing involves singlet to triplet transition in the excited state and finally relaxes to ground state (phosphorescence) (T_1 to S_0). Interestingly, the lifetime of the fluorescence is lower than phosphorescence and, in many cases, not all particles move to ground state during non-radiative relaxation. FRET is a phenomenon where the excited state fluorophore can undergo charge transfer with chromophore. The theory is based on the distance between the donor acceptor within no emitting energy. The donor atom excites to higher energy state and transfers its energy to

acceptor molecule (A). In the second stage, the acceptor chromophore undergoes emission to ground state and releases the energy.

- 1) $D + h\nu = D^*$ 2) $D^* + A = A^* + D$ 3) $A^* = A + h\nu$ where D and A denote donor and acceptor molecule and * signifies the excited state.

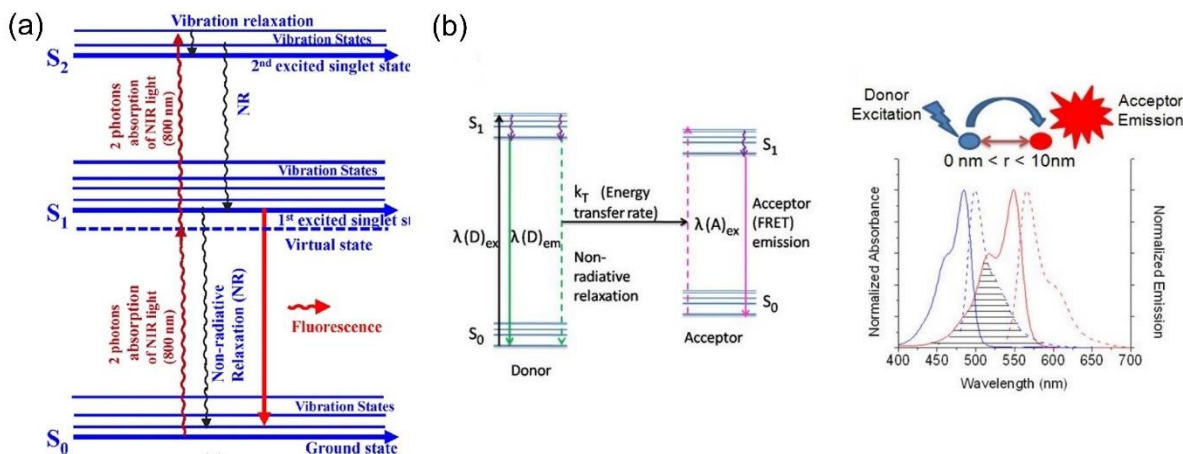


Figure 1.16: (a) Jablonski diagram and (b) FRET mechanism. [91-92]

1.3.1. Type of Fluorophores and Optical property of Nanomaterials

Fluorophores are classical organic dyes, lanthanide complexes, metal-based dyes, semiconductor quantum dots which have a potential application in nanobiotechnology such as bioimaging, detection in cancer and tumor cells, pollutant metal sensing etc. [93]. Classical dye has broad spectral range, high molar extinction coefficient, lower lifetime in nanoseconds (ns) and is easily available. In contrast, maximum organic dye is toxic, environmentally hazardous and undergoes photobleaching. The metal based fluorophores have high intensity and quantum yield, large Stokes shift and high possibility the upconversion. However, larger lifetimes, complex material synthesis, specific emission wavelength are some limitations of metal based complexes. Nanoparticles and quantum dots are now a place of interest due to broad emission spectra, high photostability and large molar extinction coefficient of up to 10^4 to $10^5 \text{ M}^{-1}\text{cm}^{-1}$. The PL properties of QD depend on size i.e., quantum confinement effect, doping, functional groups, surface defects, band gap. Different organic-inorganic nanoparticles and quantum dots like gold (Au), silver (Ag), cadmium selenide/sulfide (CdSe/S), Zinc sulfide (II-VI group), GaAs/InGaAs

(III-V group), perovskite quantum dots, Carbon and graphene quantum dots has been well established [94-99].

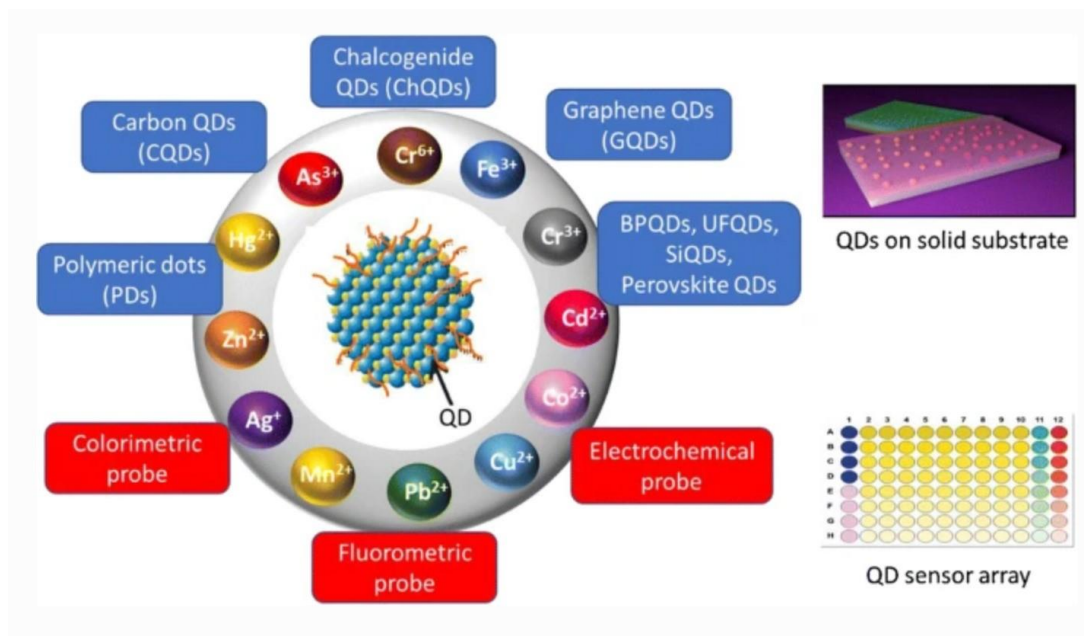


Figure 1.17: Quantum dots and applications. [100]

Carbon and Graphene quantum dots have taken much attention due to low toxicity, low photo bleaching, cost-effective synthesis and low bio-compatibility. The PL mechanism of CQD is based on two factors such as intrinsic and extrinsic. The intrinsic blue emission (near 400 nm) originates from core level i.e. sp^2 hybridized hexagons. The other broad emission upto 500 nm is mainly due to different oxygen functional groups. The extrinsic nature due to foreign groups can be optimized by reaction conditions, surface passivation. However the blue emission due to core level of graphite intercalation compound (GIC)-based GQDs has higher intensity than other GQD or CQD which depends on the subdomains and band gap energies. It is evident that doping of nitrogen involves different functional groups like pyridinic, amine, and graphitic nitrogen, impacting the PL profile [101-102]. Recently, polyamide supported small molecules and pyrene derivatives in CQD are most likely responsible for blue and red emissions [103-104]. Since depending upon various synthetic conditions and heteroatoms doping, the broadband PL property of N-CQD modifies where the involvement of individual functional groups (defects) towards PL broadening needs to be investigated.

1.3.2. Type of sensors and mathematical tools

1.3.2.1. PL quenching

The fluorescence based metal ion sensors have been widely used due to large PL intensity of CQD. Different types of metals like Fe^{3+} , Ag^+ , Cu^{2+} , Hg^{2+} , Co^{2+} , Ni^{2+} , Pb^{2+} , Cu^{2+} , K^+ , Ca^{2+} , Zn^{2+} , Na^+ , Mg^{2+} , Al^{3+} and Pb^{2+} can be detected by various type of CQD [105]. The sensitivity depends on pH of the solution, solubility product of the quantum dot, types of dopants like nitrogen, boron, phosphorous, boron. The presence of quencher (Q) can decrease the photoluminescence (PL) intensity which is mainly two types i.e., static quenching and dynamic quenching. The decrease of PL intensity by quencher (Q) addition can be expressed from Stern- Volmer (S-V) equation as follows: [106]

$$I_0/I = 1 + K_{SV} [Q] \quad (1.43)$$

Where I and I_0 denote PL intensity in presence and absence quencher (Q). K_{SV} is the Stern-Volmer constant associated with pure static quenching. For, pure dynamic or collisional quenching S-V eqn. can be expressed as

$$I_0/I = 1 + k_q \tau_0 [Q] \quad (1.44)$$

Where k_q is the bimolecular collisional quenching constant, τ_0 is the average lifetime of fluorophore. For dynamic quenching, $(I_0/I) = (\tau_0/\tau)$, where τ denotes change in average lifetime after quenching. For mixed quenching i.e. both static and dynamic the S-V eqn are as follows: [106]

$$I_0/I = (1 + K_{SV} [Q]) (1 + k_q \tau_0 [Q]) \quad (1.45)$$

1.3.2.2. Electrochemical quenching

Different biomolecules like cholesterol, hydrogen peroxide, glucose, metal ions can undergo electrochemical reactions at the surface of electrode. Different types of electrochemical biosensors have been employed like potentiometric, capacitive, amperometry, impedance measurement. In potentiometer, the chemical reaction is based on redox potential keeping the current constant. In amperometry biosensors, potential is constant where the change in current is measured during the chemical reaction of the analyte at the electrode surface. In conductometric electrochemical analyses, conductivity of the solution is measured after sensing. The process is less sensitive and can be varied due to double layer charging, different Faradic processes.

In impedance biosensor technique, impedance is measured at a voltage in alternating current (AC) bias conditions. Different antibody, nucleic acids, carbohydrates can be measured through this process.

1.4. Aims and Objectives

The chapter sheds light on the basic understanding of the properties of nanomaterials and different applications that can reduce the recent energy crisis and generate clean environment. Hydrogen and oxygen evolution in metal air batteries, oxygen reduction reaction in fuel cells facilitates the efficiency with sustainable energy conversion and storage systems. The smart architecture of flexible supercapacitors will be the next generation energy devices rather than batteries. However, anthropogenic activities can enhance some toxic pollutants which cause environmental damage. The challenges to detection and estimation are modified by nanotechnology to protect the human health and environment. The high cost, limited lifetime, instability are the primary factors to restrict as a potential use of conventional metal based catalysts. The various synthesis methods, chemical functionalization, optimization of electronic states and understanding of the reaction pathway are essential to modify the advanced materials. The thesis is intended to focus on design of some low dimensional materials like quantum dots, 2D materials which plays a pivotal role as a catalyst and sensor in different applications. In the field of energy storage or electrocatalysis, 2 D/1D materials are less efficient due to less active sites (like TMDs), inactive basal plane (like graphene, CNT), insulating nature (like hBN). Tremendous challenges have been made by incorporating various dopants, functionalization, heterostructures, vacancy incorporation which modifies active sites, enhances conductivity, band gap modulation, and surface area. However, the catalytic mechanism, energy pathways, active site's role, durability are investigated through theoretical and various experimental techniques which provide valuable progress in nanoscience and technology.

1.5. References

1. Santamaria, A., *methods and protocols*, 2012, 1-12.
2. Binnig, G., Quate, C.F. and Gerber, C., *Physical review letters*, 1986, 56(9), 930.
3. Pokrajac, L., Abbas, A., Chrzanowski, W., Dias, G.M., Eggleton, B.J., Maguire, S., Maine, E., Malloy, T., Nathwani, J., Nazar, L. and Sips, A., 2021.
4. Manthiram, A., Fu, Y., Chung, S.H., Zu, C. and Su, Y.S., 2014, *114*(23), 11751-11787.
5. Taballione, C., van der Meer, R., Snijders, H.J., Hooijschuur, P., Epping, J.P., de Goede, M., Kassenberg, B., Venderbosch, P., Toebes, C., Vlekkert, H.V.D. and Pinkse, P.W., *arXiv preprint arXiv:2012.05673*.
6. Cho, G., Park, Y., Hong, Y.K. and Ha, D.H., *Nano Convergence*, 2019, 6, 1-17.
7. Bokov, D., Turki Jalil, A., Chupradit, S., Suksatan, W., Javed Ansari, M., Shewael, I.H., Valiev, G.H. and Kianfar, E., *Advances in Materials Science and Engineering*, 2021, 1-21.
8. Alkaç, İ.M., Çerçi, B., Timuralp, C. and Şen, F., In *Nanomaterials for Direct Alcohol Fuel Cells*, 2021, 17-33.
9. Dolez, P.I. ed., *Nanoengineering: global approaches to health and safety issues*, 2015, Elsevier
10. Rai, V., Liu, D., Xia, D., Jayaraman, Y. and Gabriel, J.C.P., A critical review. *Recycling*, 2021, 6(3), 53.
11. Turner, J.A. *Science*, 1999, 285(5428), 687-689.
12. Campisi, S., Schiavoni, M., Chan-Thaw, C.E. and Villa, A., *Catalysts*, 2016, 6(12), 185.
13. Bhattacharjee, K. and Prasad, B.L., *Chemical Society Reviews*, 2023.
14. Green, M., *Journal of Materials Chemistry*, 2010, 20(28), 5797-5809.
15. Mourdikoudis, S. and Liz-Marzán, L.M., *Chemistry of Materials*, 2013, 25(9), 1465-1476.
16. . Flory, *Principles of Polymer Chemistry*, Cornell University Press, New York, 1953.
17. Allam, N.K. and Grimes, C.A., *The Journal of Physical Chemistry C*, 2007, *111*(35), 13028-13032.
18. Neville, E.M., Mattle, M.J., Loughrey, D., Rajesh, B., Rahman, M., MacElroy, J.D., Sullivan, J.A. and Thampi, K.R., *The Journal of Physical Chemistry C*, 2012, *116*(31), 16511-16521.
19. Wang, G., Wang, H., Ling, Y., Tang, Y., Yang, X., Fitzmorris, R.C., Wang, C., Zhang, J.Z. and Li, Y., *Nano letters*, 2011, *11*(7), 3026-3033.
20. Yeo, B.S. and Bell, A.T., *The Journal of Physical Chemistry C*, 2012, *116*(15), 8394-8400.
21. Ling, Y. and Li, Y., *Particle & Particle Systems Characterization*, 2014, *31*(11), 1113-1121.
22. Kubacka, A., Fernandez-Garcia, M. and Colon, G., *Chemical reviews*, 2012, *112*(3), 1555-1614.
23. Zhang, X.F., Liu, Z.G., Shen, W. and Gurunathan, S., *International journal of molecular sciences*, 2016, *17*(9), 1534.
24. Cho, G., Park, Y., Hong, Y.K. and Ha, D.H., *Nano Convergence*, 2019, 6, 1-17.
25. Walsh, A., Yan, Y., Huda, M.N., Al-Jassim, M.M. and Wei, S.H., *Chemistry of Materials*, 2019, *21*(3), 547-551.
26. Zhang, X.F., Liu, Z.G., Shen, W. and Gurunathan, S., *International journal of molecular sciences*, 2016, *17*(9), p.1534.
27. Gu, Q., Lv, J., Mo, X. and Jiang, X., *Sensors and Actuators A: Physical*, 2022, 335, 113376.
28. Li, C., Mizuta, H. and Oda, S., InTech. 2011, 487-508.
29. Yu, M.F., *J. Eng. Mater. Technol.*, 2004, *126*(3), 271-278.
30. Lee, C., Wei, X., Kysar, J.W. and Hone, J., *science*, 2008, *321*(5887), 385-388.
31. Link, S. and El-Sayed, M.A., *The Journal of Physical Chemistry B*, 2019, *103*(21), 4212-4217.
32. Kumar, D.S., Kumar, B.J. and Mahesh, H.M., *Synthesis of inorganic nanomaterials*, 2018, 59-88.
33. Sung Lee, J., Myung Cha, J., Young Yoon, H., Lee, J.K. and Keun Kim, Y., *Scientific reports*, 2015, 5(1), 12135.
34. Cao, G., *Nanostructures and Nanomaterials. Synthesis, Properties, and Applications.*, 2004, 53.
35. Sur, U.K. Studium Press (India) Pvt. Limited, 2019.

36. Singh, B., Lohan, S., Sandhu, P.S., Jain, A. and Mehta, S.K., In *Nanobiomaterials in Medical Imaging*, 2016, 455-478.
37. Conte, L.L., Chothia, C. and Janin, J., *Journal of molecular biology*, 2019, 285(5), 2177-2198.
38. D. J. Meier, *J. Phys. Chem.*, 1967, **71**, 1861–1868.
39. Hamers, R.J., Tromp, R.M. and Demuth, J.E., *Physical Review B*, 1986, 34(8), 5343.
40. Novoselov, K.S., Geim, A.K., Morozov, S.V., Jiang, D.E., Zhang, Y., Dubonos, S.V., Grigorieva, I.V. and Firsov, A.A. *science*, 2004, 306(5696), 666-669.
41. Novoselov, K.S., Geim, A.K., Morozov, S.V., Jiang, D., Katsnelson, M.I., Grigorieva, I.V., Dubonos, S. and Firsov, A.A., *nature*, 2005, 438(7065), 197-200.
42. Lin, T., Chen, I.W., Liu, F., Yang, C., Bi, H., Xu, F. and Huang, F., Nitrogen-doped mesoporous carbon of extraordinary capacitance for electrochemical energy storage. *Science*, 2015, 350 (6267), pp.1508-1513.
43. Sarkar, S., Roy, R., Das, B.K. and Chattopadhyay, K.K., Temperature-dependent site selection of boron doping in chemically derived graphene. *Carbon*, 2021, 184, pp.253-265.
44. Li, L.H., Chen, Y., Behan, G., Zhang, H., Petracic, M. and Glushenkov, A.M., Large-scale mechanical peeling of boron nitride nanosheets by low-energy ball milling. *Journal of materials chemistry*, 2011, 21(32), pp.11862-11866.
45. Liu, Z., Gong, Y., Zhou, W., Ma, L., Yu, J., Idrobo, J.C., Jung, J., MacDonald, A.H., Vajtai, R., Lou, J. and Ajayan, P.M., Ultrathin high-temperature oxidation-resistant coatings of hexagonal boron nitride. *Nature communications*, 2013, 4(1), p.2541.
46. Yan, K., Lee, H.W., Gao, T., Zheng, G., Yao, H., Wang, H., Lu, Z., Zhou, Y., Liang, Z., Liu, Z. and Chu, S., Ultrathin two-dimensional atomic crystals as stable interfacial layer for improvement of lithium metal anode. *Nano letters*, 2014, 14(10), pp.6016-6022.
47. Wei, X., Wang, M.S., Bando, Y. and Golberg, D., Electron-beam-induced substitutional carbon doping of boron nitride nanosheets, nanoribbons, and nanotubes. *ACS nano*, 2011, 5(4), pp.2916-2922.
48. Fan, X., Shen, Z., Liu, A.Q. and Kuo, J.L., Band gap opening of graphene by doping small boron nitride domains. *Nanoscale*, 2012, 4(6), pp.2157-2165.
49. Mak, K.F., Lee, C., Hone, J., Shan, J. and Heinz, T.F., Atomically thin MoS₂: a new direct-gap semiconductor. *Physical review letters*, 2010, 105(13), p.136805.
50. Tongay, S., Zhou, J., Ataca, C., Lo, K., Matthews, T.S., Li, J., Grossman, J.C. and Wu, J., Thermally driven crossover from indirect toward direct bandgap in 2D semiconductors: MoSe₂ versus MoS₂. *Nano letters*, 2012, 12(11), pp.5576-5580.
51. Yoon, Y., Ganapathi, K. and Salahuddin, S., How good can monolayer MoS₂ transistors be?. *Nano letters*, 2011, 11(9), pp.3768-3773.
52. Ataca, C. and Ciraci, S., Functionalization of single-layer MoS₂ honeycomb structures. *The Journal of Physical Chemistry C*, 2011, 115(27), pp.13303-13311.
53. Dolui, K., Rungger, I., Pemmaraju, C.D. and Sanvito, S., Ab-initio study on the possible doping strategies for MoS₂ monolayers. *arXiv preprint arXiv*: 2013, 1304.8056.
54. Ding, Y., Wang, Y., Ni, J., Shi, L., Shi, S. and Tang, W., First principles study of structural, vibrational and electronic properties of graphene-like MX₂ (M= Mo, Nb, W, Ta; X= S, Se, Te) monolayers. *Physica B: Condensed Matter*, 2011, 406(11), pp.2254-2260.
55. Scalise, E., Houssa, M., Pourtois, G., Afanas'ev, V. and Stesmans, A., Strain-induced semiconductor to metal transition in the two-dimensional honeycomb structure of MoS₂. *Nano Research*, 2012, 5, pp.43-48.
56. Sorkin, V., Pan, H., Shi, H., Quek, S.Y. and Zhang, Y.W., Nanoscale transition metal dichalcogenides: structures, properties, and applications. *Critical reviews in solid state and materials sciences*, 2014, 39(5), pp.319-367.
57. Hamada, N., Sawada, S.I. and Oshiyama, A., New one-dimensional conductors: Graphitic microtubules. *Physical review letters*, 1992, 68(10), p.1579.
58. Teich, D., Lorenz, T., Joswig, J.O., Seifert, G., Zhang, D.B. and Dumitrica, T., Structural and electronic properties of helical TiS₂ nanotubes studied with objective molecular dynamics. *The Journal*

of *Physical Chemistry C*, 2011, 115(14), pp.6392-6396.

59. Mohideen, M.M., Ramakrishna, S., Prabu, S. and Liu, Y. Advancing green energy solution with the impetus of COVID-19 pandemic. *Journal of Energy Chemistry*, 2021, 59, pp.688-705.

60. Vincent, C.A. and Scrosati, B., *Rechargeable Lithium Cells— Modern Batteries: An Introduction to Electrochemical Power Sources*.1997.

61. Kordesch, K. and Simader, G., 1996. Fuel cells and their applications.

62. Baizer, M.M., 1971. *Organic Electrochemistry*", Marcel Dekker, New York, NY, 1973; and L. Eberson and F.I. Schafer. *Organic Electrochemistry*", *Springer-Verlag, West Berlin*.

63. Janssen, L.J.J. and Koene, L., The role of electrochemistry and electrochemical technology in environmental protection. *Chemical Engineering Journal*, 2002, 85(2-3), pp.137-146.

64. Riaz, A., Sarker, M.R., Saad, M.H.M. and Mohamed, R., Review on comparison of different energy storage technologies used in micro-energy harvesting, WSNs, low-cost microelectronic devices: challenges and recommendations. *Sensors*, 2021, 21(15), p.5041.

65. Ferreira, I., Brás, B., Martins, J.I., Correia, N., Barquinha, P., Fortunato, E. and Martins, R., Solid-state paper batteries for controlling paper transistors. *Electrochimica Acta*, 2011, 56(3), pp.1099-1105.

66. Davis, F. and Higson, S.P., Biofuel cells—recent advances and applications. *Biosensors and bioelectronics*, 2007, 22(7), pp.1224-1235.

67. Habrioux, A., Servat, K., Tingry, S. and Kokoh, K.B., Enhancement of the performances of a single concentric glucose/O₂ biofuel cell by combination of bilirubin oxidase/Nafion cathode and Au–Pt anode. *Electrochemistry Communications*, 2009, 11(1), pp.111-113.

68. Dunn, B., Kamath, H. and Tarascon, J.M., Electrical energy storage for the grid: a battery of choices. *Science*, 2011, 334(6058), pp.928-935.

69. Verma, J. and Kumar, D., Metal-ion batteries for electric vehicles: current state of the technology, issues and future perspectives. *Nanoscale Advances*, 2021, 3(12), pp.3384-3394.

70. Chen, Y., Kang, Y., Zhao, Y., Wang, L., Liu, J., Li, Y., Liang, Z., He, X., Li, X., Tavajohi, N. and Li, B., A review of lithium-ion battery safety concerns: The issues, strategies, and testing standards. *Journal of Energy Chemistry*, 2021, 59, pp.83-99.

71. He, P., Zhang, G., Liao, X., Yan, M., Xu, X., An, Q., Liu, J. and Mai, L., Sodium ion stabilized vanadium oxide nanowire cathode for high-performance zinc-ion batteries. *Advanced Energy Materials*, 2018, 8(10), p.1702463.

72. Kravchyk, K.V. and Kovalenko, M.V., Aluminum electrolytes for Al dual-ion batteries. *Communications Chemistry*, 2020, 3(1), p.120.

73. Guo, Q., Zeng, W., Liu, S.L., Li, Y.Q., Xu, J.Y., Wang, J.X. and Wang, Y., Recent developments on anode materials for magnesium-ion batteries: a review. *Rare Metals*, 2021, 40, pp.290-308.

74. Şahin, M.E., Blaabjerg, F. and Sangwongwanich, A., A comprehensive review on supercapacitor applications and developments. *Energies*, 2022, 15(3), p.674.

75. Fernández López, J.A., Morishita, T., Toyoda, M., Inagak, M., Stoeckli, F. and Álvarez Centeno, T., 2008. Performance of mesoporous carbons derived from poly (vinyl alcohol) in electrochemical capacitors.

76. He, G., Ling, M., Han, X., Abou El Amaiem, D.I., Shao, Y., Li, Y., Li, W., Ji, S., Li, B., Lu, Y. and Zou, R., Self-standing electrodes with core-shell structures for high-performance supercapacitors. *Energy Storage Materials*, 2017, 9, pp.119-125.

77. He, H., Liu, Y., Shearing, P.R., He, G. and Brett, D.J., Cham: Springer International Publishing, 2022, pp. 147-163.

78. Lei, Z., Lu, L. and Zhao, X.S., *Energy & Environmental Science*, 2012, 5(4), pp.6391-6399.

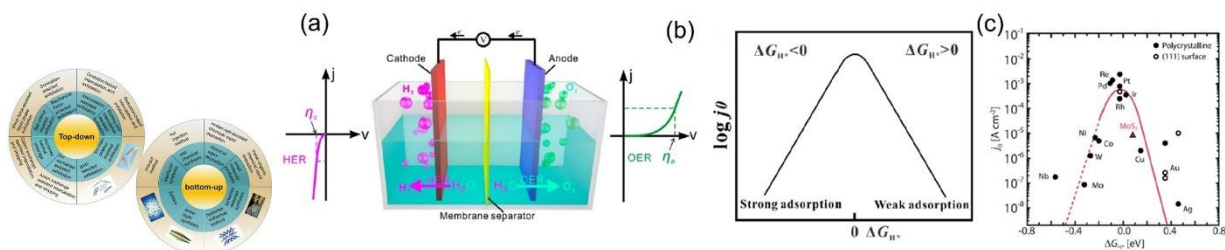
79. Kampouris, D.K., Ji, X., Randviir, E.P. and Banks, C.E., *Rsc Advances*, 2015, 5(17), pp.12782-12791.

80. Mei, B.A., Munteshari, O., Lau, J., Dunn, B. and Pilon, L., *The Journal of Physical Chemistry C*, 2018, 122(1), pp.194-206.

81. Xia, W., Mahmood, A., Liang, Z., Zou, R. and Guo, S., *Angewandte Chemie International Edition*, 55(8), 2016, pp.2650-2676.

82. Badea, N.I *Energies*, 2021,14(18), p.5783.
83. Li, Y., Li, Q., Wang, H., Zhang, L., Wilkinson, D.P. and Zhang, J., *Electrochemical Energy Reviews*, 2019, 2, pp.518-538.
84. Nørskov, J.K., Rossmeisl, J., Logadottir, A., Lindqvist, L.R.K.J., Kitchin, J.R., Bligaard, T. and Jonsson, H., *The Journal of Physical Chemistry B*, 108(46), 2004, pp.17886-17892.
85. Kulkarni, A., Siahrostami, S., Patel, A. and Nørskov, J.K., *Chemical Reviews*, 2018, 118(5), pp.2302-2312.
86. Wang, S., Yu, D., Dai, L., Chang, D.W. and Baek, J.B., *ACS nano*, 2011, 5(8), pp.6202-6209.
87. Chen, Z., Higgins, D. and Chen, Z., *Carbon*, 48(11), 2010, pp.3057-3065.
88. Walter, C., Menezes, P.W. and Driess, M., *Chemical Science*, 2021, 12(25), pp.8603-8631.
89. Wei, J., Zhou, M., Long, A., Xue, Y., Liao, H., Wei, C. and Xu, Z.J., *Nano-micro letters*, 2018, 10, pp.1-15.
90. Suen, N.T., Hung, S.F., Quan, Q., Zhang, N., Xu, Y.J. and Chen, H.M., *Chemical Society Reviews*, 2017, 46(2), pp.337-365.
91. Shi, L., Rodríguez-Contreras, A., Budansky, Y., Pu, Y., An Nguyen, T. and Alfano, R.R., *Journal of biomedical optics*, 2014,19(6), pp.066009-066009.
92. Rajdev, P. and Ghosh, S., *The Journal of Physical Chemistry B*, 2018, 123(2), pp.327-342.
93. Hötzer, B., Medintz, I.L. and Hildebrandt, N., *Small*, 2012, 8(15), pp.2297-2326.
94. S. K. Krishnan, E. Singh, P. Singh, M. Meyyappan, H. S. Nalwa, *RSC Adv.*, 2019, 9, 8778–8881.
95. Elbaum, R., Vega, S. and Hodes, G., *Chemistry of materials*, 2001, 13(7), pp.2272-2280.
96. Mukherjee, P., Shade, C.M., Yingling, A.M., Lamont, D.N., Waldeck, D.H. and Petoud, S., *The Journal of Physical Chemistry A*, 2011, 115(16), pp.4031-4041.
97. Wang, H.C., Bao, Z., Tsai, H.Y., Tang, A.C. and Liu, R.S., *Small*, 2018, 14(1), p.1702433.
98. Das, R., Bandyopadhyay, R. and Pramanik, P., *Materials today chemistry*, 2018, 8, pp.96-109.
99. Regolin, I., Sudfeld, D., Lüttjohann, S., Khorenko, V., Prost, W., Kästner, J., Dumpich, G., Meier, C., Lorke, A. and Tegude, F.J., *Journal of crystal growth*, 2007, 298, pp.607-611.
100. Yin, H., Truskewycz, A. and Cole, I.S., *Microchimica Acta*, 2020,187, pp.1-25.
101. Berger, C., Song, Z., Li, X., Wu, X., Brown, N., Naud, C., Mayou, D., Li, T., Hass, J., Marchenkov, A.N. and Conrad, E.H., *Science*, 2006, 312(5777), pp.1191-1196.
102. Hummers Jr, W.S. and Offeman, R.E., *Journal of the american chemical society*, 1958, 80(6), pp.1339-1339.
103. Mao, S., Yu, K., Cui, S., Bo, Z., Lu, G. and Chen, J., *Nanoscale*, 2011, 3(7), pp.2849-2853.
104. Wu, R., Luo, J., Guo, X., Wang, X., Ma, Z., Li, B., Cheng, L.Y. and Miao, X., *Chemical Physics Letters*, 2021, 781, p.138960.
105. Gao, X., Du, C., Zhuang, Z. and Chen, W., *Journal of Materials Chemistry C*, 2016, 4(29), pp.6927-6945.
106. Pal, A., Srivastava, S., Saini, P., Raina, S., Ingole, P.P., Gupta, R. and Sapra, S., *The Journal of Physical Chemistry C*, 2015, 119(39), pp.22690-22699.

Review of past work



2.1. Previous work on synthesis of 2D materials

In modern century, advanced nanotechnology has brought excellent progress in the field of biomedical, energy, and electronic device application. Nano based materials including zero dimensional (0 D), one dimensional (1D), two dimensional (2D) and three dimensional (3D) morphology are used as various aspects depending on their optical, electrical, mechanical and chemical properties. In the past few decades, carbon based low dimensional materials i.e. 0 D fullerenes, 1 D nanotube and 2 D graphene have unique properties and based on reaction conditions, such properties can be tuned. There are two approaches to synthesizing the 2D materials which are classified as top down and bottom up approaches. In top down method, bulk material can be converted to single or few layer nanomaterials using ultrasonication, metal ion intercalation, mechanical and chemical reduction. Bottom up approaches involve wet chemical methods like hydrothermal, solvothermal, microwave assisted synthesis, laser deposition and chemical vapour deposition (CVD) etc (Figure 2.1). In liquid phase exfoliation, the normal and lateral force overcomes the Van Der Waals interaction between the two layers and few layer nanosheets can be obtained. In mechanical exfoliation, high force is applied to separate the single layer where low yield reduces the efficiency for commercial applications.

2.1.1. CVD based synthesis

To control the size, defects, morphology, grain boundaries, layer thickness, CVD has emerged as an efficient approach to synthesizing high quality 2D materials [1]. However, CVD based material has higher purity and fewer impurities or defects than the liquid phase exfoliation method. Secondly, the crystal size domain and mobility of the 2D materials are much higher than solution based techniques. In the domain of transition metal dichalcogenides (TMDs), MoS₂ nanosheet, MoS₂/hBN vertical heterostructure, can be prepared on SiO₂ substrate by CVD method [2-3]. The CVD-assisted synthesis can produce the compressive and tensile strain of monolayer MoS₂, WS₂ which modulates the electronic, optical band gap for optoelectronic applications. The changing concentration of precursors W, Mo, or S, Se produces metal or edge specific metal chalcogenides under CVD-based growth. Moreover, temperature has a significant effect on the triangular or hexagonal shape formation of WSe₂ based materials [4]. The phase control synthesis has also been modified by CVD process. The metallic 1T or 1T' phase of TMDs is unstable and difficult to synthesize. Most commonly α phase at the intermediate can convert to metastable 1T phase under electron beam. Single layer 1T-MoTe₂ is well grown in the CVD process by controlling the temperature, precursors and promoter concentrations [5]. Knag et al, have reported monolayer WS₂ from sulfurization of WO₃ in SiO₂ substrate under high hydrogen environment [6]. Recently, theoretical studies have explored of CVD growth of 2D materials. For example, ab initio calculation suggests lower growth temperature is required for the growth buckled type silicene on Ir surfaces [7]. Monte Carlo simulations manifest layer by layer growth mechanisms of Mxene based compounds like Ti₄C₃ and Ti₅C₄ [8]. For nonmetal related materials, epitaxial growth of hBN on Cu substrate is prepared from ammonia borane at higher temperatures [9]. The 2D graphene can be synthesized from carbon in Cu substrate at 1050°C at tubular furnace with small defects [10]. The nucleation of graphene has been synthesized on Ni, Cu, Fe substrates where Fe surface promotes the growth of graphene at low carbon content [11,12]. During graphene synthesis, the deposition rate of carbon becomes critical to optimize the nanostructures. However, CVD based graphene/hBN heterostructure has a higher mobility at room temperature with a value of 7100 cm² V⁻¹ s⁻¹ [13]. However, the method becomes insufficient production of materials in the field of energy storage applications.

2.1.2. Wet chemical synthesis

Hydrothermal, solvothermal, hot injection and microwave assisted synthesis are most commonly used to prepare variety of 2D materials and nanocomposites. Depending on the solubility in the particular solvent, the moderate temperature annealing under ambient pressure can control the surface morphologies and the crystallite sizes [14]. For example, the modified Hummers method

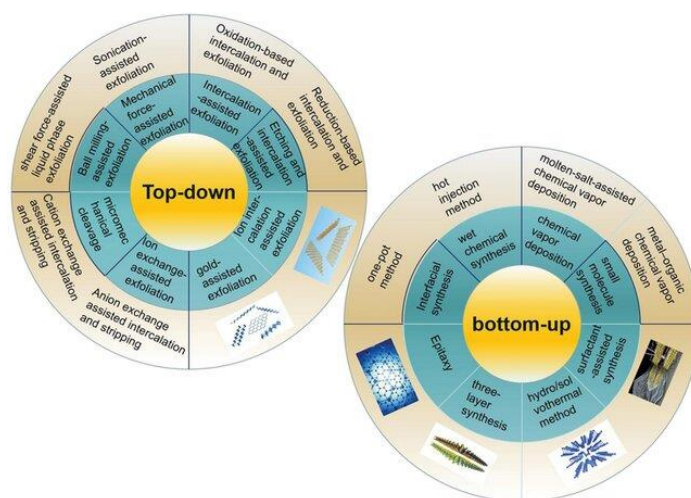


Figure 2.1: Top down and Bottom-up approaches for 2D material synthesis [15]

has been explored to prepare graphene oxide (GO) from exfoliation and oxidation of graphite sheet in presence of sulphuric acid, potassium permanganate, sodium nitrate and hydrogen peroxide [16]. The resulting GO is reduced with variable reducing agents to synthesize multilayer reduced graphene oxide (rGO) [17]. The electronic and structure modification of graphene or rGO for various applications is related to different types of defects, defect density and dopants. The nitrogen, sulphur, boron, iodine doping in rGO are achieved by different reducing agents like lysine, lawesson's reagent, borazine and hydroiodic acid respectively [18]. In TMDs, ammonium /sodium molybdate/ tungstate with thiourea or organic sulfides are the precursors to produce 2H-phase MoS_2/WS_2 . Depending on the reaction time, reducing agents, solvent polarity, temperature in solvo/hydrothermal reactions, various morphology can be prepared [19]. Depending on the nucleation and particle growth, nanoflower formation due to agglomeration and discrete nanosheet morphology can be obtained.

To prevent the oxide formation of TMDs, organic solvent and inert gas purging are used in order to remove the water or moisture traces. Using this strategy, 1T-WS₂ are prepared using organic precursors oleyl amine and oleic acid in carbon disulfide solvent under inert atmospheres [20]. However, capping ligand has various binding sites depending on hard and softness of the binding sites which can control nanosheet thickness of MoSe₂/WSe₂ related materials [21]. The synthesis of other 2D materials like TaS₂, TaSe₂, and NaTaO₃, NbSe₂ has been well established from solution reaction processes [22]. Hwang et al. have proposed the synthetic route of hexagonal boron nitride (hBN) by taking different molar ratios of boric acid and urea. The mixture was calcined over a long time at higher temperatures to produce white colored hBN [23]. Thus, the low cost, lower temperature, feasible doping and functionalization in wet chemical process can be utilized for high scale production of 2D materials. However, in uncontrolled stoichiometry, trace amounts of impurities tend to be optimized for commercial purposes.

2.1.3. Exfoliation based synthesis

Mechanical exfoliation becomes widely used to obtain the same crystal lattice with low defects. In micro-mechanical exfoliation (MME), atomic force microscopy (AFM) is used to apply the lateral force on the bulk materials. In 2004, single layer of graphene was prepared from bulk graphite via simple scotch tape method and the as-prepared graphene was exfoliated on various substrates [24]. MME method has been used to grow various TMDs like MoS₂, MoSe₂, WS₂ apart from graphene [25-27]. Interestingly, mechanical exfoliation becomes feasible for TMD based compounds due to the Van Der Waals bond becoming much weaker than in plane bonds [28]. Similar scotch tape method has been applied to prepare hBN nanosheet on Si/SiO₂ substrate with 10 layers. However, single layer hBN cannot be prepared from mechanical exfoliation due to strong interlayer bonding [29]. Solvent exfoliation process becomes suitable to produce atomically thin nanosheets from the bulk crystal (Figure 2.2). Different non polar solvents like Chlorobenzene, dimethylformamide (DMF), N-methyl-pyrrolidinone (NMP), Benzonitrile are used to exfoliate the bulk hBN whereas bulk TMDs undergo exfoliation in both polar and nonpolar solvents [30-31].

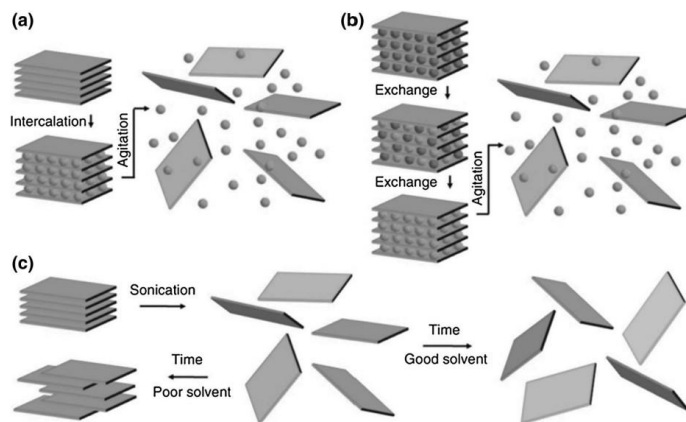


Figure 2.2: Exfoliation process of 2D materials (a,b) with and (c) without ion intercalation.[32]

Moreover graphene/TMD, graphene/hBN based hybrid composites have been designed from solvent exfoliation process. Moreover, layered double hydroxides (LDH) can be synthesized from anion exchange exfoliation with DMF solvent which has a potential application in energy and biomedical domain [33]. MXenes—metal carbide nanosheets with negative surface functionalization (hydroxyl, fluorides) are exfoliated in methanol [34]. Single nanosheets of TMDs and 1T/1T' phase are successfully prepared from Li intercalation process followed by sonication. The colloidal suspension of single layer nanosheet due to Li intercalation enhances the interlayer spacing and further filtration, washing and high annealing process [35-36]. Thus, the chemical exfoliation allows control surface functionalization of the 2D materials in basal and edge specific sites which has wide applications in biomedical, sensing and energy related applications.

2.2. Synthesis of carbon quantum dots

Carbon based quantum dots or graphene quantum dots (CQD/GQD) have gained attention in the field of optoelectronic, catalyst, sensing, biomedical applications due to surface functional groups, higher stability and wide band gaps [37]. In bottom up approaches, the size and defects can be controlled by varying reaction conditions such as temperature, solvents, and precursors [38]. Different types of oxygen functional groups like epoxy, hydroxyl, carbonyl groups are attached at the surface of CQD/GQD and the covalent oxygen based functionalization depends on nature of reactants. The hydrothermal treatment on bio-precursors like lotus roots, pomelo,

cigarette butts and different biomass are used to synthesize CQD [39-41]. Nitrogen doping on CQD/GQD surface can enhance the quantum yield and PL intensity. N doped CQD/GQD are prepared from different nitrogen containing reagents i.e. dopamine, tetrabutylammonium perchlorate, thiourea etc [42-44]. The electron donating and withdrawing groups can alter the electronic and optical properties of GQD. For example, alkylamine based surface modification of GQD occurs green to blue emission due to covalent functionalization of -COOH groups to amide groups and reduces nonradiative transitions [45]. Zhang et al have reported hydrazine hydrate based reduction of GQD undergoes yellow emission due to esterification of oxygen groups while changing reducing agent to sodium borohydride changes to weak blue emission [46]. However, the most convenient and time-consuming microwave treatment has been utilized to prepare CQD having high solubility and quantum yield. Carbon based reagents like Scallion, citric acid are commonly used in microwave reactors [47-48]. Recently, nitrogen/sulphur (N/S), nitrogen/phosphorus (N/P), boron/nitrogen (B/N) CQD increased multiple active sites and allowed its multiple applications in biomedical and photocatalysis based applications [49-51]. Strikingly, the agglomeration of small carbon nanoparticles reduces the PL intensity which can be restored by oxidative treatment and surface passivation. The CQD surfaces become passivated by PEG_{1500N} which undergoes crosslinking on the surface of CQD and gives extra stabilization [52]. The simultaneous surface passivation and functionalization of CQD surface are carried out by diamine-terminated oligomeric PEG, branched polyethylenimine (b-PEI) [53-54]. In the top down approach, chemical, laser ablation, electrochemical oxidation have been included to prepare CQD [55-57].

2.3. Previous work on Oxygen reduction reaction

The pt based carbon heterostructure has higher surface sites, high miller indices for oxygen reduction and enhances the rate of the ORR kinetics. The reducing size of the pt nanostructure and various pt based metal alloys i.e. Pt₃Ni, PtNi₃, Pt₃Co, Pt₃Ti, Pt₃Fe etc. shows ORR activity due to surface electronic states and lower adsorption energies [58-59]. Recently, M-N-C (M=Cr,Mn,Mo,Fe etc.) catalyst has been widely used as a ORR catalyst [60]. The calcination of MOF and phthalocyanine leads to produce the M-N-C bond [61-62]. Among the various configurations, the Co-N-C and Fe-N₄/C sites are active sites for ORR pathways due to oxidation state of metals, porosity and charge transfer ability [63]. The metal based graphitic carbon nitride

(g-C₃N₄) is one of the sources of stable M-N-C bonds where pyridinic nitrogen can effectively bind with metal ions [64]. Spinel oxides (A_xB_{3-x}O₄) have been utilized as a ORR catalyst and the reactivity depends on different vacancies, crystal structure and surface area [65]. Perovskite oxides (ABO₃) are also investigated for oxygen reduction having dual active sites including A site for oxygen adsorption and B site for oxygen reactivity after adsorption. Indeed, the lower mass transfer rate lowers the reaction kinetics which can be modified multiple (quadruple) metal based perovskites i.e. CaMn₇O₁₂, La(Ba_{0.5}Sr_{0.5})_{1-x}Co_{0.8}Fe_{0.2}O_{3-δ} etc. [66-67]. The compressive strain engineering on ABO₃ with foreign metals decreases the eg (d_{x²-y²}, d_{z²}) orbitals energy and subsequently, M-O bond becomes weaker and facilitates oxygen reduction [68]. Sun et al. established the metal based layered doubled hydroxide (LDH) which promotes the ORR kinetics due to d orbital electronic configuration and faradic redox reactions. [69-70]

The nonprecious carbon based materials act as an electrocatalyst due to high porosity, surface area, conductivity. The encapsulation of various nanoparticles like Fe, Au, Ag, Ni-Co on carbon nanotube (CNT) and carbon aerogels can enhance the charge transfer from metal to carbon sphere and improve the durability due to external carbon shells [71-74]. Various nonmetal doping on carbon spheres like phosphorous, nitrogen, sulphur can cause electronegativity differences near carbon atoms and improve the ORR kinetics [75-77]. The core structure of different MOF based structures is ORR sensitive and highly durable due to nitrogen doped graphitic carbon sites [78]. Moreover, the FeCl₃, PANI and cyanamide based Fe SAC material and Fe-Co dual active sites decrease the dissociation energy of O-O bond and oxygen reduction occur via four electrons transfer pathway [79].

2.4. Oxygen reduction reaction with 2D materials

In order to increase the durability and reduce the cost of fuel cells, various nonprecious materials have been used as an electrocatalysts. The ORR activity of 2D-transition metal chalcogenides (MX₂: M= Mo,W , Co,Ni etc X=S,Se,Te) depends on the type of binary metals and anions (reactivity order S>Se>Te). The activity can be modulated when the orbital d band energy and O 2p orbital energy difference is very small (Ta> Mo>Ti>Cr> W >V> Ni>Co). Thus single metal-based CoS₂, Co₃S₄ or binary composite CoNiS₂ can improve the ORR catalytic activity due to edge active S₂²⁻ site [80]. In thiospinel structure, the center metal has four coordinated sites

whereas fifth coordination site is ORR active site due to smaller size of oxygen get easily fits in the coordination site [81]. Secondly, metal incorporation in Mxene based compounds, $\text{Ti}_3\text{C}_2\text{X}_2$ ($\text{X} = \text{OH}$ and F) can improve the ORR activity due to synergistic effects and high active sites [82]. In the 20th century, Graphene and reduced graphene oxide are the alternative catalysts for ORR reduction due to large surface area, defects sites and high conductivity. The most common hexagonal, pentagonal, octagonal rings in graphene sheets can be created by introducing different point and line defects [83]. Foreign substituents like nitrogen, boron, phosphorous, sulphur doping in graphene can introduce lattice strain, surface reconstruction and band gap modulating [84-86]. For example, the incorporation of boron forms planner BC_3 sheet which opens the band gap and lowers the Fermi level [87]. Thus the electronegativity difference between boron and carbon induces the O-O adsorption and activates the ORR process [88]. However, the high resistivity above 140 ppm of boron in graphene can decelerate the ORR kinetics [89]. The N doping can form in and out of plane defects in graphene where pyrrolic and pyridinic can induce p type and amines, quaternary N can produce n type characteristics [90]. The increase in n type behavior enhances the electron density near p orbital and the high nucleophilicity promotes the ORR activation [91]. In contrast, pyridinic nitrogen can improve the onset potential for ORR and enhance the carrier concentrations [92]. The scenario becomes opposite in phosphorous (P) doped graphene due to reversal of polarity of C-P bond than C-N bond. The small electron donation by P to carbon moiety leads to produce partial n type character and is highly stable in oxygen environment than n-doped graphene [93]. Moreover, co-doping with S,O,N can create donor acceptor levels that can tune the ORR activity of graphene in different pH of the medium. In this case, the ratio of the dopants like (N/O, C/O,Fe/O) plays an important role in active site density [94]. In summary, for single dopant systems, the ORR reactivity follows the order (N doped>B doped>P doped>Sdoped) where the reactivity changes to diatom dopants (P,N doped)> (B,N doped) >(S,N doped) [95]. In advance, the most promising composite of reduced graphene oxide with mayenite electrodes (Sn-doped $\text{C}_{12}\text{A}_7\text{:e}^-$) can transfer electron donation to rGO to enhance conductivity and reduce oxygen adsorption energy [96].

Materials	Electrolyte	E _{onset}	E _{ORR}	Electron transfer number (n)	Ref
Bulk MoS ₂	0.1 M KOH	-0.44 V vs SCE	-0.44 V vs SCE	4	97
P- MoS ₂	0.1 M KOH	0.96 V vs RHE	-	4	98
MoS ₂ /graphene	0.1 M KOH	0.95 V vs RHE	0.82 V vs RHE	4	99
o- MoS ₂ -87	0.1 M KOH	0.94 V vs RHE	-	4	100
MoS ₂ /silica	0.1 M KOH	-0.14V vs. Ag/AgCl	-	4	101
MoS ₂ /AuNp	0.1 M KOH	-0.1 V vs SCE	-0.25V vs SCE	4	102
hBN	0.1 M H ₂ SO ₄	-	0.89 V vs. SCE	4	103
Graphene–PDDA	0.1 M KOH	-0.15 V vs. SCE	-0.35 V vs. SCE	4	104

CoOx/mC@MoS ₂	0.1 M KOH	0.67 V vs. RHE	-	4	105
Nb doped MoS ₂	0.1 M KOH	0.78 V vs. RHE	0.61V vs. RHE	4	106
Adenineand graphene	0.1 M KOH	-0.17 V vs SCE	-0.33V vs SCE	4	107
MoS ₂ QD	0.1 M NaOH	0.27 V vs. RHE	-0.5V vs. Ag/AgCl	4	108
2D-hBN/RGO	0.1 M KOH	0.79V vs. RHE	-	4	109
PdxSy-MoS ₂ /N-GR	0.1 M KOH	-0.242V vs SCE	-	4	110
Iodine mediated rGO	0.1 M KOH	-	-0.35V vs. Ag/AgCl	4	111
NaBH ₄ reduced rGO	0.1 M KOH	-	-0.56V vs.	4	111

			Ag/AgCl		
Nanostructured MoS ₂	0.1 M KOH	-0.14V vs. Ag/AgCl	-	4	112
WS ₂ /rGO	0.1 M KOH	0.91 V vs. RHE	-	4	113
MoSe ₂ @rGO	0.1 M KOH	0.90 V vs. RHE	0.77V vs. RHE	4	114
V-MoS ₂	0.1 M KOH	0.85 V vs. RHE	-	4	115
Mo-VS ₂ /CNT	0.1 M KOH	0.98 V vs. RHE	-	4	116
CuS@MoS ₂	0.1 M KOH	0.87 V vs. RHE	-	4	117
O-MoS ₂	0.1 M KOH	0.94 V vs. RHE	-	4	118

Table 2.1. ORR performance of various 2D material based catalysts.

2.5. Previous work on supercapacitive performances

The metal oxides like RuO₂, TiO₂, Mn₃O₄, Ni(OH)₂ etc show high capacitance at low current density due to faradic type charge transfer (oxidation-reduction) which can enhance the capacitance [119-122]. However, the lower conductivity and high cost made some restrictions which can be overcome for conducting polymer based carbon composites. The in-situ polymerization of 3,4-ethylenedioxythiophene (PEDOT) with CNT can increase the specific capacitance with high energy density [123]. However, polyaniline based CNT shows well charge storage mechanism due to charge transfer channel and chromatic color change (variable color) of PANI during charge discharge process [124]. Moreover, metal oxide and hydroxide can form composite with graphene or GO to improve the pseudo capacitance. The MnO₂/ graphene, Co₃O₄/graphene, Mn₃O₄/graphene, VOPO₄/graphene, Ni(OH)₂/graphene composite can form porous 3D structure and improve the electrochemical performances [125-129].

The electrical double layer capacitance (EDLC) depends on relative surface area, porosity, dielectric constant of the medium. Generally, carbon based materials can show EDLC type behavior where electrode-electrolyte and ion adsorption plays an important role in the charge storage capacity. In the domain of carbon based materials, carbon foam, carbon aerogels, activated carbon, carbon nanotube and graphene shows efficient charge storage mechanism depending on several factors. Firstly, the high flexibility, elasticity and different pore diameter makes carbon aerogels an electrode material. Indeed, the consistency of the pore volume can be

destroyed by reaction temperature, type of reactants, doping and pH of the medium [130]. In comparison, single and multiwalled CNT are the alternating materials due to high surface area, small size, flexibility, high mean free path of the charge carrier and less joule heating during transportation [131]. The heteroatom like nitrogen doping on CNT enhances the active sites and shows capacitance upto 206 F/g in alkaline solution [132]. However, the electrochemically synthesized CNT has higher surface area and boosts three times higher specific capacitance than commercial CNT [133]. The presence of pyridinic nitrogen can enhance capacitive performances due to the enhancement of charge on carbon atoms through protonation of nitrogen [134]. But, the actual role of different nitrogen functional groups (pyridinic-N, pyrrolic-N, graphitic-N) at the basal plane and edge state of graphene on capacitance value is completed and difficult to predict [135]. Along with the recent development, the hybrid supercapacitor is introduced which has higher energy density and power density due to Faradic reaction at cathode and non-Faradic reaction occurring at cathode. Lim *et al.* have proposed Nb₂O₅/carbon composite as a cathode and activated carbon as an anode material which remarkably enhances the energy density upto 74 Wh/kg with 90% retention rate at 1000 A/g current density [136]. The solid state asymmetric supercapacitor has been designed by intercalating the Ni(OH)₂ nanoplates into graphene sheet in order to reduce the stacking and shows excellent gravimetric capacitance at 573 F/g [137].

Graphene has emerged as a EDLC electrode material due to high mechanical strength, stability and large surface area. Depending on the reducing agent, the graphene oxide (GO) can be reduced to rGO, showing excellent specific and volumetric capacitance. Moreover, graphene based hydrogel and aerogel are used due to high adsorption capabilities and large porosity. The dispersion of GO in aqueous solution has been lost by gelation and form 3D assembly which further reduced to 3D rGO [138]. Since, the low dense and high assemble structure can show poor conductivity and decrease the volumetric capacitance [139]. Alternatively, activated carbon can be used as a energy storage material but due to microporous structures and comparable lower surface area hinders the flow of electrolyte ions in the electrode electrolyte interfaces [140]. To overcome this problem, mesoporous carbon can be utilized due to high ion transport systems [141]. For instance, the microporous and mesoporous structure of carbon based materials can be optimized by various synthesis techniques [142]. Besides, hybrid carbon materials can boost electrochemical performances due to synergistic effects with foreign substituents. For example,

the mesoporous carbon sphere forms 3D sandwich type structure between two graphene layers and enhances the efficiency of the capacitor [143]. Also, the π - π^* interaction between graphene Oxidized CNT-graphene, 3D-N doped CNT-graphene can enhance the conductivity and mechanical strength which can be beneficial for charge storage performances [144-146].

Ternary nanocomposites are another class of material that shows remarkable capacitive performance, high energy density and good cycling stability due to several factors. The variable oxidation state of metals, lower internal resistance during heterostructure formation, synergistic effect between three components lead to higher performances. For example, MoS₂/WS₂/graphene, graphene/SnO₂/polyaniline, RGO/ZnS/TiO₂ ternary composites are promising electrode materials for supercapacitor related applications [147-149].

2.6. Hydrogen evolution reaction (HER) with Nobel and Non-Nobel metals

Platinum group materials and derivatives can show facile hydrogen evolution which depends on several factors. Firstly, the adsorption and desorption energy of hydrogen on the Pt surface has optimum free energy (ΔG^*) value which enhances the Faradic efficiency, lowers Tafel slope and boosts the exchange current density (J_0). The relationship between J_0 and ΔG^* can be explained from Volcano plot where high positive or high negative ΔG^* can hinder the overall HER process and reduce the J_0 [150]. Theoretical analysis suggests that Pt, Re, Pd group metals lie at the maximum point of the volcano plot and enhance the HER kinetics due to high J_0 and lower free energy (ideally it should be zero) (Figure 2.3) [151].

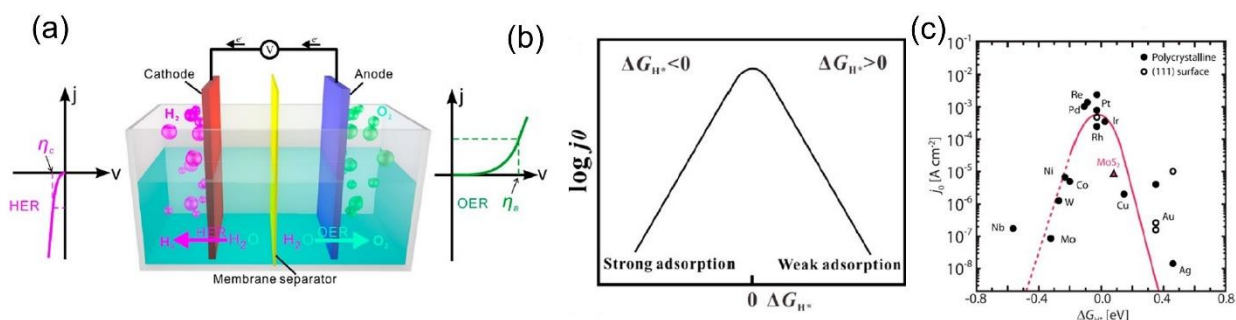


Figure 2.3: (a) Water splitting reaction (b) Volcano plot of exchange current density (J_0) vs. ΔG^* [150-152].

The smaller size (2 nm) of the metal based nanoparticle i.e. Pt, Pd has higher surface to volume

ratio, different morphologies (nanocube, nanocage, ultrathin type morphology), high surface active sites than edge sites which becomes effective for HER kinetics [153-156]. Such utilization efficiency of Pt can be achieved by controlling different synthetic techniques like seed mediated growth via chemical reduction, surfactants, halide additives [157-158]. Various reaction condition enhances the edge-to-face ratio and creates particular atomic arrangements in (100), (111) planes [159-160]. For example, by exposing (110) plane of Pt are catalytically active sites through facet controlled synthesis [161]. The single atom catalysis triggers the reaction kinetics, where high cost, lower availability, aggregation of small particles, internal strain, oxidative etching reduce the catalytic stability [162-163]. Several efforts have been established to enhance the HER performance by adsorption of platinum nanoparticles on nitrogen doped polymers, polyaniline-doped bacterial cellulose [164-165]. Similar to Pt, ruthenium (Ru) 0001 surface can form strong H bond with high negative ΔG^* and the bond weakens in presence of tungsten (W), facilitating the HER kinetics [166]. However, the Ru based metal phosphides, Ni@Ni₂P–Ru nanorods can enhance the overall electrocatalytic process involving moderate ΔG^* in the hydrogen adsorption-desorption process [167]. Interestingly, the loading of Ru on the catalytic surfaces like PANI based derivatives can play important role in the surface active sites and high catalytic activity [168]. To improve the catalytic performances, various shaped non noble metals like nickel, cobalt, molybdenum, copper have been known to catalyze hydrogen evolution [169-170]. In the nickel based heterostructure, Ni/NiO/CoSe₂ nanocomposites, Ni doped graphene, MoNi₄/MoO₂@Ni has been investigated as a HER catalyst [171-173]. In contrast, Ni/NiO/CoSe₂ shows poor stability whereas carbon-Ni bond in Ni doped graphene can enhance the stability and lower the overpotential. For metal hydrogen binding d-band energy becomes a crucial factor that determines the nature of adsorption in metals. The d band center near Fermi level signifies strong adsorption with other atoms and the bond becomes weak when d band center lies far from Fermi level. The interaction between oxygen deficient MoO₂ and metallic phase MoNi₄ can regulate the d band center and enhance the conductivity. The dual effect reveals lower adsorption energy of water than platinum in the preliminary step of HER kinetics [174]. Similar to nitrogen different cobalt based composites like Co-g-C₃N₄, Fe-Co-CNT (FeCo/NCNTs-NH) alloy, Co–Ni nanoalloy, Fe–Co alloy, Co based metal-organic framework (ZIF-67), N-doped CuCo nanoalloy, Co₃Mo alloy shows excellent HER activity due to core-shell heterostructure, variable active sites

[175-179]. Recently, ternary alloys like Pt–Ru–Ni, Pt–Ru–Fe, Pt–Ru–Co, Pt–Ru–Cr are gained interest in hydrogen evolution reactions [180-181]. Thus, the choice of compound and ratio of the active sites, atom contents, morphology can enhance the overall HER performances in acidic and alkaline medium.

2.7. Hydrogen evolution reaction (HER) with 2D materials

The metal based electrocatalyst shows tremendous electrocatalytic performance, but the agglomeration to larger particle, acid corrosion, poor stability, and small scale production makes it reductant to significant HER electrocatalyst. In the field of transition metal oxides (TMO), molybdenum and tungsten-based oxide (MoO_2 , WO_2) are most common electrocatalysts where the performance can be enhanced by formation of composites with metal based substrates (nickel foam, Ni/NiO/ MoO_x), Phosphorous-doped rGO [182-185]. The oxygen vacancy of MoO_{3-x} and WO_{3-x} can induce Mo^{5+} state with Mo^{6+} which are catalytically active in alkaline HER [186]. The nitrogen defect in transition metal nitrides (TMN) produces lattice strain and optimizes the d band center near Fermi level and attracted considerable attention to the HER performances [187]. However, δ -MoN nanosheets and γ - Mo_2N have HER active sites and the performance depends on the thickness of the atomic layer, type of restacking [188]. Sun et al. have reported Ni_3 that N on Ni foam and later nitrogen vacancy via plasma treatment can optimize the HER catalysis [189]. In catalyzing HER, cobalt based nitrides i.e. Co- Mo_2N , NiCo_2N , Co_4N show moderate hydrogen adsorption energy, leading to lower overpotential [190-192]. It should be noted the d band centre of Co_4N lies far away from Fermi level which deaccelerates the HER kinetics. The shifting of d band center has been modified by vanadium doping in Co_4N [193]. In metal carbide complexes, the molybdenum carbide (Mo_2C) has widened d band structure due to overlap between metal d orbital with carbon s and p orbitals [194]. The crystal phase, morphology has been tuned to optimize the HER kinetics. The high temperature annealing during the production of Mo_2C generates some nanoparticles which reduce the surface area and enhance the surface active sites [195]. In addition, the change in crystal structure of carbide complexes such as α - Mo_2C , β - Mo_2C , δ - Mo_2C , γ - Mo_2C shows different activity towards HER in different electrolyte mediums [196]. Among them, β - Mo_2C shows tremendous activity where the durability towards HER can be modified by transition metal doping like Chromium, iron, nickel, cobalt [197-199].

However, the embedding of Mo₂C/WC nanoparticle on CNT, N-doped carbon monolayer, N and P co-doped rGO, B and N co-doped rGO can show good HER properties due to variable donor-acceptor state and trigger the electron conduction [200-205]. Recently, controlling the Mo vacancies on Mo₂C can modify the Mo³⁺/Mo²⁺ ratio which can evaluate the suitable (lower) adsorption energy of hydrogen on the catalytic surface [206]. The metal carbides can form heterostructure with carbon based and metal phosphides and show robust electrocatalytic activities. Most commonly, the Mo₂N–Mo₂C heterojunction on rGO has N-Mo-C active sites, having lower adsorption energy ($\Delta G^* - 0.046$ eV) of intermediate hydrogen occurring at the N site [207]. Apart from carbides, metal borides can be next generation electrocatalysts which were first proposed by Hu's group [208]. In spite of the electron deficiency of boron, the metal boride complexes cannot form in pure form due to mixing of α -MoB and β -MoB. β -MoB is catalytically active and smaller concentration than α -MoB can reduce the HER efficiency [209]. Fokwa's group has designed Mo₂B₄ which consists of two phases of graphene and phosphorene like boron layer [210]. The graphene like layer is active and adsorption energy is close to zero whereas puckered like B layer is catalytic inactive.

Transition metal Dichalcogenides (TMDs) are most extensively studied as an electrocatalyst in proton reduction, oxygen reduction, oxygen evolution, batteries. The theoretical and experimental analyses suggest edge sites of TMDs are active for hydrogen evolution where basal plane is inactive [211]. To enhance the active edge site density of TMDs like MoS₂, WS₂, WSe₂ etc., the specific area at the edge site is enhanced by optimizing the morphology like nanosphere, nanosheet, nanoflakes [212]. The vertical arrangements of the parallel layer in MoS₂ nanobelts have high edge sites at the top surface and enhance the HER performances [213]. The edge active sites are mainly due to unsaturated Sulphur (S) and selenium (Se) atoms which can form discrete energy states between the valence and conduction band. Depending on the percentage of unsaturation, the local density state can be modified and closer to hydrogen reduction potential leading to favorable HER kinetics [214]. The sulphur vacancy can create tensile strain and hydrogen adsorption is favorable on the exposed Mo centers [215]. However, the incorporation of heteroatom doping like Pt, Pd, Co, Fe, Zn can activate the sulphur in basal plane and ideal free energy change is observed after hydrogen adsorption and desorption [216-220]. It has been proposed theoretically that Fe, Cr, Ti, Mn can form six coordinated sulphur atoms where Pt, Ni,

Pd can form four coordinated sulphur atoms [221]. The two uncoordinated sites are active sites for hydrogen adsorption. Similarly, non-metal dopants like oxygen, phosphorous, nitrogen enhance the conductivity and improve the high onset potential and turnover frequency. The semiconducting, 2H- MoS₂, WS₂ based materials have lower conductivity and show poor HER activity. The phase transformation to 1T phase after Li intercalation enhances the interplanar distance between two layers and activates the basal planes [222]. The dual activity of basal Mo center and edge centers, metallic phase of 1T phase of TMDs favors the charge transfer kinetics to H⁺ ions. Binary TMDs based hybrid structures exhibit high catalytic performances due to synergistic effects. Fe-Ni sulfides, Co-Ni sulfides, Co-Mo sulfides, Ni-Mo sulphides based binary TMDs have large defect sites and presence of M-Mo-S (M= Fe,Co,Ni) bond serve as an active site for hydrogen evolution [223-226]. Moreover, the presence of S₂²⁻ and S²⁻ ions improves the catalytic sites of binary TMDs [227]. Thus electron transport, active sites, favorable adsorption energy, mass loading are the key factors for water electrolysis specially the hydrogen gas evolution.

2.8. Metal Sensing based applications

Depending on the various excitation and emission wavelengths, UV-Vis absorption spectroscopy and Fluorescence spectroscopy have been employed to detect such compounds due to high sensitivity of the carbon dots. GQD has been explored as a sensing material for heavy metal ions (Hg²⁺, Cd²⁺), toxic phenolic derivatives (di-hydroxybenzene, chloramphenicol, p-nitrophenol) and hydroquinone [228-229]. In many organic dyes insecticides and industrial waste release p-nitro phenol (PNP) which is not degradable in water and is harmful to living beings. The polymer coated GQD has -NH₂ groups which can effectively bind with PNP [230]. However, different metal doping (Ag, Au, Cu) on various TMDs, carbon nanotubes, N-doped GQD and metal nanoparticle based graphene oxides are used as prominent catalysts for nitrophenol reduction to aminophenol [231-234]. Also, the π - π stacking influences pyrocatechol detection for GQD based quantum dots [235]. Besides, the nitrogen doping, the electron withdrawing Sulphur atoms can change the local states of CQD which interacts with Fe³⁺ ions and promising reagent for Fe detection in human serum [236]. Recently, CQD has been employed as immunosensor with very low detection limit. CQD are very sensitive to various nucleic acid due to π - π stacking mechanism

and CQD-DNA based biosensors are designed by DNA complementation principles [237]. Sensitive detection of antigens like immunoglobulin CQD based antigen-antibody quencher has been developed [238]. Thus, the sensitivity, sensing mechanism and selectivity of various CQD/GQD need to be understood more details which depends on the type of functionalization and synthesis conditions.

2.9. References

1. Xiao, X., Wang, H., Urbankowski, P. and Gogotsi, Y., *Chemical Society Reviews*, 47(23), 2018, pp.8744-8765.
2. Zhan, Y., Liu, Z., Najmaei, S., Ajayan, P.M. and Lou, J., *small*, 2012, 8(7), pp.966-971.
3. Wang, S., Wang, X. and Warner, J.H., *ACS nano*, 2015, 9(5), pp.5246-5254.
4. Zhang, Y., Ji, Q., Han, G.F., Ju, J., Shi, J., Ma, D., Sun, J., Zhang, Y., Li, M., Lang, X.Y. and Zhang, Y., *ACS nano*, 2014, 8(8), pp.8617-8624.
5. Empante, T.A., Zhou, Y., Klee, V., Nguyen, A.E., Lu, I.H., Valentin, M.D., Naghibi Alvillar, S.A., Preciado, E., Berges, A.J., Merida, C.S. and Gomez, M., *ACS nano*, 2017, 11(1), pp.900-905.
6. Kang, K.N., Godin, K. and Yang, E.H., *Scientific reports*, 2015, 5(1), p.13205.
7. Gu, C., Zhao, S., Zhang, J.L., Sun, S., Yuan, K., Hu, Z., Han, C., Ma, Z., Wang, L., Huo, F. and Huang, W., *ACS nano*, 2017, 11(5), pp.4943-4949.
8. Sang, X., Xie, Y., Yilmaz, D.E., Lotfi, R., Alhabeb, M., Ostadhossein, A., Anasori, B., Sun, W., Li, X., Xiao, K. and Kent, P.R., *Nature communications*, 2018, 9(1), p.2266.
9. Chen, X., Yang, H., Wu, B., Wang, L., Fu, Q. and Liu, Y., *Advanced Materials*, 2019, 31(12), p.1805582.
10. Ruan, G., Sun, Z., Peng, Z. and Tour, J.M., *ACS nano*, 2011, 5(9), pp.7601-7607.
11. Page, A.J., Wang, Y., Li, H.B., Irle, S. and Morokuma, K., *The Journal of Physical Chemistry C*, 2013, 117(28), pp.14858-14864.
12. Li, G., Huang, S.H. and Li, Z., *Physical Chemistry Chemical Physics*, 2015, 17(35), pp.22832-22836.
13. Zhu, J., Kang, J., Kang, J., Jariwala, D., Wood, J.D., Seo, J.W.T., Chen, K.S., Marks, T.J. and Hersam, M.C., *Nano letters*, 2015, 15(10), pp.7029-7036.
14. Novoselov, K.S., Mishchenko, A., Carvalho, A. and Castro Neto, A.H., *Science*, 2016, 353(6298), p.aac9439.
15. Lei, Z.L. and Guo, B., *Advanced Science*, 2022, 9(4), p.2102924.
16. Dasmahapatra, A.K., Powe, D.K., Dasari, T.P. and Tchounwou, P.B., *Data in Brief*, 2020, 32, p.106218.
17. Chua, C.K. and Pumera, M., *Chemical Society Reviews*, 2014, 43(1), pp.291-312.
18. Wang, Y., Shi, Z. and Yin, J., *ACS applied materials & interfaces*, 2011, 3(4), pp.1127-1133.
19. Sun, D., Feng, S., Terrones, M. and Schaak, R.E., *Chemistry of Materials*, 2015, 27(8), pp.3167-3175.
20. Mahler, B., Hoepfner, V., Liao, K. and Ozin, G.A., *Journal of the American Chemical Society*, 2014, 136(40), pp.14121-14127.

21. Jung, W., Lee, S., Yoo, D., Jeong, S., Miró, P., Kuc, A., Heine, T. and Cheon, J., *Journal of the American Chemical Society*, 2015, 137(23), pp.7266-7269.
22. Sekar, P., Greyson, E.C., Barton, J.E. and Odom, T.W., *Journal of the American Chemical Society*, 2005, 127(7), pp.2054-2055.
23. Nag, A., Raidongia, K., Hembram, K.P., Datta, R., Waghmare, U.V. and Rao, C.N.R., *ACS nano*, 2010, 4(3), pp.1539-1544.
24. Lu, X., Yu, M., Huang, H. and Ruoff, R.S., *Nanotechnology*, 1999, 10(3), p.269.
25. Fang, H., Chuang, S., Chang, T.C., Takei, K., Takahashi, T. and Javey, A., *Nano letters*, 2012, 12(7), pp.3788-3792.
26. Novoselov, K.S., Jiang, D., Schedin, F., Booth, T.J., Khotkevich, V.V., Morozov, S.V. and Geim, A.K., *Proceedings of the National Academy of Sciences*, 2005, 102(30), pp.10451-10453.
27. Braga, D., Gutiérrez Lezama, I., Berger, H. and Morpurgo, A.F., *Nano letters*, 2012, 12(10), pp.5218-5223.
28. Bianco, E., Butler, S., Jiang, S., Restrepo, O.D., Windl, W. and Goldberger, J.E., *ACS nano*, 2013, 7(5), pp.4414-4421.
29. Alem, N., Erni, R., Kisielowski, C., Rossell, M.D., Gannett, W. and Zettl, A.J.P.R.B., *Physical review B*, 2009, 80(15), p.155425.
30. Coleman, J.N., Lotya, M., O'Neill, A., Bergin, S.D., King, P.J., Khan, U., Young, K., Gaucher, A., De, S., Smith, R.J. and Shvets, I.V., *Science*, 2011, 331(6017), pp.568-571.
31. Das, S., Kim, M., Lee, J.W. and Choi, W., *Critical Reviews in Solid State and Materials Sciences*, 2014, 39(4), pp.231-252.
32. Huo, C., Yan, Z., Song, X. and Zeng, H., *Science bulletin*, 2015, 60(23), pp.1994-2008.
33. Ma, R., Liu, Z., Li, L., Iyi, N. and Sasaki, T., *Journal of Materials Chemistry*, 2006, 16(39), pp.3809-3813.
34. Naguib, M., Mashtalir, O., Carle, J., Presser, V., Lu, J., Hultman, L., Gogotsi, Y. and Barsoum, M.W., *ACS nano*, 2012, 6(2), pp.1322-1331.
35. Eda, G., Yamaguchi, H., Voiry, D., Fujita, T., Chen, M. and Chhowalla, M., *Nano letters*, 2011, 11(12), pp.5111-5116.
36. Tsai, H.L., Heising, J., Schindler, J.L., Kannewurf, C.R. and Kanatzidis, M.G., *Chemistry of materials*, 1997, 9(4), pp.879-882.
37. Subedi, S., Rella, A.K., Trung, L.G., Kumar, V. and Kang, S.W., *ACS nano*, 2022, 16(4), pp.6480-6492.
38. Kumawat, M.K., Thakur, M., Gurung, R.B. and Srivastava, R., *ACS Sustainable Chemistry & Engineering*, 2017, 5(2), pp.1382-1391.
39. Zhou, M., Zhou, Z., Gong, A., Zhang, Y. and Li, Q., *Talanta*, 2015, 143, pp.107-113.
40. Han, Z., Zhang, H., He, L., Pan, S., Liu, H. and Hu, X., *Microchemical Journal*, 2019, 146, pp.300-308.
41. Cheng, C., Xing, M. and Wu, Q., *Materials Science and Engineering: C*, 2019, 99, pp.611-619.
42. Hu, Z., Jiao, X.Y. and Xu, L., *Microchemical Journal*, 2020, 154, p.104588.
43. Li, Y., Zhao, Y., Cheng, H., Hu, Y., Shi, G., Dai, L. and Qu, L., *Journal of the American Chemical Society*, 2012, 134(1), pp.15-18.
44. Lu, M. and Zhou, L., *Materials Science and Engineering: C*, 2019, 101, pp.352-359.
45. Mei, Q., Zhang, K., Guan, G., Liu, B., Wang, S. and Zhang, Z., *Chemical communications*, 2010, 46(39), pp.7319-7321.
46. Zhang, M., Bai, L., Shang, W., Xie, W., Ma, H., Fu, Y., Fang, D., Sun, H., Fan, L., Han, M. and Liu, C., *Journal of materials chemistry*, 2012, 22(15), pp.7461-7467.

47. Zhang, M., Su, R., Zhong, J., Fei, L., Cai, W., Guan, Q., Li, W., Li, N., Chen, Y., Cai, L. and Xu, Q., *Nano Research*, 2019, 12, pp.815-821.
48. Qin, Z., Wang, W., Zhan, X., Du, X., Zhang, Q., Zhang, R., Li, K., Li, J. and Xu, W., *Spectrochimica Acta Part A: Molecular and Biomolecular Spectroscopy*, 2019, 208, pp.162-171.
49. Markovic, Z.M., Labudova, M., Danko, M., Matijasevic, D., Micusik, M., Nadazdy, V., Kovacova, M., Kleinova, A., Spitalsky, Z., Pavlovic, V. and Milivojevic, D.D., *ACS Sustainable Chemistry & Engineering*, 2020, 8(43), pp.16327-16338.
50. Shangguan, J., Huang, J., He, D., He, X., Wang, K., Ye, R., Yang, X., Qing, T. and Tang, J., *Analytical chemistry*, 2017, 89(14), pp.7477-7484.
51. Xiao, N., Liu, S.G., Mo, S., Li, N., Ju, Y.J., Ling, Y., Li, N.B. and Luo, H.Q., *Talanta*, 2018, 184, pp.184-192.
52. Sun, Y.P., Zhou, B., Lin, Y., Wang, W., Fernando, K.S., Pathak, P., Mezziani, M.J., Harruff, B.A., Wang, X., Wang, H. and Luo, P.G., *Journal of the American Chemical Society*, 2006, 128(24), pp.7756-7757.
53. Dong, Y., Shao, J., Chen, C., Li, H., Wang, R., Chi, Y., Lin, X. and Chen, G., *Carbon*, 2012, 50(12), pp.4738-4743.
54. Huang, X., Zhang, F., Zhu, L., Choi, K.Y., Guo, N., Guo, J., Tackett, K., Anilkumar, P., Liu, G., Quan, Q. and Choi, H.S., *ACS nano*, 2013, 7(7), pp.5684-5693.
55. Liu, M., Xu, Y., Niu, F., Gooding, J.J. and Liu, J., *Analyst*, 2006, 141(9), pp.2657-2664.
56. Russo, P., Liang, R., Jabari, E., Marzbanrad, E., Toyserkani, E. and Zhou, Y.N., *Nanoscale*, 2016, 8(16), pp.8863-8877.
57. Li, Z., Yu, H., Bian, T., Zhao, Y., Zhou, C., Shang, L., Liu, Y., Wu, L.Z., Tung, C.H. and Zhang, T., *Journal of Materials Chemistry C*, 2015, 3(9), pp.1922-1928.
58. Xiong, Y., Xiao, L., Yang, Y., DiSalvo, F.J. and Abruña, H.D., *Chemistry of Materials*, 2018, 30(5), pp.1532-1539.
59. Stamenkovic, V.R., Mun, B.S., Arenz, M., Mayrhofer, K.J., Lucas, C.A., Wang, G., Ross, P.N. and Markovic, N.M., *Nature materials*, 2007, 6(3), pp.241-247.
60. Xu, H., Wang, D., Yang, P., Liu, A., Li, R., Li, Y., Xiao, L., Ren, X., Zhang, J. and An, M., *Journal of Materials Chemistry A*, 2020, 8(44), pp.23187-23201.
61. Eisenberg, D., Slot, T.K. and Rothenberg, G., *ACS Catalysis*, 2018, 8(9), pp.8618-8629.
62. Zhu, Y.P., Guo, C., Zheng, Y. and Qiao, S.Z., *Accounts of chemical research*, 2017, 50(4), pp.915-923.
63. Gao, F., Zhao, G.L., Wang, Z., Bagayoko, D. and Liu, D.J., *Catalysis Communications*, 2015, 62, pp.79-82.
64. Zhu, Y.P., Guo, C., Zheng, Y. and Qiao, S.Z., *Accounts of chemical research*, 2017, 50(4), pp.915-923.
65. Cheng, F., Shen, J., Peng, B., Pan, Y., Tao, Z. and Chen, J., *Nature chemistry*, 2011, 3(1), pp.79-84.
66. Jung, J.I., Risch, M., Park, S., Kim, M.G., Nam, G., Jeong, H.Y., Shao-Horn, Y. and Cho, J., *Energy & Environmental Science*, 2016, 9(1), pp.176-183.
67. Yamada, I., Fujii, H., Takamatsu, A., Ikeno, H., Wada, K., Tsukasaki, H., Kawaguchi, S., Mori, S. and Yagi, S., *Advanced Materials*, 2017, 29(4), p.1603004.
68. Petrie, J.R., Cooper, V.R., Freeland, J.W., Meyer, T.L., Zhang, Z., Lutterman, D.A. and Lee, H.N., *Journal of the American Chemical Society*, 2016, 138(8), pp.2488-2491.
69. Qian, L., Lu, Z., Xu, T., Wu, X., Tian, Y., Li, Y., Huo, Z., Sun, X. and Duan, X., *Advanced energy materials*, 2015, 5(13), p.1500245.

70. Zhang, Z., Wang, X., Cui, G., Zhang, A., Zhou, X., Xu, H. and Gu, L., *Nanoscale*, 6(7), 2014, pp.3540-3544.
71. Deng, D., Yu, L., Chen, X., Wang, G., Jin, L., Pan, X., Deng, J., Sun, G. and Bao, X., *Angewandte Chemie International Edition*, 2013, 52(1), pp.371-375.
72. Alexeyeva, N., Laaksonen, T., Kontturi, K., Mirkhalaf, F., Schiffrin, D.J. and Tammeveski, K., *Electrochemistry communications*, 2006, 8(9), pp.1475-1480.
73. Gabe, A., García-Aguilar, J., Berenguer-Murcia, Á., Morallón, E. and Cazorla-Amorós, D., *Applied Catalysis B: Environmental*, 2017, 217, pp.303-312.
74. Fu, G., Chen, Y., Cui, Z., Li, Y., Zhou, W., Xin, S., Tang, Y. and Goodenough, J.B., *Nano letters*, 2016, 16(10), pp.6516-6522.
75. Cheon, J.Y., Kim, K., Sa, Y.J., Sahgong, S.H., Hong, Y., Woo, J., Yim, S.D., Jeong, H.Y., Kim, Y. and Joo, S.H., *Advanced Energy Materials*, 2016, 6(7), p.1501794.
76. Hu, C. and Dai, L., *Angewandte Chemie International Edition*, 2016, 55(39), pp.11736-11758.
77. Wu, M., Wang, Y., Wei, Z., Wang, L., Zhuo, M., Zhang, J., Han, X. and Ma, J., *Journal of Materials Chemistry A*, 2018, 6(23), pp.10918-10925.
78. Wang, Z., Lu, Y., Yan, Y., Larissa, T.Y.P., Zhang, X., Wu, D., Zhang, H., Yang, Y. and Wang, X., *Nano Energy*, 2016, 30, pp.368-378.
79. Wang, J., Huang, Z., Liu, W., Chang, C., Tang, H., Li, Z., Chen, W., Jia, C., Yao, T., Wei, S. and Wu, Y., *Journal of the American Chemical Society*, 2017, 139(48), pp.17281-17284.
80. Behret, H., Binder, H. and Sandstedt, G., *Electrochimica Acta*, 1975, 20(2), pp.111-117.
81. Deng, Y., Xiao, S., Zheng, Y., Rong, X., Bai, M., Tang, Y., Ma, T., Cheng, C. and Zhao, C., *Chemical Engineering Journal*, 2023, 451, p.138514.
82. Liu, C.Y. and Li, E.Y., *ACS Applied Materials & Interfaces*, 2018, 11(1), pp.1638-1644.
83. Jia, Y., Zhang, L., Du, A., Gao, G., Chen, J., Yan, X., Brown, C.L. and Yao, X., *Advanced materials*, 2016, 28(43), pp.9532-9538.
84. Liu, Y., Shen, Y., Sun, L., Li, J., Liu, C., Ren, W., Li, F., Gao, L., Chen, J., Liu, F. and Sun, Y., *Nature communications*, 2016, 7(1), p.10921.
85. Shi, Z., Kutana, A. and Yakobson, B.I., *The Journal of Physical Chemistry Letters*, 2015, 6(1), pp.106-112.
86. Mohamed, S.G., Attia, S.Y., Barakat, Y.F., Hassan, H.H. and Zoubi, W.A., *ChemistrySelect*, 2018, 3(22), pp.6061-6072.
87. Cloke, R.R., Marangoni, T., Nguyen, G.D., Joshi, T., Rizzo, D.J., Bronner, C., Cao, T., Louie, S.G., Crommie, M.F. and Fischer, F.R., *Journal of the American Chemical Society*, 2015, 137(28), pp.8872-8875.
88. Jiao, Y., Zheng, Y., Jaroniec, M. and Qiao, S.Z., *Journal of the American Chemical Society*, 2014, 136(11), pp.4394-4403.
89. Wang, L., Sofer, Z., Šimek, P., Tomandl, I. and Pumera, M., *The Journal of Physical Chemistry C*, 2013, 117(44), pp.23251-23257.
90. Schiros, T., Nordlund, D., Pálová, L., Prezzi, D., Zhao, L., Kim, K.S., Wurstbauer, U., Gutiérrez, C., Delongchamp, D., Jaye, C. and Fischer, D., *Nano letters*, 2012, 12(8), pp.4025-4031.
91. Lai, L., Potts, J.R., Zhan, D., Wang, L., Poh, C.K., Tang, C., Gong, H., Shen, Z., Lin, J. and Ruoff, R.S., *Energy & Environmental Science*, 2012, 5(7), pp.7936-7942.
92. Yu, H., Shang, L., Bian, T., Shi, R., Waterhouse, G.I., Zhao, Y., Zhou, C., Wu, L.Z., Tung, C.H. and Zhang, T., *Advanced Materials*, 2016, 28(25), pp.5080-5086.
93. Wang, H.M., Wang, H.X., Chen, Y., Liu, Y.J., Zhao, J.X., Cai, Q.H. and Wang, X.Z., *Applied Surface Science*, 2013, 273, pp.302-309.

94. Sun, X., Zhu, Q., Kang, X., Liu, H., Qian, Q., Zhang, Z. and Han, B., *Angewandte Chemie*, 2016, 128(23), pp.6883-6887.
95. Khan, K., Tareen, A.K., Aslam, M., Zhang, Y., Wang, R., Ouyang, Z., Gou, Z. and Zhang, H., *Nanoscale*, 2019, 11(45), pp.21622-21678.
96. Menamparambath, M.M., Park, J.H., Yoo, H.S., Patole, S.P., Yoo, J.B., Kim, S.W. and Baik, S., *Nanoscale*, 2014, 6(15), pp.8844-8851.
97. Wang, T., Gao, D., Zhuo, J., Zhu, Z., Papakonstantinou, P., Li, Y. and Li, M., *Chemistry–A European Journal*, 2013, 19(36), pp.11939-11948.
98. Huang, H., Feng, X., Du, C. and Song, W., *Chemical Communications*, 2015, 51(37), pp.7903-7906.
99. Du, C., Huang, H., Feng, X., Wu, S. and Song, W., *Journal of Materials Chemistry A*, 2015, 3(14), pp.7616-7622.
100. Huang, H., Feng, X., Du, C., Wu, S. and Song, W., *Journal of Materials Chemistry A*, 2015, 3(31), pp.16050-16056.
101. Suresh, C., Mutyala, S. and Mathiyarasu, J., *Materials Letters*, 2016, 164, pp.417-420.
102. Wang, T., Zhuo, J., Chen, Y., Du, K., Papakonstantinou, P., Zhu, Z., Shao, Y. and Li, M., *ChemCatChem*, 2014, 6(7), pp.1877-1881.
103. Khan, A.F., Ferrari, A.G.M., Hughes, J.P., Smith, G.C., Banks, C.E. and Rowley-Neale, S.J., *Sensors*, 2022, 22(9), p.3330.
104. Wang, S., Yu, D., Dai, L., Chang, D.W. and Baek, J.B., *ACS nano*, 2011, 5(8), pp.6202-6209.
105. He, L., Cui, B., Liu, J., Wang, M., Zhang, Z. and Zhang, H., *ACS Sustainable Chemistry & Engineering*, 2018, 6(7), pp.9257-9268.
106. Chua, X.J., Luxa, J., Eng, A.Y.S., Tan, S.M., Sofer, Z. and Pumera, M., *ACS Catalysis*, 2016, 6(9), pp.5724-5734.
107. Xu, Y., Chen, C., Zhou, M., Guangyi, F.U., Zhao, Y. and Chen, Y., *RSC advances*, 2017, 7(43), pp.26722-26728.
108. Tadi, K.K., Palve, A.M., Pal, S., Sudeep, P.M. and Narayanan, T.N., *Nanotechnology*, 2016, 27(27), p.275402.
109. Patil, I.M., Lokanathan, M. and Kakade, B., *Journal of Materials Chemistry A*, 2016, 4(12), pp.4506-4515.
110. Bach, L.G., Thi, M.L.N., Bui, Q.B. and Nhac-Vu, H.T., *Synthetic Metals*, 2019, 254, pp.172-179.
111. Das, A.K., Srivastav, M., Layek, R.K., Uddin, M.E., Jung, D., Kim, N.H. and Lee, J.H., *Journal of Materials Chemistry A*, 2014, 2(5), pp.1332-1340.
112. Suresh, C., Mutyala, S. and Mathiyarasu, J., *Materials Letters*, 2016, 164, pp.417-420.
113. Tang, J., Wang, C., Zhang, H. and Guo, J., *Journal of Alloys and Compounds*, 2022, 911, p.164991.
114. Xin, S., Liu, Z., Ma, L., Sun, Y., Xiao, C., Li, F. and Du, Y., *Nano Research*, 2016, 9, pp.3795-3811.
115. He, T., Xu, L., Zhang, Y., Huang, H. and Jiao, H., *New Journal of Chemistry*, 2019, 43(3), pp.1611-1616.
116. Wang, S., Iyyamperumal, E., Roy, A., Xue, Y., Yu, D. and Dai, L., *Angewandte Chemie International Edition*, 2011, 50(49), pp.11756-11760.
117. Bar-Hen, A., Bar-Ziv, R., Ohaion-Raz, T., Mizrahi, A., Hettler, S., Arenal, R. and Sadan, M.B., *Chemical Engineering Journal*, 2021, 420, p.129771.

118. Huang, H., Feng, X., Du, C., Wu, S. and Song, W., *Journal of Materials Chemistry A*, 2015, 3(31), pp.16050-16056.
119. Jang, J.H., Kato, A., Machida, K. and Naoi, K., *Journal of The Electrochemical Society*, 2005, 153(2), p.A321.
120. Yuan, C., Zhang, X., Su, L., Gao, B. and Shen, L., *Journal of Materials Chemistry*, 2009, 19(32), pp.5772-5777.
121. Patil, U.M., Gurav, K.V., Fulari, V.J., Lokhande, C.D. and Joo, O.S., *Journal of Power Sources*, 2009, 188(1), pp.338-342.
122. Reddy, A.L.M. and Ramaprabhu, S., *The Journal of Physical Chemistry C*, 2007, 111(21), pp.7727-7734.
123. Bai, X., Hu, X., Zhou, S., Yan, J., Sun, C., Chen, P. and Li, L., *Electrochimica Acta*, 2013, 87, pp.394-400.
124. Chen, X., Lin, H., Chen, P., Guan, G., Deng, J. and Peng, H., *Advanced materials*, 2014, 26(26), pp.4444-4449.
125. Wang, X., Liu, S., Wang, H., Tu, F., Fang, D. and Li, Y., *Journal of Solid State Electrochemistry*, 2012, 16, pp.3593-3602.
126. Gao, H., Xiao, F., Ching, C.B. and Duan, H., *ACS applied materials & interfaces*, 2012, 4(12), pp.7020-7026.
127. Yan, J., Fan, Z., Wei, T., Qian, W., Zhang, M. and Wei, F., *Carbon*, 2010, 48(13), pp.3825-3833.
128. Yan, J., Fan, Z., Sun, W., Ning, G., Wei, T., Zhang, Q., Zhang, R., Zhi, L. and Wei, F., *Advanced Functional Materials*, 2012, 22(12), pp.2632-2641.
129. Lee, K.H., Lee, Y.W., Lee, S.W., Ha, J.S., Lee, S.S. and Son, J.G., *Scientific reports*, 2015, 5(1), p.13696.
130. Moreno-Castilla, C. and Maldonado-Hódar, F.J., *Carbon*, 2005, 43(3), pp.455-465.
131. Coleman, J.N., Khan, U., Blau, W.J. and Gun'ko, Y.K., *Carbon*, 2006, 44(9), pp.1624-1652.
132. Gueon, D. and Moon, J.H., *ACS applied materials & interfaces*, 2015, 7(36), pp.20083-20089.
133. Pan, H., Poh, C.K., Feng, Y.P. and Lin, J., *Chemistry of Materials*, 2007, 19(25), pp.6120-6125.
134. Bulusheva, L.G., Fedorovskaya, E.O., Kurennya, A.G. and Okotrub, A.V., *physica status solidi (b)*, 2013, 250(12), pp.2586-2591.
135. Deng, Y., Xie, Y., Zou, K. and Ji, X., *Journal of Materials Chemistry A*, 2016, 4(4), pp.1144-1173.
136. Lim, E., Kim, H., Jo, C., Chun, J., Ku, K., Kim, S., Lee, H.I., Nam, I.S., Yoon, S., Kang, K. and Lee, J., *ACS nano*, 2014, 8(9), pp.8968-8978.
137. Li, M., Tang, Z., Leng, M. and Xue, J., *Advanced Functional Materials*, 2014, 24(47), pp.7495-7502.
138. Xu, Y., Sheng, K., Li, C. and Shi, G., *ACS nano*, 2010, 4(7), pp.4324-4330.
139. Hao, L., Ning, J., Luo, B., Wang, B., Zhang, Y., Tang, Z., Yang, J., Thomas, A. and Zhi, L., *Journal of the American Chemical Society*, 2015, 137(1), pp.219-225.
140. Yang, Z., Ren, J., Zhang, Z., Chen, X., Guan, G., Qiu, L., Zhang, Y. and Peng, H., *Chemical reviews*, 2015, 115(11), pp.5159-5223.
141. Simon, P. and Gogotsi, Y., *Nature materials*, 2008, 7(11), pp.845-854.
142. Li, W., Liu, J. and Zhao, D., *Nature Reviews Materials*, 2016, 1(6), pp.1-17.

143. Yan, J., Wei, T., Shao, B., Ma, F., Fan, Z., Zhang, M., Zheng, C., Shang, Y., Qian, W. and Wei, F. *Carbon*, 2010, 48(6), pp.1731-1737.
144. Yang, Z., Liu, M., Zhang, C., Tjiu, W.W., Liu, T. and Peng, H., *Angewandte Chemie International Edition*, 2013, 52(14), pp.3996-3999.
145. Yu, D. and Dai, L., *The Journal of Physical Chemistry Letters*, 2010, 1(2), pp.467-470.
146. You, B., Wang, L., Yao, L. and Yang, J., *Chemical communications*, 2013, 49(44), pp.5016-5018.
147. Lin, T.W., Sadhasivam, T., Wang, A.Y., Chen, T.Y., Lin, J.Y. and Shao, L.D., *ChemElectroChem*, 2018, 5(7), pp.1024-1031.
148. Jin, Y. and Jia, M., *Colloids and Surfaces A: Physicochemical and Engineering Aspects*, 2015, 464, pp.17-25.
149. Kale, D.P., Deshmukh, S.P., Shirsath, S.R. and Bhanvase, B.A., *Optik*, 2020, 208, p.164532.
150. Nørskov, J.K., Bligaard, T., Logadottir, A., Kitchin, J.R., Chen, J.G., Pandalov, S. and Stimming, U., *Journal of The Electrochemical Society*, 2005, 152(3), p.J23.
151. Conway, B.E. and Tilak, B.V., *Electrochimica acta*, 2002, 47(22-23), pp.3571-3594.
152. Zhu, J., Hu, L., Zhao, P., Lee, L.Y.S. and Wong, K.Y., *Chemical reviews*, 2019, 120(2), pp.851-918.
153. Tan, T.L., Wang, L.L., Zhang, J., Johnson, D.D. and Bai, K., *ACS Catalysis*, 2015, 5(4), pp.2376-2383.
154. Jang, H.J., Hong, S. and Park, S., *Journal of Materials Chemistry*, 2012, 22(37), pp.19792-19797.
155. Oh, A., Sa, Y.J., Hwang, H., Baik, H., Kim, J., Kim, B., Joo, S.H. and Lee, K., *Nanoscale*, 2016, 8(36), pp.16379-16386.
156. Xiong, Y. and Xia, Y., *Advanced Materials*, 2007, 19(20), pp.3385-3391.
157. Klinkova, A., Larin, E.M., Prince, E., Sargent, E.H. and Kumacheva, E., *Chemistry of Materials*, 2016, 28(9), pp.3196-3202.
158. Yin, J., Wang, J., Li, M., Jin, C. and Zhang, T., *Chemistry of Materials*, 2012, 24(14), pp.2645-2654.
159. Baker, L., Cavanagh, A.S., Yin, J., George, S.M., Kongkanand, A. and Wagner, F.T., *Applied Physics Letters*, 2012, 101(11).
160. Xie, X., Jiang, Y.F., Yuan, C.Z., Jiang, N., Zhao, S.J., Jia, L. and Xu, A.W., *The Journal of Physical Chemistry C*, 2017, 121(45), pp.24979-24986.
161. Ji, L., Wang, J., Zuo, S. and Chen, Z., *The Journal of Physical Chemistry C*, 2017, 121(16), pp.8923-8930.
162. Chen, J., Lim, B., Lee, E.P. and Xia, Y., *Nano Today*, 2009, 4(1), pp.81-95.
163. de Bruijn, F.A., Dam, V.A.T. and Janssen, G.J.M., *Fuel cells*, 2008, 8(1), pp.3-22.
164. Ji, L., Wang, J., Zuo, S. and Chen, Z., *The Journal of Physical Chemistry C*, 2017, 121(16), pp.8923-8930.
165. Zhang, Y., Tan, J., Wen, F., Zhou, Z., Zhu, M., Yin, S. and Wang, H., *International Journal of Hydrogen Energy*, 2018, 43(12), pp.6167-6176.
166. Joshi, U., Malkhandi, S., Ren, Y., Tan, T.L., Chiam, S.Y. and Yeo, B.S., *ACS applied materials & interfaces*, 2018, 10(7), pp.6354-6360.
167. Liu, Y., Liu, S., Wang, Y., Zhang, Q., Gu, L., Zhao, S., Xu, D., Li, Y., Bao, J. and Dai, Z., *Journal of the American Chemical Society*, 2018, 140(8), pp.2731-2734.
168. Wang, Z.L., Sun, K., Henzie, J., Hao, X., Li, C., Takei, T., Kang, Y.M. and Yamauchi, Y., *Angewandte Chemie International Edition*, 2018, 57(20), pp.5848-5852.

169. Miles, M.H. and Thomason, M.A., *Journal of the Electrochemical Society*, 1976, 123(10), p.1459.
170. Zhu, J., Hu, L., Zhao, P., Lee, L.Y.S. and Wong, K.Y., *Chemical reviews*, 2019, 120(2), pp.851-918.
171. Xu, Y.F., Gao, M.R., Zheng, Y.R., Jiang, J. and Yu, S.H., *Angewandte Chemie*, 2013, 125(33), pp.8708-8712.
172. Abbas, S.A., Iqbal, M.I., Kim, S.H. and Jung, K.D., *Electrochimica Acta*, 2017, 227, pp.382-390.
173. Zhang, J., Wang, T., Liu, P., Liao, Z., Liu, S., Zhuang, X., Chen, M., Zschech, E. and Feng, X., *Nature communications*, 2017, 8(1), p.15437.
174. Zhang, J., Wang, T., Liu, P., Liao, Z., Liu, S., Zhuang, X., Chen, M., Zschech, E. and Feng, X., *Nature communications*, 2017, 8(1), p.15437.
175. Chen, J., Ge, Y., Feng, Q., Zhuang, P., Chu, H., Cao, Y., Smith, W.R., Dong, P., Ye, M. and Shen, J., *ACS applied materials & interfaces*, 2019, 11(9), pp.9002-9010.
176. Deng, J., Ren, P., Deng, D. and Bao, X., *Angewandte Chemie International Edition*, 2015, 54(7), pp.2100-2104.
177. Kuang, M., Wang, Q., Han, P. and Zheng, G., *Advanced Energy Materials*, 2017, 7(17), p.1700193.
178. Wen, X., Yang, X., Li, M., Bai, L. and Guan, J., *Electrochimica Acta*, 2019, 296, pp.830-841.
179. Shang, Z., Chen, Z., Zhang, Z., Yu, J., Tan, S., Ciucci, F., Shao, Z., Lei, H. and Chen, D., *Journal of Alloys and Compounds*, 2018, 740, pp.743-753.
180. Shen, Y., Lua, A.C., Xi, J. and Qiu, X., *ACS Applied Materials & Interfaces*, 2016, 8(5), pp.3464-3472.
181. Xiao, Y., Liu, Y., Tang, Z., Wu, L., Zeng, Y., Xu, Y. and He, Y., *RSC advances*, 2016, 6(56), pp.51096-51105.
182. Yang, M.Q., Wang, J., Wu, H. and Ho, G.W., *Small*, 2018, 14(15), p.1703323.
183. Ghosh, S. and Basu, R.N., *Nanoscale*, 2018, 10(24), pp.11241-11280.
184. Tang, Y.J., Gao, M.R., Liu, C.H., Li, S.L., Jiang, H.L., Lan, Y.Q., Han, M. and Yu, S.H., *Angewandte Chemie*, 2015, 127(44), pp.13120-13124.
185. Yu, Z.Y., Lang, C.C., Gao, M.R., Chen, Y., Fu, Q.Q., Duan, Y. and Yu, S.H., *Energy & Environmental Science*, 2018, 11(7), pp.1890-1897.
186. Luo, Z., Miao, R., Huan, T.D., Mosa, I.M., Poyraz, A.S., Zhong, W., Cloud, J.E., Kriz, D.A., Thanneeru, S., He, J. and Zhang, Y., *Advanced Energy Materials*, 2016, 6(16), p.1600528.
187. Hwu, H.H. and Chen, J.G., *Chemical reviews*, 2005, 105(1), pp.185-212.
188. Chen, W.F., Sasaki, K., Ma, C., Frenkel, A.I., Marinkovic, N., Muckerman, J.T., Zhu, Y. and Adzic, R.R., *Angewandte Chemie International Edition*, 2012, 51(25), pp.6131-6135.
189. Liu, B., He, B., Peng, H.Q., Zhao, Y., Cheng, J., Xia, J., Shen, J., Ng, T.W., Meng, X., Lee, C.S. and Zhang, W., *Advanced Science*, 2018, 5(8), p.1800406.
190. Wang, Y., Zhang, B., Pan, W., Ma, H. and Zhang, J., *ChemSusChem*, 2017, 10(21), pp.4170-4177.
191. Wei, B., Tang, G., Liang, H., Qi, Z., Zhang, D., Hu, W., Shen, H. and Wang, Z., *Electrochemistry Communications*, 2018, 93, pp.166-170.
192. Zhang, Y., Ouyang, B., Xu, J., Jia, G., Chen, S., Rawat, R.S. and Fan, H.J., *Angewandte Chemie*, 2016, 128(30), pp.8812-8816.
193. Chen, Z., Song, Y., Cai, J., Zheng, X., Han, D., Wu, Y., Zang, Y., Niu, S., Liu, Y., Zhu, J. and Liu, X., *Angewandte Chemie International Edition*, 2018, 57(18), pp.5076-5080.

194. Kitchin, J.R., Nørskov, J.K., Barteau, M.A. and Chen, J.G., A density functional study. *Catalysis Today*, 2005, 105(1), pp.66-73.
195. Zhu, Y., Chen, G., Zhong, Y., Zhou, W., Liu, M. and Shao, Z., *Materials today energy*, 2017, 6, pp.230-237.
196. Zhou, G., Yang, Q., Guo, X., Chen, Y., Xu, L., Sun, D. and Tang, Y., *International Journal of Hydrogen Energy*, 2018, 43(19), pp.9326-9333.
197. Wan, C., Regmi, Y.N. and Leonard, B.M., *Angewandte Chemie*, 2014, 126(25), pp.6525-6528.
198. Xiong, K., Li, L., Zhang, L., Ding, W., Peng, L., Wang, Y., Chen, S., Tan, S. and Wei, Z., *Journal of Materials Chemistry A*, 2015, 3(5), pp.1863-1867.
199. Wan, C. and Leonard, B.M., *Chemistry of Materials*, 2015, 27(12), pp.4281-4288.
200. Zhang, K., Zhao, Y., Fu, D. and Chen, Y., *Journal of Materials Chemistry A*, 2015, 3(11), pp.5783-5788.
201. Chen, J., Zhou, W., Jia, J., Wan, B., Lu, J., Xiong, T., Tong, Q. and Chen, S., *international journal of hydrogen energy*, 2017, 42(10), pp.6448-6454.
202. Li, J.S., Wang, Y., Liu, C.H., Li, S.L., Wang, Y.G., Dong, L.Z., Dai, Z.H., Li, Y.F. and Lan, Y.Q., *Nature communications*, 2016, 7(1), p.11204.
203. Anjum, M.A.R., Lee, M.H. and Lee, J.S., *Journal of Materials Chemistry A*, 2017, 5(25), pp.13122-13129.
204. Gong, Q., Wang, Y., Hu, Q., Zhou, J., Feng, R., Duchesne, P.N., Zhang, P., Chen, F., Han, N., Li, Y. and Jin, C., *Nature communications*, 2016, 7(1), p.13216.
205. Han, N., Yang, K.R., Lu, Z., Li, Y., Xu, W., Gao, T., Cai, Z., Zhang, Y., Batista, V.S., Liu, W. and Sun, X., *Nature communications*, 2018, 9(1), p.924.
206. Wu, H.B., Xia, B.Y., Yu, L., Yu, X.Y. and Lou, X.W., *Nature communications*, 2015, 6(1), p.6512.
207. Yan, H., Xie, Y., Jiao, Y., Wu, A., Tian, C., Zhang, X., Wang, L. and Fu, H., *Advanced Materials*, 2018, 30(2), p.1704156.
208. Vrubel, H. and Hu, X., *Angewandte Chemie International Edition*, 2012, 51(ARTICLE), pp.12703-12706.
209. Park, H., Encinas, A., Scheifers, J.P., Zhang, Y. and Fokwa, B.P., *Angewandte Chemie International Edition*, 2017, 56(20), pp.5575-5578.
210. Park, H., Zhang, Y., Scheifers, J.P., Jothi, P.R., Encinas, A. and Fokwa, B.P., *Journal of the American Chemical Society*, 2017, 139(37), pp.12915-12918.
211. Hinnemann, B., Moses, P.G., Bonde, J., Jørgensen, K.P., Nielsen, J.H., Horch, S., Chorkendorff, I. and Nørskov, J.K., *Journal of the American Chemical Society*, 2005, 127(15), pp.5308-5309.
212. Kong, D., Wang, H., Cha, J.J., Pasta, M., Koski, K.J., Yao, J. and Cui, Y *Nano letters*, 2013, 13(3), pp.1341-1347.
213. Yang, L., Hong, H., Fu, Q., Huang, Y., Zhang, J., Cui, X., Fan, Z., Liu, K. and Xiang, B., *ACS nano*, 2015, 9(6), pp.6478-6483.
214. Tan, Y., Liu, P., Chen, L., Cong, W., Ito, Y., Han, J., Guo, X., Tang, Z., Fujita, T., Hirata, A. and Chen, M.W., *Advanced Materials*, 2014, 26(47), pp.8023-8028.
215. Li, H., Tsai, C., Koh, A.L., Cai, L., Contryman, A.W., Fragapane, A.H., Zhao, J., Han, H.S., Manoharan, H.C., Abild-Pedersen, F. and Nørskov, J.K., *Nature materials*, 2016, 15(1), pp.48-53.
216. Xie, J., Zhang, J., Li, S., Grote, F., Zhang, X., Zhang, H., Wang, R., Lei, Y., Pan, B. and Xie, Y., *Journal of the American Chemical Society*, 2013, 135(47), pp.17881-17888.

217. Zhou, J., Fang, G., Pan, A. and Liang, S., *ACS Applied Materials & Interfaces*, 2016, 8(49), pp.33681-33689.
218. Xiao, W., Liu, P., Zhang, J., Song, W., Feng, Y.P., Gao, D. and Ding, J., *Advanced Energy Materials*, 2017, 7(7), p.1602086.
219. Ye, R., del Angel-Vicente, P., Liu, Y., Arellano-Jimenez, M.J., Peng, Z., Wang, T., Li, Y., Yakobson, B.I., Wei, S.H., Yacaman, M.J. and Tour, J.M., *Advanced Materials*, 2016, 28(7), pp.1427-1432.
220. Liu, P., Zhu, J., Zhang, J., Xi, P., Tao, K., Gao, D. and Xue, D., *ACS Energy Letters*, 2017, 2(4), pp.745-752.
221. Deng, J., Li, H., Xiao, J., Tu, Y., Deng, D., Yang, H., Tian, H., Li, J., Ren, P. and Bao, X., *Energy & environmental science*, 2015, 8(5), pp.1594-1601.
222. Tang, Q. and Jiang, D.E., *Acs Catalysis*, 2016, 6(8), pp.4953-4961.
223. Long, X., Li, G., Wang, Z., Zhu, H., Zhang, T., Xiao, S., Guo, W. and Yang, S., *Journal of the American Chemical Society*, 2015, 137(37), pp.11900-11903.
224. Yu, L., Xia, B.Y., Wang, X. and Lou, X.W., *Advanced materials*, 2016, 28(1), pp.92-97.
225. Ren, X., Wu, D., Ge, R., Sun, X., Ma, H., Yan, T., Zhang, Y., Du, B., Wei, Q. and Chen, L., *Nano Research*, 2018, 11, pp.2024-2033.
226. Wu, Y., Liu, Y., Li, G.D., Zou, X., Lian, X., Wang, D., Sun, L., Asefa, T. and Zou, X., *Nano Energy*, 2017, 35, pp.161-170.
227. Gao, M.R., Liang, J.X., Zheng, Y.R., Xu, Y.F., Jiang, J., Gao, Q., Li, J. and Yu, S.H., *Nature communications*, 2015, 6(1), p.5982.
228. He, Y., Sun, J., Feng, D., Chen, H., Gao, F. and Wang, L., *Biosensors and Bioelectronics*, 2015, 74, pp.418-422.
229. Li, Y., Huang, H., Ma, Y. and Tong, J., *Sensors and Actuators B: Chemical*, 2014, 205, pp.227-233.
230. Zhou, Y., Qu, Z.B., Zeng, Y., Zhou, T. and Shi, G., *Biosensors and Bioelectronics*, 2014, 52, pp.317-323.
231. Qiao, X.Q., Zhang, Z.W., Tian, F.Y., Hou, D.F., Tian, Z.F., Li, D.S. and Zhang, Q., *Crystal Growth & Design*, 2017, 17(6), pp.3538-3547.
232. Liu, H., Wang, H., Qian, Y., Zhuang, J., Hu, L., Chen, Q. and Zhou, S., *ACS Applied Nano Materials*, 2019, 2(11), pp.7043-7050.
233. Jebaranjitham, J.N., Mageshwari, C., Saravanan, R. and Mu, N., *Composites Part B: Engineering*, 2019, 171, pp.302-309.
234. Swathy, T.S., Jinish Antony, M. and George, N., *Industrial & Engineering Chemistry Research*, 2021, 60(19), pp.7050-7064.
235. Benítez-Martínez, S. and Valcárcel, M., *Sensors and Actuators B: Chemical*, 2014, 197, pp.350-357.
236. Li, S., Li, Y., Cao, J., Zhu, J., Fan, L. and Li, X., *Analytical chemistry*, 2014, 86(20), pp.10201-10207.
237. Zhu, L., Cui, X., Wu, J., Wang, Z., Wang, P., Hou, Y. and Yang, M., *Analytical Methods*, 2014, 6(12), pp.4430-4436.
238. García-Mendiola, T., Bravo, I., López-Moreno, J.M., Pariente, F., Wannemacher, R., Weber, K., Popp, J. and Lorenzo, E., *Sensors and Actuators B: Chemical*, 2018, 256, pp.226-233.

Experimental Techniques



The chapter includes basic working principle of characterization techniques of the nanomaterials. X-ray Diffraction (XRD) and Rietveld Analysis are employed to obtain structural and lattice parameters of the mixed phase materials. However, High resolution transmission electron microscope (HRTEM) involves a direct way to correlate the lattice parameters and crystallinity obtained from XRD analyses. For structural determination, valance band maximum, Fermi level and exact valance state of various metal and nonmetal-based compounds, Ultraviolet photoelectron spectroscopy and X-ray photoelectron spectroscopy (UPS and XPS) are utilized. Raman and Fourier-transform infrared spectroscopy (FTIR) provide direct determination of type of defects, lattice strain, layer numbers of multilayer complex and functional groups respectively. Optical band gap, absorption and emission properties are carried out by UV-Vis absorption spectroscopy and Photoluminescence Spectroscopy. The energy storage based applications, multiple electrocatalysis are characterized by cyclic voltammetry, charge discharge, Nyquist analysis and linear sweep voltammetry.

3.1. X-ray Diffraction (XRD) and Rietveld Analysis

X-ray Diffraction (XRD) is used to investigate different physical properties of the nanocomposites i.e. lattice, parameters, interlayer spacing, shape, crystal structures. When a monochromatic X-Ray falls on the lattice, diffracted beam is generated from the parallel lattice planes. The reflected beam produces an angle and forms constructive interference which are integral multiple of λ . The relationship between interplanar distance (d) and angle of reflection (2θ) is explained from Bragg's equation as follows [1]:

$$d = \frac{\lambda}{2 \sin \theta} \quad (3.1)$$

Where d is the interlayer spacing calculated in Å, λ is the incident wavelength of X-ray, θ is the half of the diffraction angle. X-ray Diffraction measurements are carried out from XRD, D8 Advance, Bruker instruments. Cu K_{α} irradiation source ($\lambda = 1.5460\text{Å}$) is used which is operated at 35KV, 35 mA with scanning speed of 0.2s/steps. The solid and thin film samples are also measured with Rigaku MiniFlex powder X-ray diffractometer using monochromatic Cu K_{α} radiation at a measuring speed of $0.5^{\circ} \text{ min}^{-1}$ under operating voltage and current 40 KV and 10 mA. The crystallite size (D) of the nanomaterials is determined from Debye-Scherrer equation as follows [1]:

$$D = \frac{0.89 * \lambda}{\beta * \cos \theta} \quad (3.2)$$

Where, β is the FWHM of the corresponding XRD peak.

Rietveld refinement is a powerful technique to simulate the experimentally obtained XRD pattern using different analytical functions. Due to numerous defects, vacancies, particle size, grain boundaries, strain, the XRD peak undergo broadening effect and pseudo-voigt function is used due to asymmetric nature of the individual peak [2]. High quality XRD patterns with prominent peaks of the crystalline materials, background factor, space group, atomic occupancy, lattice parameters, atomic positions are essential components for better refinement. The two reliability index parameters such as weighted residual error (R_{wp}) and expected error (R_{exp}) are monitored to obtain best goodness of fit. The R_{wp} and R_{exp} are expressed as follows [2-4]:

$$R_{wp} = \left[\frac{\sum_i w_i (Y_{io} - Y_{ic})^2}{\sum_i w_i Y_{io}^2} \right]^{\frac{1}{2}} \quad (3.3)$$

$$R_{exp} = \left[\frac{(N-P)}{\sum_i w_i Y_{io}^2} \right]^{\frac{1}{2}} \quad (3.4)$$

Where, W_i , Y_{io} and Y_{ic} in R_{wp} refer to statistical weight, observed and calculated XRD peak intensity respectively. N and P component in R_{exp} indicates number of observations and fitting parameters respectively. To analyze the refinement analysis, goodness of fit can be measured

from the ratio between R_{WP} and R_{exp} . Rietveld software FULLPROF program is utilized to determine crystal structures and lattice parameters in our present study.



Figure 3.1. Rigaku model for XRD measurement.

3.2. High-Resolution Transmission Electron Microscope (HRTEM)

High-Resolution Transmission Electron Microscope (HRTEM) is a sophisticated technique to determine lattice spacing (d), morphology, and structure of the nanomaterials. The operating voltage in HRTEM lies between 150 kV-300 kV and the image resolution depends on accelerating voltage. As electrons move with speed of light and interact with the material, the collision mean free path must be minimized. The process is carried out by maintaining the chamber with high vacuum ($\sim 10^{-10}$ Pa) using rotary and diffusion pumps. The particle sizes should be a few nanometres in thickness where transmitted electrons fall on the sample to obtain the image formation. For this purpose, two condenser lenses, one objective lens and intermediate lens are used for the image formation. Sulphur hexafluoride (SF_6) is used for the insulation to protect electrical breakdown. Carbon or gold coated copper grids with diameter 3 mm are used as a TEM grid in which electrons are passed through the pores or holes of the TEM grid. Periodic fringe patterns obtained from high magnification HRTEM are correlated with Bragg's plane and interlayer distance (d). Diffraction patterns of amorphous, single and polycrystalline materials are provided by selected area electron diffraction (SAED) patterns. SAED principle obeys reciprocal lattice (Ewald's sphere) phenomenon. The measurement is carried out by blocking

centered electron beam by choosing of particular area of the sample specimen. The single and diffracted ring pattern is characteristic of nanocrystalline materials whereas amorphous materials show diffuse ring (single plane) pattern. The diffraction ring diameter (D) and interlayer spacing (d) are correlated as follows: [5]

$$d = \frac{\lambda L}{D} \quad (3.5)$$

Where d is the interlayer spacing, λ and L are wavelength and effective length of camera.



Figure 3.2: High-Resolution Transmission Electron Microscope (HRTEM) instrumentation.

For powder sample analysis, the sample is crushed into fine powder and dispersed in ethanol solution. The solution are then ultrasonicated for 30 minutes to get homogeneous solution. Few μL of ethanolic solution are then drop cased on Cu grid and dried in vacuum oven for four hours at 70°C .

3.3. Raman Spectroscopy

Raman spectroscopy gives quantitative and qualitative analysis of the nanomaterial by measuring intensity, peak positions (frequencies) and nature of the peak. The inelastic scattering between the sample and monochromatic light source exhibits the emitted frequency which is slightly lower or higher than the incident radiation. The phenomenon is known as Raman shift and the process depends on the polarizability of the molecule. Under external electric field, the induced dipole moment of the molecules creates Rayleigh scattering, Stokes and anti Stokes lines. When the light emits to the same frequency w.r.t external wavelength, the interaction becomes purely elastic and Rayleigh scattering will be observed. The lower and higher frequency tends to rise Stokes and anti Stokes lines respectively. In order to determine highly sensitive structural

determination at low concentrations, imaging, lower signal-to-noise ratio, high resolution, geometry in excited state etc., Raman spectroscopy has been classified with different parts i.e. confocal Raman spectroscopy (CRS), resonance Raman spectroscopy (RRS), Surface Enhanced Raman Spectroscopy (SERS), Tip-Enhanced Raman Spectroscopy (TERS) [6]. The most common laser source in Raman spectroscopy is Neodymium–Yttrium Aluminum (Nd:YAG) laser. Here, Raman spectra are studied from WiTec-alpha with Nd:YAG laser source at excitation wavelength 532 nm. Charge-coupled devices (CCDs), photo diode arrays are most common detectors used in Raman spectroscopy. For 2D materials, individual Raman active modes correspond to crystal structure as well as lattice strain, doping and lattice disorder.

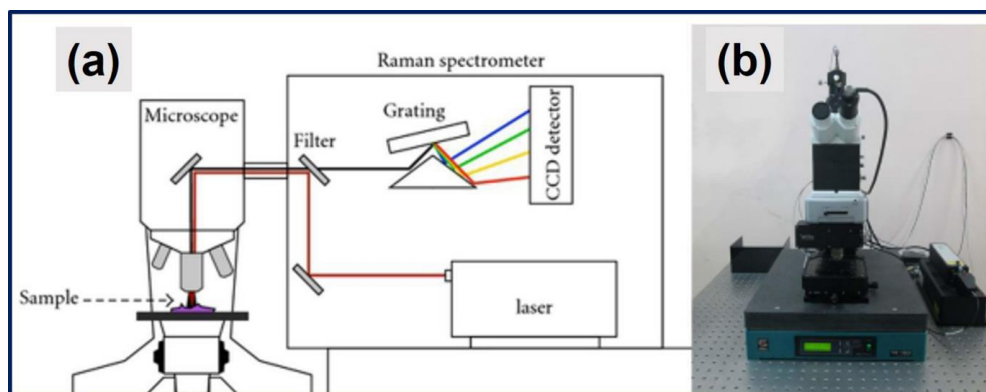


Figure 3.3. Raman spectroscopy.

3.4. Fourier-transform infrared spectroscopy (FTIR)

Infrared spectroscopy (IR) has been developed for infrared active materials (vibrational modes) and used to determine the functional groups, and chemical components qualitatively. The IR stretching frequencies of different functional groups lie between the range of $400\text{--}4000\text{ cm}^{-1}$. The incident IR radiation is divided into two optical beams by Michelson interferometers (beam splitter) [7]. One of the optical beams falls on a fixed mirror and is reflected back to the beam splitter. Another optical beam path can be optimized by changing the position of the movable mirror. The phase difference changes with time in movable mirror and two beams are combined in the interferometer and fall on the sample. The Fourier transformation of time domain to frequency domain gives information on vibrational frequencies of different groups. Attenuated Total Reflectance, diffuse Reflectance, solid, liquid based measurements are well known procedures for FTIR analyses. Here, solid state based FTIR analyses are employed using KBr

pellet as a standard method. KBr and sample are well grinded and small pellet is prepared using pelletizer.



Figure 3.4. FTIR spectroscopy.

3.5. UV-Vis and Photoluminescence Spectroscopy

Ultraviolet visible (UV-Vis) spectroscopy relates to absorption phenomenon of the molecule. The light source has wavelength range of 200- 800 nm range falls on sample specimen that can absorb, transmit, or reflect the radiation. Deuterium arc and tungsten-halogen lamps are widely used as UV sources in UV-Vis spectrometers. Here, dual beam spectrometer i.e. sample chamber and reference chamber is used for background or baseline correction. Photomultiplier tube is used as a detector due to very low signal-to-noise ratio. Ultraviolet–Visible Diffuse Reflectance Spectroscopy (UV–Vis DRS) is used to measure optical band gap for solid samples using barium sulfate as a reference. Tauc plots are calculated from UV-Vis absorbance and diffuse reflectance spectra to determine the band gap according to the following eqn [8]:

$$(\alpha h\nu)^{1/n} = C (h\nu - E_g) \quad (3.6)$$

Where α is the absorption coefficient, h is Planck's constant, ν is the frequency, and C is a normalization constant. The absorption coefficient can be determined by $\alpha = 2.303 (A/d)$, where d is thickness. In our study (chapter 7), as-prepared N-CQD shows a direct electronic transition. Thus, n is 0.5, and the bandgap is calculated as the intercept point on the abscissa of a plot $(\alpha h\nu)^2$ vs. $h\nu$.

Photoluminescence spectroscopy (PL) determines the electric transition, average lifetime, and ground and excited state dynamics of the nanomaterials. Xe lamp and Photomultiplier tube are commonly utilized as a source and detector in PL spectra used

as a detector (signal to noise ratio > 5500:1.). The excitation source has wavelength accuracy ± 0.5 for better accuracy. Generally, PL quantum yield has been studied with a reference material. In Chapter 7, quinine Sulphate dissolved in DI water ($\Phi_R \sim 0.546$) for relative quantum yield measurements is used as a reference solution. Relative fluorescence quantum yield of CQDs has been calculated according to the following equation [8]:

$$\Phi_S = \Phi_R \times (G_S / G_R) \times (\eta^2 / (\eta_R^2)) \quad (3.7)$$

Where S and R refer to sample and reference solution. Φ denotes quantum yield (QY), G implies gradient of the plot between an integrated area of PL emission and optical density, η is the refractive index of the solvent. The excitation wavelength is 330 nm and 310 nm for N-CQD and Rhodamine B, respectively. Four different solutions of the sample (N-CQD) and Rhodamine B are prepared and all of which the optical density becomes less than 0.1 at the respective excitation. The refractive index of DI is taken as 1.33. Time resolved PL spectra can be expressed as

$$I(t) = \sum_{m=1}^n A_m e^{-\left(\frac{t}{\tau_m}\right)} \quad (3.8)$$

Where τ_m is the decay time (lifetime) of the m th component, t is the time measurement for fluorescence lifetime, n is the total number of components, A_m is the amplitude of the m th components. Here, the decay is fitted as a sum of two components with χ^2 close to 1. The amplitude is denoted as A_1 and A_2 . The average lifetime has been calculated from the amplitude and individual lifetime components as:

$$\tau_{av} = \left(\sum_{m=1}^n A_m \tau_m^2 \right) / \left(\sum_{m=1}^n A_m \tau_m \right) \quad (3.9)$$

The measurements for N- CQD are conducted at two emission maxima at ~ 450 nm and ~ 510 nm, and all the decays are fitted by the sum of two components. The instrument response function (IRF) is measured by the LUDOX solution in water of nonfluorescent scatters.



Figure 3.5: Ultraviolet visible (UV-Vis) and Photoluminescence spectrometer.

3.6. Field Emission Scanning Electron Microscope (FESEM)

Field Emission Scanning Electron Microscope (FESEM) is a topographical measurement to determine surface morphology. High accelerated electrons are ejected from field emission source which is known as primary electrons. The field emission requires a high vacuum ($\sim 10^{-8}$ torr) to generate the stable electron beam having high lifetime. Tungsten needles or tungsten dips are the common primary electron sources and the voltage generated between cathode and anode in field emitting source lies within 30 KV. In our analysis, morphology of the nanomaterials has been studied with 15 kV operating voltage. The primary electrons are deflected by lens and narrow beam falls on the sample specimen. In this regard, condenser lens, and objective lens are used to maintain the diameter of the beam, resolution and deflection of electron beam. The inelastic scattering between the primary electron source and sample displaces electrons from the outer orbit of the sample and is simply known as secondary electrons. The velocity and angles of the secondary electrons vary from material to material [9]. The electrons fall on scintillator and the signal is amplified and finally produces real time image.

For powder sample measurement, finely grained small amounts of powder samples are required for FESEM measurement. In the case of thin film samples small area of the film is cut for characterization. However, gold or silver is used for coating with sputtering techniques to enhance the conductivity of the insulating samples. The conductivity of the surface is required for better interaction of the external electron beam and the ejected electrons.



Figure 3.6: Field Emission Scanning Electron Microscope (FESEM) (Hitachi S-4800).

3.7. X-ray and Ultraviolet photoelectron spectroscopy (XPS and UPS)

X-ray photoelectron spectroscopy describes surface state of the nanomaterials and is based on the principle of photoelectric effect. X-ray radiation with shorter wavelength strikes on sample and the ejected electrons are directly proportional to the binding energy. Al $K\alpha$ X-ray source ($h\nu = 1486.6$ eV) with hemispherical analyzer (SPECS HSA 3500) is commonly used as an XPS source. In this thesis, operating voltage and current of the X-ray source are 10 kV and 15 mA respectively. Kinetic energy of the ejected electrons and binding energy is different for different atoms. To avoid the scattering of ejected electrons by contaminates and low mean free path of electrons, high vacuum ($\sim 10^{-7}$ torr) is used between surface of the analyzer. The binding energy of atomic orbital is estimated to the following Eqn: [10-11]

$$B.E = h\nu - K.E - \Phi_s \quad (3.10)$$

Where B.E and K.E are the binding energy and kinetic energy of the ejected electrons, h and ν are the Plank constant and incident X-ray frequency and Φ_s are instrumental parameters.

Wide range of binding energy of primary peaks in XPS spectra involves mixing of individual atomic compositions of the composite nanomaterials. Molecular environment of the surroundings, oxidation states, atomic percentage are calculated from the peak shape, area and shift in binding energy. For higher order orbitals except s orbital, spin-orbit coupling creates two doublet peaks which depend on angular momentum and atomic number of the corresponding atom [10]. The background spectra are generated from inelastic scattering of electrons near the surfaces. Auger electrons are created during relaxation of outer orbit electron transition to inner orbit transition which depends only on energy difference and is independent of excited radiation source. However second order XPS profiles are generated due to surface plasmon, satellite peaks and multiple splitting [10]. For solid sample characterization, 10-12 mm pellet is used to improve signal to noise ratio. Ultraviolet photoelectron spectroscopy gives vital information on valance band states, density of bound electrons, band structure of the semiconductor based nanomaterials. The loosely bound electrons near the valance band have low kinetic energy and therefore low energy excitation source (HeI line, less than 50 eV) is required for UPS measurement. Gold is used as a standard material due to its metallic in nature. The work function of the sensing surface with respect to Au has been calculated by employing the equation [11]:

$$\Phi = 21.22 - (E_{Cut-off} - E_{Fermi}) \quad (3.11)$$

where $E_{Cut-off}$ is the secondary electron cut-off energy, E_{Fermi} is the Fermi energy, and Φ is the work function.

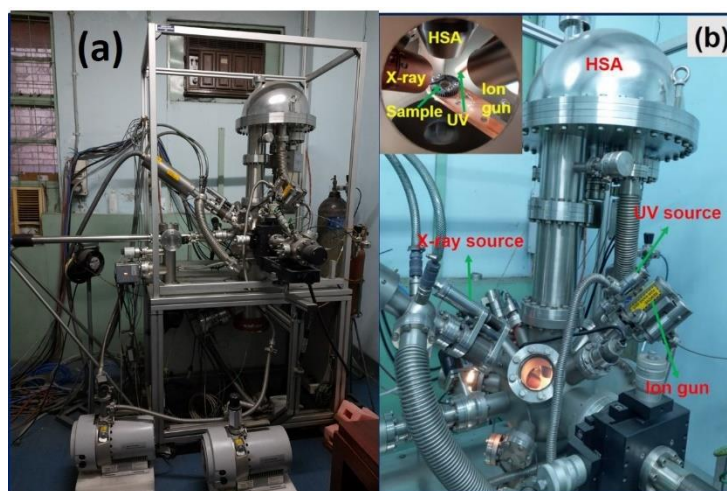


Figure 3.7: X-ray photoelectron spectroscopy.

3.8. Brunauer-Emmett-Teller (BET) analysis

Brunauer-Emmett-Teller (BET) measurement directly estimates surface area, pore diameter and pore volume of nanocomposites. Ideally, six types of BET isotherm have been established to determine microporous, mesoporous, macroporous, nonporous structures of the material. In the adsorption-desorption procedure, adsorption of gas molecules undergoes weak adsorption or chemical bonding with adsorbent (sample) molecules. The monolayer adsorption increases with pressure and BET measurement is used to determine the surface area. For multilayer adsorption along with interaction between the mesopores and adsorbate molecules promotes capillary condensation. Therefore, a hysteresis loop has been observed in adsorption-desorption mechanism. Barrett–Joyner–Halenda (BJH) method is used to determine pore diameter for multilayer adsorption. Inert nitrogen gas is used as an adsorbate and 200-300 mg of sample is poured into gas chamber. The BET equation and surface area calculation are measured according to the following equation:[12]

$$\frac{1}{v\left(\left(\frac{P_0}{P}\right)-1\right)} = \frac{1}{v_m C} + \frac{C-1}{v_m C} \left(\frac{P}{P_0}\right) \quad (3.12)$$

$$S_t = \frac{v_m N_s}{V} \quad (3.13)$$

Where P/P_0 is relative pressure, C is BET constant, v_m and v are volume of monolayer adsorption and gas quantity, V and N are volume of adsorbed gas and Avogadro's number, S_t is total surface area. From the slope and intercept v_m can be calculated. BET surface area is calculated by dividing total surface area by weight of the material.



Figure 3.8: Brunauer-Emmett-Teller (BET) surface area analyzer.

3.9. Electrochemical characterization

Electrochemical measurements are classified into two components i.e. potentiostatic mode and galvanostatic mode. In potentiostatic mode, potential is measured between the two electrodes where galvanostatic mode controls the current in between two electrodes). All the electrochemical tests i.e. Cyclic Voltammetry (CV), charging/discharging (GCD) and electrical Impedance spectroscopy (EIS), electrocatalysis is carried out in Autolab Nova 1.1.

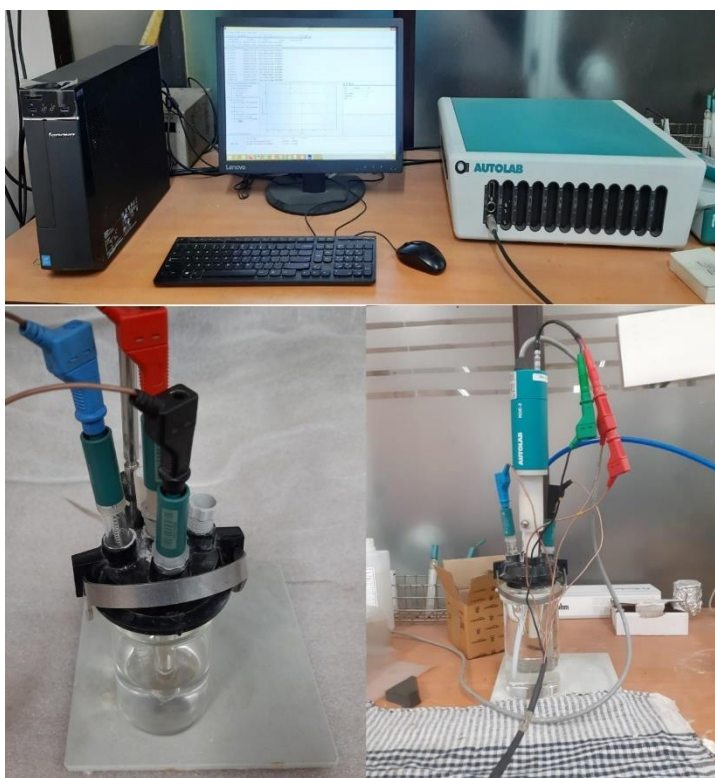


Figure 3.9: Electrochemical workstation (autolab).

Oxygen reduction reaction (ORR)

For the oxygen reduction reaction (ORR), glassy carbon electrode (diameter -3 mm) was taken as a working electrode, Ag/AgCl (Saturated with 3M KCl) and Pt acted as a reference and counter electrode respectively for cyclic voltammetry measurement and linear sweep voltammetry (LSV) by rotating disk electrode (RDE). All experiments were carried out in 0.1 M KOH in a PGSTAT 302 N Autolab at room temperature. Before experiments, high-quality O₂ gas was purged into the KOH solution for 40 minutes. The sample ink was prepared by pouring the synthesized samples into 200 μ L ethanol solution and 5 % 10 μ L Nafion in a glass vial and the mixture was

ultrasonicated for 30 minutes. The resultant paste was pipetted out (5 μL) and drop-casting on the working area of the glassy carbon electrode to obtain a homogeneous black coating of the sample on the active surface of the electrode. The electrode was then dried in a vacuum oven at 45°C for 1 hour.

The measured potential against reference electrode Ag/AgCl was converted to a reversible hydrogen electrode (RHE) according to the following equation:

$$E_{\text{RHE}} = E_{\text{Ag/AgCl}} + 0.9056 \text{ V, at pH-12 (0.1(M) KOH solution)} \quad (3.14)$$

. The durability and methanol crossover test towards ORR were measured at a fixed potential - 0.3 V vs. Ag/AgCl at 1600 rpm in 0.1 M KOH saturated with O_2 . The cell was equipped with a 3 M saturated Ag/AgCl for reference electrode, Pt wire as a counter electrode and a glassy carbon electrode with a diameter of 3 mm as a working electrode.

The Tafel slope is calculated from the equation [13]:

$$\eta = a + b \log j \quad (3.15)$$

Where η , b , and j are the overpotential, Tafel slope, and current density, respectively. For the crossover test, 2 (M) Methanol was added after 400 s for measurement of the catalysts. All the measurements were performed at room temperature and current densities were calculated to the geometric area of the glassy carbon disk electrodes.

Hydrogen evolution reaction (HER)

HER measurements are carried out using a three electrode system at room temperature (a PGSTAT 302N Autolab) using a glassy carbon electrode (GCE) as the working electrode, and Ag/AgCl (3.5M KCl) and graphite rod as reference and counter electrodes, respectively. Initially, the catalyst ink is prepared by adding 1 mg of catalyst in 50 μL DMF. Then 10 μL of 5 wt. % Nafion is added to the solution and sonicated further for a few minutes to obtain the catalyst ink. Finally, 6 μL of the suspension is drop-casted on GCE. Then the electrode is dried in a vacuum oven at 45°C for 1 hour. For HER measurements, 0.5 M aqueous H_2SO_4 and 1 M KOH solution are initially purged with high quality N_2 gas (Indian Refrigeration system, India, 99.99% purity) for 30 minutes in a polytetrafluoroethylene (PTFE) container. Linear sweep voltammetry (LSV) measurements are measured at scan rate $v = 10 \text{ mV s}^{-1}$. The current densities are calculated from the geometric area of the GCE electrodes.

The measured potential against reference electrode Ag/AgCl was converted to a reversible hydrogen electrode (RHE) according to the following equation:

$$E_{\text{RHE}} = E_{\text{Ag/AgCl}} + 0.9056 \text{ V, at pH-1 (0.5(M) H}_2\text{SO}_4 \text{ solution)} \quad (3.16)$$

Electrochemical impedance spectroscopy (EIS) measurements are performed at potential -0.4 V vs.RHE with an ac amplitude at a frequency range of 0.01–1000 kHz.

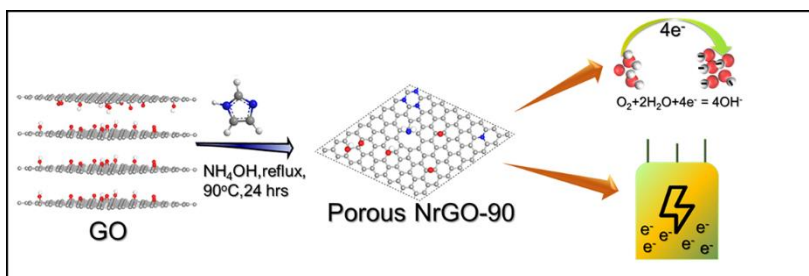
3.10. References

1. Saini, P., Sharma, R. and Chadha, N., *Indian Journal of Pure & Applied Physics (IJPAP)*, 2017, 55(9), pp.625-629.
2. Young, R.A., (Vol. 5, pp. 1-38). International union of crystallography, 1993.
3. Lutterotti, L., Scardi, P. and Maistrelli, P., *Journal of applied crystallography*, 1992, 25(3), pp.459-462.
4. Young, R.A. and Wiles, D.B., *Journal of Applied Crystallography*, 1982, 15(4), pp.430-438.
5. <https://cmrf.research.uiowa.edu/transmission-electron-microscopy>, Facility, C. M. R.; Building, E. M. R.; City, I.
6. Bumbrah, G.S. and Sharma, R.M., *Egyptian Journal of Forensic Sciences*, 2016, 6(3), pp.209-215.
7. B.C. Smith, *Fundamentals of Fourier transform infrared spectroscopy*; CRC press, 2011.
8. Karami, K., Lighvan, Z.M., Barzani, S.A., Faal, A.Y., Poshteh-Shirani, M., Khayamian, T., Eigner, V. and Dušek, M., *New Journal of Chemistry*, 2015, 39(11), pp.8708-8719.
9. Kaeck, A. *An introduction to electron microscopy instrumentation, imaging and preparation*, Cent. Microsc. Image Anal, 2002, 1-26.
10. Crist, B.V. and Crisst, D.B. *Handbook of monochromatic XPS spectra*; Wiley New York, 2000; Vol. 1.
11. Luo, Z., Li, J., Li, Y., Wu, D., Zhang, L., Ren, X., He, C., Zhang, Q., Gu, M. and Sun, X *Advanced Energy Materials*, 2022, 12(12), p.2103823.
12. Walton, K.S. and Snurr, R.Q., *Journal of the American Chemical Society*, 2007, 129(27), pp.8552-8556.
13. Chen, Z., Higgins, D. and Chen, Z., *Carbon*, 2010, 48(11), pp.3057-3065.

Site specific nitrogen incorporation in reduced graphene oxide using imidazole as a novel reducing agent for efficient oxygen reduction reaction and improved supercapacitive performance

Abstract

Nitrogen-functionalized reduced graphene oxide (NrGO) has emerged as an inexpensive and metal-free electrocatalyst for the oxygen reduction reaction (ORR) due to the presence of pyridinic, amine, and/or graphitic nitrogen on the reduced graphene oxide sheet. Herein a facile synthetic route has been designed to prepare NrGO at 90 °C (NrGO-90) using imidazole as a novel reducing agent as well as a targeted nitrogen precursor while circumventing the high-temperature annealing step. The substantial atomic percentage of pyridinic and amine nitrogen has been incorporated in NrGO-90, which facilitates the ORR via the four-electron pathway. NrGO-90 exhibits higher limiting-diffusion current density (-3.7 mA/cm^2), onset potential (0.82 vs. RHE), and lower Tafel slope (67 mV /Decade), as compared to hydrazine hydrate reduced graphene oxide (rGO). In addition, our samples exhibit higher performances in tolerance of methanol corrosion and longer cycling stability (90%) after 3.5 hours compared to standard Pt/C. Furthermore, the NrGO-90 sample exhibits a specific capacitance maximum of 287.5 F g^{-1} at 0.5 A g^{-1} with 90% retention after 10000 cycles suggests facile interaction between electrolyte ions and active sites of rGO sheets.



4.1. Introduction

The restoration of energy consumption is a multifaceted gridlock in the modern century leading to the advent of cost effective, eco-friendly, efficient devices i.e. batteries, supercapacitors, proton exchange membrane fuel cells, anion exchange membrane fuel cell, etc. Coherent oxidation (at anode) and reduction (at cathode) in the fuel cell have become a necessity to improve their prolonged performance. Thus, increasing the kinetic efficiency and stability of the oxygen reduction reaction (ORR) of a fuel cell is the most scrutinized protocol in the modern study [1,3]. So far platinum (Pt) is set the benchmark as an efficient electrocatalyst for ORR kinetics [4], nevertheless, its high cost, inefficient durability and crossover effect in methanol (MeOH) with the formation of toxic carbon monoxide (CO) gas during the reduction process urge to develop new alternatives [5,9]. In the domain of metal based catalysts, Co-doped metal oxides [10], metal organic frameworks [11] and/or metal sulfides [12] are capable of ORR. However, a multistep reaction procedure, low stability in the acidic medium compared to the alkaline medium poses a great challenge in the development of metal-doped functional materials [13]. To counter the above-mentioned problems many protocols are designed to develop metal-free catalysts for ORR based on carbon and its allotropes [14].

On the other hand, for energy storage devices, electrical double layer capacitors (EDLC) and pseudocapacitors involve the interplay of kinetics between the working electrode and electrolyte solution. High surface area and large interlayer spacing involve a faster rate of movement of ions leading to facile deposition of ions at the electrode surface [15]. Among the carbonaceous materials, single layer graphene has attracted the most attention from researchers due to its high conductivity, large surface area which is favorable for various device fabrication purposes [16,17]. Nevertheless, the chemical synthesis of large scale single layer graphene from bulk graphite is an exceedingly challenging due to the restacking nature of graphitic layers [16,18]. This fact thrusts the development of chemical oxidation of graphite to produce graphene oxide (GO) and subsequently reduces to reduced GO (rGO) which holds almost identical properties to graphene [19]. Different reducing agents such as hydrazine [20], hydroxylamine [21], urea [22], dimethyl ketoxime [23], pyrrole[24], ammonia [25] have been used so far to prepare rGO from GO. In this list, different types of oxygen containing groups like ascorbic acid [26,27], hydroquinone [28],

gallic acid [29] and metals like Fe Powder [30], Zn/HCl [31] have also been added. Explicitly, nitrogen and oxygen containing groups are preferred over other chemical components for the reduction as these functionalities on carbon moiety can initiate the formation of sp^3 carbon leading to defect density whose synergetic effect is solely responsible for different electrochemical aspects. Compared to pristine rGO, nitrogen doped rGO (NrGO) is preferred in ORR applications as electronegativity difference between nitrogen and carbon atoms creates a positive center which in turn boosts the separation of the oxygen molecule from the material's surface accelerating the overall ORR kinetics. Additionally, nitrogen-free rGO (synthesized by conventional reducing agents) uses nearly 2.3 to 2.5 electron pathways for ORR with low current density and low onset potential. Different protocols i.e. thermal reduction of GO by plasma incorporated microwave treatment [32], as well as various composite formation i.e. transition metal nitride/rGO [33], melamine [34], polyelectrolyte, functionalized graphene [35], promotes the ORR kinetics of carbon based materials. However, theoretical and experimental studies suggest that the presence of nitrogen towards a carbon network in rGO mainly occur at high temperature where graphitic and pyridinic carbon atom increases the limiting current density and onset potential respectively, in turn, improving the ORR performance [36]. The higher annealing temperature requires more safety issues as well as high cost and inert gas environment. Therefore, finding a non-toxic reducing agent and designing synthesis protocol at a moderate reaction condition for nitrogen atoms containing rGO which facilitates 4-electron transfer pathways is of huge importance.

To address the above-mentioned challenge, herein, we developed a novel, simple and cost effective one-step chemical reduction of GO by a non-toxic compound imidazole in the presence of aqueous ammonia at a temperature as low as 90°C to produce scalable, high quality nitrogen functionalized rGO (NrGO-90). The resulting NrGO-90 has been utilized as a good electrocatalyst for ORR with higher half wave potential and faster reaction kinetics follows four electron transfer processes. Moreover, the remarkable cycling stability, minimization of methanol crossover, higher onset potential and diffusion-limiting current density and lower Tafel slope values construct the NrGO material as a promising catalyst for ORR kinetics. Additionally, the developed NrGO-90 also exhibits EDLC type good super capacitive behavior with specific

capacitance (287.5 F/g at 0.5 A/g) as well as excellent cyclic Stability. The superior performance of the NrGO-90 is attributed to the incorporation of nitrogen groups from the reducing agent imidazole and ammonia.

4.2. Experimental Section

4.2.1 Materials

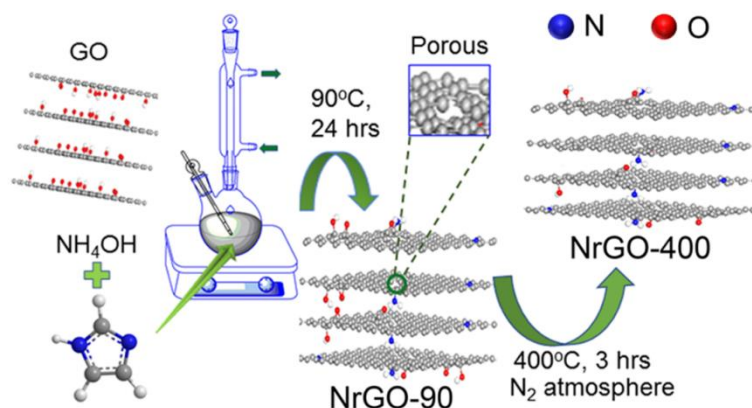
Graphite flakes (7–10 μm grain size, 99% purity) from Alfa Aesar; sodium nitrate (NaNO_3), 99% purity), sulfuric acid (H_2SO_4), 98% by weight, G.R.), potassium permanganate (KMnO_4 , 99% purity), imidazole, hydrazine Hydrate, nafion (5 wt % solution H_2O), 20% Pt/C from Sigma-Aldrich, potassium hydroxide (KOH , 99% purity), ethanol ($\text{C}_2\text{H}_5\text{OH}$, 99% purity), hydrochloric acid (HCl), ammonia solution (NH_4OH , 25% by weight), hydrogen peroxide (H_2O_2 , 30% by weight, A.R.) from Merck were used for synthesis and application purposes. Deionized (DI) water was taken from a Direct-Q Millipore deionized (18 Ω at 25° C).

4.2.2. Preparation of Graphene Oxide (GO)

GO was prepared from oxidation and exfoliation of graphite powder from the modified Hummers method [19]. Typically, 3 gm graphite powder and 3 gm sodium nitrate were taken in a 500 ml beaker containing 180 ml concentrated sulphuric acid and undergo stirring for 2 hours. Then, 10 gm KMnO_4 was slowly added to the black solution for 30 min keeping the temperature below 15 °C. The resulting mixture was kept for 24 hours with continuous stirring. After that 200 ml, DI and 10 ml 30% H_2O_2 were slowly added to the solution keeping the temperature around 40 °C to obtain a colour change from black to golden yellow. The mixture was then settled down and cooled to room temperature. The clear supernatant was decanted and the bottom part was centrifuged and washed with 5% hydrochloric acid two times at 12000 rpm for 15 minutes and the supernatant was removed. The bottom part (Brown color) was then washed with DI and centrifuged at 12000 rpm for 10 minutes to obtain three layers in the centrifuged tube. The top colorless part was removed at first and the middle light brown color was extracted. The bottom part containing GO and excess graphite was further centrifuged 5 times and every time the middle part containing a few layers of GO was taken and the lower part was removed at last. The light brown suspension was then dried in a vacuum oven for 24 Hours at 48 °C to obtain freshly prepared GO. The as-obtained GO was dispersed in different solvents (DI, Ethanol, and NMP) where the GO concentration is 0.5 mg/ml. The pH value was around 6 to all solvents.

4.2.3. Preparation of Nitrogen functionalized reduced Graphene Oxide (NrGO)

To prepare the rGO powder, 50 ml (0.5 mg/ml) GO dispersion in water was taken in a round bottom flask and subsequently, 100 mg imidazole and 5mL ammonia solution were then added to the solution. The pH was around 10 before starting the reaction. The mixture was then heated up to 90 °C in the reflux condition for 24 hours. After the reaction, the solution was cooled to room temperature and pH value was checked (Around 12). The resultant mixture was then centrifuged at 3000 rpm for 10 minutes and the supernatant was removed. Further washing with DI and acetone to remove excess precursors and centrifuged black products were dried in a vacuum oven at 50 °C for 12 hours. The resultant product was dispersed in water and the pH value of the corresponding solution is around 7. The rGO formed was mentioned as NrGO-90. Further NrGO-90 was calcined at 400 °C in the N₂ atmosphere for four hours denoted as NrGO-400 (Scheme 4.1).



Scheme 4.1. Schematic representation of the reduction of NrGO-90 and NrGO-400 from GO.

4.2.4. Preparation of reduced Graphene Oxide (rGO):

Typically, 25ml of GO dispersion (1 mg/ml) was poured into a 100 ml beaker with vigorous stirring for 10 minutes. Then 25 μL hydrazine Hydrate (80 wt% in water) and 175 μL ammonia solution (25 wt% in water) were added to the solution dropwise with continuous stirring. The resultant mixture was placed in a water bath at 95°C for 1 hour. The black product was then cooled to room temperature and filtered. The black residue was washed several times with water and ethanol to remove excess hydrazine and ammonia to keep the pH around 7. The product dried in a vacuum oven at 48°C for 12 hours and the product was utilized for further characterization and application purposes.

4.2.5. Characterization

The phase purity of all the synthesized powder samples was determined by X-ray Diffraction (XRD, D8 Advance, Bruker) using Cu K α irradiation source ($\lambda = 1.5460\text{\AA}$) operated at 35KV, 35 mA with scanning speed of 0.2s/steps. Morphology was studied using field emission scanning electron microscope (FESEM, Hitachi S-4800), high-resolution transmission electron microscope (JEOL 2100) operated at 200 kV. X-ray Photoelectron Spectroscopy (XPS) using a monochromatic Al K α X-ray source ($h\nu = 1486.6\text{ eV}$) and a hemispherical analyzer (SPECS HSA 3500), Fourier transformed infrared spectrophotometer (FTIR-8400S), Raman/AFM spectrometer (Witec Alpha300R, $\lambda_{\text{ex}} = 532\text{ nm}$) for structural and compositional analysis. Absorption maxima were determined by UV–Vis spectrophotometer (Shimadzu UV-3600). The Brunauer–Emmett–Teller (BET) surface area of the heterostructures was examined with a Quantachrome NovaWin2 Instrument at 77K.

4.2.6. Electrochemical Measurement

The ORR measurement has been illustrated in chapter 3 experimental section.

For the Mott-Schottky analysis, the potential window has taken between -0.2 V to + 0.4 V vs. Ag/AgCl at 100 MHz frequency in 0.1(M) KOH. The relationship between capacitance and

potential from Mott-Schottky analysis is given as follows [37]:

$$\frac{1}{C^2} = \frac{2}{\epsilon\epsilon_0 e A^2 N_d} \left[V - \left(V_{FB} + \frac{KT}{e} \right) \right] \quad (4.1)$$

Where V_{FB} is flat band potential, A is BET surface area; K is Boltzmann Constant, T absolute temperature. The C^{-2} vs. V plot will result in a straight line with a positive slope and from the intercept at Y=0 flat band potential can be measured

In our experiment, the CV has measured before and after the long-time durability (3.5 hours) in a non faradic region at a fixed potential of 0.95 V vs. RHE of NrGO-90 to calculate the double-layer capacitance (C_{dl}) and Electrochemically active surface area (ESCA).

Capacitive Measurement

Capacitive Performance of NrGO-90 and NrGO-400 were performed by cyclic voltammetry (CV) and galvanostatic charge-discharge (CD) in 1 M KOH aqueous electrolyte. Typically, in

the three electrode systems, Ag/AgCl and Pt foil was act as a reference and counter electrode respectively. The working electrode was composed of NrGO, carbon black and polytetrafluoroethylene (PVDF) with a ratio of 8:1:1. The mixture was stirred with 250 μ L NMP for 4 hours to obtain a slurry black product. Ni foam was washed with 5% hydrochloric acid (HCl), distilled water (DI), Acetone and dried in a vacuum oven for 12 hours at 45 °C. The resulting mixture was coated in dry Ni Foam and dried at 40 °C for 6 hours. The mass loading of NrGO-90 and NrGO-400 was 2 mg cm⁻² and 3.84 mg cm⁻². CV scan was performed with a scan rate from 2 mV/s to 100 mV/S. Galvanostatic charge-discharge measurement was carried out in the same 1M KOH from 0.1 A/g to 15 A/g. The potential windows of both experiments were - 0.8V to 0V (vs. Ag/AgCl). Electrochemical Impedance Spectroscopy (ESI) was done from 0.01 Hz to 100 kHz with AC amplitude.

4.2.7. Therotitcal Methods

We carried out the first principles calculation using the Vienna Ab-initio Simulation Package (VASP) [38-40] with projector-augmented-wave (PAW) [41] approach. Within the generalized gradient approximation (GGA) the Perdew-Burke-Ernzerhof (PBE) [42] functional was implemented to deal with the exchange-correlation terms. A Plane wave basis set up to an energy cut-off 500 eV was considered in all the calculations. As sufficiently large cells were considered to study the di-oxygen adsorption and subsequent ORR steps, the Brillouin zone integrations were performed using (1 \times 1 \times 1) Γ centered k-point mesh. The structures were allowed to relax until the total energies converged below 10⁻⁵ eV/ atom. The effect of dispersive forces was taken into account via the PBE + D2 force field method (Grimme's method) as implemented in the VASP package [43]. During the structure relaxations and energy calculations, a vacuum slab of 24 Å was considered perpendicular to the catalyst surface to minimize any spurious interaction between the periodic images. All the calculations were performed in a spin unrestricted manner. The di-oxygen adsorption energy values were calculated using the following formula:

$$E_{\text{Ads}} = E_{\text{P+O}_2} - E_{\text{P}} - E_{\text{O}_2} \quad (4.2)$$

Where $E_{\text{P+O}_2}$ is the energy of the system in the O₂ adsorbed state, E_{P} is the energy of the pristine system and E_{O_2} is the energy of the free O₂ molecule. Lower values of adsorption energies, as obtained from the above, imply stronger adsorption. The free energy differences of the ORR intermediates were calculated using the following formula:

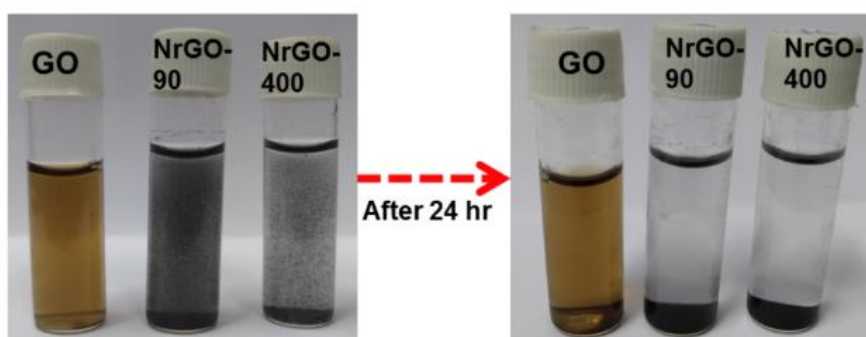
$$\Delta G = \Delta E - T\Delta S - neU \quad (4.3)$$

Where ΔE is the change in enthalpy which is equivalent to the difference in energy values between two reaction intermediates as calculated from the first principles calculation. $T\Delta S$ is the entropy-temperature terms which were taken from standard physical chemistry table for gas phase molecules [44]. n is the number of electrons transferred in a reaction step and U is the electrode potential vs. standard hydrogen electrode (SHE). The whole free energy calculation was carried out considering an ideally alkaline medium with $\text{pH} = 14$.

4.3. Results and Discussion

4.3.1. Phase Purity, Atomic percentage and Morphology analyses

NrGO was prepared from GO which was preliminarily confirmed by colour change (brown to black) during the reaction. The prepared rGO was dispersed into the water with the aid of sonication in a vial and after 24 hours the solid black product was precipitated at the bottom (Scheme 4.2.). From UV-Vis spectroscopy, two absorption peaks at 230 nm and 309 nm of GO which indicate $\pi-\pi^*$ transition of aromatic C=C bond and $n-\pi^*$ transition of oxygenated functionalities, respectively [45]. The synthesized NrGO-90 and NrGO-400 absorb at a region 265 nm and 267 nm respectively (red shifted from GO) with no significance peak at 310 nm which clearly indicates the reduction occurs shown in Figure 4.1a,b.



Scheme 4.2: Dispersion of GO, NrGO-90, and NrGO-400 in water before and after 24 hours.

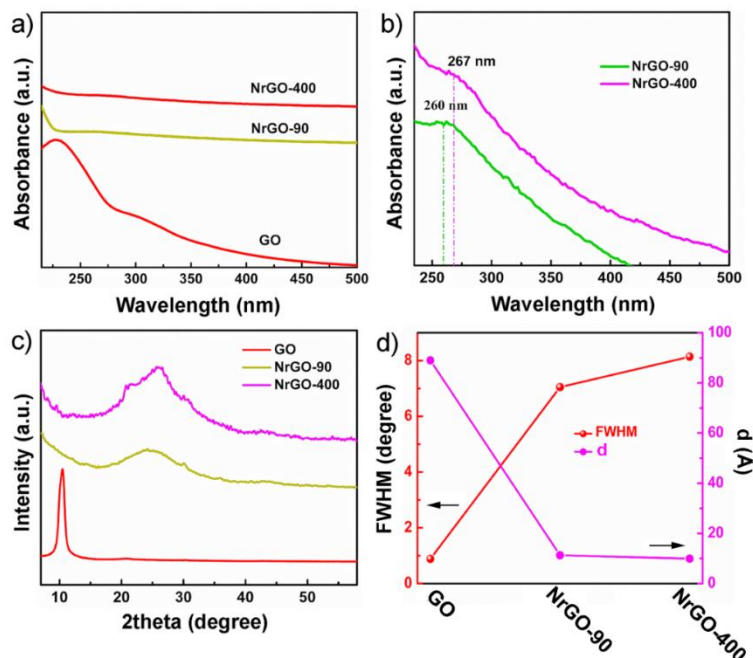


Figure 4.1: (a,b) UV-VIS spectroscopy of GO, NrGO-90 and NrGO-400 dispersed in water after 20 minutes sonication (c) XRD pattern of synthesized GO, NrGO-90 and NrGO-400 (d) Variation of full width half maxima (FWHM) and Out of plane crystallite width of GO, NrGO-90 and NrGO-400 from XRD analysis.

X-Ray Diffraction (XRD) measurement results at a sharp peak of (002) at $2\theta = 26.4^\circ$ (interlayer spacing (d) 3.37 \AA) of pure graphite powder. After oxidation of graphite, the resultant GO gives a peak at $2\theta = 10.51^\circ$ (FWHM-0.88629) having interlayer spacing 8.40 \AA with increasing interlayer distance due to large oxygen functionality groups like $-\text{CHO}$, $-\text{COOH}$, $-\text{C-O}$ present in the GO sheet [46]. In the XRD analysis of NrGO-90 shows a broad peak corresponds to (002) plane at $2\theta = 24.10^\circ$ (FWHM- 7.0515) with interlayer distance 3.68 \AA . The decrease in interspacing distance which confirms the loss of oxygen atom into the sheet [47]. The NrGO-400 shows the same broad peak at $2\theta = 25.90^\circ$ (FWHM-8.143) which is more right shifted than NrGO-90 with decreasing interlayer distance by 3.485 \AA denotes significant enhancement of the van der Waals interaction and stacking between the RGO sheets (Figure 4.1c). Out of plane crystallite size decreases from GO to RGO is mainly due to the eviction of graphene layers for reduction and increasing the in-plane grain size.

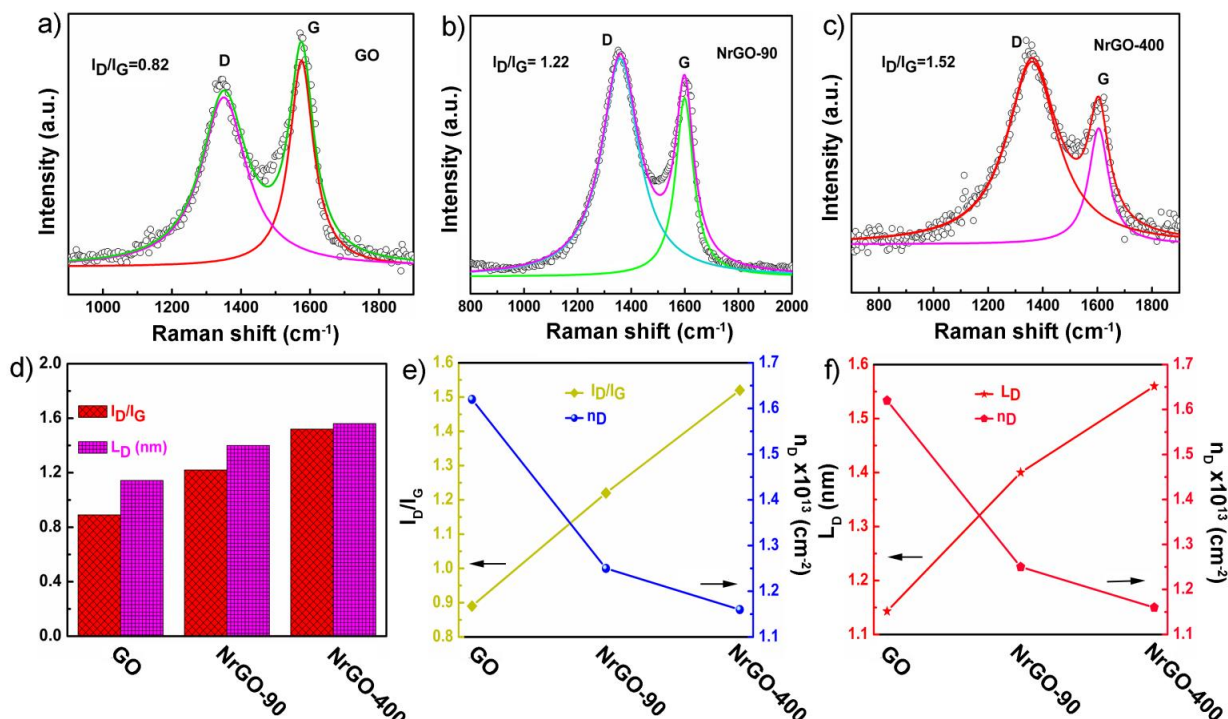


Figure 4.2: (a,b,c) Raman spectra of GO, NrGO-90 and NrGO-400 with different I_D/I_G ratio (d) Variation of I_D/I_G ratio with average defect distance (L_D) (e) Relationship between I_D/I_G ratio (f) average defect distance (L_D) with Defect density (n_D) of GO, NrGO-90 and NrGO-400.

Figure 4.1d suggests the out of plane size significantly decreases of GO to NrGO-90 and NrGO-400 from 171 Å to 12.7 Å and 10.3 Å respectively. Such a kind of behavior is strongly dependent on annealing temperature as we increase the temperature from 90 °C to 400 °C. The change of average layer numbers from GO to NrGO is strongly dependent upon reducing agent and reduction time. Another characteristic peak of GO, NrGO-90, and NrGO-400 were determined nearly at 2θ - 43°, 43.40° and 43.23° which is deconvoluted to give two components (100) and (101) [48].

Raman spectra of GO and NrGO have two characteristic peaks of defect band D and in-plane stretching vibration of the sp^2 carbon G band at the region 1340 cm^{-1} and 1610 cm^{-1} respectively [49]. D band has a useful significance to detect the defect state due to hetero-oxygen and nitrogen atoms are present as well as restoration of breathing mode in sp^2 hybridized hexagonal graphene

ring. The D and G bands of NrGO-90 are located at 1338 cm^{-1} and 1591 cm^{-1} respectively where RGO-400 reveals the position of D band at 1365 cm^{-1} and G band at 1603 cm^{-1} (Figure 4.2a,b,c). The intensity ratio (I_D/I_G) increases from GO to NrGO-90 from 0.82 to 1.22 and further goes to 1.52 for NrGO-400. The FWHM of G band for GO is 84.56 which is noticeably higher than NrGO-90 (81.31) and NrGO-400 (80.56). With decreasing FWHM of G band, it is expected that in-plane crystallinity of the NrGO sheet restored due to loss of oxygen groups covalently attached to the graphene sheet. Now, we can observe that FWHM of G band and the I_D/I_G ratio is varying oppositely from GO to NrGO-400 system. Hence, these systems are expected to have quite a large number of defects where I_D/I_G ratios go high with the more restoration of Csp^2 ring structure essential for the formation of breathing mode i.e. D band [49]. The average defect distance shrinks with the I_D/I_G ratio from 12.12 nm (NrGO-400), 11.88 nm (NrGO-90) to 11.77 nm (GO) (Figure. 4.2d). Consequently, with increasing the average defect distance and I_D/I_G ratio, the defect density per unit area shrinks from 1.62×10^{13} (GO), 1.25×10^{13} (NrGO-90) to 1.16×10^{13} (NrGO-400) (Figure 4.2e,f). Hence starting from GO, more reduced and more restored graphene structures have been obtained here in NrGO-90 to NrGO-400.

FESEM and TEM images of NrGO-90 and NrGO-400 are described in Figure 4.3. Typically an aggregation of few layers is observed in NrGO-90 which is mainly due to solvent evaporation. NrGO-400 exhibits a thin sheet of layers stacked with each other. The TEM image of both samples contains a thin sheet containing few layers with porosity (Figure 4.3c,d). The reduction process of GO implies the removal of oxygen functional groups (mainly hydroxyl, carbonyl, epoxy) which were determined from FTIR and XPS analysis (Figure. 4.4). In our new reduction process, some extent of functional groups removed from the basal plane and edge site of GO with the addition of nitrogen functionalities. FTIR stretching frequency of GO were determined at 3200 cm^{-1} , 2930 cm^{-1} , 1724 cm^{-1} , 1620 cm^{-1} , 1385 cm^{-1} , 1218 cm^{-1} , 1040 cm^{-1} corresponds to –OH, –C–H, C=O, C=C, O–H in plane bend, C–O–C and C–O stretching frequencies of vibration respectively (Figure 4.4a) [34,51]. After reduction at 90°C , the intensity of OH frequency mode decreases where it was completely diminished in NrGO-400. C=C band locates at 1537 cm^{-1} and 1531 cm^{-1} for NrGO-90 and RGO-400. Similarly, carbonyl (–C=O) stretching frequency at 1724 cm^{-1} for GO was contracted for both NrGO-90 and NrGO-400. Moreover, the C–O vibrational mode of NrGO-400 was almost diminished after annealing.

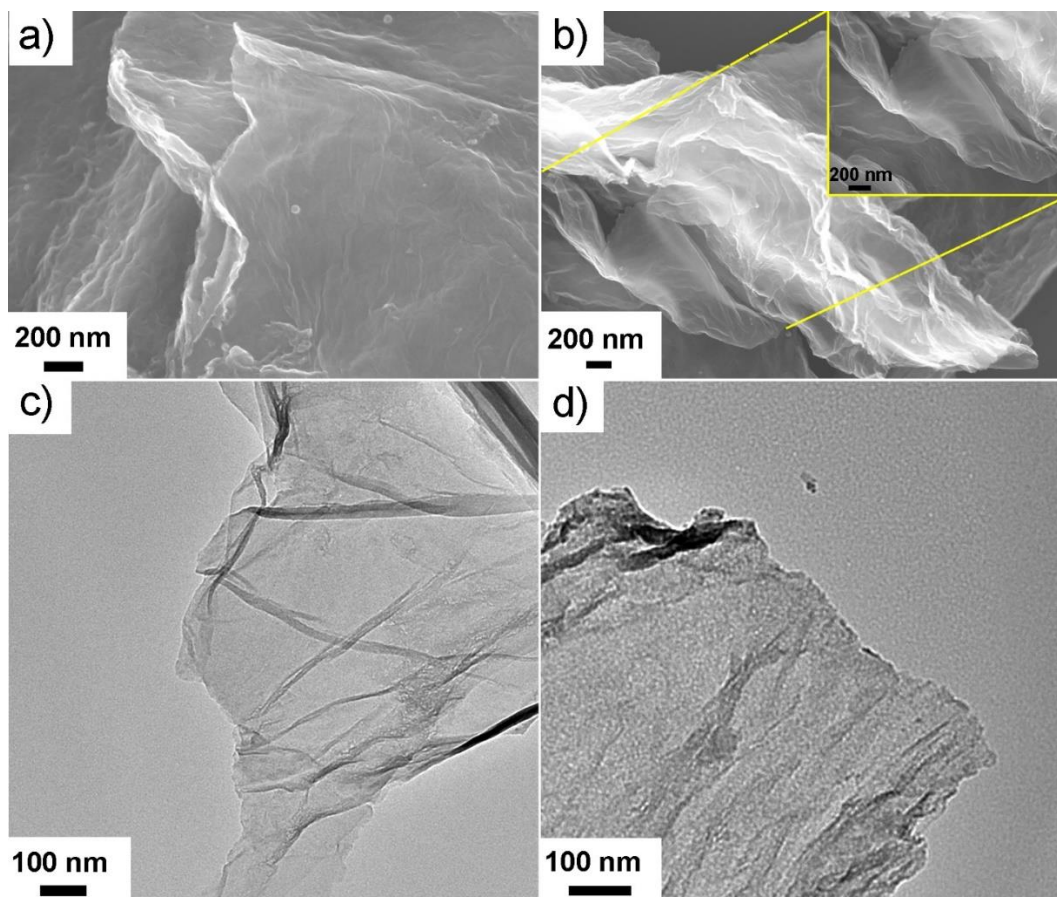


Figure 4.3: (a) FESEM image of NrGO-90 (b) NrGO-400 showing sheet like morphology with few layers (c) HRTEM image of NrGO-90 (d) reveals a thin sheet with the distribution of porosity.

Only a small new peak appears at 1170 cm^{-1} of both RGO correlates to C-N vibrational mode [51]. X-ray photoelectron spectroscopy (XPS) is an important tool to determine the nitrogen functionalization after reduction and the percentage of the number of groups present in GO and NrGO. High resolution C 1s spectra indicate different functional groups have attached in GO which are mainly located at 284.1 eV (C=C), 285.6 eV (C-O), 286.7 eV (epoxy carbon), 288.2 eV (C=O), 289 eV (O=C-O) (Figure 4.4b). After reduction corresponding NrGO-90, epoxy carbon and O=C-O groups are almost eliminated from the surface of NrGO-90 moiety. The corresponding three peaks at 284.1 eV for C=C, 285.1 eV for C-O, 288.2 eV for C=C have been determined for NrGO-90 where Intensity of C-O and C=O is lower than GO (Figure 4.4c). Figure

4.4d evaluates a new peak at 285.9 eV generated after reduction attributed as C=N in both NrGO-90 and NrGO-400. The percentage of groups of all samples is shown in (Table 4.1). The sp^2 carbon content has been remarkably enhanced from GO (53.5%) to NrGO-90(58%) and NrGO-400 (62%) which confirms successful reduction occurs. N 1s spectra of NrGO-90 are assigned at 397.8 eV, 399.2 eV, 400.1 eV, and 401.3 eV corresponding to pyridinic, amine, pyrrolic and graphitic nitrogen respectively [53]. The percentage of amine and pyridinic nitrogen in NrGO-90 is comparably larger extent than graphitic nitrogen in NrGO-90 (Figure 4.4d,f). In our analysis, the percentage of amine and pyrrolic group shrinks whereas the graphitic content increases after annealing to 400°C. NrGO-400 reveals the position of four deconvoluted peaks of pyridinic, amine, pyrrolic and graphitic nitrogen at 398.3 eV, 399.2 eV and 400.1 eV and 400.6 eV respectively (Figure 4.4d). The content of the amine and pyridinic nitrogen groups has significantly reduced from 57.58% (NrGO-90) than 41.45 % (NrGO-400) and 19% (NrGO-90) to 9% (NrGO-400) respectively evaluated from N 1s spectra. Moreover, the graphitic nitrogen becomes double in percentage from NrGO-90 (9.18%) to NrGO-400 (19.51%).

The porous nature has also been confirmed by Brunauer -Emmett –Teller (BET) analysis [22]. A hysteresis loop of type IV of NrGO-90 is observed in N_2 adsorption-desorption isotherm. Figure 4.5a,b suggests the specific surface area of NrGO-90 is $180.6 \text{ m}^2/\text{g}$ with high pore volume ($0.0046 \text{ cm}^3/\text{g}$). The hysteresis loop is governed mainly between the ranges of p/p_0 to a value of 0.4 to 1 in both NrGO systems. Pore volume and pore size distribution are calculated From Barrett–Joyner–Halenda (BJH) analysis [22,53,54]. Larger pore volume is important to show capillary condensation above $P/P_0 = 0.4$ which is mainly responsible for the hysteresis loop. Large pore volume ($0.084 \text{ cm}^3/\text{g}$) and pore diameter (5.22 nm) of NrGO-90 indicate mesoporous in nature. NrGO-400 reveals a low surface area ($77.253 \text{ m}^2/\text{g}$) due to annealing with loss of oxygen functionalities. The pore volume ($0.046 \text{ cm}^3/\text{g}$) and size distribution (3.2 nm) in NrGO-400 shrinks significantly compared to NrGO-90. Figure 4.5c suggests the linear plot to determine the weight of monolayer (W) and C constant which is positive in both of NrGO. The positive value suggests good adsorbate-adsorbent interaction [53]. The noticeable decrease in pore size with the surface area for NrGO-400 is mainly governed by two factors. Primarily loss of oxygen and restoration of C sp^2 ring into the NrGO-400 sheet enhances in-plane crystallite width whereas the defect density is minimum in comparison with GO and NrGO-90 with lower pore diameter.

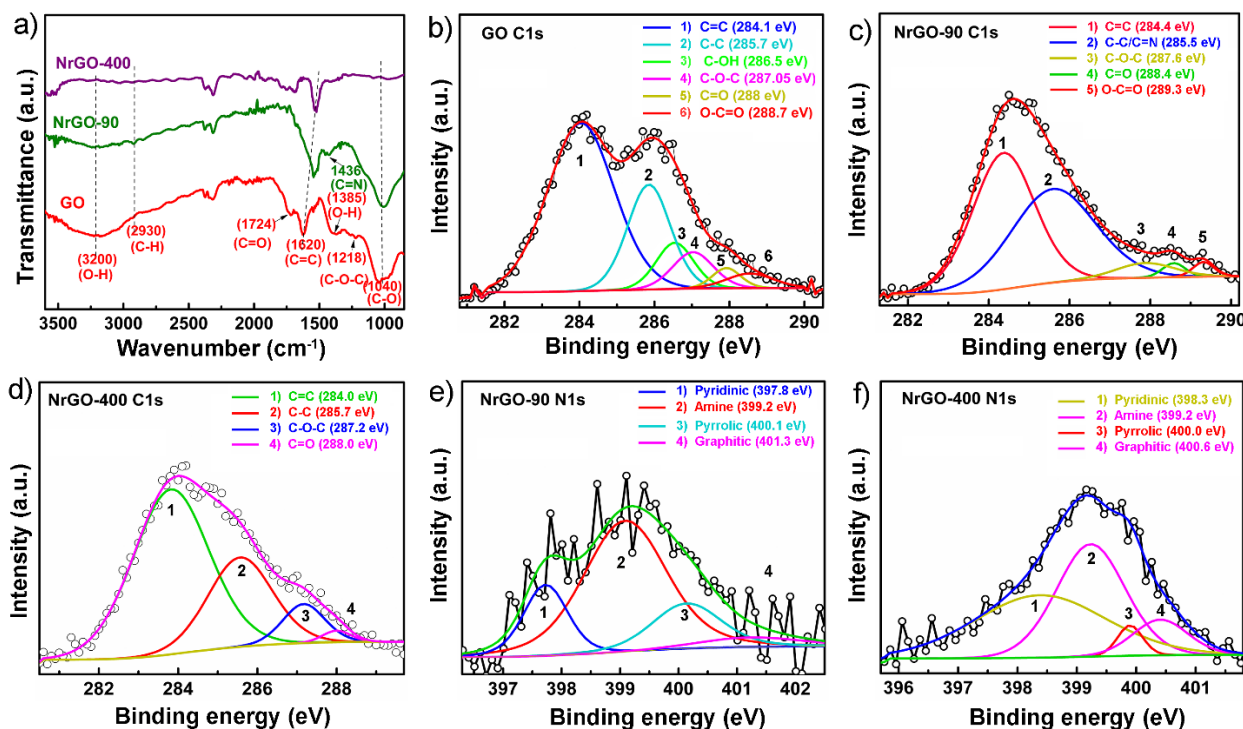


Figure 4.4: (a) FTIR spectra of GO, NrGO-90 and NrGO-400 (b) XPS spectra of C1s spectra of GO (c) NrGO-90 (d) NrGO-400 implies successful reduction of oxygen containing groups (-C=O), (C-OH), (O-C=O), (C-O-C) (e) N 1s spectra of NrGO-90 (f) NrGO-400 with different composition of pyridinic, amine, pyrrolic and graphitic nitrogen content.

The large diameter of the mesopore of NrGO-90 indicates facile diffusion of electrolyte ions into the graphene sheet improves the reduction reaction, faster electron transfer rate constant and good capacitive performance.

Materials	C=C (eV)	C-C/C-N (eV)	C=O (eV)	C-O-C (eV)	O-C=O (eV)
GO	55%	22.27%	2.85%	7.36%	3.42%
NrGO-90	58.5%	44%	1.80%	4.82%	1.74%
NrGO-400	62 %	32.37%	1.59%	3.82%	-

Table 4.1: Percentage of different functional groups of GO, NrGO-90 and NrGO-400 from C1s XPS analysis.

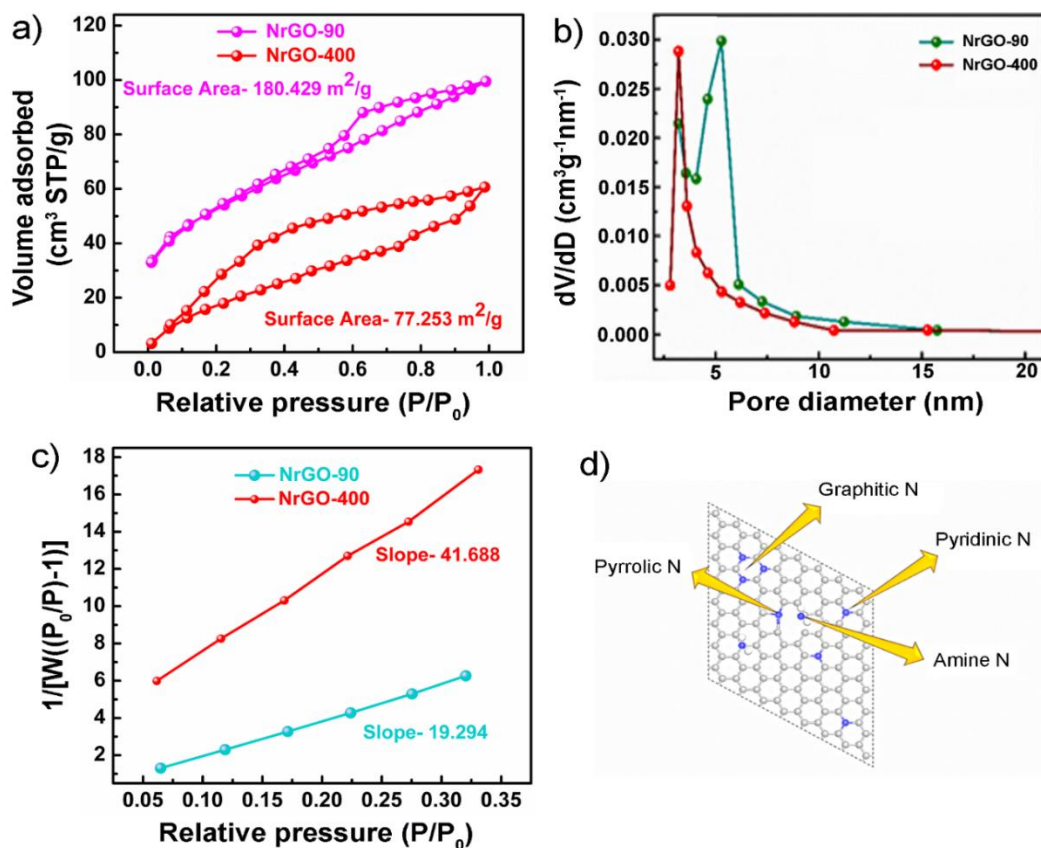


Figure 4.5: (a) N_2 adsorption-desorption isotherm of NrGO-90 and NrGO-400 (b,c) Distribution of pore diameter with relative pressure of NrGO-90 and NrGO-400. (d) Schematic representation of various nitrogen functional groups on NrGO.

4.3.2. ORR results and analysis

To investigate the oxygen reduction of NrGO material it is very essential to determine any reduction peak (cathodic peak) that appears in nitrogen saturated solution in 0.1 (M) KOH solutions. In our observation, no such peak has noticed in all four samples in N_2 saturated solution whereas a cathodic peak positioned at -0.30 V (vs. Ag/AgCl) for NrGO-90 and -0.37 V (vs. Ag/AgCl) for NrGO-400 are noticed in O_2 saturated solution which concludes the reduction occurs in presence of saturated oxygen (Figure 4.6a). The more positive potential of reduction influences the efficient catalyst for the ORR. In this experiment, reduction at a potential occurs at -0.30 V (vs. Ag/AgCl) for NrGO-90 which is more positive in comparison with previously reported $NaBH_4$ reduced rGO (-0.56 V vs. Ag/AgCl) [55], iodine mediated rGO (-0.35 V vs. Ag/AgCl) [55], bare graphene electrode (-0.47 V vs. SCE) [35], graphene-PDDA composite (-

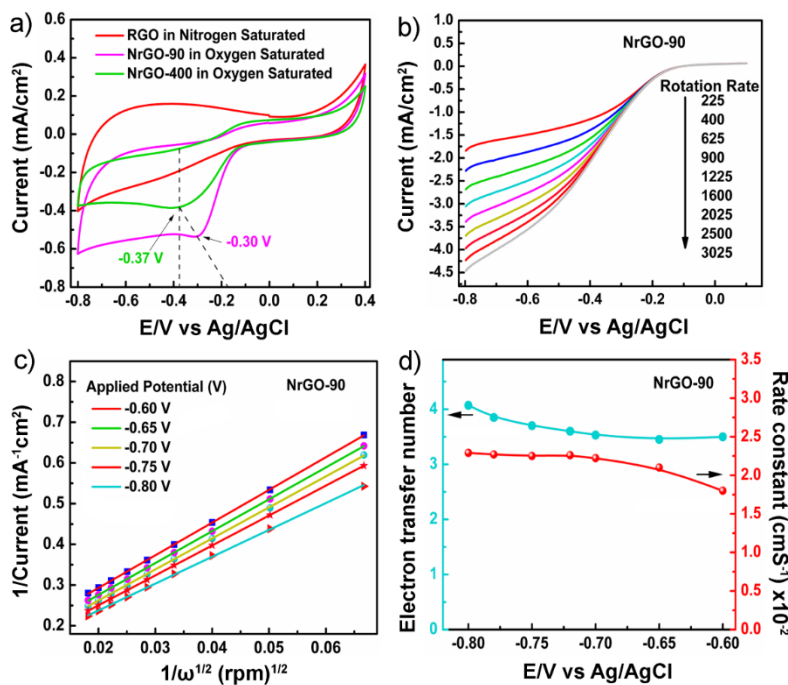


Figure 4.6: (a) Cyclic Voltammogram of NrGO-90 and NrGO-400 in N₂ and O₂ saturated solution in 0.1 (M) KOH at 10 mV/s scan rate (b) Linear sweep voltammogram of NrGO-90 in 0.1 (M) KOH at a scan rate 10 mV/s with the different rotation speed (225-3025 rpm) via rotating disk electrode (RDE) (c) Koutecky-Levich (K-L) plot of NrGO-90 at different potential from -0.8 V to -0.6 V (vs. Ag/AgCl) (d) The plot of electron transfer number and rate constant of electron transfer of NrGO-90 at different potentials.

0.35 V vs. SCE) [35], carbon nanotube and graphene composition by adenine functionalization (-0.33 V vs. SHE) [56]. Significantly NrGO-90 exhibits 50 mV shifts in reduction potential towards a positive direction in comparison to Iodine mediated rGO. Moreover, after the annealing of NrGO, the reduction potential decreases to a value of -0.37 V (vs. Ag/AgCl) in the case of NrGO-400. To analyze the study of oxygen reduction kinetics we have performed rotating disk voltammetry of NrGO-90 and NrGO-400 with increasing the rotation from 225 rpm to 3025 rpm at a scan rate of 10 mV/s (Figure 4.6b & 4.7a). In LSV analysis, the current density increases with the rotation speed are mainly ascribed to abbreviate the diffusion layers. NrGO-90 exhibits an onset potential at -0.086 V vs. Ag/AgCl (0.82 V vs. RHE) having half wave potential -0.39 V vs. Ag/AgCl (0.52 vs. RHE). The onset potential of NrGO-90 is quite closer to Pt/C which indicates a good catalyst for oxygen reduction.

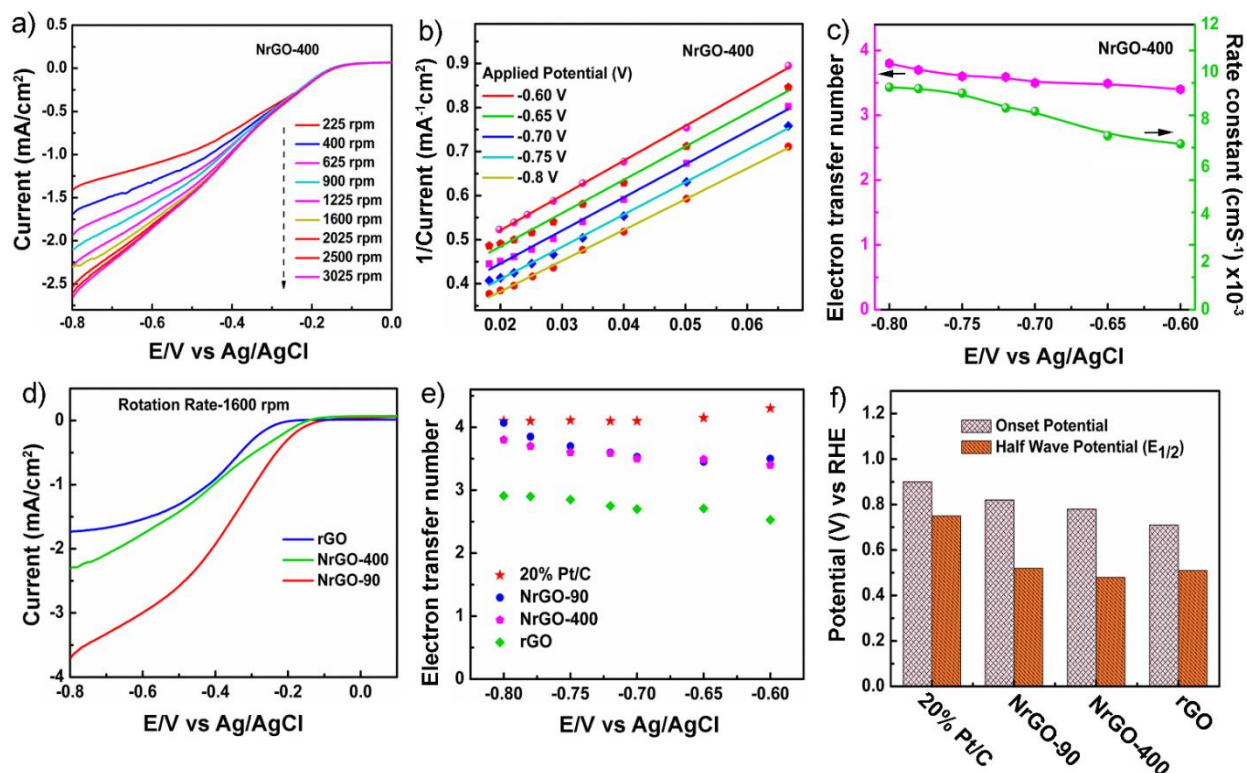


Figure 4.7:(a) Rotating disk electrode (RDE) Linear sweep voltammogram of NrGO-400 in 0.1 (M) KOH at a scan rate 10 mV/s with different rotation speed (225-3025 rpm) (b) Koutecky-Levich (K-L) plot of NrGO-400 at different potential from -0.8 V to -0.6 V (vs. Ag/AgCl) (c) The plot of electron transfer number and rate constant of electron transfer of NrGO-400 at different potentials (d) Variation of limiting-diffusion current density (J_K) of NrGO-90, NrGO-400 and rGO at 1600 rpm (e) Comparison of electron transfer number with potential of 20% Pt/C, NrGO-90, NrGO-400 and rGO (f) Plot of onset potential and half wave potential with the potential window of 20% Pt/C, NrGO-90, NrGO-400 and rGO.

Figure 4.6c shows K-L plot having a linear relationship between $1/J$ vs. $1/\omega$ was determined for all samples at the various potentials from -0.8 V to -0.6 V. The current density (J) is higher at lower potential (-0.8V) and slope ($1/B$) of K-L plot increases from negative to a positive potential with the parallel character of the linear curve at a potential which confirms first order kinetics remains intact for all the samples (Figure 4.6c & 4.7b). The mechanism of ORR kinetics undergoes two electrons or four electron pathways. Previous two electron pathways involve the formation of the hydrogen peroxide and later four-electron pathway results in water formation which is most convenient for oxygen reduction.

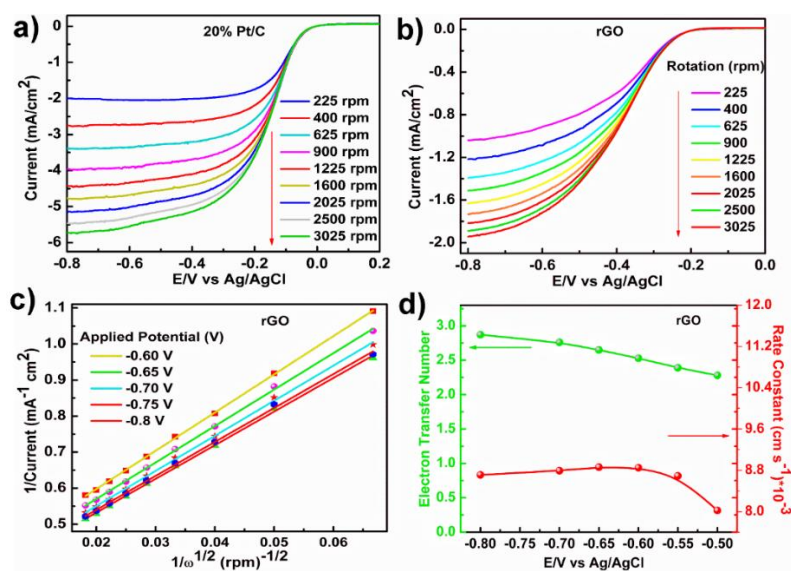


Figure 4.8: Linear sweep voltammogram of (a) 20% Pt/C (b) rGO in 0.1 (M) KOH at a scan rate 10 mV/s with different rotation speeds (225-3025 rpm) via rotating disk electrode (RDE) (c) Koutecky-Levich (K-L) plot of rGO at different potential from -0.8 V to -0.6 V (vs. Ag/AgCl) (d) The variation of electron transfer number and rate constant of electron transfer of rGO.

In NrGO-90 the value of n varies with over potential $n = 4.1$ at 0.10 V vs. RHE and 3.5 at 0.30 V vs. RHE which is very close to Pt/C catalyst (Figure 4.6d & 4.7e). After annealing product, the NrGO-400 shows $n = 3.8$ at 0.10 V vs. RHE which indicates our synthesized nitrogen functionalized reduced graphene oxide is a better catalyst (Via nearly 4 electron transfer) for ORR and fuel cell applications than commercial rGO. We have also evaluated the rate constant of the electron transfer which is much faster in the case of NrGO-90. The rate constant shows in the range of 10^{-2} order of NrGO-90 which is one order higher than NrGO-400 and rGO (Figure 4.6d & 4.7e). The rate constant faintly decreases from 0.1 V to 0.3 V vs. RHE to a value of 2.29×10^{-2} to 2.13×10^{-2} cm s⁻¹ respectively in NrGO-90 have shown in Figure 4.6d. NrGO-400 reveals rate constant of 9.36×10^{-3} cm s⁻¹ at 0.1 V vs. RHE which is 1.35% slower than NrGO-90 (Figure 4.7c). As the electron transfer number and limiting-diffusion current density are lower in rGO, the electron transfer rate constant is expected to be lower value 8.79×10^{-3} cm s⁻¹ at 0.1 V vs. RHE shown in Figure. 4.8. The Pt/C shows four electron reduction processes with the independence of the potential range. At -0.8 V (0.10 V vs. RHE) and -0.6 V (0.3 V vs. RHE), the electron involved per oxygen reduction of Pt/C is $n = 4.1$ and 4.3 respectively

where rGO involves nearly two electron pathways 2.53 at 0.3 V vs. RHE and 2.93 at 0.1 vs. RHE. The comparison table of ORR onset and half wave potential has been shown in Figure 4.7f and table 4.2-4.3.

Materials	Onset Potential (V)	$E_{1/2}$ (V)	J_L (mA/cm ²) at 1600 rpm	n	Tafel Slope (mV/decade)
20% Pt/C	0.9	0.75	-4.77	4.2	62
NrGO-90	0.82	0.52	-3.70	4.1	67
NrGO-400	0.78	0.51	-2.32	3.8	74
rGO	0.71	0.49	-1.70	2.9	82

Table 4.2: Comparison of the various parameters of ORR for all materials. All the potential has been calculated in RHE.

Catalyst	Electrode	Electrolyte	E_{ORR} (V)	E_{Onset} (V)	J_L at 1600 rpm	n	Ref.
2D-hBN/RGO	Glassy carbon (GC)	0.1 M KCl	-	0.798 V vs. RHE	-3 mA/cm ²	3.7	57
bare graphene	bare graphene electrode	0.1 (M) KOH	(-0.47 V vs. SCE)	-0.25 V vs. SCE	-	3.5-4	35
NaBH ₄ reduced rGO	-	-	(-0.56 V vs. Ag/AgCl)	-	-	-	55
Iodine mediated rGO	(GC)	0.1 (M) KOH	(-0.35 V vs. Ag/AgCl)	-	-	-	55
Adenine and graphene	-	0.1 (M) KOH	(-0.33 V vs. SHE)	-0.17 V vs. SCE	-4.5 mA/cm ²	3	56
Graphene-PDDA composite	bare graphene electrode	0.1 (M) KOH	(-0.35 V vs. SCE)	-0.15 V vs. SCE	-	3.5-4	35
Surfactant-exfoliated 2D hBN	(SPE)	0.1 (M) H ₂ SO ₄	-0.71 V vs. SCE	-	-	-	58
N- MoS ₂ /carbon	GC	0.1 M KCl	-	-	-2.78 mA/cm ²	-	59
2D-MoS ₂	SPE	0.1 (M) H ₂ SO ₄	-0.53 V vs. SCE	0.16 V vs. SCE	-	4	60
Nb doped MoS ₂	GC	0.1 (M) KOH	0.61 V vs. RHE	0.78 V vs. RHE	-	-	61

MoS ₂	GC	0.1 (M) KOH	-0.42 V Vs. SCE	-	-2 mA/cm ²	2.7	62
MoS ₂ /Nitrogen-doped graphene	GC	0.1 (M) KOH	-0.23 V Vs. SCE	-0.12 V vs SCE	-3.8 mA/cm ²	3.75	62
Nanostructured MoS ₂	GC	0.1 (M) KOH	-	-0.14 V vs. Ag/AgCl	-2.4 mA/cm ²	-	63
AuNP/MoS ₂	GC	0.1 (M) KOH	-0.41 V vs. SCE	-0.12 V vs. SCE	-3 mA/cm ²	-	64
MoS ₂ -rGO Nanosheets	GC	0.1 (M) KOH	-	0.8 V vs. RHE	-2.72 mA/cm ²	3.3	65
Co(OH) ₂ -MoS ₂ /rGO	GC	0.1 (M) KOH	0.7 V vs. RHE	0.805 V vs. RHE	-4.1 mA/cm ²	3.2-3.6	66
2D-hBN	SPE	0.1 (M) H ₂ SO ₄	-0.81 V vs. SCE	-	-	2.45	67
CoOx/mC@MoS ₂	GC	0.1 (M) KOH	-	0.67 V vs. RHE	-2.4 mA/cm ²	2.68-3.2	68
MoS ₂ /N-GR	(RDE)	0.1 (M) KOH	-	-0.156 V vs. SCE	-3.7 mA/cm ²	2.85-2.95	69
PdxSy-MoS ₂ /N-GR	RDE	0.1 (M) KOH	-	-0.242 V vs. SCE	-4.2 mA/cm ²	3.75-3.8	69
NrGO-90	GC	0.1 (M) KOH	-0.3 V vs. Ag/AgCl	0.82 V vs. RHE	-3.70 mA/cm²	4	This Work

Table 4.3: Comparison of ORR Performance of previously reported NonPGM catalyst.

The long durability tests and methanol (MeOH) crossover are the main concerns of fuel cell applications [13,70]. Figure 4.9 shows the relative current drops to 85 % from the initial current density of 20% Pt/C after 3.5 hours. In comparison to Pt, the response of current insignificantly shrinks to 90% and 87 % from initial current density NrGO-90 and NrGO-400 respectively after 3.5 hours (Figure 4.9a). Pt as cathode material in the fuel cell has a significant impact, especially in direct methanol fuel cells (DMFC) under alkaline media [35]. The oxidation of methanol by platinum is more favorable which sluggishes the kinetics of reduction of oxygen in the fuel cell. However, the percentage of formation of toxic gas carbon monoxide (CO) by methanol oxidation is maximum, especially for Pt electrocatalysts [71,72]. To minimize the formation of CO in alkaline medium where the incorporation of catalysts in cathode may overcome the problem to accelerate the ORR process. From Figure 4.9b the current density for 20% Pt/C sharply decreases (85% retention) after adding methanol. Similarly, the response of current varies almost constant for NrGO-90 and NrGO-400 (97% retention for both) after the addition of methanol. This methanol crossover and cycling stability indicate NrGO catalyst has an efficient catalyst towards ORR in fuel cells than Pt catalysts. Fig. 4.9c explains the Tafel plot of four samples at higher over the potential region.

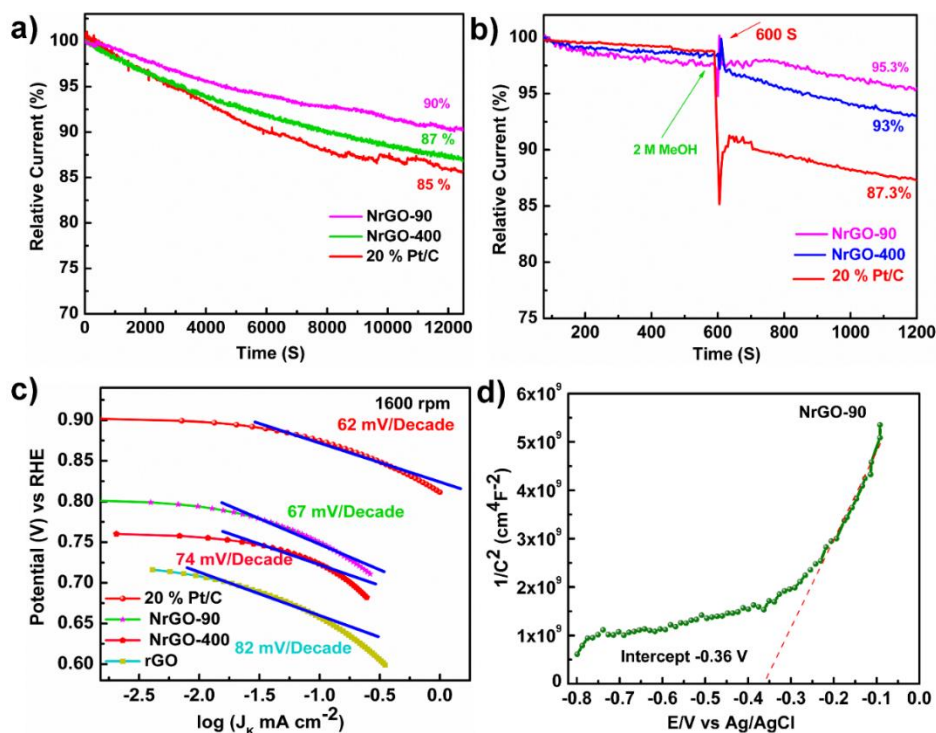


Figure 4.9: (a) Chronopotentiometric experiments of 20% Pt/C, NrGO-90, NrGO-400 at -0.3 V vs. Ag/AgCl in O₂ saturated 0.1 (M) KOH at 1600 rpm for 3.5 hours (b) Response of relative current of 20% Pt/C, NrGO-90, NrGO-400 in 0.1 (M) KOH at 1600 rpm with constant potential -0.3 V by adding methanol after 600 s (c) Tafel plot of 20% Pt/C, NrGO-90, NrGO-400 and rGO (d) Mott-schottky plot of NrGO-90.

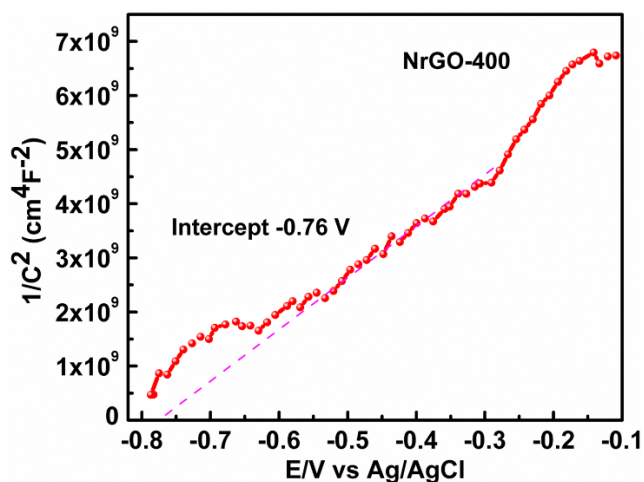


Figure 4.10: Mott-Schottky plot of NrGO-400.

At higher potential, Pt/C shows a slope of 62 mV/decade involves Temkin adsorption isotherm. Figure 4.9c suggests Tafel slope increases from NrGO-90 (67 mV/decade), NrGO-400 (74 mV/decade) to rGO (82 mV/decade). The slope between Pt/C and NrGO-90 is closer which implies the adsorption pathway and kinetics of reduction are almost the same for both materials. By extrapolating linear region of eqn. (4.6) at zero potential exchange, the current density can be calculated. The lower Tafel slope involves a higher exchange current density. From previous literature, it is evident nitrogen incorporation on carbon material increases the electron density on the conduction band to behave as an n-type semiconductor. The behavior of n-type semiconductors has been determined from the Mott-Schottky analysis [73]. Mott-Schottky plot is an important tool for determining the flat band potential, carrier concentration. More positive flat band potential indicates a facile charge transfer reaction due to low overpotential. The positive slope implies the synthesized new materials are an n-type semiconductor. From our calculation NrGO-90 exhibits higher flat band potential (-0.385V vs. Ag/AgCl) compared with annealed product NrGO-400 (-0.785V vs. Ag/AgCl) which indicates low overpotential is required to fascinate the reduction reaction in NrGO-90 (Figure 4.9d & 4.10).

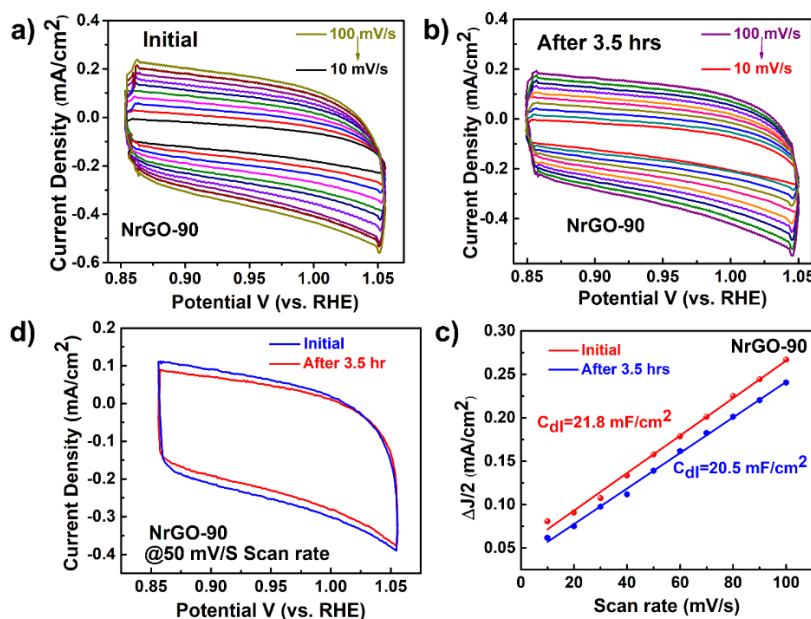


Figure 4.11: Cyclic Voltammetry of NrGO-90 at (a) before and (b) after 3.5 hours with scan rates from 10 mV/s to 100 mV/s. Comparison of (c) CV curves and (d) C_{dl} value of NrGO-90 before and after 3.5 hours cycling stability.

Moreover, the electrochemically active surface area (ESCA) and double-layer capacitance (C_{dl}) are negligible changes before and after the durability test for NrGO-90 (Figure 4.11). The ESCA has quite changed compared to pristine NrGO-90 from $1090 \text{ cm}^2/\text{g}$ to $1020 \text{ cm}^2/\text{g}$ i.e. 93 % retention of active surface area which coincides with durability test which is ~90% retention for NrGO-90.

4.3.3. Active sites and DFT analyses in ORR mechanism

From the previous study, the quinonoid type functional group on the RGO sheet is ORR active [74]. Moreover, the aryloxy radical can stabilize the sp^2 moiety of rGO via conjugation to make the surface charged which promotes facile oxygen reduction [75]. Besides, nitrogen doping was incorporated into rGO by high temperature treatment to improve oxygen reduction [34]. The catalytic active sites of NrGO-400 decrease with increasing the nitrogen content into the graphene sheet which undergoes restacking between the graphene layers shrink the migration of ions into the layers [76]. So, in order to reduction of GO to rGO with nitrogen incorporation, a modified experiment is essential to control the ratio of nitrogen to carbon as there is a chance of stacking probability with high nitrogen content. In our study NrGO-90 exhibits a low amount of nitrogen (7%) than NrGO-400 (13.5%). Previously reported data to explain the ORR activity of carbon based materials like N doped graphene is more facile in presence of pyridinic nitrogen and with increasing the heat treatment pyrrolic and graphitic nitrogen is converted to pyridinic nitrogen leading to higher ORR activity of the annealed product [73].

We further carried out the first principles calculation to study the activity of RGO with functional groups towards ORR in alkaline medium. Initially, we took bare graphene surface with vacancy defect and studied the attachments of functional groups like amino ($-NH_2$), hydroxyl ($-OH$), carbonyl ($=CO$), epoxy ($-O-$) along with the substitution of nitrogen doping at different positions and orientations. We found that the configuration with minimum energy prefers the carbonyl and the amino group to get attached to the carbon atoms at the vacancy defect region whereas the hydroxyl and oxygen atom in epoxy configuration gets adsorbed at a distance from the vacancy on two nearest carbon atoms. The optimized geometry of the minimum energy configuration is shown in Figure 4.12a. Once the minimum energy configuration was identified we proceeded towards the next step which was the adsorption of the di-oxygen molecule on the RGO surface. We considered various probable adsorption sites on the RGO surface and the best

ones were determined in terms of the lowest values of adsorption energy as calculated using eqn. (4.3). Our study revealed that O₂ is most likely to get adsorbed in side-on mode over the carbon atoms near the amino group (configuration 1 in Figure 4.12b) as well as on the carbon atoms near the doped nitrogen atom (pyridinic) (configuration 2 in Figure 4.12c) with identical adsorption energy value -1.531 eV. The amount of stretching in the adsorbed O₂ molecule was observed to be about 21% and 20% for configuration 1 and configuration 2 respectively. The subsequent ORR steps were studied on these configurations. The probability of ORR along both the pathways was examined thoroughly and the best one for each of the configurations was identified in terms of free energy. The free energy difference for all the reaction intermediates was calculated using eqn. (4.4) taking the free energy of the final reaction coordinate as reference. Also, the reaction intermediates and the number of protons and electron transferred to the catalyst surface are similar to the acidic medium. Thus, the operating potential, which is considered to be -0.83 V (0 V) vs. SHE (vs. RHE) throughout our calculation is insensitive to the pH when referenced to the reversible hydrogen electrode (RHE). The first protonation process (reaction coordinate 3) can occur on either of the O atoms of the adsorbed O₂ molecule and the possibilities of both were tested thoroughly. We found that the first protonation can occur on either of the O atoms of the O₂ molecule in configuration 1 with comparable free energy difference values of 2.48 eV (configuration 1(a)) and 2.07 eV (configuration 1(b)) forming an *O+*OH type structure on the surface which denotes that ORR on configuration 1 would follow the four electron pathway. The scenario was quite different for configuration 2 as protonation on one of the O atoms formed the *O+*OH type configuration with free energy difference value of 2.49 eV while protonation on the other O atom formed a peroxide ion (HO₂⁻) but with relatively higher free energy difference value confirming spontaneous occurrence of ORR via the four electron pathway on this configuration too. The following steps were studied on configuration 1(a) and configuration 1(b) as well as configuration 2. The subsequent steps, reaction coordinates 4 and 5, progressed spontaneously with free energy difference values within the range 0.06 eV – 0.65 eV and -0.96 eV – -1.03 eV respectively for all three until the final step (reaction coordinate 6) i.e. the desorption of hydroxyl group from the catalyst surface and simultaneous transfer of an electron. The free energy barrier was observed for the final reaction step for all three configurations which corresponds to the strong attachment of the hydroxyl group on the catalyst surface in the

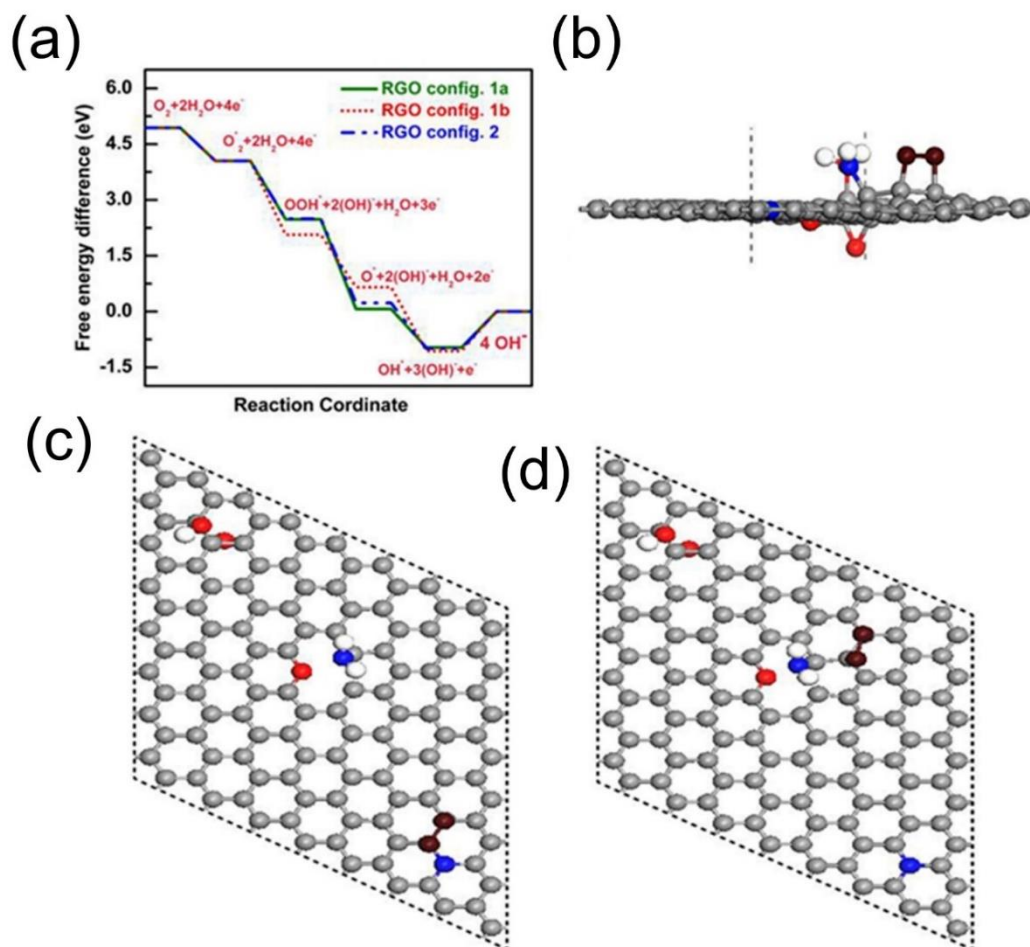


Figure 4.12: Red, blue, white and brown are Oxygen, nitrogen, hydrogen, and adsorbed oxygen atom during ORR (a) Free energy diagram of ORR kinetics for all configurations including config.1a, config.1b and config.2 (b) Config.1a indicates Oxygen adsorption into the carbon atoms near the amine group of the graphene sheet (c) config.2 for carbon atoms near the pyridinic nitrogen (d) Configuration 1b.

preceding step. Our first principles study clearly reveals the ORR mechanism on RGO functional groups catalyst surface at the atomistic level and strongly supports our experimental observation that ORR will occur spontaneously via the four electron pathway.

4.3.4. Capacitive performance and analysis

In CV analyses a distorted curve at a higher scan rate has been observed which concludes kinetically limitation of interaction between the NrGO-90 on Ni foam electrode and electrolyte ions. In both two cases with increasing the scan rate feedback of current enhances which indicates

well capacitive behavior (Figure 4.13a,b). The Gravimetric capacitance of NrGO-90 from CV was 270 F/g at 5mV/s and gradually decreased to 152 F/g at 100 mV/s. NrGO-400 exhibits specific capacitance 121 F/g at 2mV/s from CV compared to NrGO-90. At 0.5 A/g current density NrGO-90 shows excellent capacitance 287 F/g and 152 F/g at 5 A/g (Figure 4.13c). The enhancement of such behavior is mainly due to porous nature, larger surface area as well as restoration of π conjugated double bond. NrGO-400 reveals specific capacitance of 65 F/g at 0.1 A/g which is lower than NrGO-90 (Figure 4.13d). The noticeable drop of capacitance for NrGO-400 than NrGO-90 results Surface area and loss of amine groups is the dominant factor for analyzing the capacitive behavior. Long cycling stability of NrGO-90 was determined by the CD experiment at current density 2 A/g up to 10000 cycles.

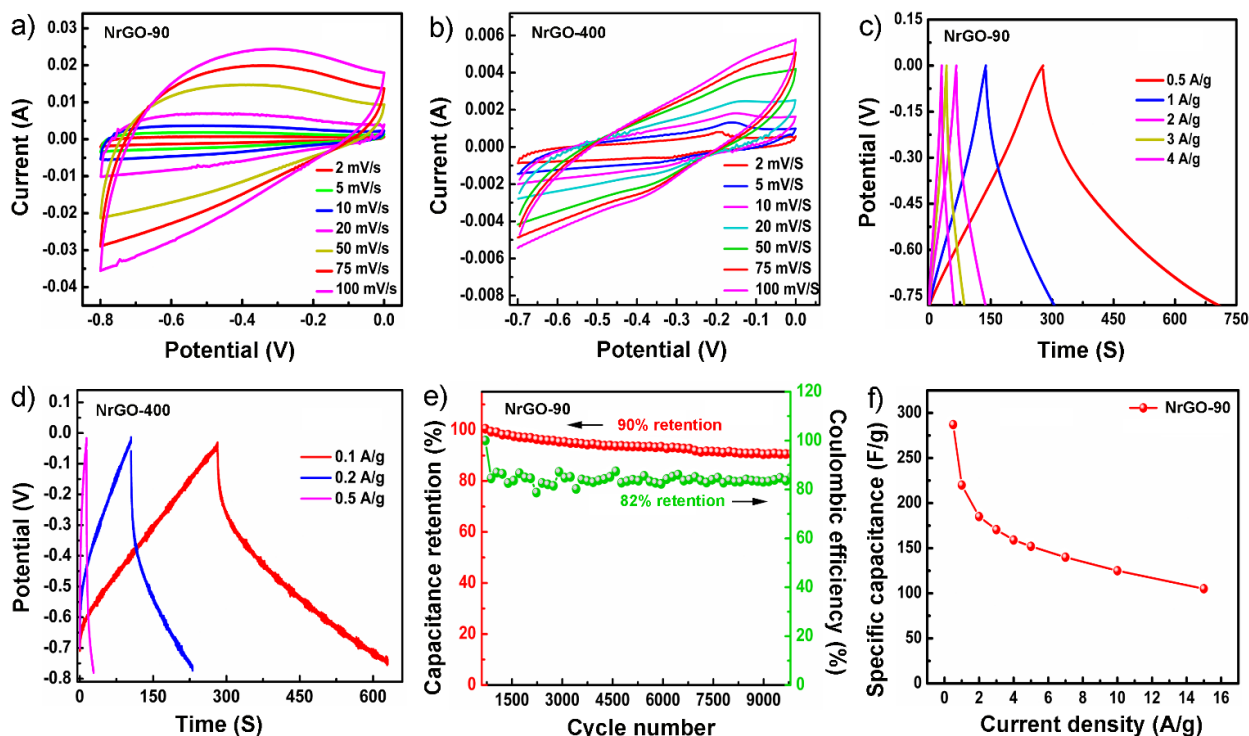


Figure 4.13: (a) Cyclic voltammetry of NrGO-90 (b) NrGO-400 in 1(M) KOH at different scan rates from 2mV/s to 100 mV/s in 1(M) KOH (c) Galvanostatic charge discharge curve of NrGO-90 from 0.5 A/g to 4 A/g in 1(M) KOH (d) NrGO-400 in 1(M) KOH (e) Cycling stability and coulombic efficiency of NrGO-90 after 10000 cycles at 2A/g in 1(M) KOH (f) Variation of specific capacitance with current density from Galvanostatic charge discharge measurement of NrGO-90.

Cycling stability of NrGO-90 was retained at 90 % and 82% columbic efficiency upon 10000 cycles which indicates effective potential application in the energy storage device (Figure 4.13e). The specific capacitance from EDLC showed a higher value than previously reported rGO reduced by urea (255 F/g), Na-NH₃ (263 F/g), Hydrazine (100-200 F/g) (Figure 4.13f & Table-4.4). Oxygen functional groups have a significant role in faradic redox reaction with electrolyte ions at anodic peak -0.5 V and cathodic peak (-0.7 V) with respect to Ag/AgCl reference electrode [22,77]. However, we have investigated the relationship between current density with scan rate to understand the effect of foreign groups in pseudocapacitance. In NrGO-90, at -0.5 V a linear variation has been observed at a scan rate 20 mV/s and the deviation occurs from 20 mV/s to high scan rate 100 mV/s (Figure 4.14a) while NrGO-400 exhibits a sharp deviation after scan rate 10 mV/s. This concludes oxygen functional group cannot participate Faradic redox reaction

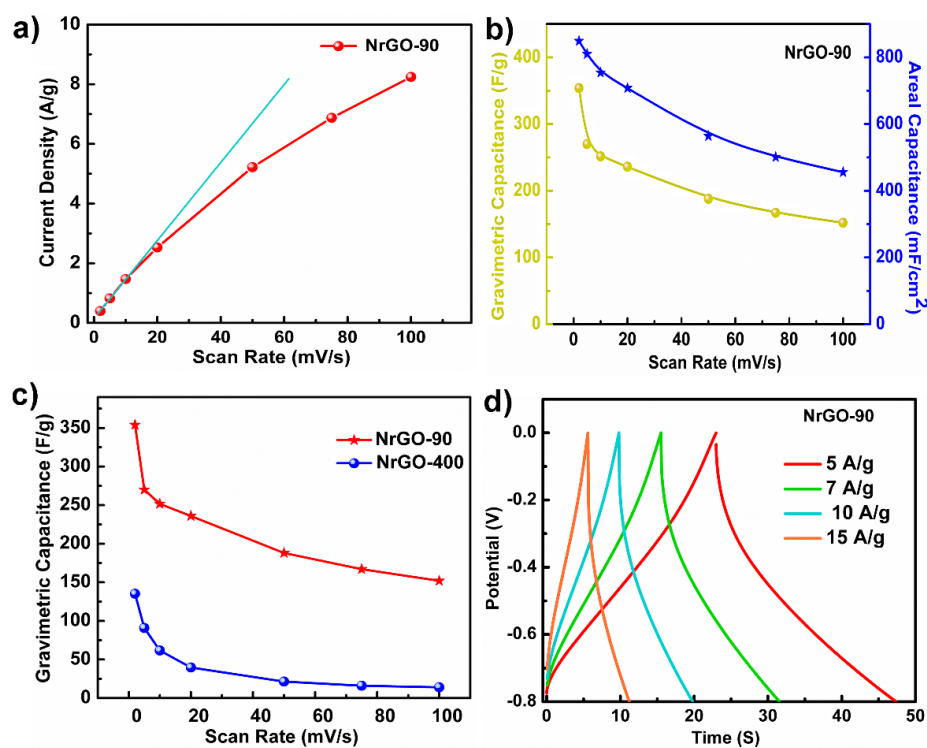


Figure 4.14: (a) Plot of current Density with different scan rates at a potential -0.5 V (vs. Ag/AgCl) of NrGO-90 and NrGO-400 showing deviation from linearity (b) Plot of gravimetric and areal Capacitance of NrGO-90 with various scan rates (c) Differentiation of gravimetric Capacitance between NrGO-90 and NrGO-400 (d) Galvanostatic charge-discharge plot of NrGO-90 from 5A/g to 15 A/g.

especially at higher scan rates in both NrGO systems. The areal capacitance is 880 mF/cm^2 at a scan rate of 2 mV/s of NrGO-90 suggests a very well capacitive performance. Figure 4.14b,c suggests the variation of both gravimetric and areal capacitance with scan rates of NrGO-90. Fig. 4.15a,b implies Nyquist plots of both NrGOs which reveal small semicircle at high frequency regions. Generally, a small semicircle is the indication of an ideal capacitor with low charge transfer resistance between the electrolyte ions and the working electrode. Inset showing Equivalent circuit diagram (EIS) consequences smaller charge transfer resistance of NrGO-90 ($R_{ct}=1.4\Omega$) than NrGO-400 ($R_{ct}=22.8\Omega$).

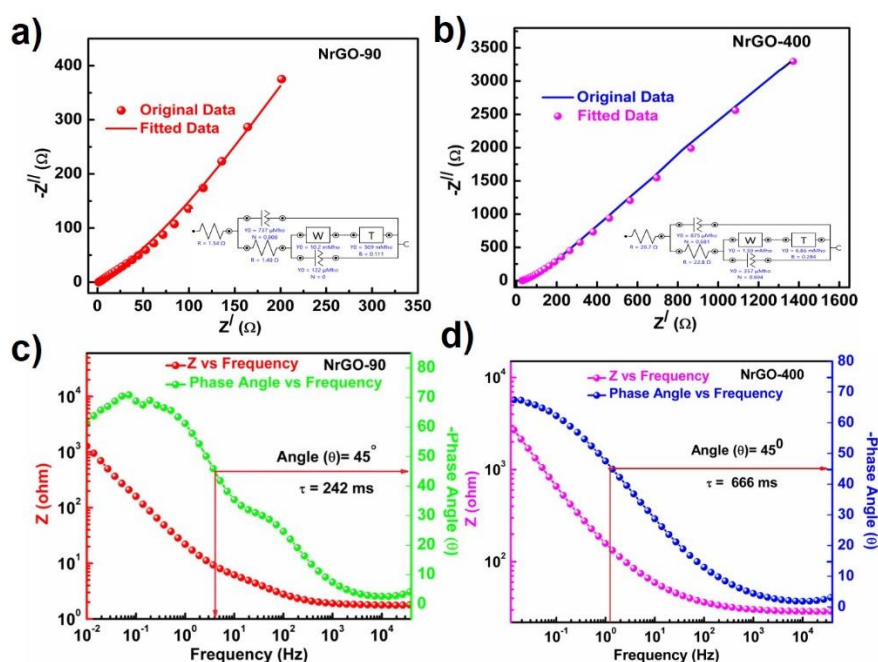


Figure 4.15: (a,b) Nyquist plot of NrGO-90 and NrGO-400 with equivalent circuit diagram. (c,d) Bode plot of NrGO-90 and NrGO-400.

Low R_{ct} value is compatible to enhance the conductivity of the annealed NrGO (NrGO-400). The high R_{ct} of NrGO-400 is probably due to low surface area and low pore volume. Bulk solution resistance (R_s) of NrGO-90 is 1.54Ω having consistent with R_{ct} . Similarly, the R_s value has enhanced for NrGO-400 to 28.7Ω . The increasing R_s value denotes the sensitivity of the electrode surface. Kinetics of charge -discharge rate can be evaluated from the Bode plot [78]. The smaller time constant or relaxation time (τ) value means higher the knee frequency (f_0) indicates a fast

rate of charge-discharge process. τ Value is inversely related to knee frequency (f_0) at phase angle -45° . Figure 4.14c,d indicates NrGO-90 has a smaller τ value (242 mS) than NrGO-400 (666 mS). The corresponding knee frequency is much higher ($f_0 = 4.02$ Hz at -45°) in the case of NrGO-90 than NrGO-400 ($f_0 = 1.45$ Hz at -45°) respectively.

Previously Reported	Process	Capacitance of RGO	Reference
Na/NH ₃	Low Temp, 30 min	263 F/g at 0.5 A/g	79
Ethylene Glycol in ammonia	180°C, 10 h	217.8 F/g at 0.4 A/g	80
Thermal reduction	300°C	151 F/g at 1 A/g	81
Dimethyl ketoxime	100°C	143 F/g at 10 mV/s	82
Hydrazine	120°C, 30 h	480.5 F/g at 10 mV/s	83
Alcohols	100°C, Reflux	35 F/g at 25 mV/s	84
Aqueous phytoextracts reduced GO	Reflux	23 F/g	85
Electrochemically-reduced GO	Electrochemical Reduction	128 F/g	86
Thermally exfoliated and reduced GO	1050°C, Furnace	117 F/g	87
Reduced GO	200 °C, 5h	262 F g ⁻¹ at 1 mV/s	88
Urea	Reflux at 95°C, 30 Hours	255 F/g at 0.5 A/g	89
Zn/ NH ₃	Room Temp, 10 min	116 F/g at 0.05 A/g	90
Imidazole/NH ₃	90°C, Reflux, 24 hours	287.5 F/g at 0.5 A/g	Our Work

Table 4.4: Comparison of Capacitive Performance of previously reported rGO.

The time constant value predicts NrGO materials are fast electron transfer rate during the charge discharge process. Thus, modification of surface area, the porosity of reduced graphene oxide (NrGO-90) influences well cycling stability, facile charge transfer reaction and excellent energy storage performance.

4.4. Conclusion

In summary, we have reported a facile and safer chemical method to achieve a simultaneous reduction of GO and nitrogen functionalization within the resultant rGO sheet at ordinary temperature using imidazole as a reducing agent under alkaline conditions. The as-prepared NrGO-90 sample has a high atomic percentage of pyridinic and amine nitrogen, large surface area, moderate interlayer spacing, and adequate pore diameter which makes it an efficient electrocatalyst for ORR. Unlike reported by others, when heat-treated at high temperature sample (NrGO-400) shows rather less efficiency towards ORR and deteriorates charge capacity with respect to pristine NrGO-90. However, both the NrGO materials show 4-electron pathways with the intermediate peroxide radicals which can convert to water. The specific capacitance was remarkably good (287.5 F/g at 0.5 A/g) for NrGO-90 due to the large surface area of the rGO sheet. Therefore, our method offers low-cost and an approachable way without the requirement of inert gas protection and high-temperature to produce NrGO-90 which has a potential application as an efficient catalyst in a fuel cell for oxygen reduction as well as in energy storage devices.

4.5. References

1. Hou, J., Shao, Y., Ellis, M.W., Moore, R.B. and Yi, B., *Physical Chemistry Chemical Physics*, 2011, 13(34), pp.15384-15402.
2. Peng, Z. and Yang, H., *Journal of the American Chemical Society*, 2009, 131(22), pp.7542-7543.
3. Zhang, J., Vukmirovic, M.B., Xu, Y., Mavrikakis, M. and Adzic, R.R., *Angewandte Chemie*, 2005, 117(14), pp.2170-2173.
4. Yang, W., Wang, Y., Li, J. and Yang, X., *Energy & Environmental Science*, 2010, 3(1), pp.144-149.
5. Wang, S. and Wang, X., *Nanotechnology*, 2008, 19(26), p.265601.
6. Wang, S., Yang, F., Chen, S. and Wang, X., *Electrochemistry communications*, 2010, 12(11), pp.1646-1649.
7. Wang, S., Wang, X. and Jiang, S.P., *Langmuir*, 2008, 24(18), pp.10505-10512.
8. Wang, S., Kristian, N., Jiang, S. and Wang, X., *Nanotechnology*, 2008, 20(2), p.025605.
9. Wang, S., White, T.J. and Wang, X., *Electrochimica acta*, 2010, 55(26), pp.7652-7658.

10. Goswami, C., Hazarika, K.K. and Bharali, P., *Materials Science for Energy Technologies*, 2018, 1(2), pp.117-128.
11. Li, L., He, J., Wang, Y., Lv, X., Gu, X., Dai, P., Liu, D. and Zhao, X., *Journal of materials chemistry A*, 2019, 7(5), pp.1964-1988.
12. Rowley-Neale, S.J., Fearn, J.M., Brownson, D.A., Smith, G.C., Ji, X. and Banks, C.E., *Nanoscale*, 2016, 8(31), pp.14767-14777.
13. Hu, C., Zhou, Y., Ma, R., Liu, Q. and Wang, J., *Journal of Power Sources*, 2017, 345, pp.120-130.
14. Wei, W., Tao, Y., Lv, W., Su, F.Y., Ke, L., Li, J., Wang, D.W., Li, B., Kang, F. and Yang, Q.H., *Scientific reports*, 2014, 4(1), p.6289.
15. Chen, T. and Dai, L., *Materials Today*, 2013, 16(7-8), pp.272-280.
16. Geim, A.K. and Novoselov, K.S., *Nature materials*, 2007, 6(3), pp.183-191.
17. Novoselov, K.S., Geim, A.K., Morozov, S.V., Jiang, D., Katsnelson, M.I., Grigorieva, I.V., Dubonos, S. and Firsov, A.A., *nature*, 2005, 438(7065), pp.197-200.
18. Berger, C., Song, Z., Li, X., Wu, X., Brown, N., Naud, C., Mayou, D., Li, T., Hass, J., Marchenkov, A.N. and Conrad, E.H., *Science*, 2006, 312(5777), pp.1191-1196.
19. Hummers Jr, W.S. and Offeman, R.E., *Journal of the american chemical society*, 1958, 80(6), pp.1339-1339.
20. Stankovich, S., Dikin, D.A., Piner, R.D., Kohlhaas, K.A., Kleinhammes, A., Jia, Y., Wu, Y., Nguyen, S.T. and Ruoff, R.S., *carbon*, 2007, 45(7), pp.1558-1565.
21. Mao, S., Yu, K., Cui, S., Bo, Z., Lu, G. and Chen, J., *Nanoscale*, 2011, 3(7), pp.2849-2853.
22. Lei, Z., Lu, L. and Zhao, X.S., *Energy & Environmental Science*, 2012, 5(4), pp.6391-6399.
23. Jiang, M., Zhang, J.L., Qiao, F., Zhang, R.Y., Xing, L.B., Zhou, J., Cui, H. and Zhuo, S., *RSC advances*, 2016, 6(54), pp.48276-48282.
24. Amarnath, C.A., Hong, C.E., Kim, N.H., Ku, B.C., Kuila, T. and Lee, J.H., *Carbon*, 2011, 49(11), pp.3497-3502.
25. Roy, R., Thapa, R., Biswas, S., Saha, S., Ghorai, U.K., Sen, D., Kumar, E.M., Kumar, G.S., Mazumder, N., Roy, D. and Chattopadhyay, K.K., *Nanoscale*, 2018, 10(35), pp.16822-16829.
26. Gao, J., Liu, F., Liu, Y., Ma, N., Wang, Z. and Zhang, X., *Chemistry of Materials*, 2010, 22(7), pp.2213-2218.
27. Zhang, J., Yang, H., Shen, G., Cheng, P., Zhang, J. and Guo, S., *Chemical communications*, 2010, 46(7), pp.1112-1114.
28. Wang, G., Yang, J., Park, J., Gou, X., Wang, B., Liu, H. and Yao, J., *The Journal of Physical Chemistry C*, 2008, 112(22), pp.8192-8195.
29. Li, J., Xiao, G., Chen, C., Li, R. and Yan, D., *Journal of Materials Chemistry A*, 2013, 1(4), pp.1481-1487.
30. Fan, Z.J., Kai, W., Yan, J., Wei, T., Zhi, L.J., Feng, J., Ren, Y.M., Song, L.P. and Wei, F., *ACS nano*, 2011, 5(1), pp.191-198.
31. Dey, R.S., Hajra, S., Sahu, R.K., Raj, C.R. and Panigrahi, M.K., *Chemical Communications*, 2012, 48(12), pp.1787-1789.
32. Kumar, N.A., Nolan, H., McEvoy, N., Rezvani, E., Doyle, R.L., Lyons, M.E. and Duesberg, G.S., *Journal of Materials Chemistry A*, 2013, 1(14), pp.4431-4435.
33. Dong, Y., Deng, Y., Zeng, J., Song, H. and Liao, S., *Journal of Materials Chemistry A*, 2017, 5(12), pp.5829-5837.
34. Du, D., Li, P. and Ouyang, J., *ACS Applied Materials & Interfaces*, 2015, 7(48), pp.26952-26958.
35. Wang, S., Yu, D., Dai, L., Chang, D.W. and Baek, J.B., *ACS nano*, 2011, 5(8), pp.6202-6209.

36. Lai, L., Potts, J.R., Zhan, D., Wang, L., Poh, C.K., Tang, C., Gong, H., Shen, Z., Lin, J. and Ruoff, R.S., *Energy & Environmental Science*, 2012, 5(7), pp.7936-7942.
37. Bera, B., Chakraborty, A., Kar, T., Leuua, P. and Neergat, M., *The Journal of Physical Chemistry C*, 2017, 121(38), pp.20850-20856.
38. Kresse, G. and Hafner, J., *Physical review B*, 1993, 47(1), p.558.
39. Kresse, G. and Hafner, J., *Physical Review B*, 1994, 49(20), p.14251.
40. Kresse, G. and Furthmüller, J., *Computational materials science*, 1996, 6(1), pp.15-50.
41. Blöchl, P.E., Först, C.J. and Schimpl, J., *Bulletin of Materials Science*, 2003, 26, pp.33-41.
42. Perdew, J.P., Burke, K. and Ernzerhof, M., *Physical review letters*, 1996, 77(18), p.3865.
43. Grimme, S., *Journal of computational chemistry*, 2006, 27(15), pp.1787-1799.
44. Nørskov, J.K., Rossmeisl, J., Logadottir, A., Lindqvist, L.R.K.J., Kitchin, J.R., Bligaard, T. and Jonsson, H., *The Journal of Physical Chemistry B*, 2004, 108(46), pp.17886-17892.
45. Luo, D., Zhang, G., Liu, J. and Sun, X., *The Journal of Physical Chemistry C*, 20111115(23), pp.11327-11335.
46. Xu, Y., Bai, H., Lu, G., Li, C. and Shi, G., *Journal of the American Chemical Society*, 2008, 130(18), pp.5856-5857.
47. Cote, L.J., Kim, F. and Huang, J., *Journal of the American Chemical Society*, 2009, 131(3), pp.1043-1049.
48. Rahman, O.A., Chellasamy, V., Ponpandian, N., Amirthapandian, S., Panigrahi, B.K. and Thangadurai, P., *RSC Advances*, 2014, 4(100), pp.56910-56917.
49. Ferrari, A.C. and Basko, D.M., *Nature nanotechnology*, 2013, 8(4), pp.235-246.
50. Stankovich, S., Piner, R.D., Nguyen, S.T. and Ruoff, R.S., *Carbon*, 2006, 44(15), pp.3342-3347.
51. Lin, Y., Jin, J. and Song, M., *Journal of Materials Chemistry*, 2011, 21(10), pp.3455-3461.
52. Tian, X., Sun, X., Jiang, Z., Jiang, Z.J., Hao, X., Shao, D. and Maiyalagan, T., *ACS Applied Energy Materials*, 2017, 1(1), pp.143-153.
53. Gómez-Gualdrón, D.A., Moghadam, P.Z., Hupp, J.T., Farha, O.K. and Snurr, R.Q., *Journal of the American Chemical Society*, 2016, 138(1), pp.215-224.
54. Dhillon, A. and Kumar, D., *Journal of Materials Chemistry A*, 2015, 3(8), pp.4215-4228.
55. Das, A.K., Srivastav, M., Layek, R.K., Uddin, M.E., Jung, D., Kim, N.H. and Lee, J.H., *Journal of Materials Chemistry A*, 2014, 2(5), pp.1332-1340.
56. Xu, Y., Chen, C., Zhou, M., Guangyi, F.U., Zhao, Y. and Chen, Y., *RSC advances*, 2017, 7(43), pp.26722-26728.
57. Patil, I.M., Lokanathan, M. and Kakade, B., *Journal of Materials Chemistry A*, 2016, 4(12), pp.4506-4515.
58. Khan, A.F., Brownson, D.A., Foster, C.W., Smith, G.C. and Banks, C.E., *Analyst*, 2017, 142(10), pp.1756-1764.
59. Hao, L., Yu, J., Xu, X., Yang, L., Xing, Z., Dai, Y., Sun, Y. and Zou, J., *Journal of Power Sources*, 2017, 339, pp.68-79.
60. Rowley-Neale, S.J., Smith, G.C. and Banks, C.E., *ACS applied materials & interfaces*, 2017, 9(27), pp.22539-22548.
61. Chua, X.J., Luxa, J., Eng, A.Y.S., Tan, S.M., Sofer, Z. and Pumera, M., *ACS Catalysis*, 2016, 6(9), pp.5724-5734.
62. Zhao, K., Gu, W., Zhao, L., Zhang, C., Peng, W. and Xian, Y. *Electrochimica Acta*, 2015, 169, pp.142-149.
63. Suresh, C., Mutyala, S. and Mathiyarasu, J., *Materials Letters*, 2016, 164, pp.417-420.
64. Wang, T., Zhuo, J., Chen, Y., Du, K., Papakonstantinou, P., Zhu, Z., Shao, Y. and Li, M., *ChemCatChem*, 2014, 6(7), pp.1877-1881.

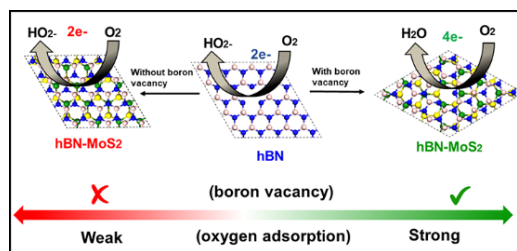
65. Zhou, J., Xiao, H., Zhou, B., Huang, F., Zhou, S., Xiao, W. and Wang, D., *Applied Surface Science*, 2015, 358, pp.152-158.
66. Illathvalappil, R., Unni, S.M. and Kurungot, S., *Nanoscale*, 7(40), 2015, pp.16729-16736.
67. Khan, A.F., Randviir, E.P., Brownson, D.A., Ji, X., Smith, G.C. and Banks, C.E., *Electroanalysis*, 2017, 29(2), pp.622-634.
68. He, L., Cui, B., Liu, J., Wang, M., Zhang, Z. and Zhang, H., *ACS Sustainable Chemistry & Engineering*, 2018, 6(7), pp.9257-9268.
69. Bach, L.G., Thi, M.L.N., Bui, Q.B. and Nhac-Vu, H.T., *Synthetic Metals*, 2019, 254, pp.172-179.
70. Mao, J., Liu, P., Du, C., Liang, D., Yan, J. and Song, W., *Journal of Materials Chemistry A*, 2019, 7(15), pp.8785-8789.
71. Huang, H., Feng, X., Du, C., Wu, S. and Song, W., *Journal of Materials Chemistry A*, 2015, 3(31), pp.16050-16056.
72. Cao, D., Lu, G.Q., Wieckowski, A., Wasileski, S.A. and Neurock, M., *The Journal of Physical Chemistry B*, 2005, 109(23), pp.11622-11633.
73. Bera, B., Chakraborty, A., Kar, T., Leuaa, P. and Neergat, M., *The Journal of Physical Chemistry C*, 2017, 121(38), pp.20850-20856.
74. Tammeveski, K., Kontturi, K., Nichols, R.J., Potter, R.J. and Schiffrin, D.J., *Journal of Electroanalytical Chemistry*, 2001, 515(1-2), pp.101-112.
75. Paliteiro, C., Hamnett, A. and Goodenough, J.B., *Journal of electroanalytical chemistry and interfacial electrochemistry*, 1987, 233(1-2), pp.147-159.
76. Dumont, J.H., Martinez, U., Artyushkova, K., Purdy, G.M., Dattelbaum, A.M., Zelenay, P., Mohite, A., Atanassov, P. and Gupta, G., *ACS Applied Nano Materials*, 2019, 2(3), pp.1675-1682.
77. Bichat, M.P., Raymundo-Piñero, E. and Béguin, F., *Carbon*, 2010, 48(15), pp.4351-4361.
78. Wang, S., Yu, D., Dai, L., Chang, D.W. and Baek, J.B., *ACS nano*, 2011, 5(8), pp.6202-6209.
79. Feng, H., Cheng, R., Zhao, X., Duan, X. and Li, J., *Nature communications*, 2013, 4(1), p.1539.
80. Lai, L., Chen, L., Zhan, D., Sun, L., Liu, J., Lim, S.H., Poh, C.K., Shen, Z. and Lin, J., *Carbon*, 2011, 49(10), pp.3250-3257.
81. Xu, Y., Li, J. and Huang, W., *Materials*, 2017, 10(8), p.936.
82. Su, P., Guo, H.L., Tian, L. and Ning, S.K., *Carbon*, 2012, 50(15), pp.5351-5358.
83. Rahman, O.A., Chellasamy, V., Ponpandian, N., Amirthapandian, S., Panigrahi, B.K. and Thangadurai, P., *RSC Advances*, 2014, 4(100), pp.56910-56917.
84. Dreyer, D.R., Murali, S., Zhu, Y., Ruoff, R.S. and Bielawski, C.W., *Journal of Materials Chemistry*, 2011, 21(10), pp.3443-3447.
85. Thakur, S. and Karak, N., *Carbon*, 2012, 50(14), pp.5331-5339.
86. Peng, X.Y., Liu, X.X., Diamond, D. and Lau, K.T., *Carbon*, 2011, 49(11), pp.3488-3496.
87. Vivekchand, S.R.C., Rout, C.S., Subrahmanyam, K.S., Govindaraj, A. and Rao, C.N.R., *Journal of Chemical Sciences*, 2008, 120, pp.9-13.
88. Lv, W., Tang, D.M., He, Y.B., You, C.H., Shi, Z.Q., Chen, X.C., Chen, C.M., Hou, P.X., Liu, C. and Yang, Q.H., *ACS nano*, 2009, 3(11), pp.3730-3736.
89. Lei, Z., Lu, L. and Zhao, X.S., *Energy & Environmental Science*, 2012, 5(4), pp.6391-6399.
90. Liu, Y., Li, Y., Zhong, M., Yang, Y., Wen, Y. and Wang, M., *Journal of Materials Chemistry*, 2011, 21(39), pp.15449-15455.

CHAPTER 5

Boron Vacancy: A strategy to boost the Oxygen Reduction Reaction of hexagonal boron nitride nanosheet in hBN-MoS₂ heterostructure

Abstract

Incorporation of vacancies in a system considered as proficient defect engineering in general catalytic modulation. Among the two-dimensional materials, surface active sites' deficiency and high band gap restrict hexagonal boron nitride (hBN) material's catalytic activity towards oxygen reduction reaction (ORR) which hinders its applicability in fuel cells. A *bane to boon* strategy has been introduced here by coupling two ORR sluggish materials (hBN & MoS₂) by probe-sonication method forming a heterostructure (termed as HBPS) which fosters four electron pathways assisted reduction of oxygen. Theoretical and experimental studies suggest kinetically and thermodynamically favorable boron vacancy (B-vacancy) formation in presence of MoS₂, which acts as an active site for oxygen adsorption in HBPS. B-vacancy induced uneven charge distribution together with band gap depression promote rapid electron transfer from the valance band to conduction band which prevailing over the kinetic limitation of pure hBN nanosheets towards ORR kinetics. The formed B-vacancy induced HBPS further exhibit a Tafel slope (66 mV/decade), high onset potential (0.80 V vs. RHE) with unaltered electrochemical active surface area (ESCA) after long-cycle. Thus, vacancy engineering in hBN has proved to be an efficient approach to unlock the potential of catalytic performance enhancement.



5.1. Introduction

Defect engineering is considered as a competent artistry in catalyst field as defect induced high distortion energy and diverse atomic rearrangements significantly improve the overall performance of the catalysts by providing higher active-site exposure or modulating the electronic band structure [1]. A variety of defect engineering strategies i.e., plasma treatment [2], heteroatom functionalization [3], template-based synthesis [4], controllable solvothermal growth [5], chemical etching [6], etc. are effectively utilized for achieving desired catalytic performance. A plethora of recent reports exhibit interesting electrocatalytic activities of layer materials such as, MoS₂, WS₂, MXenes which are considered as two-dimensional (2D) materials “beyond graphene” [7-9]. Although, different protocols are extensively used to promote the reaction kinetics of layered materials but their stand-alone performance in oxygen reduction reaction (ORR) is found to be trailing that of the benchmarked metallic counterparts [10]. Hence, recent research is focused on electrochemical and chemical protection of metals with atomic layers while keeping the superior electrochemical activity of underneath metal intact. Electrically non-conducting, thermally, and chemically highly stable hexagonal boron nitride (hBN) in this regard is considered as a prominent candidate although, pristine hBN is photo-/electro- catalytically inactive due to high band gap and insufficient active sites [11]. However, manipulation of electronic properties via orbital mixing (dz^2 - p_z) with the incorporated transition metals largely tailors the catalytic activity of hBN [12]. Theoretically, the band gap of hBN monolayer can be significantly reduced by introducing B- and N-vacancies or impurity defects via heteroatom doping uplifting its electrocatalytic activity [13]. However, most heteroatom doping approaches are restricted by high-temperature annealing or harsh reaction conditions. To avoid the processed gridlock, Patil et al. combined rGO with hBN to elucidate the synergetic advantages of carbon network and B-N interface. In their work, minimization of surface functional groups along with effective charge distribution in the heterostructure framework enhanced the active interface which boosts the catalytic activity of the as-prepared heterostructure towards ORR. As previously mentioned, theoretically band gap engineering by vacancy formation plays a pivotal role in uplifting hBN's performance towards ORR activity; herein we have integrated MoS₂ nanosheets with the hBN nanosheets to investigate catalytic activity towards ORR of the as prepared

heterostructure. Similar to hBN nanosheets, ORR performance of few-layer MoS₂ nanosheets is also hindered by two electron transfer pathways involving inactive basal plane which can only be stimulated by fruitful defect engineering i.e. proper surface modification [14], lower particle size [15], development of effective edge center [16] and incorporation of foreign elements [17-19].

Herein, hBN and MoS₂ nanosheets are successfully integrated (HBPS) via a facile probe-sonication mediated liquid exfoliation as depicted in Figure 5.1a. Electrochemical study clearly manifests the superior electrocatalytic performance of exfoliated HBPS with four electron transfer pathways compared to toxic peroxide formation mediated two electron pathways exhibited by individually prepared hBN and MoS₂ sheets from their bulk counterpart. Integration of MoS₂ with the prepared hBN sheets via prolonged sonication time largely facilitates the B-vacancy formation in HBPS which acts as an activation centre for oxygen adsorption in ORR kinetics. Further, theoretical investigations clearly demonstrate the formation energy of B-vacancy of pristine hBN is much higher than hBN-MoS₂ heterostructure (B_{vac}-hBN-MoS₂) which is mainly attributed to MoS₂ integration. Moreover, the MoS₂ induced B-vacancy not only provides facile charge transfer towards oxygen, it also reduces the band gap of HBPS enabling facile electron transfer from valance band to the conduction band. The enhanced electron density in conduction band accelerates the electron transfer towards the adsorbed oxygen in ORR kinetics exhibiting favourable aspects compared to other hBN and MoS₂ based composites/heterostructure. This strategy enables the intuitive design of highly active hBN based catalysts by tailoring the activity towards ORR via modulating B-vacancy amount in it. This study opens a new avenue in the development of ORR active materials from individual inactive materials.

5.2. Experimental Section

5.2.1. Reagents and chemicals

Hexagonal boron nitride (hBN) (1 µm grain size, 99% purity), Molybdenum (IV) sulphide (MoS₂), (<2 µm grain size, 98%), sodium cholate hydrate (99% purity), nafion (5 wt % solution H₂O), 20% Pt/C, potassium hydroxide (KOH, 99% purity), dimethyl-formamide (99% purity), from Merck were used for synthesis and application purposes. Deionized (DI) water was taken from a Direct-Q Millipore deionized (18 Ω at 25° C).

5.2.2. Preparation of hBN Sheet

The hBN sheet utilized throughout this work was synthesized *via* a surfactant-based liquid exfoliation, sonication, and centrifugation methodology. Liquid exfoliation was performed by adding bulk hBN powder into an aqueous solution of sodium cholate hydrate (concentration, 6 g/L) in a 100 mL beaker. The resultant dispersion was then sonicated using a probe sonicator (55% Power) for 1 hour, before a centrifugation step that was performed at 5000 rpm for 90 minutes. Following centrifugation, the corresponding supernatant was discarded and the resulting sediment was re-dispersed into Deionized water (2 g/L, 100 mL). Next, the solution was probe sonicated using a probe sonicator (PKS-750FM, max. power rating-15000 watt) for 5 hours. Upon completion of the sonication treatment, the solution was separated into 20 mL aliquots before each sample was centrifuged at 2000 rpm for 90 mins (separately). The sediment from this process contained un-exfoliated hBN that was consequently discarded. The remaining supernatant was subjected to a further centrifugation period at 5000 rpm for 90 minutes. Finally, the forthcoming supernatant was removed and found to contain the hBN sheet nanosheets that are utilized herein.

5.2.3. Preparation of hBN and MoS₂ heterostructure (HBPS)

10 mg of hBN sheet and 10 mg of bulk MoS₂ powder was mixed with 40 ml of *N, N*-dimethyl formamide (DMF) and the mixture was stirred for 10 minutes at room temperature. The mixture was kept in probe sonicator and sonicated for 10 hours at 30°C (55% Amplitude). The solution was then centrifuged at 1500 rpm for 30 min. The as-obtained residue at the bottom of the centrifuge was filtered under vacuum and dried at 60°C to obtain HBPS (Figure 5.1a).

5.2.4. Preparation of MoS₂ (MS)

The procedure to prepare MS is the same as HBPS without adding the hBN sheet.

5.2.5. Characterization

The diffraction patterns of all the synthesized powder samples were obtained from a Rigaku MiniFlex powder X-ray diffractometer over the scattering angle range $15^\circ \leq 2\theta \leq 80^\circ$ in steps of 0.02° using monochromatic CuK α radiation at a measuring speed of $0.5^\circ \text{ min}^{-1}$. The crystalline structures were refined by Rietveld's method using a pseudo-Voigt function to fit peak-profiles employing the FULLPROF program [20]. Morphology was studied using a field emission

scanning electron microscope (FESEM, Hitachi S-4800), high-resolution transmission electron microscope (JEOL 2100) operated at 200 kV. X-ray Photoelectron Spectroscopy (XPS) using a monochromatic Al K_{α} X-ray source ($h\nu = 1486.6$ eV) and a hemispherical analyzer (SPECs HSA 3500), Fourier transformed infrared spectrophotometer (FTIR-8400S), Raman/AFM spectrometer (Witec Alpha300R, $\lambda_{\text{ex}} = 532$ nm) for structural and compositional analysis. Absorption maxima were determined by UV–Vis spectrophotometer (Shimadzu UV-3600). The Brunauer–Emmett–Teller (BET) surface area of the heterostructures was examined with a Quantachrome NovaWin2 Instrument at 77K.

5.2.6. Theoretical methods

All the first principles calculations were carried out using Vienna ab-initio simulation package (VASP) [22,23]. Generalized gradient approximation (GGA) along the projector augmented wave (PAW) approach was implemented during the geometry optimizations [24]. The exchange correlation terms of the energy Hamiltonian were dealt with the Perdew–Burke–Ernzerhof (PBE) functional as implemented in VASP [25]. Vacuum slab of length 24 Å was positioned in the direction normal to the 2D plane of the systems to ward off any spurious interaction. Γ centered ($7 \times 7 \times 1$) k-point mesh was used during the geometry optimization of the pristine systems whereas Γ centered ($1 \times 1 \times 1$) k-point mesh was used for the sufficiently large heterostructure. For density of states calculations, k point meshes of ($30 \times 30 \times 1$) and ($7 \times 7 \times 1$) were utilized for Brillouin zone integration of the pristine unit cells and the heterostructure system respectively. The effects of dispersive forces were taken into account via the DFT+D2 force field (Grimme's) method [26]. All the calculations were done in spin unrestricted manner. We have further investigated the origin of boron (B) vacancy formation in the h-BN-MoS₂ heterostructure system by means of first principles calculations. The h-BN-MoS₂ heterostructure was made using a (5×5) and a (4×4) supercell of h-BN and MoS₂ unit cells respectively to minimize the strain on each layer. One boron atom was removed from the heterostructure and the defected system was allowed to relax completely. A mono-boron vacancy was similarly created in a free-standing h-BN monolayer of same dimension as in the heterostructure. The neutral boron vacancy formation energies were calculated using the following equation:

$$E_f = E_v - E_p + n_B \mu_B \quad (5.1)$$

Where E_f is the vacancy formation energy, E_v is the energy of the system with boron vacancy, E_p is the energy of the pristine system, n_B is the number of boron atoms removed from the pure host and μ_B is the chemical potential of boron. μ_B was calculated from the rhombohedral α -boron system as reference. Lower formation energy as calculated using the eqn. (5.2) indicates better stability of the system after vacancy formation. Bader charge analysis was used to calculate the charge transfer between the atoms with and without the presence of boron vacancy [27]. The efficiency of the heterostructure was evaluated in terms of free energy and the free energy difference value for each ORR intermediate step was calculated using the following equation:

$$\Delta G = \Delta E + \Delta ZPE - T\Delta S, \quad (5.2)$$

where, ΔE is the enthalpy of the reaction, ΔZPE is the zero point energy correction term which is ignored in our calculations due to its insignificant contribution to the free energy in general and $T\Delta S$ is the entropy temperature term the value of which for gas phase molecules were taken from standard physical chemistry table [28]. The free energy of coupled proton and electron ($H^+ + e^-$) was calculated as suggested by Norskov et. al in their pioneering work [28].

The adsorption energies of di-oxygen molecule on the catalyst surface were calculated using the following formula

$$E_{ads} = E_{P+O_2} - E_P - E_{O_2} \quad (5.3)$$

Where E_{ads} is the di-oxygen molecule adsorption energy, E_{P+O_2} , E_P and E_{O_2} are the ground state energy of the O_2 adsorbed system, pristine catalyst, and free O_2 molecule respectively.

5.2.7. Electrochemical measurement

Electrochemical measurements are discussed in electrochemical characterization chapter 3.

CV has measured before and after the long-time durability (3.5 hours) at a non-faradic region to calculate the double-layer capacitance (C_{dl}) and electrochemically active surface area (ESCA).

The ESCA is proportional to double-layer capacitance (C_{dl}) which is determined by CV at a non-Faradic region in 0.1 (M) KOH solution under different scan rates from 10 to 100 mV/s. The relationship between ESCA and C_{dl} is as follows [29,30]:

$$ESCA = \frac{C_{dl}}{C_s} \quad (5.4)$$

Where C_s is the specific capacitance which is $40 \mu\text{F}/\text{cm}^2$ per cm^2 for the flat electrode. The C_{dl} has calculated by plotting between ΔJ (mA/cm^2) ($J_{\text{Anodic}} - J_{\text{Cathodic}}$) vs. scan rate at a fixed potential 0.95 V vs. RHE.

5.3. Results and Discussions

5.3.1. Phase purity, composition, structure, and morphological investigations

X-ray diffraction and Rietveld refinement were carried out of commercial hBN powder, hBN sheet, and HBPS to determine phase purity, crystallinity, atomic positions, degree of stoichiometry, and detailed lattice parameters (Figure 5.1b-d). For, the better clarity diffraction pattern of virgin MoS_2 synthesized via probe sonication (MS) has also been carried out. HBPS have produced major XRD peaks at 14.39° , 39.67° , 41.72° , corresponding to the reflection planes (002), (100), (105) of 2H type of MoS_2 respectively. Moreover, the (002) plane originates from hBN was positioned at $2\theta \sim 26.74^\circ$ ($d=3.33\text{\AA}$) in case of HBPS, which validates the hBN/ MoS_2 heterostructure formation. The obtained atomic occupancies from Rietveld refinement clearly reveal the presence of point defects in all three systems *viz.* bulk hBN, hBN sheet, and HBPS heterostructure (Table 5.1) [31,32]. From Table 5.1, the estimated off-stoichiometry parameter (δ) for $\text{hB}_{(1-\delta)}\text{N}$ follows an increment tendency from hBN bulk (0.0570), hBN sheet (0.0765) to HBPS (0.2884). MoS_2 assisted prolonged sonication time triggers more point-defects in HBPS compared to hBN sheets, manifesting large B-vacancy which plays a pivotal role in the formation of highly non-stoichiometric heterostructure. Thus, the boron deficiency has significantly enhanced for hBN sheets ($\sim 7\%$) from bulk counterparts (5%) and maximized to HBPS (28%). The deficiency of boron atom commensurately inflicts rise in the micro-strain levels of HBPS. Nevertheless, the stoichiometry remains unaltered for Mo and S (1:2) in HBPS. From XPS analysis, the Mo 3d core level spectrum can be well resolved with two spin-orbit doublets corresponding to $\text{Mo}^{4+} 3d_{5/2}$ (228.6 eV) and $\text{Mo}^{4+} 3d_{3/2}$ (231.7 eV) of HBPS (Figure 5.1e). In case of B 1s (Figure 5.1f), the major peak is observed at 189.8 eV, along with a tiny shoulder peak at 192 eV corresponding to B-N bond and B-OH bond of hBN respectively (table-5.2) [10, 33]. From XPS survey analysis, the estimated atomic percentage of boron is quite low to 17% in comparison with nitrogen content (22.27%) (Figure 5.1g). The percentage of boron vacancy has become 24% for hBN counterpart in HBPS. Thus, type of non-stoichiometry in HBPS is well-

correlated with the previously discussed Rietveld refinement where the percentage of boron atoms remains almost same in both the analyses. Similarly, in N 1s spectrum a dominant peak at 397.1 eV was observed which is well matched with the conventional B-N bond of hBN (Figure 5.2).

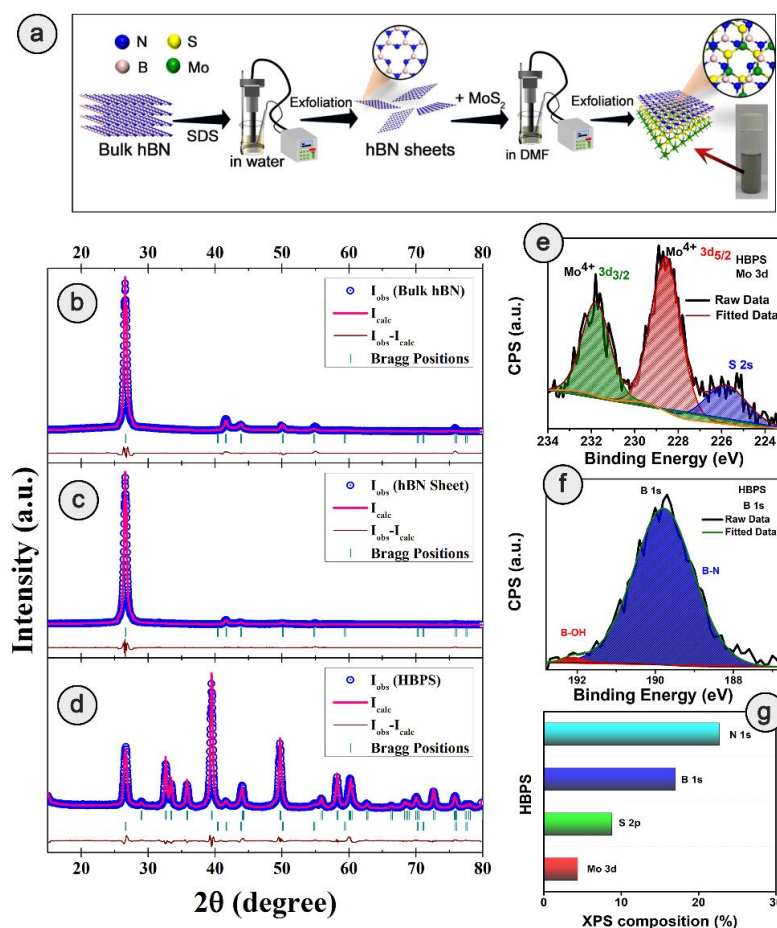


Figure 5.1: (a) Schematic of synthesis process of hBN 2-H MoS₂ heterostructure; Powder X-ray diffraction patterns and associated Rietveld refinement for (b) Bulk hBN, (c) hBN nanosheets, and (d) hBN/MoS₂ heterostructure (HBPS). The pink curve is the best fit obtained for the experimental diffraction traces (open blue circles). The green vertical lines represent the positions of the Bragg peaks and the maroon curve indicates the difference between the experimentally obtained intensities and calculated values. High resolution X-ray photoelectron spectroscopy (XPS) spectra of (e) Mo 3d (f) B 1s. (g) Different atomic percentages of HBPS from XPS survey analysis.

Sample Name	Atom	x	y	z	Atomic Occupancy	Lattice parameters (Å)		Strain (η %)	Off-stoichiometry parameter (δ) for $hB_{(1-\delta)}N$	χ^2	Space-group	
						a = b	c					
Bulk hBN	B	0	0	1/2	0.8337	2.506320	6.703041	0.0438	0.0570	1.36	P – 6m2 (No. 187) and Z = 2 $\alpha = 90^\circ, \beta = 90^\circ$ & $\gamma = 120^\circ$	
	B	1/3	2/3	0	0.92815							
	N	0	0	0	0.98791							
	N	1/3	2/3	1/2	1.00080							
hBN Sheet	B	0	0	1/2	0.75435	2.505496	6.703004	0.0487	0.0765	1.49		
	B	1/3	2/3	0	1.04117							
	N	0	0	0	0.93547							
	N	1/3	2/3	1/2	1.18449							
HBPS heterostructure	B	0	0	1/2	0.71388	2.505496	6.703001	0.0564	0.2884	1.67		
	B	1/3	2/3	0	0.52075							
	N	0	0	0	1.48826							
	N	1/3	2/3	1/2	1.42849							
	Mo	1/3	2/3	1/4	0.07653	3.168793	12.327536	0.0202			P 63/mmc	
	S	1/3	2/3	0.623	0.14938							

Table 5.1. Refined crystallographic parameters obtained from XRD analysis.

Element Spectrum	Components	Position (eV)	Atomic %
Mo 3d	Mo 3d _{5/2}	231.7	52%
	Mo 3d _{3/2}	228.6	38%
	2S	225.3	18%
S 2p	S 2p _{1/2}	163	27.33%
	S 2p _{3/2}	161.7	72.67%
B 1s	B-N	189.8	98.85%
	B-O	192	1.15%
N 1s	B-N	397.1	95.69%
	Mo 3p _{3/2}	394.5	4.31%

Table 5.2: Different percentages of components deconvoluted from Mo 3d, S 2p, B 1s, and N 1s respectively of HBPS from XPS analysis.

Elements	Mo 3d	S 2p	B 1s	N 1s	O 1s	C 1s
% components	4.38%	8.8%	17%	22.27%	12.65%	33.5%

Table 5.3: Different percentages of components of HBPS from XPS survey analysis.

In addition, a small peak positioned at 394.5 eV was also detected which is originated due to the Mo 3P_{3/2}. The absence of any other well-resolved peak in N 1s strongly eliminates any type of chemical bonding between Mo and N in HBPS heterostructure (Table- 5.2) [34]. Additionally, HBPS constitutes weak Mo-S vibrations at 469 cm⁻¹ which confirms the presence of MoS₂ in the prepared heterostructure (Figure 5.2a) [35]. The presence of the B-O bond infers the functionalization of exfoliated hBN sheets with the negatively charged hydroxyl group due to prolonged sonication in aqueous dispersion of Sodium cholate. High chemical potential induced sodium and hydroxyl ions facilitate their adsorption into the interlayer space of hBN, diminishing the interlayer interaction. Moreover, from FTIR study a broad hump around 3300-3400 cm⁻¹ with small peaks observed at around 1350 cm⁻¹ and 809 cm⁻¹ corresponding to OH group, B-N stretching, and bending vibrations of HBPS respectively (Fig. 5.2d) [36].

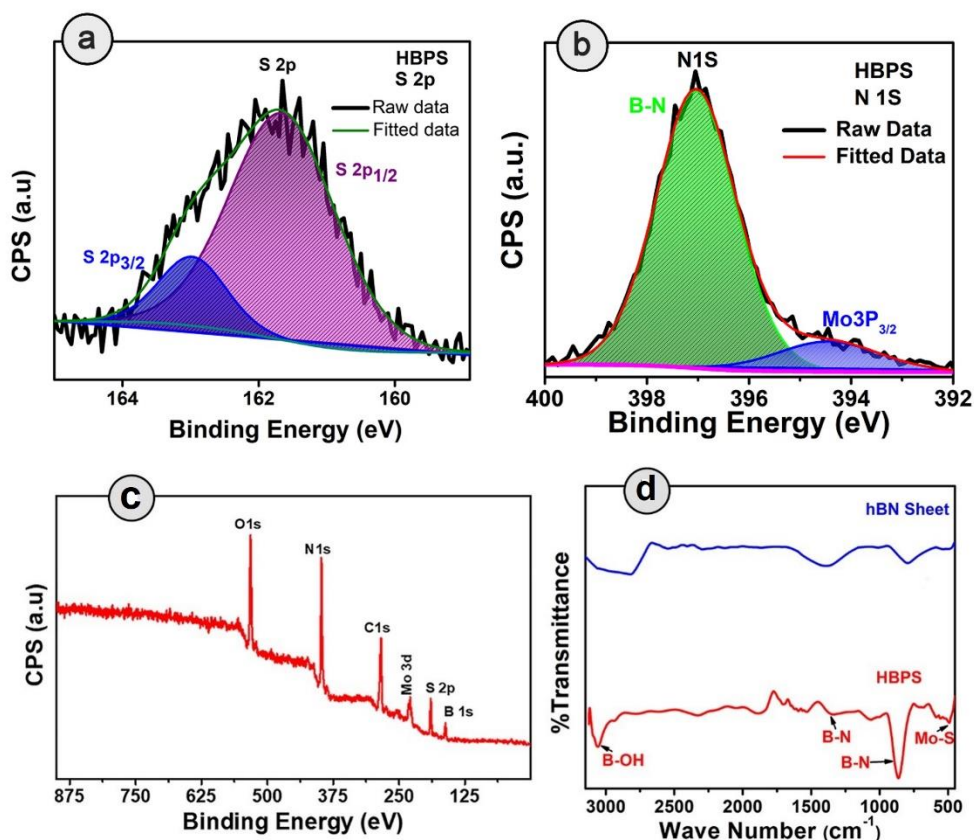


Figure 5.2: High resolution X-ray photoelectron spectroscopy (XPS) spectra of (a) S 2p (b) N 1s of HBPS. (c) X-ray photoelectron spectroscopy (XPS) survey of HBPS (d) FT-IR spectra of hBN sheet, and HBPS.

This synergetic effect accelerates the self-curling process to a great extent which in turn boosts the exfoliation of bulk counterpart to sheets [37]. Figure 5.3 shows FESEM images of HBPS reveal thick MoS_2 sheets rather than flower type morphology. The inhomogeneous distribution of the distorted few layers of hBN sheet has decorated on the surface of MoS_2 sheets. Elemental mapping via EDX clearly validates our afore-mentioned conclusion of hBN sheet decoration on exfoliated MoS_2 nanosheets (Figure. 5.3).

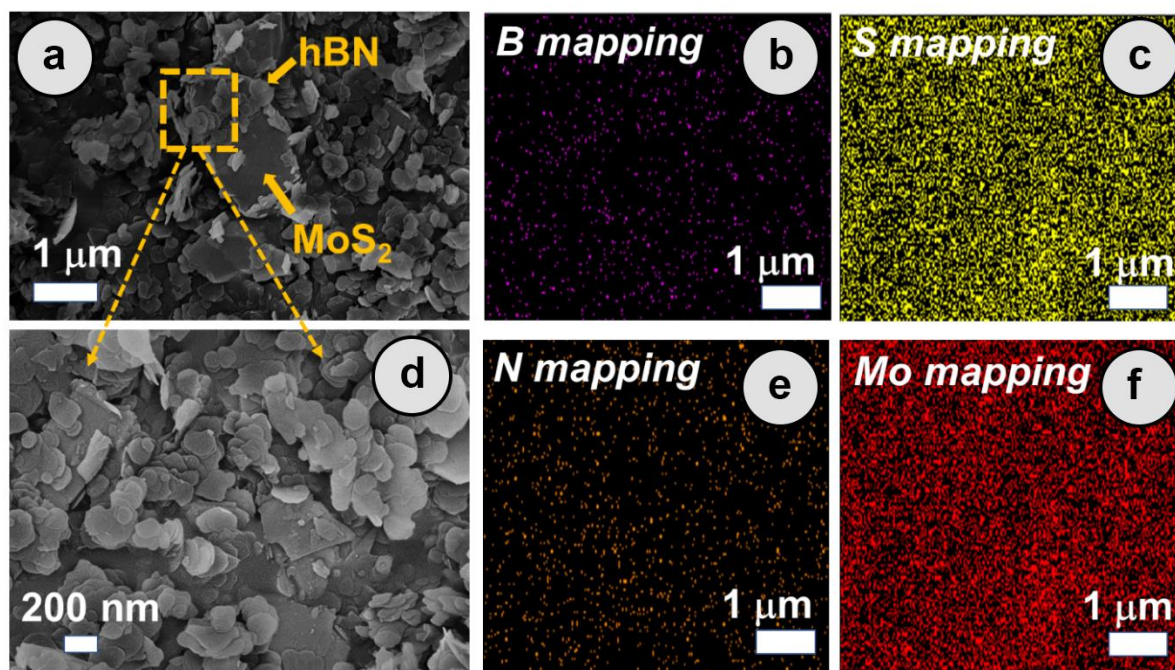


Figure 5.3: (a,b) FESEM Image of HBPS. (c-f) EDX mapping of HBPS containing Boron, sulfur, Nitrogen, and Mo.

Further insight regarding the morphology and lattice parameters have been determined from High Resolution Transmission electron microscopy (HRTEM) analysis. The low magnification image exhibits the ultralow thickness of the synthesized hBN sheets (Figure 5.4). The average lateral size is around 156 nm per nanosheet (calculated by *Image J* software). Clear lattice fringe pattern of the Synthesized hBN has been also captured using high magnification which is further processed by Inverse Fast Fourier transform (IFFT) by *Image J* to measure actual inter-planar distance more accurately. The calculated inter-planar distance is 3.3 Å corresponding to (002) plane of hBN sheet (Figure 5.4). Figure 5.5 elucidates the TEM image of HBPS where the ultrathin hBN sheet is decorated on relatively large MoS_2 sheets. Lattice fringes with an interplanar spacing of 0.61 nm are well matched with the (002) plane of MoS_2 in HBPS (Figure

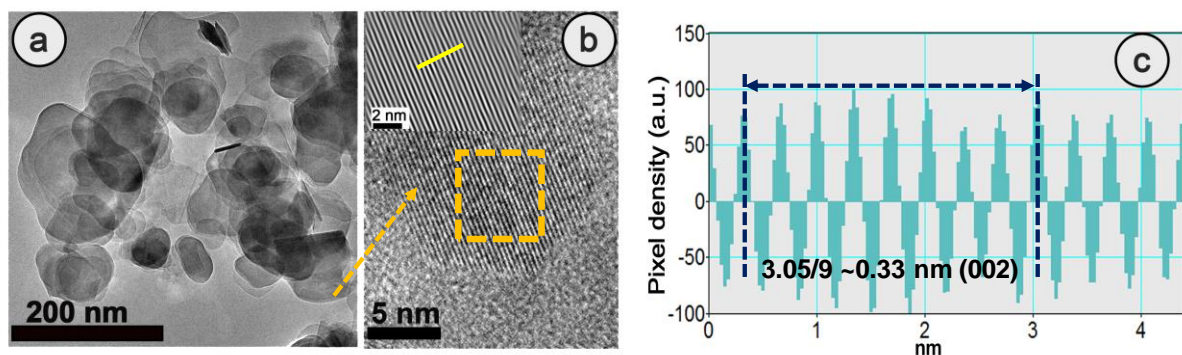


Figure 5.4: a) HRTEM image of hBN sheet (b) Fringe pattern of hBN sheet (c) Inverse fast Fourier transformation (IFFT) indicates (002) plane of hBN sheet.

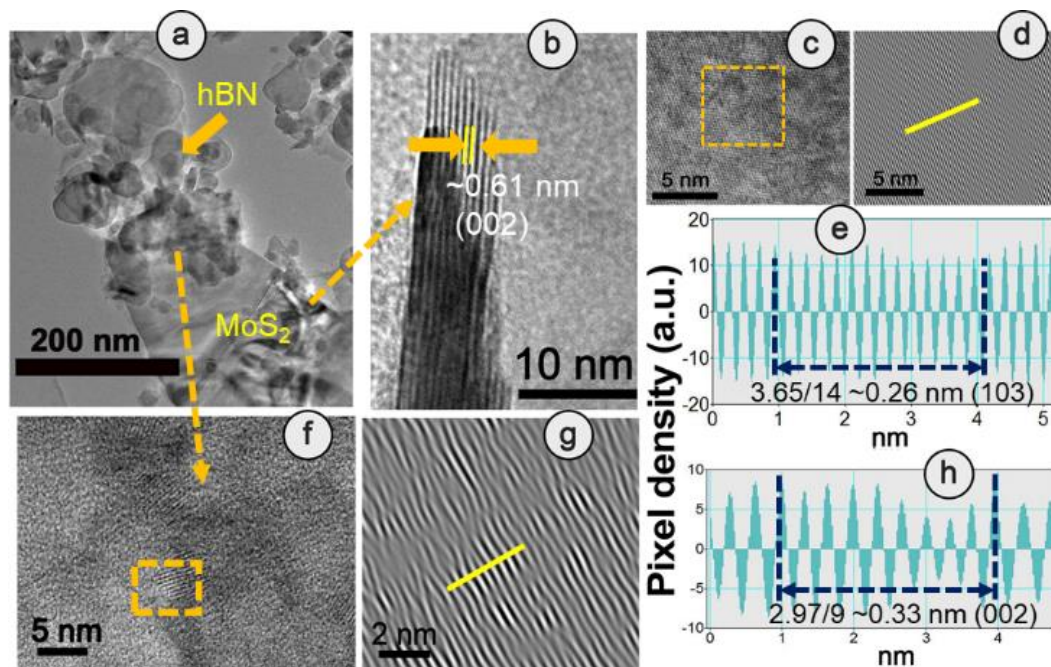


Figure 5.5: a) HRTEM image and Fringe pattern correspond to (b) (002) and (c,d) (103) plane of MoS₂ (e) IFFT analysis of (103) plane of MoS₂ counterpart in HBPS (f,g,h) Fringe pattern and IFFT analysis of (002) plane of hBN counterpart in HBPS.

(Figure 5.5d,g) of the HRTEM images was carried out via *Image J* software to obtain accurate lattice spacing. The calculated d values are 0.26 nm and 0.33 nm which are well-matched with the (103) plane of MoS₂ and (002) plane of hBN respectively of HBPS (Figure 5.5e,h). Thus, the lattice spacing of hBN and MoS₂ remains unaltered with respect to XRD analysis in the HBPS heterostructure formation.

5.5). Moreover, the IFFT analysis Raman spectra suggest the in plane E_{2g} mode of MoS_2 in HBPS positioned at 384 cm^{-1} with an energy separation of 24.7 cm^{-1} from out of plane A_{1g} mode which implies a diminution in layer number as well as shrinkage in the interlayer coupling compared to bulk MoS_2 (Figure 5.6a). Observed redshift (1.3 cm^{-1}) of A_{1g} mode in HBPS (408.7 cm^{-1}) compared to pristine MoS_2 's (MS) A_{1g} mode (410.12 cm^{-1}) furthermore confirms a synergistic interaction between hBN and MoS_2 (Figure 5.6b). Notably, no characteristic peaks (J1, J2, and J3) at 150 cm^{-1} , 219 cm^{-1} , and 327 cm^{-1} conclude the exfoliated MoS_2 are purely 2H form instead of metallic 1T phase [38].

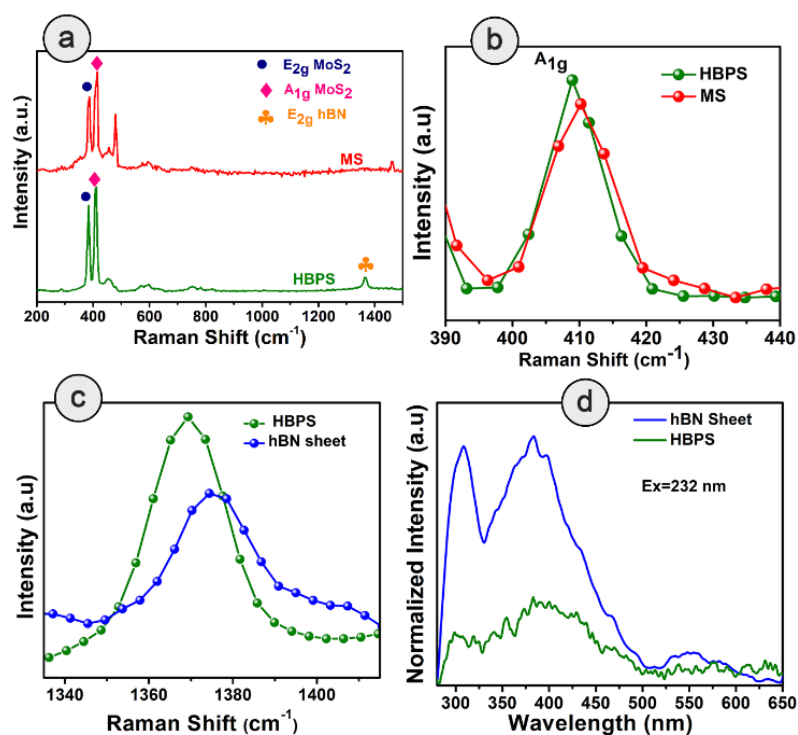


Figure 5.6: Raman spectra of (a) HBPS, and hBN sheets under a 532 nm laser source. (b) Raman shift of A_{1g} of HBPS compared to MS. (c) Shifting the peak position of E_{2g} mode of hBN site of hBN sheet and HBPS. (d) Photoluminescence (PL) spectra of hBN sheet, HBPS under excitation at 232 nm.

Thus, in the case of HBPS Columbic force predominates over interlayer coupling prevailing a shrinkage in separation of E_{2g} and A_{1g} phonons to 24.7 cm^{-1} whereas in MS both two aforementioned factors play a stipulated role in preserving the separation to 26 cm^{-1} . Raman mode (E_{2g}) of hBN was also observed in HBPS at around $1365\text{--}66 \text{ cm}^{-1}$. Compared to heterostructure,

a blue shift in E_{2g} mode has been determined at 1374 cm^{-1} of hBN sheet [7]. The significant blue shift is mainly due to distorted surface and thinner sheet of hBN sheet (Figure 5.6c) [39]. Photoluminescence (PL) measurement indicates two broad emission peaks centered at 308 nm (4 eV) and 383 (3.32 eV) under the 232 nm excitation by the exfoliated hBN sheets which are well-corroborated with the previous reports [40,41]. However, a significant PL quenching was observed in the case of HBPS (Figure 5.6d). The PL quenching phenomenon and Raman analysis validate a strong interaction between hBN and MoS_2 in HBPS [42,43].

5.3.2. Electrochemical (ORR) performance study

ORR activities were studied through linear sweep voltammograms (LSVs) at 1600 rpm using rotating disk electrode technique (RDE) (Figure 5.7). HBPS exhibits quite similar onset potential ($\sim 0.80\text{ V}$ vs. RHE) with the commercial electrocatalyst 20% Pt/C ($\sim 0.82\text{ V}$ vs. RHE). The E_0 follows a gradual decrement tendency from HBPS to hBN sheets (0.65 V vs. RHE), MS (0.60 V vs. RHE) (Figure 5.7a-c). Additionally, a significant shift towards positive potential from hBN sheet (0.51 V vs. RHE) to HBPS (0.60 V vs. RHE) of the half wave potential ($E_{1/2}$) is observed.

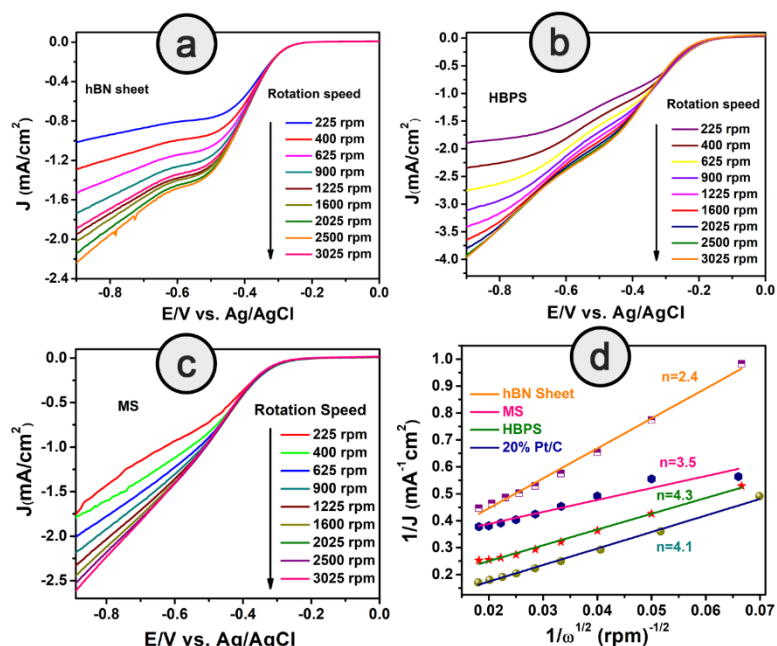


Figure 5.7: Linear sweep voltammogram of (a) hBN sheet (b) HBPS (c) MS in 0.1 (M) KOH at a scan rate 10 mV/s with different rotation speed (225-3025 rpm) via rotating disk electrode (RDE). (d) Koutecky-Levich (K-L) plot of 20 % Pt/C, hBN sheet, HBPS, MS at the different potential at -0.8 V vs. Ag/AgCl.

Moreover, the limiting-diffusion current density (J_L) at 1600 rpm is drastically truncated for hBN sheet (1.8 mA/cm^2), MS (2.5 mA/cm^2), compared to 3.6 mA/cm^2 of HBPS at -0.8 V vs Ag/AgCl. The demonstrated linear fitting of the Koutecky-Levich (K-L) plots of all the synthesized samples at different potentials reveals 1^{st} order reaction kinetics (Figure 5.7d & 5.8).

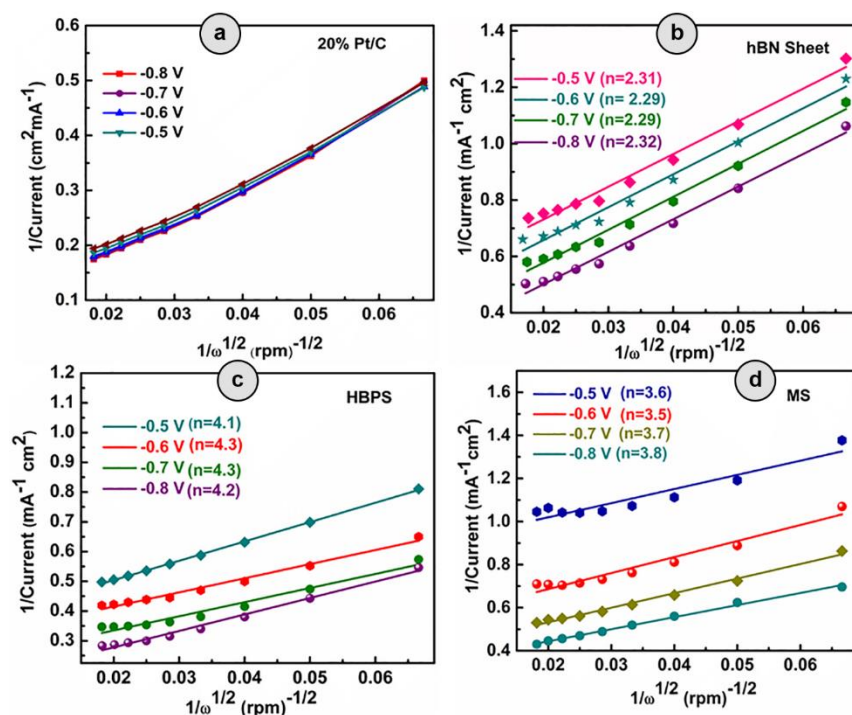


Figure 5.8: Koutecky-Levich (K-L) plot of (a) 20% Pt/C (b) hBN sheet (c) HBPS (d) MS at different potentials from -0.8 V to -0.5 V vs. Ag/AgCl.

Generally, in case of MoS_2 two reduction peaks at -0.790 V and -0.047 V vs. Ag/AgCl which implies two steps two electron reduction process [44]. The positive shift of these two reduction peaks implies facile ORR activity. In our study, the intense cathodic ORR peak (E_{ORR}) has been positioned at -0.280 V vs. Ag/AgCl (0.625 V vs. RHE) for HBPS which is 127 mV and 102 mV more positive than MS (-0.407 V vs. Ag/AgCl, 0.49 V vs. RHE) and hBN sheet (-0.3835 V vs. Ag/AgCl, 0.52 V vs. RHE) respectively (Figure 5.9a). The second reduction peak is positioned at -0.6 V vs. Ag/AgCl which becomes 200 mV more positive than MS. Additionally, with the positive shifting of E_{ORR} , the corresponding current density is increased (0.34 mA/cm^2) compared to the MS (0.16 mA/cm^2) and hBN sheet (0.24 mA/cm^2), indicating the efficacy of HBPS over the individual pristine materials and previously MoS_2 based catalysts (table 5.4). Figure 5.9a

Catalyst	Electrode & Electrolyte	E _{ORR} (V)	E _{Onset} (V)	J _L at 1600 rpm	n	Ref.
2D-hBN/RGO	GC* & 0.1 M KCl	-	0.798 V vs. RHE	-3 mA/cm ²	3.7	45
Surfactant-exfoliated 2D hBN	SPE [#] & 0.1 (M) H ₂ SO ₄	-0.71 V vs. SCE	-	-	-	46
Nitrogen-doped MoS ₂ /carbon	GC & 0.1 M KCl	-	-	-2.78 mA/cm ²	-	47
2D-MoS ₂	SPE & 0.1 (M) H ₂ SO ₄	-0.53 V vs. SCE	0.16 V vs. SCE	-	4	48
Nb doped MoS ₂	GC & 0.1 (M) KOH	0.61 V vs. RHE	0.78 V vs. RHE	-	-	49
AuNP/MoS ₂	GC & 0.1 (M) KOH	-0.41 V vs. SCE	-0.12 V vs. SCE	-3 mA/cm ²	-	50
MoS ₂ -rGO Nanosheets	GC & 0.1 (M) KOH	-	0.8 V vs. RHE	-2.72 mA/cm ²	3.3	51
Co(OH) ₂ -MoS ₂ /rGO	GC & 0.1 (M) KOH	0.7 V vs. RHE	0.805 V vs. RHE	-4.1 mA/cm ²	3.2-3.6	52
2D-hBN	SPE & 0.1 (M) H ₂ SO ₄	-0.81 V vs. SCE	-	-	2.45	53
MoS ₂ Quantum Dots	GC & 0.1 M NaOH	-0.5 V vs. Ag/AgCl	0.27 V vs. RHE	-1.4 mA/cm ²	1.8	54
CoOx/mC@MoS ₂	GC & 0.1 (M) KOH	-	0.67 V vs. RHE	-2.4 mA/cm ²	2.68-3.2	55
PdxSy-MoS ₂ /N-GR	RDE ^{\$} & 0.1 (M) KOH	-	-0.242 V vs. SCE	-4.2 mA/cm ²	3.75-3.8	56
Porus BCN catalyst	GC & 0.1 (M) KOH	0.8 V vs. RHE	0.94 V vs. RHE	-5 mA/cm ²	3.93	57
O-MoS ₂ -87	GC & 0.1 (M) KOH	-	0.94 V vs. RHE	-3.1 mA/cm ²	4	58
Nanostructured MoS ₂	GC & 0.1 (M) KOH	-	-0.14 V vs. Ag/AgCl	-2.4 mA/cm ²	-	59
hBN/MoS₂ (HBPS)	(GC) & 0.1 (M) KOH	-0.28 V vs. Ag/AgCl (0.63 V vs. RHE)	0.80 V vs. RHE	~3.70 mA/cm²	~4.1	This Work

Table 5.4: Comparison of ORR Performance of different 2D materials.

*GC: Glassy Carbon; #SPE: screen-printed graphite electrode; \$RDE: Ring disk electrode.

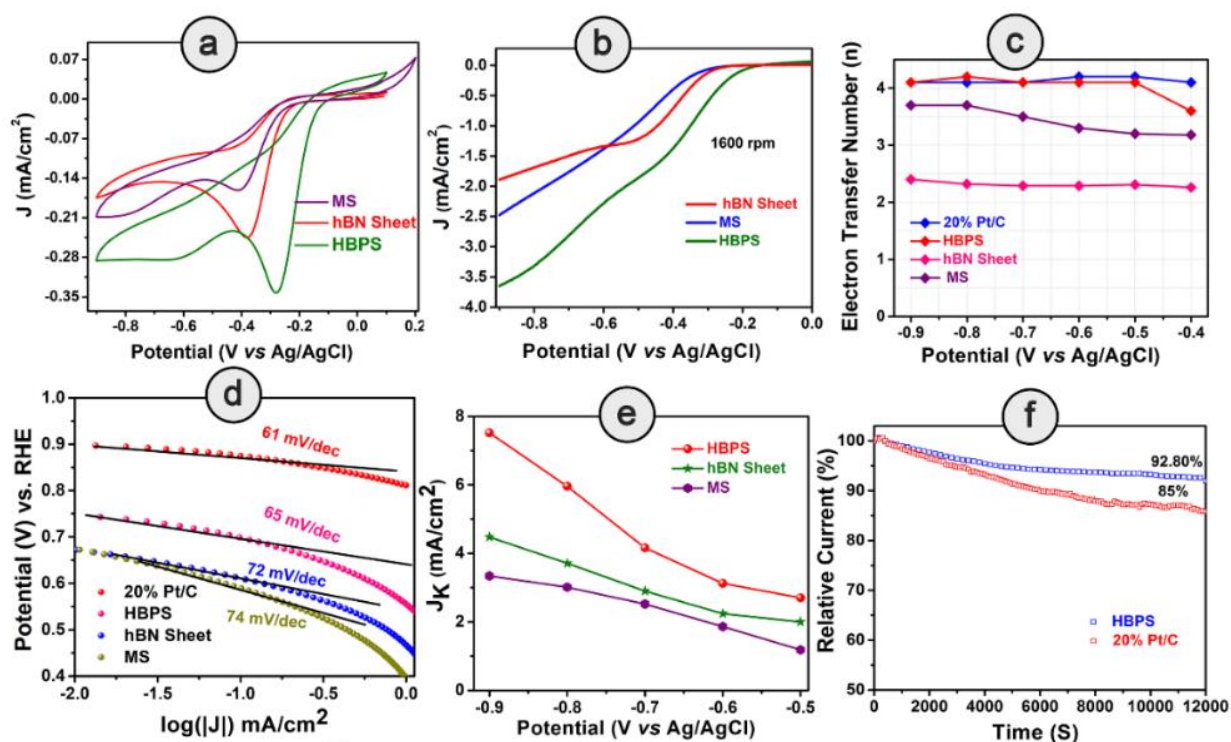


Figure 5.9: HBPS, MS and hBN sheet in O_2 saturated solution in 0.1 (M) KOH at 10 mV/s scan rate (a) Cyclic voltammogram of (b) Linear sweep voltammogram at 1600 rpm via rotating disk electrode (RDE) (c) Electron transfer number (n) from RDE measurement in potential -0.9 to -0.4 V (vs. Ag/AgCl) (d) Tafel plot of 20% Pt/C, HBPS, MS, hBN sheet (e) Variation of kinetic current Density (J_k) with potential range -0.9 V to -0.5V (vs. Ag/AgCl) of HBPS, hBN sheet, and MS (f) Chronoamperometry measurement of 20% Pt/C and HBPS in O_2 saturated 0.1 (M) KOH at -0.3 V vs. Ag/AgCl under 1600 rpm for 12000 s.

suggests E_{ORR} -0.16 V vs. Ag/AgCl (0.745 vs. RHE) of 20 % Pt/C which is 120 mV positive than HBPS. Previously, Khan et al. observed a 50 mV shift of E_{ORR} due to sodium cholate mediated hBN ($E_{ORR} \sim -0.59$ V vs. SCE or ~ -0.635 V vs. Ag/AgCl) rather than pristine hBN sheet ($E_{ORR} \sim -1.09$ V vs. SCE or ~ -0.635 V vs. Ag/AgCl) although in both cases the ORR pathway follows two electron transfer process [60]. Here, the prepared hBN sheet exhibits more positive E_{ORR} reduction potential (-0.383 V vs. Ag/AgCl) compared to previously reported literature validating the contribution of surfactant in hBN sheet towards oxygen reduction kinetics. However, the observed E_{ORR} of hBN sheet is not sufficiently positive to show efficient catalytic performance towards oxygen reduction in comparison with HBPS and 20% Pt/C. Further in our investigation,

less positive E_{ORR} , E_{onset} , and lower J_L make MS a poor electrocatalyst for ORR kinetics. Thus, in Figure 5.9c, the variations of electron transfer number (n) within the potential range (-0.9 to -0.4V) are depicted which further validates, the HBPS's ability to perform as efficient catalysis by constantly following four electron pathways in the potential range. The top-notch kinetics behavior of HBPS was similarly illustrated from the quite low Tafel slope (66 mV/dec) which is analogous to 20% Pt/C (61 mV/decade) but lower than other prepared materials (Figure 5.9d & Table 5.5). In HBPS the observed Kinetic current density (J_k) was 7.52 mA/cm² where it has reduced to 4.47 mA/cm² and 3.34 mA/cm² at -0.9 V vs Ag/AgCl for hBN sheet and MS respectively (Figure 5.9e). Thus, ORR stability of the HBPS was evaluated following by chronoamperometric protocol. Figure Figure 5.9f shows the retention of relative current density is much higher in HBPS (92.80%) compared to 20 % Pt/C (85%) after 12000 s. In addition tolerance towards methanol is also a vital parameter for developing electrocatalysts as methanol and its intermediates can poison the active sites of catalysts through equilibrium loss in the electrode materials. This ruinous effect drastically decreases the energy density and increases the overpotential of the cathodic reactions restricting its overall electrochemical utilization rate [61]. HBPS has exhibited an admirable tolerance toward methanol poisoning effect compare to commercial 20% Pt/C electrode during chronoamperometric measurements when 2 M methanol (20 volume%) was injected into O₂ saturated 0.1 M KOH solution after 400s (Figure 5.10). Only 4% change was observed in the relative current of HBPS compared to 14% change in 20% Pt/C which, proves its efficacy in methanol tolerance over 20% Pt/C.

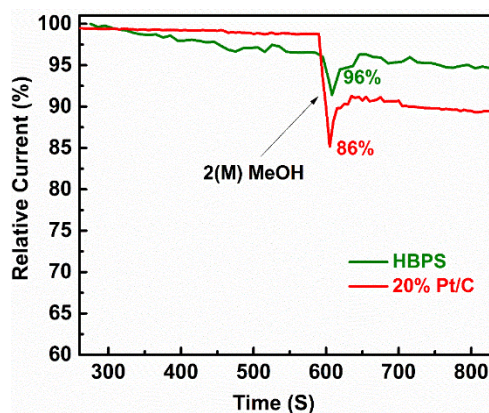


Figure 5.10: Tolerance of methanol of 20% Pt/C and HBPS at -0.3 V vs. Ag/AgCl in O₂ saturated 0.1 (M) KOH at 1600 rpm with the addition of methanol after 400 s.

From RRDE analysis, the corresponding electron transfer number (n) of hBN sheet and HBPS has been found to be two and four electron transfer pathways respectively which is consistent with prior RDE analysis. Figure 5.11 implies rotating-ring disk electrode (RRDE) measurements which illustrate negligible (12-15%) formation of OH_2^- for HBPS in the potential range from -0.8 V to -0.2 V (vs. Ag/AgCl) in comparison, the H_2O_2 yield was 65-75% for hBN sheet. Thus, B_{vac} -hBN-MoS₂ heterostructure can carry out ORR in alkaline medium in the energetically efficient four electron pathway without forming any hazardous final product like peroxide ions in contrary to the defect free one.

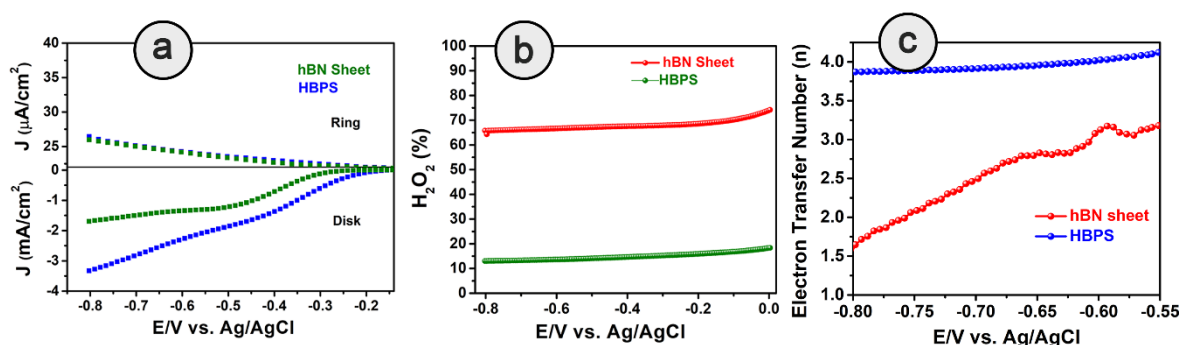


Figure 5.11: a) RRDE current-voltage curve at 25°C for 0.1 (M) KOH solution with GC electrode with rotation rate 1600 rpm. b) Percentage of H_2O_2 yield for various catalysts (C) Electron Transfer number of hBN sheet and HBPS from RRDE analysis.

Catalysts	E_{ORR} (V)	E_{Onset} (V)	J_L at 1600 rpm (mA/cm ²)	J_K at 0.1 (V) (mA/cm ²)	n	Tafel Slope (mV/Decade)
HBPS	0.63	0.80	3.6	5.96	~4.1	66
hBN Sheet	0.52	0.60	2	3.71	~2.5	72
MS	0.49	0.65	2	3.01	~3.3	74

Table 5.5: Comparison of the different parameters of ORR for all materials. All the potential has calculated in RHE.

5.3.3. Active surface sites in ORR catalysis

From Figure 5.12a-c the CVs at non-faradic regions in different scan rates were first carried out and the double layer capacitance (C_{dl}) and ESCA were evaluated. The double-layer capacitance (C_{dl}) is maximum in case of HBPS (12.3 mF/cm²) where it gradually decreases to 9.8 mF/cm² and 3.1 mF/cm² for hBN sheet and MS respectively (Figure 5.12d). As C_{dl} is directly proportional

to ESCA, the higher C_{dl} and ESCA of HBPS indicates formation of maximum active sites. Besides activity and selectivity, durability is a vital parameter for evaluating the ORR performance of electrocatalysis. Further to support the excellent durability of HBPS, C_{dl} and ESCA were also calculated after 12000s by taking CVs in the same potential window (Figure 5.12e-h). The calculated ESCA, C_{dl} , and J_L of HBPS all these parameters show minor violation from the initial values after long time durability (Figure 5.12h). The LSV of HBPS shows a negligible 3 mV degradation in $E_{1/2}$ as well as J_L after 2000 cycles (Figure 5.12i).

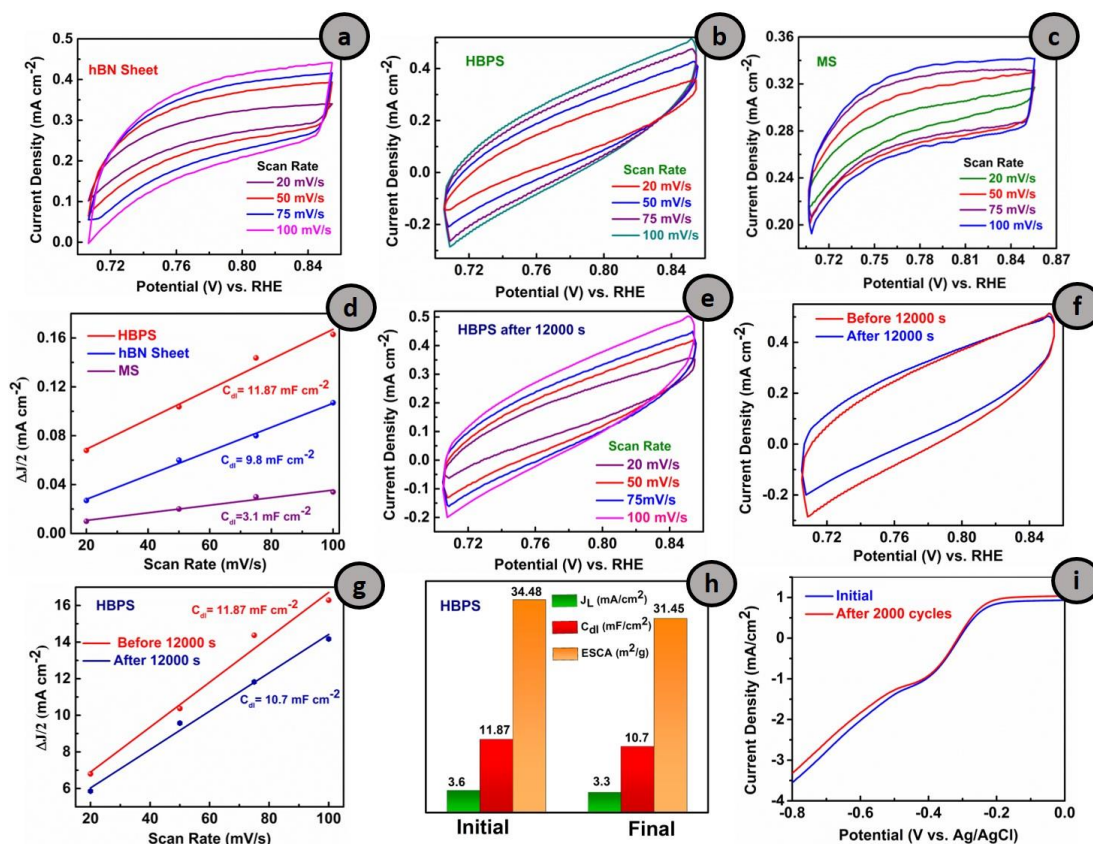


Figure 5.12. Cyclic Voltammograms of (a) hBN sheet (b) HBPS and (c) MS at non- Faradic region with scan rates 20 mV/s to 100 mV/s (d) Plot of $\Delta J/2$ vs. Scan rates to the determination of C_{dl} of hBN sheet, HBPS, and MS. Cyclic Voltammograms (CV) of (e) HBPS at scan rates 20 mV/s to 100 mV/s after durability test (f) Comparison of CV at 100 mV/s, (g) Plot of $\Delta J/2$ vs. Scan rates (h) Determination of C_{dl} , J_L and ESCA of HBPS before and after durability test of HBPS. (i) LSV measurement of HBPS at scan rate 10 mV/s in 0.1 (M) KOH at 1600 rpm initially and after 2000 cycles.

The BET surface area of HBPS and hBN sheet has been determined to a value of $99.383 \text{ m}^2/\text{g}$ and $33.350 \text{ m}^2/\text{g}$ respectively. It is obvious exfoliated MoS_2 nanosheet exhibits a quite low surface area of $8.6 \text{ m}^2/\text{g}$ [62]. The pore diameter of hBN sheet and HBPS are quite comparable to 3.5 nm and 3.2 nm respectively indicates mesopores in nature of both the prepared samples (Figure 5.13). Generally, large surface area and pore diameter have a better probability of acting as surface-active sites for oxygen adsorption. However, here larger pore size of hBN sheet in comparison with HBPS reveals the surface area and pore diameter do not act as a major role in the ORR activity of as-prepared materials. The ultrasonic treatment i.e. cavitation modulates the shear force, pressure, temperature and enhances the rate of exfoliation of the layered materials in solvents. In addition, cavitation induces structural defects, surface modification of the basal plane via B-OH bond formation promotes the layer separations from bulk hBN counterpart [63,64]. The OH functionalization weakens the B-N double bonds (due to $p\pi$ - $p\pi$ overlap) converting those bonds into single bonds. The polarity of the formed bonds particularly increases due to the presence of electronegative nitrogen and OH groups. As a result, long ultrasonication time induces boron vacancy or defects from the surface of hBN sheet.

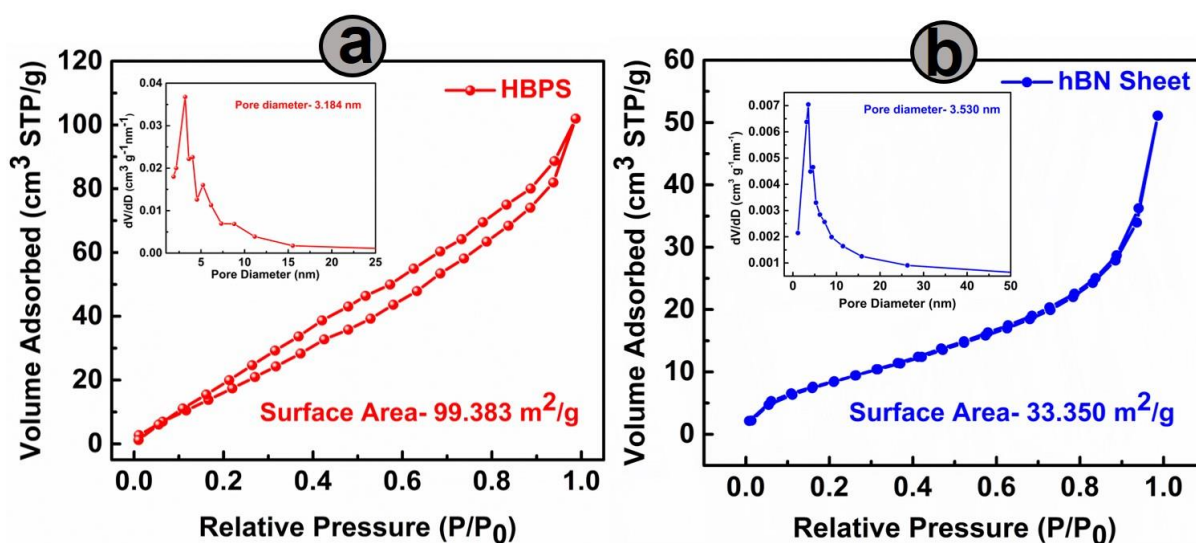


Figure 5.13: N_2 adsorption-desorption isotherm of (a) hBN sheet (b) HBPS. Inset showing the distribution of pore diameter with relative pressure.

Our Rietveld analyses suggest boron deficiency significantly enhances for hBN sheets ($\sim 7\%$) from bulk counterparts after ultrasonication. However, in presence of MoS_2 , van der Waals type

interaction occurs rather than covalent bond formation between hBN and MoS₂ sheet in HBPS which have been confirmed from multiple spectroscopic investigations i.e. XPS, RAMAN, and PL scrutiny. The shift of A_{1g} of MoS₂ from bulk counterpart clearly validates the interactions between two nanosheets. Furthermore, PL quenching of HBPS under 232 nm excitation indicates some charge transfer between two sheets (as no bond or complex formation occurs). Inter-sheet van der Waals interaction and charge transfer between hBN & MoS₂ shrink the B-N bond strength and enhance the rate of B-vacancy formation under prolonged ultrasonication.

5.3.4. Theoretical validation of electrochemical investigations

Computational investigations are further carried out to understand the role of MoS₂ in B-vacancy formation in HBPS. The aforementioned details of oxygen reduction activity clearly indicate the superior performance of HBPS compared to others. It is evident, the formed B-vacancy plays a pivotal role in ORR performance enhancement. To elucidate the effect of MoS₂ in B-vacancy formation density functional theory (DFT) calculations were performed. Lower formation energy (1.96 eV) of B-vacancy of hBN-MoS₂ heterostructure system (B_{vac}-hBN-MoS₂) compared to hBN monolayer's (2.49 eV) clearly validates MoS₂ assisted promotion of B-vacancy formation (via charge transfer & van der Waals interaction) in the hBN monolayer. Minimization of the prerequisite activation energy of oxygen for ORR to upsurge materials performance can be achieved by prompting vacancy formation or band gap depreciating which uplifts the electronic transition from valance band to conduction band [65]. In a similar fashion, Ferrari et al. show how the physical line defects (PLD) modulate the band gap of inert 2D-hBN sheets (from insulating to semiconducting) and modify the in-active surface to electrochemically active in nature [66]. From the first principles calculations, the band gap was found to be 4.56 eV, 1.59 eV, 1.66 eV, and 1.45 eV for pristine h-BN, pristine MoS₂, hBN-MoS₂ heterostructure, and hBN-MoS₂ heterostructure system with boron vacancy (B_{vac}-hBN-MoS₂) respectively (Figure 5.14a-d). It is evident from the DFT, the formed B- vacancy reduces band gap of the hBN/MoS₂ system along with a defect band formation just below the conduction band empowering swift electron transfer from the valance band to the conduction band. Normally, the B-vacancy formation in hBN not only reduces the band gap but also facilitates charge transfer and the interaction with different transition metals, activating/amplifying the catalytic efficiency of hBN towards ORR [19, 67-70]. To understand the effect of formed B-vacancy on the band gap of prepared materials,

band gap was estimated from Tauc's plot approximating the Kubelka-Munk function (Figure 5.14e,f). As exhibited, the band gap follows completely opposite trend with the increment of B-vacancy (estimated from Rietveld refinement previously). Moreover, the band gap of HBPS (4.56 eV) is lower than both bulk hBN sheets (5.7 eV) and prepared hBN sheet (5.66 eV) (Figure 5.14e,f).

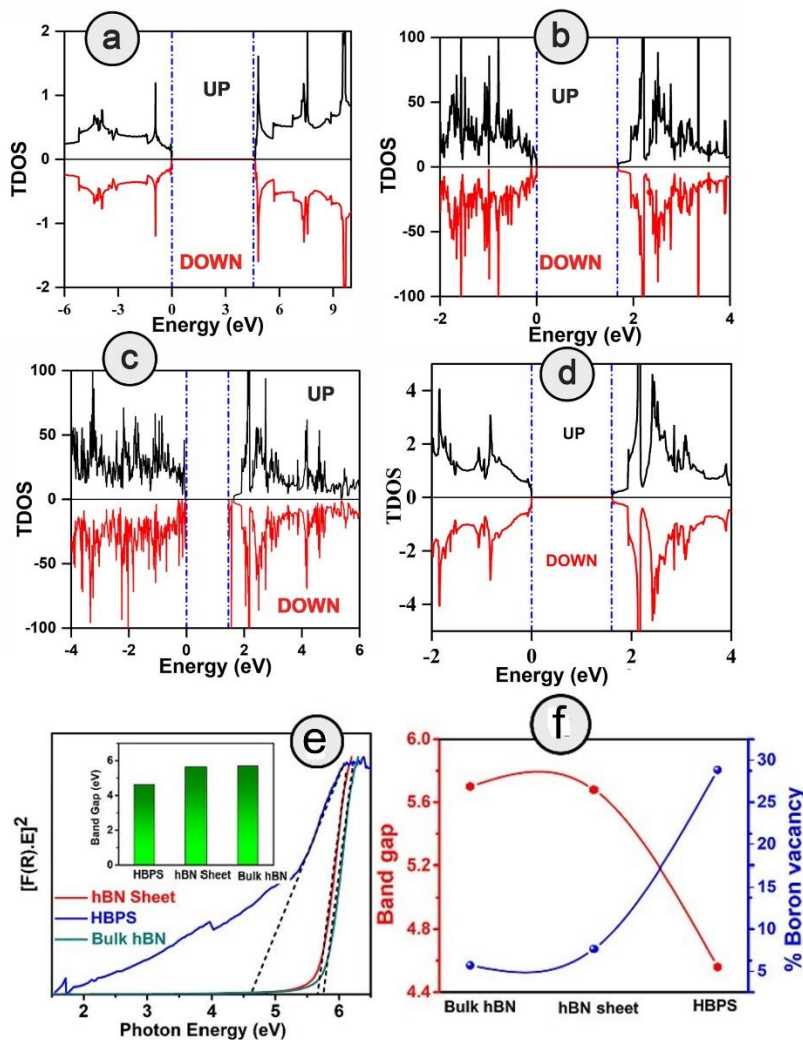


Figure 5.14: Band structure and DOS plot of (a) hBN, (b) hBN/MoS₂ heterostructure (c) B_{vac}-hBN-MoS₂ heterostructure and (d) MoS₂. (e) Tauc plots of bulk hBN, hBN sheet, HBPS (Inset showing the difference in the band gap) (f) correlation of boron vacancy on hBN with band gap.

Recently, the edge and basal plane defect enhances the electroactive area of hBN surface and promotes boosting the current density and recyclability of hydrogen evolution

formation on the charge distribution in the considered systems. All the calculated amounts of charge transferred to or from the atoms (Bader partial charge value) corresponding to the marked neighboring atoms are documented in table 5.6 and Figure. 5.15. From table 5.6, it is prominent that the incorporation of boron vacancy largely reduces the charge transfer to the three nearest-neighbour (NN) nitrogen atoms (N1, N3, N5) by $\sim 0.5 e$ in both the free-standing hBN monolayer and the B_{vac} -hBN-MoS₂ heterostructure system. This B-vacancy induced non uniform charge distribution in NN atoms of B_{vac} -hBN-MoS₂ enhances its specific activity towards ORR, while uniform charge distribution in B-vacancy free hBN-MoS₂ diminishes the catalytic activity. Undoubtedly, the possibility of B-vacancy formation is much higher in the hBN-MoS₂ heterostructure compared to the freestanding hBN sheets and the redistribution of charge on the atoms near boron vacancy modulates the otherwise inert composite system into a perfect host for O₂ adsorption and subsequent oxygen reduction process on the vacant site.

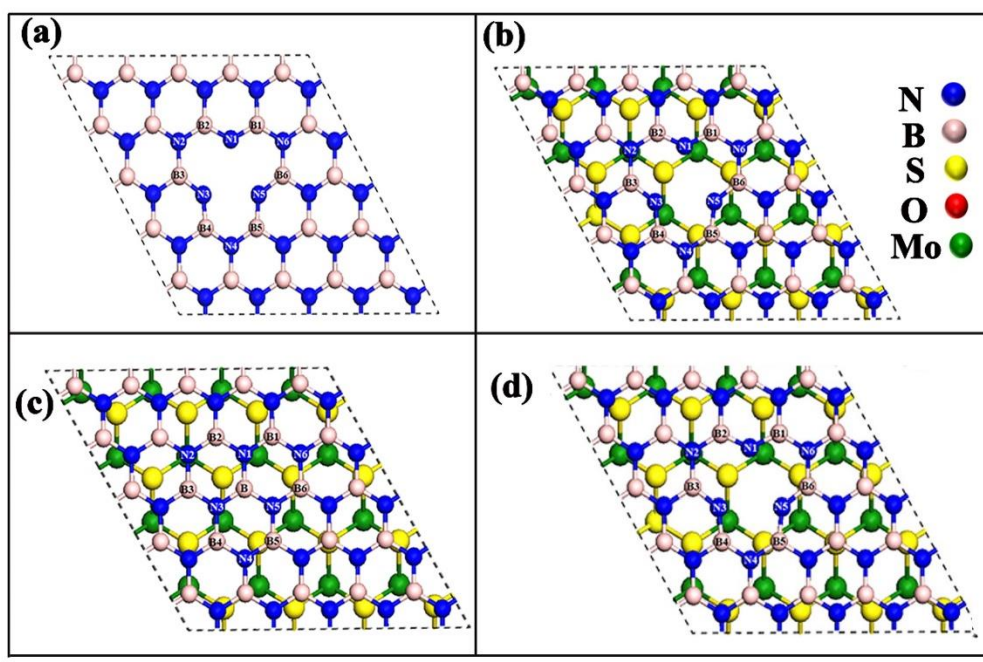


Figure 5.15: Top view of (a) hBN with boron vacancy (b) B_{vac} -hBN-MoS₂ (c) hBN-MoS₂ where the atom indexes correspond to the atoms for which amount of Bader charge transferred is shown in table 5.6. (d) Top view of B_{vac} -hBN-MoS₂.

To elucidate the effect of B-vacancy in hBN-MoS₂ heterostructure towards ORR mechanism, the first principles calculation on the defect free hBN-MoS₂ heterostructure system are studied its activity towards ORR in alkaline medium. In the first step, O₂ was adsorbed weakly

on the heterostructure in side on mode which was followed by the first electron transfer process and breakage of one H_2O molecule into H^+ and OH^- ion spontaneously. But in the next step, via electron and proton transfer coupling process, HO_2^- was formed spontaneously indicating less efficient two-electron pathways based ORR by defect free hBN-MoS₂ heterostructure (Figure.

Atom index as denoted in figure S14	Charge transferred hBN with B-vacancy	Charge transferred (e) B _{vac} -hBN-MoS ₂	Charge transferred hBN-MoS ₂
N1	-1.569	-1.591	-2.141
N2	-2.147	-2.144	-2.159
N3	-1.564	-1.588	-2.148
N4	-2.161	-2.155	-2.153
N5	-1.579	-1.591	-2.151
N6	-2.161	-2.147	-2.156
B1	2.158	2.149	2.152
B2	2.155	2.154	2.146
B3	2.155	2.141	2.161
B4	2.158	2.150	2.155
B5	2.157	2.149	2.150
B6	2.157	2.148	2.143
B	-	-	2.154

Table 5.6: Charge transferred to/ from the atoms near the vacancy site for free standing hBN sheet with boron vacancy.

5.16a). O_2 adsorption on pure hBN-MoS₂ system is highly endothermic in nature with adsorption energy value of 2.10 eV. Such brittle O_2 adsorption process usually leads to peroxide ion formation after first protonation via the two-electron pathways. The protonation process was checked by placing the H atom on both the non-equivalent O atoms one by one and the formation of HO_2^- ion was observed to be the energetically most favorable reaction pathway. Further, we have created about 4% B-vacancy in the heterostructure keeping in line with the experiment, and studied ORR mechanisms step by step on the B_{vac}-hBN-MoS₂ heterostructure. At first, O_2 molecule is strongly adsorbed by B_{vac}-hBN-MoS₂ contrary to the defect free one (“B” in Figure 5.16b,c). The O_2 adsorption process on hBN-MoS₂ system with boron vacancy was observed to be exothermic in nature with energy -0.27 eV opposite compared to the same on pure hBN-MoS₂ system. Lower adsorption energy corresponds to stronger adsorption of oxygen molecules towards the active site.

In the next step, the breakage of H-OH bond and subsequent adsorption of the H^+ ion on one of the O atoms is occurred spontaneously by completely dissociating the di-oxygen (O-O) bond, hence eradicating the possibility of ORR proceeding through the two-electron pathways (Figure 5.16a). Considering, the free energy of the final product of ORR via alkaline medium, i.e., $\text{B}_{\text{vac}}\text{-hBN-MoS}_2$ and four free hydroxyl ions as reference, the free energy difference of each ORR intermediates (OOH^* , OH^* , O^*) was calculated.

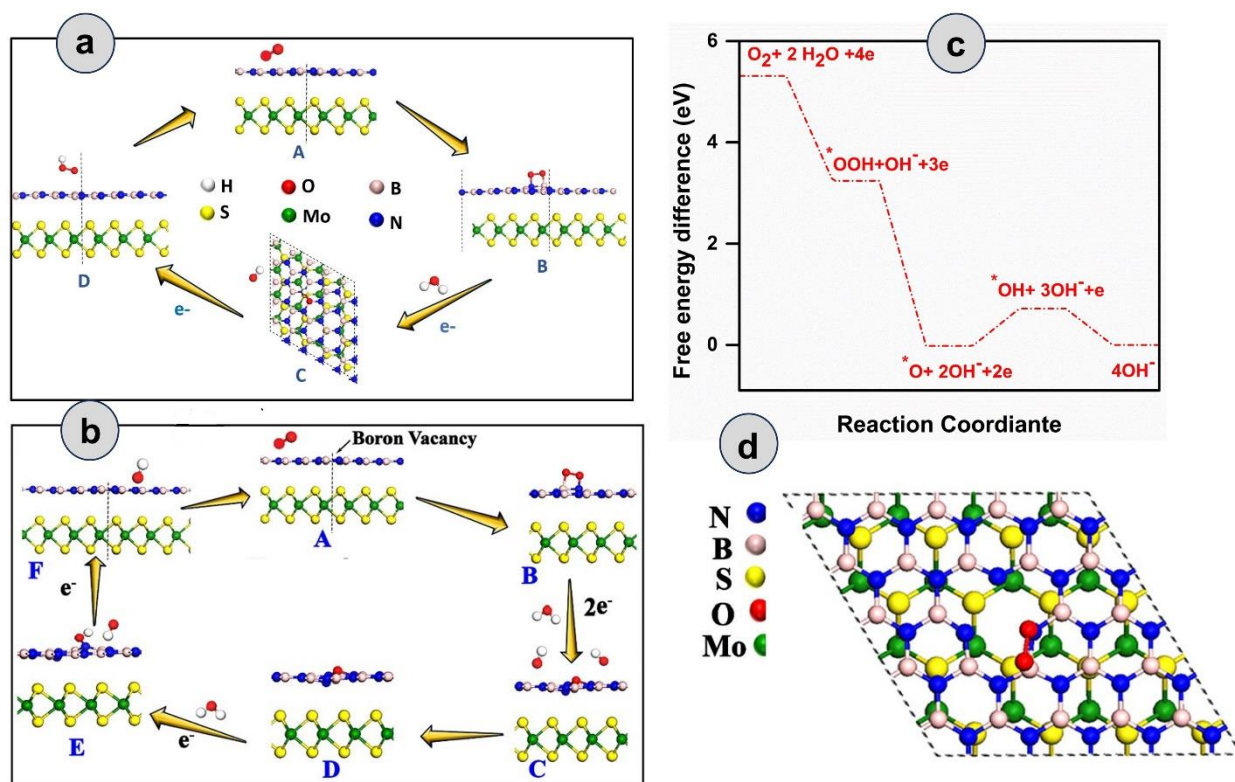


Figure 5.16: (a) Two electron pathway ORR mechanism involving (A, B) adsorption of dioxygen molecule (O_2) on the B and N site; (C) peroxide (HO_2^-) ion formation on the active site and (D) after desorption of the peroxide ion of the hBN-MoS₂ heterostructure without boron vacancy. (b) Mechanism of ORR pathway of $\text{B}_{\text{vac}}\text{-hBN-MoS}_2$ from DFT analysis. (c) Gibbs Free energy (ΔG) diagram of ORR on $\text{B}_{\text{vac}}\text{-hBN-MoS}_2$ heterostructure system. Here * denotes surface adsorbed oxygen. (d) Top view of the adsorption of oxygen towards the active site of $\text{B}_{\text{vac}}\text{-hBN-MoS}_2$ during ORR.

The free energy difference of the first step (ΔG_1) was calculated to be 3.26 eV (Figure 5.16b). In the next step, i.e., the second electron transfer process, the hydroxyl radical (OH^*) got detached from the surface taking one electron forming a free hydroxyl ion spontaneously with free energy difference (ΔG_2) -0.02 eV substantiating the $\text{B}_{\text{vac}}\text{-hBN-MoS}_2$'s progress via energetically efficient four electron pathway unlike the defect free one (“C” of Figure 5.16b,c). As the OH^- was formed, the other O atom remained strongly adsorbed on the surface in epoxy formation as indicated by the exergonic value of the free energy difference of this step (“D” in Figure 5.16b,c). In the next step, after complete dissociation of another water molecule into H^+ and OH^- , the formed H^+ gets adsorbed on the O atom on the catalyst surface (“E” of Figure 5.16b,c). A small endothermic reaction barrier was observed in aforementioned facile step (OH^* form O^*) with free energy difference value of 0.72 eV since the single O molecule was strongly adsorbed on the catalyst surface in the preceding step. From the above discussion, the breaking of di-oxygen bond and simultaneous formation of the free OH^- ion was concluded as a key electrochemical step for ORR kinetics exhibited by $\text{B}_{\text{vac}}\text{-hBN-MoS}_2$. The final electron transfer step proceeded spontaneously with the desorption of the hydroxyl ion from the surface (F of Figure 5.16b,c,d).

5.4. Conclusion

In a nutshell, vacancy engineering in ORR sluggish material hBN by integrating it with MoS_2 via liquid exfoliation method effectively boosts the catalytic activity of this formed heterostructure HBPS enhancing intrinsic B-vacancy formation in it. The electronic and geometric structure of hBN with the support of MoS_2 including B-vacancy on the basal plane of hBN serves most catalytic active sites for ORR activity by quick electron transfer from the valance band to conduction band owing to band gap minimization of formed heterostructure. The experimentally realized work is well-corroborated with carried out theoretical predictions. The corresponding superior ORR performance of HBPS is harvested with large kinetic current density (5.96 mA/cm^2 at 0.1 V vs. RHE), and reduction potential (E_{ORR}) (0.63 V vs. RHE), along with smaller Tafel Slope (66 mV/decade) as well as four electron pathway selectivity. Additionally, long-term durability (92.80%) and lower tolerance of methanol corrosion of the prepared HBPS heterostructure suggest the inclusive applicability of the afore-mentioned vacancy engineering's potential of developing cost-effective and durable hBN- MoS_2 based catalysis.

5.5. References

1. Wang, X., Zhang, Y., Si, H., Zhang, Q., Wu, J., Gao, L., Wei, X., Sun, Y., Liao, Q., Zhang, Z. and Ammarah, K., *Journal of the American Chemical Society*, 2020, 142(9), pp.4298-4308.
2. Mohan, R., Modak, A., Schechter, A., *ACS Appl. energy Mater.*, 2021, 4, pp, 564-594.
3. Roy, D., Sarkar, S., Bhattacharjee, K., Panigrahi, K., Das, B.K., Sardar, K., Sarkar, S. and Chattopadhyay, K.K., *Carbon*, 2020, 166, pp.361-373.
4. Mun, Y., Lee, S., Kim, K., Kim, S., Lee, S., Han, J.W. and Lee, J., *Journal of the American Chemical Society*, 2019, 141(15), pp.6254-6262.
5. Zhang, Q., Bedford, N.M., Pan, J., Lu, X., Amal, R.A. *Adv. Energy. Mater.*, 2019, 9, pp, 1901312-1901325.
6. Dou, S., Tao, L., Huo, J., Wang, S. and Dai, L., *Energy & Environmental Science*, 2016, 9(4), pp.1320-1326.
7. Lin, Y., Williams, T.V. and Connell, J.W., *The Journal of Physical Chemistry Letters*, 2010, 1(1), pp.277-283.
8. Chhowalla, M., Shin, H.S., Eda, G., Li, L.J., Loh, K.P. and Zhang, H., *Nature chemistry*, 2013, 5(4), pp.263-275.
9. Xue, Q., Pei, Z., Huang, Y., Zhu, M., Tang, Z., Li, H., Huang, Y., Li, N., Zhang, H. and Zhi, C., *Journal of Materials Chemistry A*, 2017, 5(39), pp.20818-20823.
10. Rastogi, P.K., Sahoo, K.R., Thakur, P., Sharma, R., Bawari, S., Podila, R. and Narayanan, T.N., *Physical Chemistry Chemical Physics*, 2019, 21(7), pp.3942-3953.
11. Patil, I.M., Lokanathan, M. and Kakade, B., *Journal of Materials Chemistry A*, 2016, 4(12), pp.4506-4515.
12. Uosaki, K., Elumalai, G., Noguchi, H., Masuda, T., Lyalin, A., Nakayama, A. and Taketsugu, T., *Journal of the American Chemical Society*, 2014, 136(18), pp.6542-6545.
13. Back, S. and Siahrostami, S., *Nanoscale Advances*, 2019, 1(1), pp.132-139.
14. Chia, X., Eng, A.Y.S., Ambrosi, A., Tan, S.M. and Pumera, M., *Chemical reviews*, 2015, 115(21), pp.11941-11966.
15. Wang, T., Gao, D., Zhuo, J., Zhu, Z., Papakonstantinou, P., Li, Y. and Li, M., *Chemistry—European Journal*, 2013, 19(36), pp.11939-11948.
16. Jayabal, S., Saranya, G., Wu, J., Liu, Y., Geng, D. and Meng, X., *Journal of Materials Chemistry A*, 2017, 5(47), pp.24540-24563.
17. Gomez, I.J., Arnaiz, B., Cacioppo, M., Arcudi, F. and Prato, M., *Journal of Materials Chemistry B*, 2018, 6(35), pp.5540-5548.
18. Mao, J., Liu, P., Du, C., Liang, D., Yan, J. and Song, W., *Journal of Materials Chemistry A*, 2019, 7(15), pp.8785-8789.
19. Gopalakrishnan, K., Pramoda, K., Maitra, U., Mahima, U., Shah, M.A. and Rao, C.N.R., *Nanomaterials and Energy*, 2015, 4(1), pp.9-17.
20. Rodríguez-Carvajal, J., *Physica B: Condensed Matter*, 1993, 192(1-2), pp.55-69.
21. Saini, P., Sharma, R. and Chadha, N., *Indian Journal of Pure & Applied Physics (IJPAP)*, 2017, 55(9), pp.625-629.
22. Kresse, G. and Hafner, J., *Physical review B*, 1993, 47(1), p.558.
23. Kresse, G. and Hafner, J., *Physical Review B*, 1994, 49(20), p.14251.
24. Blöchl, P.E., *Physical review B*, 1994, 50(24), p.17953.

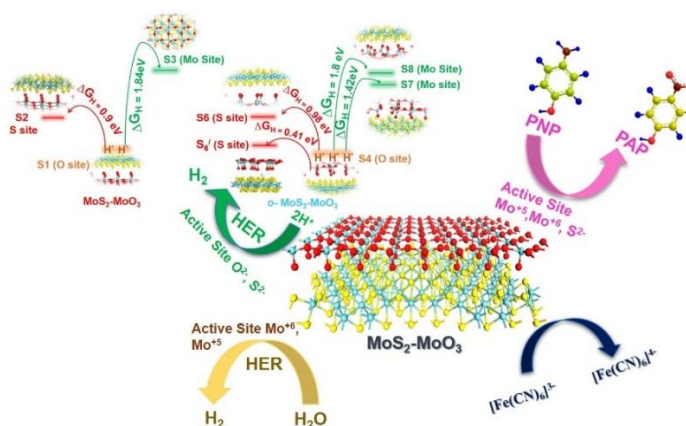
25. Perdew, J.P., Burke, K. and Ernzerhof, M., *Physical review letters*, 1996, 77(18), p.3865.
26. Grimme, S., *Journal of computational chemistry*, 2006, 27(15), pp.1787-1799.
27. Tang, W., Sanville, E. and Henkelman, G., *Journal of Physics: Condensed Matter*, 2009, 21(8), p.084204.
28. Back, S. and Siahrostami, S., *Nanoscale Advances*, 2019, 1(1), pp.132-139.
29. Li, X., Fang, Y., Lin, X., Tian, M., An, X., Fu, Y., Li, R., Jin, J. and Ma, J., *Journal of Materials Chemistry A*, 2015, 3(33), pp.17392-17402.
30. Deng, H., Zhang, C., Xie, Y., Tumlin, T., Giri, L., Karna, S.P. and Lin, J. *Journal of Materials Chemistry A*, 2016, 4(18), pp.6824-6830.
31. Kim, Y.I., Jung, J.K., Ryu, K.S., Nahm, S.H. and Gregory, D.H., *Journal of Physics D: Applied Physics*, 2005, 38(8), p.1127.
32. Ramos, M., Galindo-Hernández, F., Arslan, I., Sanders, T. and Domínguez, J.M., *Scientific Reports*, 2017, 7(1), p.12322.
33. Saha, S., Jana, M., Khanra, P., Samanta, P., Koo, H., Murmu, N.C. and Kuila, T., *ACS applied materials & interfaces*, 2015, 7(26), pp.14211-14222.
34. Wu, C., Liu, D., Li, H. and Li, J., *Small*, 2018, 14(16), p.1704227.
35. Sudeep, P.M., Vinod, S., Ozden, S., Sruthi, R., Kukovecz, A., Konya, Z., Vajtai, R., Anantharaman, M.R., Ajayan, P.M. and Narayanan, T.N., *RSC advances*, 2015, 5(114), pp.93964-93968.
36. Gao, D., Si, M., Li, J., Zhang, J., Zhang, Z., Yang, Z. and Xue, D., *Nanoscale research letters*, 2013, 8, pp.1-8.
37. Li, X., Hao, X., Zhao, M., Wu, Y., Yang, J., Tian, Y. and Qian, G., *Advanced Materials*, 2013, 25(15), pp.2200-2204.
38. Jiang, L., Zhang, S., Kulinich, S.A., Song, X., Zhu, J., Wang, X. and Zeng, H., *Materials Research Letters*, 2015, 3(4), pp.177-183.
39. Chen, Y., Li, K., Li, Z., Hu, S., Sun, X., Shi, Z., Liu, X. and Li, D., *Journal of Alloys and Compounds*, 2019, 797, pp.262-268.
40. Lee, D. and Song, S.H., *RSC advances*, 2017, 7(13), pp.7831-7835.
41. Museur, L., Feldbach, E. and Kanaev, A., *Physical review B*, 2008, 78(15), p.155204.
42. Mawlong, L. P. L., Bora, A., Giri, P. K. *Sci. Rep.*, 2019, 9, pp.19414-19427.
43. Yuan, J., Najmaei, S., Zhang, Z., Zhang, J., Lei, S., Ajayan, P.M., Yakobson, B.I. and Lou, J., *Acs Nano*, 2015, 9(1), pp.555-563.
44. Wang, T., Gao, D., Zhuo, J., Zhu, Z., Papakonstantinou, P., Li, Y. and Li, M., *Chemistry—A European Journal*, 2013, 19(36), pp.11939-11948.
45. Patil, I.M., Lokanathan, M. and Kakade, B., *Journal of Materials Chemistry A*, 2016, 4(12), pp.4506-4515.
46. Khan, A.F., Down, M.P., Smith, G.C., Foster, C.W. and Banks, C.E., *Journal of Materials Chemistry A*, 2017, 5(8), pp.4103-4113.
47. Hao, L., Yu, J., Xu, X., Yang, L., Xing, Z., Dai, Y., Sun, Y. and Zou, J., *Journal of Power Sources*, 2017, 339, pp.68-79.
48. Rowley-Neale, S.J., Smith, G.C. and Banks, C.E., *ACS applied materials & interfaces*, 2017, 9(27), pp.22539-22548.
49. Chua, X.J., Luxa, J., Eng, A.Y.S., Tan, S.M., Sofer, Z. and Pumera, M., *ACS Catalysis*, 2016, 6(9), pp.5724-5734.
50. Wang, T., Zhuo, J., Chen, Y., Du, K., Papakonstantinou, P., Zhu, Z., Shao, Y. and Li, M., *ChemCatChem*, 2014, 6(7), pp.1877-1881.

51. Zhou, J., Xiao, H., Zhou, B., Huang, F., Zhou, S., Xiao, W. and Wang, D., *Applied Surface Science*, 2015, 358, pp.152-158.
52. Illathvalappil, R., Unni, S.M. and Kurungot, S., *Nanoscale*, 2015, 7(40), pp.16729-16736.
53. Khan, A.F., Randviir, E.P., Brownson, D.A., Ji, X., Smith, G.C. and Banks, C.E., *Electroanalysis*, 2017, 29(2), pp.622-634.
54. Tadi, K.K., Palve, A.M., Pal, S., Sudeep, P.M. and Narayanan, T.N., *Nanotechnology*, 2016, 27(27), p.275402.
55. He, L., Cui, B., Liu, J., Wang, M., Zhang, Z. and Zhang, H., *ACS Sustainable Chemistry & Engineering*, 2018, 6(7), pp.9257-9268.
56. Perivoliotis, D.K., Sato, Y., Suenaga, K. and Tagmatarchis, N., *Nanoscale*, 2020, 12(35), pp.18278-18288.
57. Wang, J., Hao, J., Liu, D., Qin, S., Portehault, D., Li, Y., Chen, Y. and Lei, W., *ACS Energy Letters*, 2017, 2(2), pp.306-312.
58. Huang, H., Feng, X., Du, C., Wu, S. and Song, W., *Journal of Materials Chemistry A*, 2015, 3(31), pp.16050-16056.
59. Suresh, C., Mutyala, S. and Mathiyarasu, J., *Materials Letters*, 2016, 164, pp.417-420.
60. Khan, A.F., Down, M.P., Smith, G.C., Foster, C.W. and Banks, C.E., *Journal of Materials Chemistry A*, 2017, 5(8), pp.4103-4113.
61. Huang, H., Feng, X., Du, C., Wu, S. and Song, W., *Journal of Materials Chemistry A*, 2015, 3(31), pp.16050-16056.
62. Wang, R., Gao, S., Wang, K., Zhou, M., Cheng, S. and Jiang, K., *Scientific Reports*, 2017, 7(1), p.7963.
63. Lin, Y., Williams, T.V., Xu, T.B., Cao, W., Elsayed-Ali, H.E. and Connell, J.W., *The Journal of Physical Chemistry C*, 2011, 115(6), pp.2679-2685.
64. Zhao, X., Song, P., Wang, C., Riis-Jensen, A.C., Fu, W., Deng, Y., Wan, D., Kang, L., Ning, S., Dan, J. and Venkatesan, T., *Nature*, 2020, 581(7807), pp.171-177.
65. Liu, H., Long, W., Song, W., Liu, J. and Wang, F., *Chemistry—A European Journal*, 2017, 23(11), pp.2599-2609.
66. García-Miranda Ferrari, A., Rowley-Neale, S.J. and Banks, C.E. *Analytical and Bioanalytical Chemistry*, 2021, 413, pp.663-672.
67. Li, X., Wu, X., Zeng, X.C. and Yang, J., *Acs Nano*, 2012, 6(5), pp.4104-4112.
68. Banerjee, S. and Majumder, C., *Applied Surface Science*, 2020, 515, p.145978.
69. Xu, D., Liu, Y.J., Zhao, J.X., Cai, Q.H. and Wang, X.Z., *The Journal of Physical Chemistry C*, 2014, 118(17), pp.8868-8876.
70. Lyalin, A., Nakayama, A., Uosaki, K. and Taketsugu, T., *The Journal of Physical Chemistry C*, 2013, 117(41), pp.21359-21370.
71. Ferrari, A.G.M., Brownson, D.A., Dena, A.S.A., Foster, C.W., Rowley-Neale, S.J. and Banks, C.E., *Nanoscale Advances*, 2020, 2(1), pp.264-273.

Oxygen vacancy induced band engineering and metal unsaturation in MoS₂-MoO₃ with spillover based confined catalysis

Abstract

The chemical reduction and hydrogen evolution reaction (HER) holds promise in sustainable energy generation and reducing global warming emissions. We have employed oxygen vacancy induced band restructuring and multiple active sites in MoS₂-MoO₃, showing para-nitrophenol (PNP), ferricyanide reduction and HER activity. The oxygen vacancy lowers work function, band gap and d band center, stabilizing the antibonding state of MoS₂-MoO₃ and accelerating the H₂ production with PNP reduction having a high turnover frequency (1.02 mmol g⁻¹ min⁻¹). However, the Mo^{5+/6+} site is a bifunctional center for alkaline HER and PNP reduction, analyzed with X-ray Photoelectron Spectroscopy (XPS) and SCN⁻ insertion during catalysis. For acidic HER, the exothermically adsorbed H^{*} on O²⁻ site (MoO₃) undergoes favorable H^{*} spillover to S²⁻ (MoS₂) in a confined space due to low thermodynamic barrier (0.41 eV), enhances the active surface area and mass activity with an overpotential of 114 mV at 10 mA cm⁻². The work demonstrates the vacancy induced band alignment of highly efficient MoS₂ based multifunctional catalysis.



6.1. Introduction

Electro and chemical catalysis accelerate energy conversion pathways in many commercial ways, such as water splitting, fuel cells, etc., where hydrogen evolution (HER) becomes a crucial part of water electrolysis pathways [1,3]. In the last decade, platinum based metals and non noble catalysts have been utilized for electrochemically producing H_2 from renewable energy sources, where high cost and low durability hinder HER activity [4,5]. Therefore, various non-platinum based catalysts have been designed to overcome the sluggish kinetic rate of HER [6-10]. The vacancy promoted structural optimization and superior HER activity have been widely reported in metal oxide, metal phosphide, metal sulphide based materials [11-13]. Besides the single or double vacancy, doping with most electronegative element fluorine modulates the electronic structure and adsorption free energy of the reaction intermediate. The anion vacancy facilitates the charge transfer and enhances active catalytic sites for several HER and OER kinetics [14,15]. After the discovery of graphene, two dimensional transition-metal dichalcogenides (TMDs) like MoS_2 and WS_2 have manifested in the field of electronic, sensors, biomedical, surface-enhanced Raman scattering (SERS), and catalytic application due to their high mobility, and unique optical activity [16-18]. However, the 2H phase of MoS_2 or WS_2 has inactive basal plane as compared to the edge states with high rate of Sulphur etching during electrocatalytic reduction leading to lower intrinsic activities towards catalytic performances [19,20]. Recent study reveals the presence of metallic 1T phase as catalytic sites for acidic hydrogen evolution reaction (HER) due to exposed basal and edge Sulphur (S^{2-}) atoms [21]. Nevertheless, the metastable 1T MoS_2 is unstable and interconverted to the 2H phase at ambient temperature, restricting its chemical or electrochemical catalytic performances [21]. It has been established that electron donation from substrates, composites, mechanical exfoliation, or ion intercalation induces some lattice strain and band restructuring effect in 1T MoS_2 octahedra, improving its kinetic and thermodynamic stability [22-29]. For instance, band engineering plays a pivotal role in determining the potential barrier and availability of the electron density for intermediate adsorption/ desorption rate for acidic and alkaline HER. Such correlation between the active site density and band engineering must be considered a valid approach to determining the catalytic mechanism. Since single active sites of 1T- MoS_2 with metallic phase show acidic HER activity, MoS_2 is inert to the alkaline HER which limits its practical application in the field of water splitting.

Apart from water electrolysis, para nitrophenol (PNP) and ferricyanide reduction are most widely used in drug delivery and the petroleum industry [30]. The reaction occurs in aqueous medium with sodium borohydride (NaBH_4) and highly reactive catalytic surface following first order Langmuir-Hinshelwood mechanism [31]. However, such model reactions are highly influenced by rich active sites, conductivity, oxygen saturation, surface reconstructions, temperature and pH of the medium [32]. Heterogenous catalysts using metal nanoparticles doped (Pd, Au, or Ag) at the edge of MoS_2 enhance the rate of PNP reduction [33]. However, the complicated procedures, expensive synthesis techniques, slow kinetics, and low rate constant restrict its effective catalytic activity compared to various precious and non-precious metal catalysts. Nevertheless, the catalyst's surface must be metallic, having high electrical conductivity, surface area, and active sites for facile adsorption to promote significant catalytic reduction. In this regard, the interfacial chemistry between different binding sites, surface energy and band engineering must be adequately explored. In recent studies, the influence of charge transfer in binary nanocomposite plays a pivotal role in enhancing the surface charge and reactive sites [34]. So far, no report has been established to study the intrinsic property and surface modification of oxygen vacancy induced binary nanocomposites such as MoS_2 - MoO_3 , which can be an efficient catalyst for model chemical reduction and pH universal HER kinetics.

Herein, we have demonstrated MoS_2 - MoO_3 as a multi-functional catalyst for PNP, $[\text{Fe}(\text{CN})_6]^{3-}$ reduction and pH universal HER activity. Although the significant ex-situ process has been utilized to synthesize MoS_2 based composite, we have synthesized in-situ MoS_2 - MoO_3 in single step hydrothermal method under oxygen environment. Generally, chemical reduction from ammonium tetra thiomolybdate (Mo^{+6}) with hydrazine hydrate depends on reaction time and environments. The reduction of Mo^{+6} to Mo^{+4} leads to the formation of MoS_2 where free Mo^{+6} undergoes MoO_3 formation with high oxygen vacancy. This strategy affords a new concept of metal unsaturation due to oxygen vacancy, which plays a pivotal role in alkaline HER and PNP reduction than single reactive site of 1T-2H- MoS_2 . The oxygen deficiency and the heterostructure formation between MoS_2 and MoO_3 have been examined through optical, morphological, and surface analyses. The oxygen vacancy lowers the work function of MoS_2 - MoO_3 which is well corroborated with DFT simulation and ultraviolet photoelectron spectroscopy (UPS)

measurements. The metallic phase, high hydrophilicity and high surface area are beneficial for proton diffusion, which is a crucial step in acidic and alkaline HER. DFT result suggests different possible sites of hydrogen adsorption in HER catalysis, indicating the O site in MoO₃ layer is catalytically favorable for proton adsorption. The hydrogen spillover between O²⁻ site of MoO₃ to endothermic S²⁻ site of MoS₂ occurs in a confined space due to low thermodynamic barrier, accelerating facile hydrogen adsorption desorption rate in acidic medium. The post-XPS analysis and masking of the metal centers with SCN⁻ during catalysis have been established to correlate the theoretical analyses and shed light on active sites' role in catalytic pathways. Furthermore, lowering the effective work function and shifting the valence band maxima near Fermi level with multiple catalytic sites (O²⁻, S²⁻, and Mo^{5+/6+}) reduce the activation energy of the reaction pathways for PNP reduction and enhance the rate constant and turnover frequency. The work demonstrates a novel approach to the interfacial chemistry of the active sites, which optimizes the band structure between two binary heterostructures for the benchmark multifunctional catalytic performances.

6.2. Experimental section

6.2.1. Reagent and materials

Ammonium tetra thiomolybdate ((NH₄)₂MoS₄), sodium molybdate dihydrate, Thiourea, hydrazine Hydrate (35%), Molybdenum (IV) sulphide (MoS₂), (<2 μm grain size, 98%), 20% Pt/C, potassium hydroxide (KOH, 99% purity), dimethyl-formamide (99% purity), ethanol, H₂SO₄ (98%), nafion on solution (5%), 4-nitrophenol (>99%), sodium borohydride, potassium hexacyanoferrate(III), Sodium thiocyanate (>98%) are supplied from Sigma–Aldrich. Deionized (DI) water is utilized from a Direct-Q Millipore deionized (18 Ω at 25 °C).

6.2.2. Preparation of oxygen vacancy induced MoS₂-MoO₃ heterostructure

The MoS₂-MoO₃ nanosheets are synthesized by a facile one-step hydrothermal reaction. First, 100 mg of ammonium tetra thiomolybdate and 2 mL of hydrazine hydrate are added to 80 ml DI, and the mixture is bath-sonicated for 1 hour. This solution is transferred into a 100 mL Teflon-lined stainless-steel autoclave and maintained at 200 °C for 8 h in a temperature-programmed electric oven up to a ramping rate of 5 °C/min. After cooling naturally, black precipitates are washed five times with ethanol and distilled water and dried in a vacuum oven at 50 °C for 12 h. The composite obtained in the last step is used for material characterization and application.

Notably, the synthetic procedure is repeated five times, and the as-obtained product displays no structural or morphological changes.

6.2.3. Preparation of 2H-MoS₂, of MoS₂ nanosheet (MoS₂ Ns) and Quantum Dots (MoS₂ QD)

The flower, like 2H-MoS₂, is synthesized by one-step hydrothermal method. The as-purchased 30 mg sodium molybdate dihydrate is dissolved in 40 mL of DI water and magnetically stirred for 30 min. Then, 65 mg thiourea (NH₂CSNH₂) is added as a sulfur source and reducing agent (dual role), and the solution is stirred for another 30 min. Finally, the two solutions are transferred into a 100 mL Teflon-lined autoclave and undergo heating up to 180°C for 24 hours. The products are washed with DI water and ethanol 5 times. The final product is collected by centrifugation at 5000 rpm for 10 minutes. The sediment is dried in a vacuum oven at 50 °C for 12 h to obtain flower like 2H-MoS₂ (Figure 6.1b).

Bulk MoS₂ powder is exfoliated to nanosheets by liquid phase exfoliation method [35]. Typically, 100 mg of MoS₂ powder is added to 50 ml DMF in 100 ml beaker and undergoes stirring for 30 minutes at room temperature to obtain a well dispersed black solution. The solution is suspended for 4 hours using a probe sonicator (output power 55%). The resultant dispersion is then allowed to settle for 30 minutes, and top part (2/3) of the dispersion is centrifuged for 10 min at 4000 rpm to separate the thin nanosheet from the unexfoliated bulk residue. The process is repeated twice to obtain green color supernatant MoS₂ nanosheet (MoS₂ Ns). The dispersion is decanted into round bottom flask and undergoes reflux for 6 h at 150 °C. Then the mixture is settled for 5 minutes and undergoes centrifuge for 5 min at 2000 rpm. The light-yellow supernatant is stored in a vial termed MoS₂ quantum dots (MoS₂ QD) (yield 15wt % from nanosheet) (Figure 6.1b).

6.2.4. Characterization

The diffraction patterns of all the synthesized powder samples are obtained from a Rigaku MiniFlex powder X-ray diffractometer over the scattering angle range of $15^\circ \leq 2\theta \leq 80^\circ$ in steps of 0.02° using monochromatic CuK α radiation at a measuring speed of $0.5^\circ \text{ min}^{-1}$. Energy-dispersive X-ray, spectroscopic (EDS) analysis along with the morphologies of the samples, are studied using a field emission scanning electron microscope (FESEM, Hitachi S-4800) and a high-resolution transmission electron microscope (HR-TEM) (JEOL 2100) operated at 200 kV. For atomic and weight percent estimation, X-ray Photoelectron Spectroscopy (XPS) is carried out using a monochromatic Al K α X-ray source ($h\nu = 1486.6 \text{ eV}$) with a hemispherical analyzer

(SPECS HSA 3500). Work function is estimated by Ultraviolet Photoelectron Spectroscopy (UPS) with He I ($h\nu = 21.22$ eV) as the UV source. Fourier transformed infrared spectrophotometer (FTIR-8400S), Raman/AFM spectrometer (Witec Alpha300R, $\lambda_{\text{ex}} = 532$ nm) have been utilized for structural and compositional analysis. Absorption maxima are determined by UV-Vis spectrophotometer (Shimadzu UV-3600). The Brunauer–Emmett–Teller (BET) surface is examined with a Quantachrome NovaWin2 Instrument at 77K. The GC-MS spectra are obtained using GC 2014, Shimadzu instrument. The Zeta potential (ζ) has been measured by Malvern Zeta sizer Nano-ZS 90 instrument.

The photoluminescence excitation (PLE) and photoluminescence (PL) spectra are carried out on Edinburgh FLSP-980 luminescence spectrometer, with a microsecond flash lamp as the excitation source. The contact angle measurements are analyzed by OCA 15 EC DATA PHYSICS. Electron spin resonance spectroscopy (ESR) measurements are analyzed by JEOL, Japan, JES-FA200 ESR spectrometer with X and Q bands. EXAFS measurements are investigated at energy scanning EXAFS beamline (BL-09) at Indus-2 Synchrotron source (2.5 GeV, 300 mA) at the Raja Ramanna Centre for Advanced Technology (RRCAT), Indore, India, where beam line functions in the photon energy range of 4-25 KeV.

6.2.5. Electrochemical Characterization

Electrochemical measurements are discussed in electrochemical characterization chapter 3.

The C_{eff} or C_{dl} are determined from constant phase element (CPE) components according to the following equations [39].

$$Y_0 = Q(i\omega)^n \quad (6.1)$$

$$C_{dl} = Q^{\frac{1}{n}} \left(\frac{1}{R_p} + \frac{1}{R_{ct}} \right)^{\frac{(n-1)}{n}} \quad (6.2)$$

Where, i is the imaginary number, and the ω the angular frequency in rad s^{-1} , Q is the CPE constant, R_{ct} is equivalent charge resistance (Ω), R_s is solution resistance (Ω), Y_0 (Mho) signifies conductance or capacitance, n is a constant ($0 < n < 1$) (for ideal capacitor $n=1$).

For durability measurements, linear sweep voltammetry (LSV) is carried out at a scan rate of 10 mV/s up to 1000 cycles. The double-layer capacitance (C_{dl}), electrochemically

active surface area (ESCA), and Roughness factor (RF) is determined from Cyclic Voltammetry (CV) at the non faradaic region (-0.1 V to 0.2 V vs. RHE) of the MoS₂ catalysts. CV is carried out under different scan rates from 10 to 100 mV/s. The relationship between ESCA and C_{dl} is as follows:

$$ESCA = \frac{C_{dl}}{C_s} \quad (6.3)$$

Where. C_s is the specific capacitance of 35 μF/cm² and 40 μF/cm² per cm² for the flat electrode in 0.5 M H₂SO₄ and 1 M KOH. The C_{dl} has been calculated by plotting between ΔJ (mA/cm²) (J_{Anodic} - J_{Cathodic}) vs. scan rate at a potential 0.05 V vs. RHE and -0.06 V vs. RHE for acidic and alkaline medium, respectively.

Roughness factor can be calculated as follows [40]:

$$RF = C_{dl} / C_{dl(MoS_2)} \quad (6.4)$$

Non-faradaic capacitance of MoS₂ flat standard is taken as 60 μF cm⁻². The formed products have been detected using GC using N₂ as a transporter gas and identified by a Flame ionization detector (FID). For controlled experiment, sodium thiocyanate solution (0.01 M-0.02 M) is added in both acidic and alkaline solutions before starting the experiment. The long-term durability of the catalyst is tested by chronoamperometry at -0.3 V vs. RHE.

6.2.6. Calculation of turnover frequency (TOF)

The number of electrochemically accessible surface sites (catalyst) can be estimated using the formula (Jaramillo et al.): [40,41]

$$\frac{\# \text{ surface sites (catalyst)}}{\text{cm}^2 \text{ geometric area}} = \frac{\# \text{ surface-sites (flat standard)}}{\text{cm}^2 \text{ geometric area}} \times RF \quad (6.5)$$

Generally, the surface site density and MoS₂ flat standard capacitance are not exactly equal to MoS₂-MoO₃. However, surface site density is taken as ~ 10¹⁵ sites/cm², and this approximation is quite reasonable for MoS₂-MoO₃ composite. According to eq. 7 the surface sites for MoS₂-MoO₃, 2H- MoS₂ and MoS₂ QD to a value of 4.5 × 10¹⁷ sites/ cm², 2.5 × 10¹⁶ sites/ cm² and 6 × 10¹⁵ sites/ cm² respectively in 0.5 M H₂SO₄ solution.

$$\text{TOF per site} = \frac{\text{Total H}_2 \text{ Turnover} \times \text{Current density}}{\text{Surface Sites (catalyst)}} \quad (6.6)$$

Total Hydrogen turnover is calculated as follows [40,41]:

$$\begin{aligned}
 & \left(j \frac{mA}{cm^2} \right) \left(\frac{1A}{1000mA} \right) \left(\frac{1 \frac{C}{s}}{1 A} \right) \left(\frac{1 \text{ mol } e^-}{96485.3C} \right) \left(\frac{1 \text{ mol } H_2}{2 \text{ mol } e^-} \right) \left(\frac{6.02214 \times 10^{23} \text{ molecules } H_2}{1 \text{ mol } H_2} \right) \\
 & = 3.12 \times 10^{15} \frac{H_2/s}{cm^2} \text{ per } \frac{mA}{cm^2} \quad (6.7)
 \end{aligned}$$

The current density has been calculated at different overpotentials from 100 mV to 200 mV vs. RHE. The TOF per site for MoS₂-MoO₃ in acidic medium is calculated as follows:

At η -300 mV, TOF is

$$\left(3.12 \times 10^{15} \frac{H_2/s}{cm^2} / \frac{mA}{cm^2} \right) \left(81.95 \frac{mA}{cm^2} \right) \left(\frac{1cm^2}{4.5 \times 10^{17} \text{ surface sites}} \right) = 0.57 \frac{H_2/s}{\text{surface sites}}$$

The Mass Activity (MA) is calculated through Eq. 4

$$MA \text{ (mA mg}^{-1}\text{)} = \frac{J}{m} \quad (6.8)$$

Where J is the current density (mA cm⁻²) at two overpotentials (η) at 200 mV and 300 mV, m is mass loading of the active sites (mg cm⁻²). The active mass loading has been estimated from weight percentage (Wt%) of each component. However, the atomic percentage is obtained from XPS survey spectra, carried out three times to get the standard deviation (< 0.1). As postulated, S²⁻, O²⁻ and Mo^{5+/6+} centers are catalytically active sites in acidic and alkaline mediums respectively. The number of atomic percentages (At%) of total Mo, O and S sites obtained from XPS analyses is converted to weight percentage (Wt%) according to following equation:

$$Wt \% = \frac{At \% \times \text{atomic mass of each component}}{At \% \times \text{atomic mass of total components}} \quad (6.9)$$

The weight percentage (Wt %) of Mo, O and S sites are (58.9 \pm 0.8) %, (29.8 \pm 0.2)% and (11.2 \pm 0.12)%, respectively. Initially, 1 mg of the catalyst was taken on 60 μ L solution in which 6 μ L was utilized on GC electrode in both HER catalysis. We proposed total S²⁻, O²⁻ and Mo^{5+/6+} surface sites are catalytic sites for acidic and alkaline HER activity. The Wt % is converted to mass loading (m) and MA is calculated from Eq. 4. Similarly, MA can be calculated for 2H-MoS₂ and MoS₂ QD involving S²⁻ sites are catalytically active sites.

6.2.7. Catalytic Reduction of PNP

The reduction kinetics of PNP are performed in a 3 ml quartz cell using Shimadzu UV-3600 UV-VIS-NIR spectrophotometer. Firstly, 10 mg of PNP (substrate) is added to 50 ml DI water which undergoes bath sonication for 5 minutes to obtain a green homogeneous solution (1.5 mM). In an absorption experiment, some amount of MoS₂ catalysts and 2.7 ml of 0.1 M NaBH₄ are mixed in

a quartz cell, and then the as-prepared 0.3 ml PNP (1.5 mM) solution is added into the quartz cell. The absorption spectra are collected in a 1 min interval by monitoring the absorbance maxima λ_{\max} of PNP with time at ambient conditions. For controlled experiments, concentration of catalyst (0.8 mg to 3 mg), NaBH_4 (0.1 M to 1M) and PNP (1.5 mM to 4.5 mM) has been varied at 298 K temperature. Temperature dependent kinetic measurements are performed with a temperature controller equipped with the UV-VIS-NIR spectrophotometer. The temperature dependent catalytic study was carried out where 0.01 mol% MoS_2 QDs and 1 mg $\text{MoS}_2\text{-MoO}_3$ have been used as the catalysts and mixed with 0.25 M NaBH_4 and 1.5 mM PNP at four different temperatures (278K-308K). For the O_2 purging procedure, 3 ml of PNP and NaBH_4 solutions are purged with high purity O_2 gas (Indian Refrigeration system, India, 99.99% purity) at a constant flow rate of 5 min, 10 min, and 15 min separately. The dissolved oxygen in the solution has been measured from a digital dissolved oxygen (DO) meter with a DO probe consisting of silver and gold electrode cells with ring electrolyte tube (filled with 75 % KCl solution). A 2% sodium sulphide solution has been utilized for this measurement to attain equilibrium. DO saturation of DI water is taken as a reference for calibration. After DO measurement of four solutions, the PNP and NaBH_4 solutions are quickly transferred to the quartz tube after adding the catalyst. The quartz tube is sealed tightly with parafilm, and the absorption experiment is carried out. The experiment was measured three times to evaluate the standard deviation. For a controlled experiment, variable concentrations of sodium thiocyanate (NaSCN) solution (0.01 M-0.02 M) are added to the $\text{MoS}_2\text{-MoO}_3/\text{NaBH}_4$ mixture before adding PNP at ambient temperature. To check the stability of the catalyst on the PNP reduction, the $\text{MoS}_2\text{-MoO}_3$ has been reused five times after the complete disappearance of the absorption peak of PNP, keeping the NaBH_4 and PNP concentration constant. The turnover frequency for the PNP reduction is calculated as follows:

$$\text{TOF} = \frac{\text{the amount of consumed PNP (mmol)}}{\text{The mass of the metal in catalyst (g)} \times \text{reaction time (min)}} \quad (6.10)$$

6.2.8. Potassium Ferricyanide $\text{K}_3[\text{Fe}(\text{CN})_6]$ reduction

The Reduction is performed by adding 0.8 mg, 1 mg or 0.01 mol% MoS_2 catalysts, 2.7 ml NaBH_4 (0.1 M), 0.3 ml of 1.5 mM $\text{K}_3[\text{Fe}(\text{CN})_6]$ in a 3 mL quartz cell. The measurements are performed by monitoring the absorbance at 420 nm with 1 min time interval. The catalysis experiments are performed under ambient conditions.

6.2.9. Theoretical Methods

The first principles calculations were carried out within the generalized gradient approximation by means of the Perdew–Burke–Ernzerhof (PBE) functional with the projector augmented wave (PAW) method as implemented in the Vienna ab-initio simulation package (VASP) [42-45]. A plane of cut-off of 600 eV was utilized with a Γ centered ($1 \times 1 \times 1$) k-mesh throughout all the calculations. In order to neutralize the periodic interaction between the recurrent images, a vacuum slab of 25 Å was utilized in the direction perpendicular to the two-dimensional surface configurations. Structural optimization calculations were carried out with an energy convergence limit of 10^{-4} eV/atom. The dispersive forces were considered via the DFT + D3 method of Grimme as implemented in VASP [46]. All the calculations were done in spin unrestricted manner. The charge amount of charge transfer between adsorbent and adsorbate systems was calculated via the Bader charge analysis [47].

In order to prepare the 1T-MoS₂-MoO₃ heterostructure, One MoO₃ monolayer was isolated from the bulk MoO₃ layered structure. To match the rectangular symmetry of the MoO₃ layer, the lattice vector of 1T-MoS₂ unit cell was rotated along the (2 1 0) direction and a ($2 \times 5 \times 1$) and ($3 \times 4 \times 1$) supercell of the rotated 1T-MoS₂ unit cell and MoO₃ unit cell was considered respectively in order to minimized the strain on each layer with exact lattice match. The adsorption energy of PNP on the electrocatalyst system was calculated using the following equation:

$$E_{Ads} = E_{P+PNP} - E_P - E_{PNP} \quad (6.11)$$

Where E_{P+PNP} , E_P , E_{PNP} are the ground state energy of the PNP adsorbed host system, the pristine host system and one PNP molecule in vacuum respectively. The oxygen vacancy formation energy was calculated using the following formula:

$$E_{Vac} = E_D - E_P + n_O \mu_O \quad (6.12)$$

Where E_D and E_P are the ground state energies of the system with and without defect respectively. n_O is the number of oxygen atoms removed from the system and μ_O is the chemical potential of an oxygen atom calculated with the O₂ molecule in gas phase as reference. The free energy change (ΔG) of H⁺ ion adsorption for HER was calculated according to the following formula:

$$\Delta G = \Delta E + \Delta ZPE - T\Delta S \quad (6.13)$$

Where ΔE is the change in enthalpy as calculated from the DFT calculations, ΔZPE is the change in zero-point energy and $T\Delta S$ is the entropy-temperature term. In order to replicate an absolute acidic medium, the pH value was considered to be zero. The value of $T\Delta S$ for the gas phase molecules was adapted from a standard physical chemistry table. The ΔZPE and $T\Delta S$ for the adsorbed *H configuration were calculated using the following formulae:

$$\Delta ZPE = \frac{1}{2} \sum_i h\nu_i \quad (6.14)$$

$$-TS = kT \sum_i \ln(1 - e^{-\frac{h\nu_i}{kT}}) - \sum_i h\nu_i (e^{\frac{h\nu_i}{kT}} - 1)^{-1} \quad (6.15)$$

Where h is Planck's constant and ν_i is the vibrational frequencies (calculated using the density functional perturbation theory (DFPT) method). The temperature was taken as 298.15 K during the calculations. During the free energy calculations, the free energy of ($H^+ + e^-$) was calculated as equal to the free energy of $1/2H_2$ at standard conditions ($U = 0$, $pH = 0$) as suggested by Norskov et. Al [48].

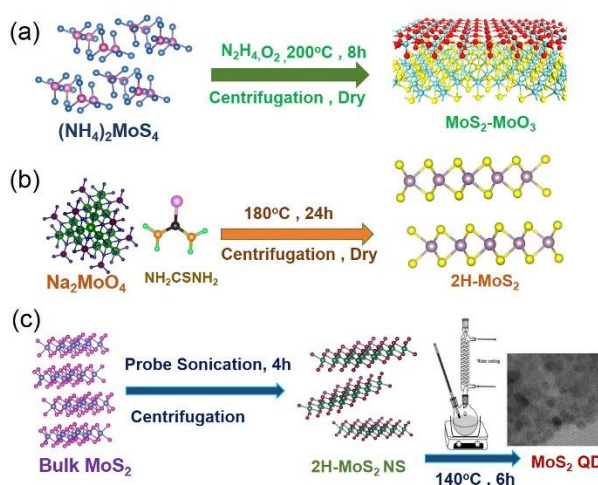
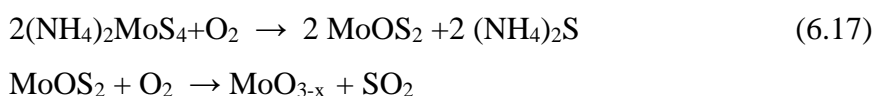
6.3. Results and Discussion

6.3.1. Structural and Morphological analyses of different MoS₂ based composites

Scheme 6.1 shows a schematic illustration of oxygen vacancy induced MoS₂-MoO₃, Sulfur vacancy induced 2H-MoS₂, 2H-MoS₂ Ns, and MoS₂ QD. The formation mechanism of MoS₂ from ammonium tetrathiomolybdate has been well established from Thermogravimetric Analysis (TGA) and Differential Thermal Analysis (DTA) analyses [49]. In the thermal dissociation process, the first step involves the removal of hydrogen sulphide and ammonia gas to form molybdenum thiosulphate (MoS₃) within the temperature range of around 180°C. In the second step, MoS₃ undergoes chemical reduction to form MoS₂ via loss of Sulphur between 230°C to 350°C temperature. Above 350°C, MoS₂ will ultimately convert into MoO₃. In the synthesis procedure followed by us, the single precursor ammonium tetrathiomolybdate undergoes reduction with hydrazine hydrate to form MoS₂. The reaction kinetics depend entirely on chemical environments like concentration, temperature, and time [50]. The formation of MoS₂ is shown as follows:



The above reaction occurs within 24 hours with complete reduction of Mo^{+6} to Mo^{+4} state when the precursor concentration is maintained at 5 mg of ammonium tetrathiomolybdate and 0.5 ml of hydrazine hydrate [50]. In our synthesis technique, we have utilized 100 mg of ammonium tetrathiomolybdate and 2 ml of hydrazine hydrate involving lower concentration of reducing agent. Apart from the lower concentration of hydrazine hydrate, the reaction takes place in 8 hours suggesting that insufficient time and lower concentration promote partial reduction of Mo^{6+} to Mo^{4+} . Thus, this effect influences unreacted Mo^{6+} to the oxide formation due to dissolved and open oxygen environment to form molybdenum oxysulphide (MoOS_2) [51]. However, the stable $\text{Mo}=\text{O}$ bond formation and Sulphur etching (weak S-Mo bond) tend to form MoO_{3-x} with some oxygen vacancies.



Scheme 6.1: (a,b,c) Schematic diagram for preparing $\text{MoS}_2\text{-MoO}_3$, 2H-MoS_2 , MoS_2 Ns, and MoS_2 QD.

The incomplete reduction from Mo^{6+} to Mo^{4+} and partial oxide formation have been preliminarily determined from XPS analyses. The deconvoluted XPS spectra of Mo 3d exhibits at 228.5 eV, 231.2 eV, 230.1 eV and 232.9 eV for $\text{MoS}_2\text{-MoO}_3$ correspond to Mo^{4+} 3d_{5/2} (1T), 3d_{3/2} (1T), 3d_{5/2} (2H), 3d_{3/2} (2H) with a spin-orbit splitting ~ 2.6 eV and ~ 2.7 eV respectively (Figure 6.1a and table 6.1) [52,53]. The percentage of 1T and 2H phase in $\text{MoS}_2\text{-MoO}_3$ has been estimated as ~ 20

% and ~18 %, respectively (Figure 6.2). The formation of 1T-MoS₂ is dependent on interlayer spacing, charge transfer and structural phase transition from 2H-MoS₂[54-57]. The intercalation of NH₄⁺ ion expands the interlayer spacing and promotes the charge transfer which changes the Mo coordination geometry to 1T-MoS₂ [58-59]. The other doublets at 231.9 eV and 235 eV have been determined as Mo⁶⁺ 3d_{5/2} and 3d_{3/2} XPS spectra. Notably, a small peak at 233.4 eV is well-indexed to Mo⁵⁺ state due to oxygen vacancy [60].

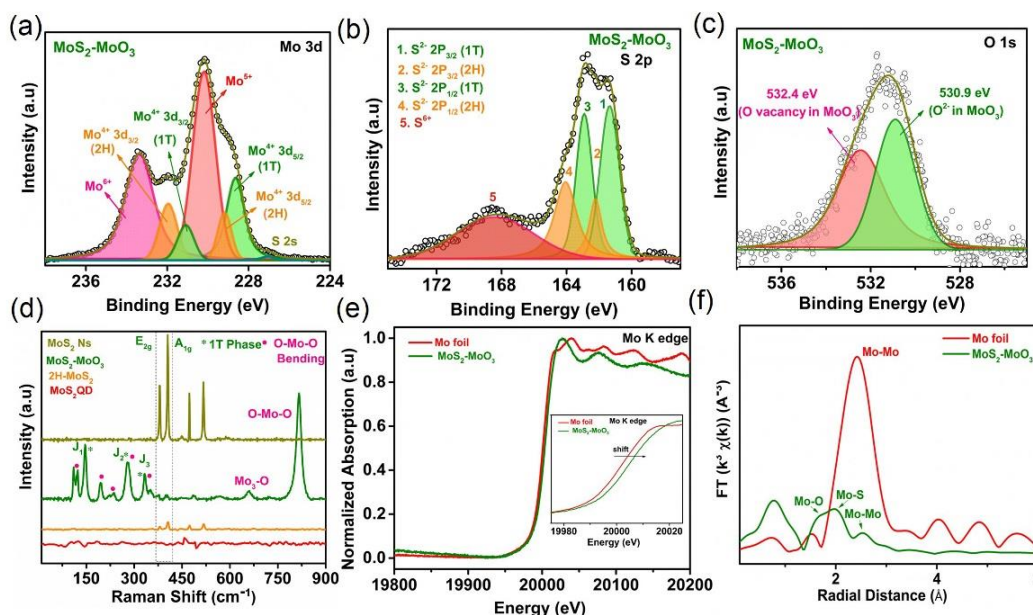


Figure 6.1: X-ray photoelectron spectroscopy (XPS) spectra of (a) Mo 3d (b) S 2p (c) O 1s of MoS₂-MoO₃ (d) Raman spectrum (e) XANES spectra recorded at the Mo K-edge of MoS₂-MoO₃, and Mo foil (inset showing positive shift in energy between Mo foil and MoS₂-MoO₃). (f) Fourier transforms (FT) EXAFS spectra of MoS₂-MoO₃.

Table 6.1: Different Mo 3d components of MoS₂ based catalyst from XPS analyses.

Materials	Mo ⁴⁺ 3d _{3/2} (2H)	Mo ⁵⁺	Mo ⁶⁺ 3d _{3/2}	Mo ⁶⁺ 3d _{5/2}	Mo ⁴⁺ 3d _{3/2} (1T)	Mo ⁴⁺ 3d _{5/2} (2H)	Mo ⁴⁺ 3d _{5/2} (1T)
MoS ₂ -MoO ₃	232.9 eV	233.4 eV	235 eV	231.9 eV	231.2 eV	230.1 eV	228.5 eV
2H-MoS ₂	232.4 eV	-	-	-	-	229.3 eV	-
MoS ₂ -QD	232.2 eV	-	-	-	-	230.02 eV	-
MoS ₂ -Ns	232.9 eV	-	-	-	-	230.14 eV	-

Materials	Mo ⁴⁺ S 2p _{3/2} (1T)	Mo ⁴⁺ S 2p _{1/2} (1T)	Mo ⁴⁺ S 2p _{3/2} (2H)	Mo ⁴⁺ S 2p _{1/2} (2H)
MoS ₂ -MoO ₃	161.3 eV	162.9 eV	162.6 eV	164.05 eV
2H-MoS ₂	-	-	163.2 eV	164.3 eV
MoS ₂ -QD	-	-	163.3 eV	164.45 eV
MoS ₂ -Ns	-	-	163.3 eV	164.5 eV

Table 6.2: S 2p components of MoS₂ based catalyst from XPS analyses.

Therefore, the ratio of oxidation states of Mo is attributed as Mo⁶⁺ (60%), Mo⁴⁺ (37%), and Mo⁵⁺ (3%) in MoS₂-MoO₃. The Mo⁵⁺ state is highly reactive, which can probably stabilize the 1T phase via electron transfer to a filled t_{2g} orbital of Mo⁴⁺. Figure 6.1b reveals S 2p spectra centered at 161.3 eV and 162.9 eV belong to S²⁻ 2p_{3/2} and 2p_{1/2} of 1T MoS₂ respectively (table- 6.2) [61]. However, the peaks belonging to 162.6 eV and 164.05 eV mainly originate from S²⁻ 2p_{3/2} and 2p_{1/2} of 2H-MoS₂, respectively. The peak positioned at 168.2 eV denotes S⁶⁺ state [62]. The result is corroborated with O 1s spectra suggesting two peaks at 530.9 eV and 532.4 eV, attributed to O²⁻ and oxygen vacancy of MoO₃ (Figure 6.1c) [63]. The electronic structure of MoS₂ is examined by Raman spectroscopy with an excitation wavelength of 532 nm, and the corresponding spectra exhibit two characteristic peaks at 380 cm⁻¹ and 404 cm⁻¹ corresponding to in-plane E_{2g} and out of phase A_{1g} mode of 2H phase, respectively (Figure 6.1d). The peak at 150 cm⁻¹ (J₁), 240 cm⁻¹ (E_{1g}), 280 cm⁻¹ (J₂), and 330 cm⁻¹ (J₃) imply 1T phase formation of MoS₂-MoO₃ [64]. Interestingly, the peak positions at 240 cm⁻¹, 280 cm⁻¹ and 330 cm⁻¹ are also attributed to bending modes of O-Mo-O which overlap with three characteristic peaks of 1T phase of MoS₂. However, no distinct peak of 1T phase has been observed at 2H-MoS₂, MoS₂ Ns, and MoS₂ QD, which concludes that the synthesized MoS₂ are 100% pure 2H phase. Moreover, the peaks positioned at 658 cm⁻¹ and 816 cm⁻¹ are assigned to asymmetric stretching of triply coordinating Mo-O₃ and symmetric stretching of O-Mo-O bond (Figure 6.1d) [62,63]. Mo k edge X-ray absorption near-edge spectroscopy (XANES) has been analyzed to investigate the local electronic structure around Mo. The spectra possess a more positive shift in the absorption edge than Mo foil, which proves the increase in the Mo oxidation state of MoS₂-MoO₃ (Figure 6.1e). The normalized Fourier transform (FT) k³χ(k) functions of the extended X-ray absorption fine structure (EXAFS)

data of the MoS₂-MoO₃ suggest that the radial distances are 1.98 Å, 2.54 Å, and 1.71 Å, which originate from the Mo-S, Mo-Mo and Mo-O bonding, respectively (Figure 6.1f) [65,66]. The deconvoluted XPS spectra of Mo 3d and S 2p for 2H-MoS₂, MoS₂ Ns, and MoS₂ QD have been shown in Figure 6.2 and table -6.1-2. From the XPS analyses no 1T phase is present in 2H-MoS₂, MoS₂ Ns, and MoS₂ QD. The Mo:S ratio for 2H-MoS₂ ~ 0.8 indicates large amount of Sulphur vacancy in the system (Figure 6.2).

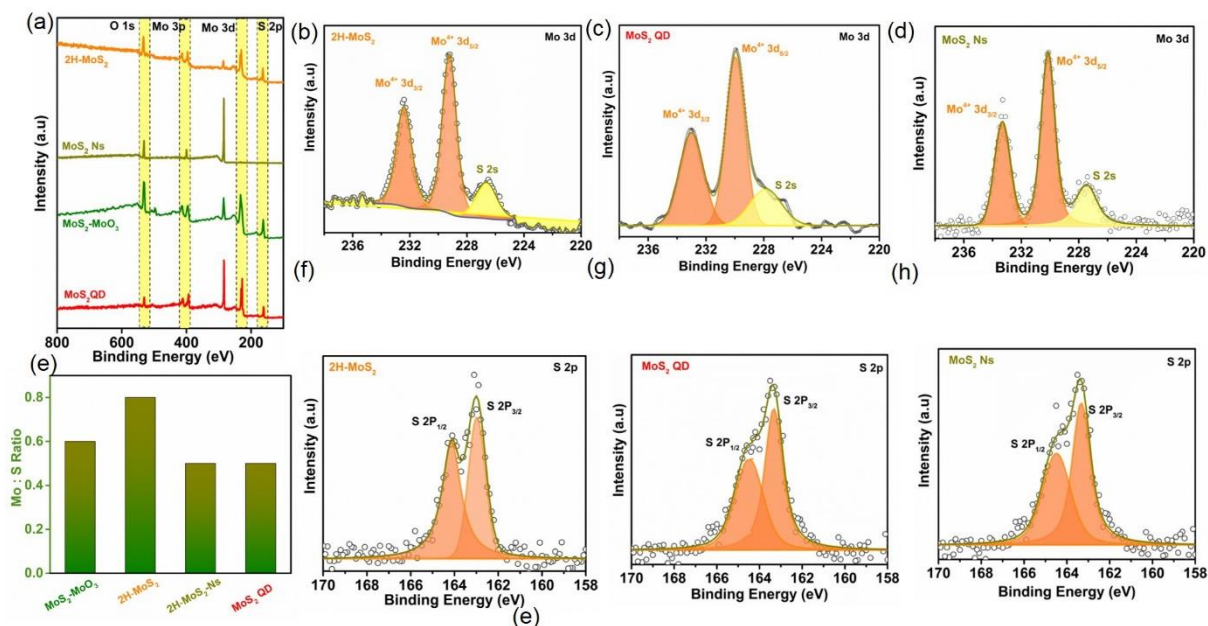


Figure 6.2: (a,e) XPS survey spectra and atomic percentage of Mo: S. Comparison of Mo 3d and S 2p XPS spectra of (b,f) 2H-MoS₂ (c,g) MoS₂ QD and (d,h) MoS₂ Ns respectively.

The lateral dimension, homogeneity and morphology have been determined from high-resolution HR-TEM, atomic force microscopy (AFM), field emission scanning electron microscope (FESEM), and EDS spectroscopy. Figure 6.3 reveals SEM image and EDS spectroscopy of MoS₂ Ns shows small nanosheets with different lateral sizes. HR-TEM image of MoS₂-MoO₃ has a few layers stacked thin nanosheets of MoS₂ and MoO₃ having interlayer distance (d) 0.63 nm and 1.36±0.02 nm, which is indexed to (002) and (001) plane of 2H and 1T MoS₂ respectively (Figure 6.4a-c). The expansion of lattice spacing result is suitable in accordance with our XRD analyses and further proves the intercalation of NH₄⁺ ion leading to the formation of 1T phase MoS₂. The d value at 0.53 nm belongs to the (100) plane of MoO₃, suggesting formation of MoS₂-MoO₃ [62,63].

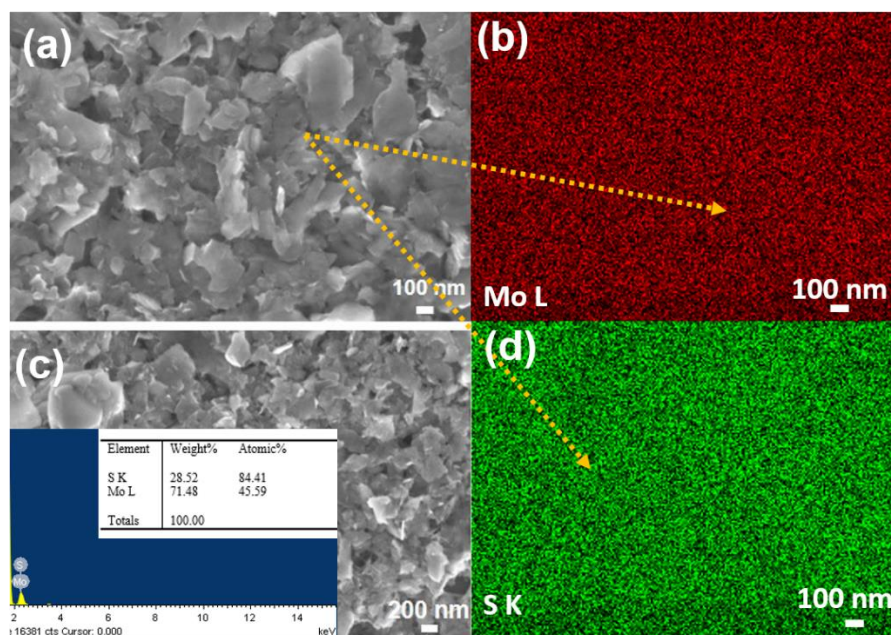


Figure 6.3: FESEM image of (a,c) MoS₂ nanosheet (MoS₂ Ns). EDX and elemental mapping results (Mo: red, S: green) are shown in Figure (b-d).

The X-ray diffraction pattern of MoS₂-MoO₃ having major peaks at $2\theta \sim 14^\circ$ ($d \sim 0.614$ nm), 33° ($d \sim 0.27$ nm), 40° ($d \sim 0.23$ nm) and 60° ($d \sim 0.15$ nm) corresponds to (002), (100), (103) and (110) plane (Figure 6.4d) [67]. Interestingly, a small peak has been determined at $2\theta \sim 6.5^\circ$ ($d \sim 1.3$ nm) denoting the (001) plane of 1T-2H MoS₂ heterostructure [67]. A broad hump at $2\theta \sim 44.5^\circ$ corresponds to the (006) plane of MoS₂ QD, mainly due to the restacking nature of QDs during thermal drying [61,68]. FESEM and Energy-dispersive X-ray spectroscopy (EDS) suggest homogeneous distribution of Mo and sulphur atoms in MoS₂-MoO₃ (Figure 6.4e). Figure 6.4f suggests AFM image of MoS₂-MoO₃ having thickness of ~ 69 nm with lateral dimension of ~ 500 nm due to restacking and agglomeration of nanosheets. The particle size distributions of MoS₂ QD lie within the range of 4.4 ± 0.2 nm with $d \sim 0.27$ nm corresponding to (100) planes (Figure 6.5). Figure 6.5c suggests MoS₂ QD has a thickness of ~ 4.2 nm and lateral dimension of ~ 150 nm due to agglomeration during drying process. The height profile is shown in Figure 6.5d. For efficient catalytic performance, high BET surface area with highly active sites becomes crucial for catalysts to carry out different chemical and electrochemical adsorptions. Generally, bulk MoS₂ possesses low BET surface area of $8.6 \text{ m}^2/\text{g}$ [37].

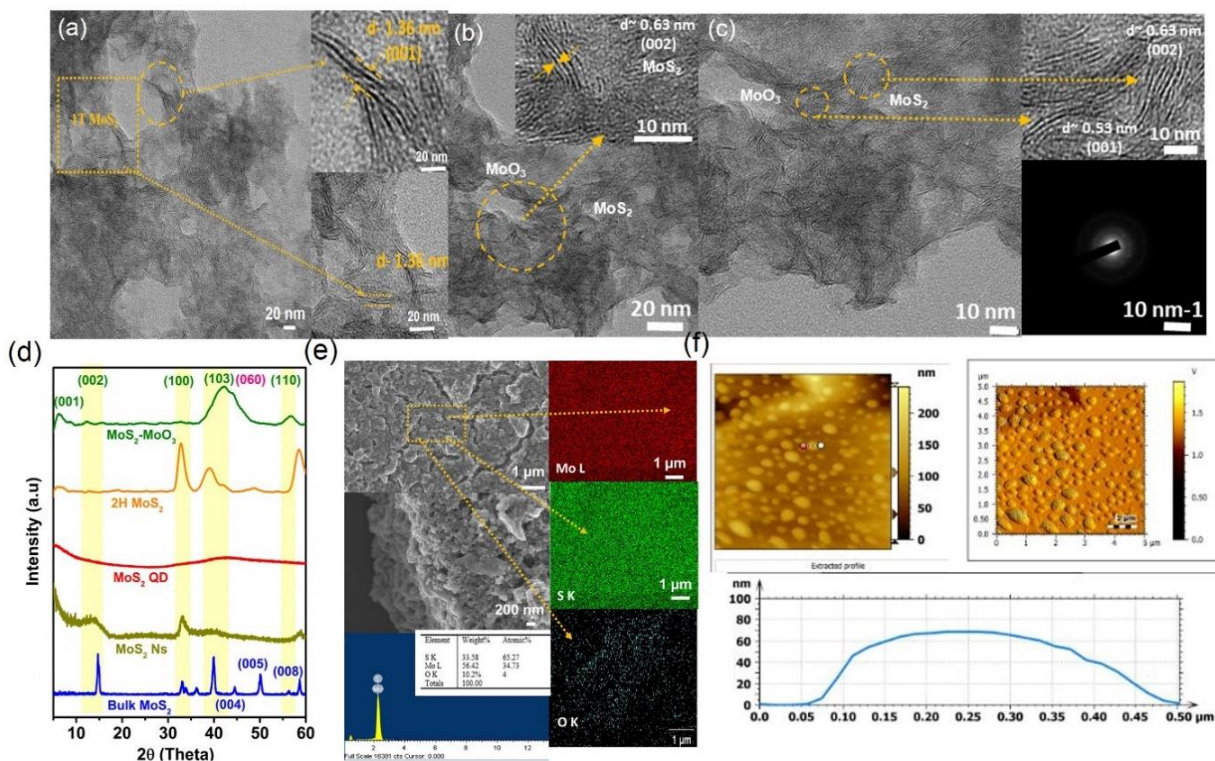


Figure 6.4: (a-c) Low-magnification TEM image of MoS₂-MoO₃ Inset: the corresponding interlayer distance (d) and SAED pattern of 1T-2H MoS₂ and MoO₃ counterpart. (d) XRD pattern of as-prepared samples. FESEM image of hydrothermally synthesized MoS₂-MoO₃ composite at (e) low and high magnification. EDX and elemental mapping results with elements indicated in different colors (Mo: red, S: green, O: cyan) of MoS₂-MoO₃. (f) AFM image and height profile of MoS₂-MoO₃.

Our study reveals the BET surface area of MoS₂-MoO₃ and 2H MoS₂ to be 119 m²/g and 25 m²/g with pore diameter of 2.2 nm, respectively (Figure 6.6a-c). We employed diffuse reflectance infrared Fourier transform spectroscopy (DRIFTS) of MoS₂, where stretching frequency at 442 cm⁻¹ indicates Mo-S bond shown in Figure 6.6d [69]. Additionally, four distinct stretching frequencies at 600 cm⁻¹, 763 cm⁻¹, 908 cm⁻¹, and 943 cm⁻¹ are assigned to Mo₃-O, Mo-O, O-Mo-O, and Mo-O-Mo type of vibrations of MoO₃ (Figure 6.6d) [70].

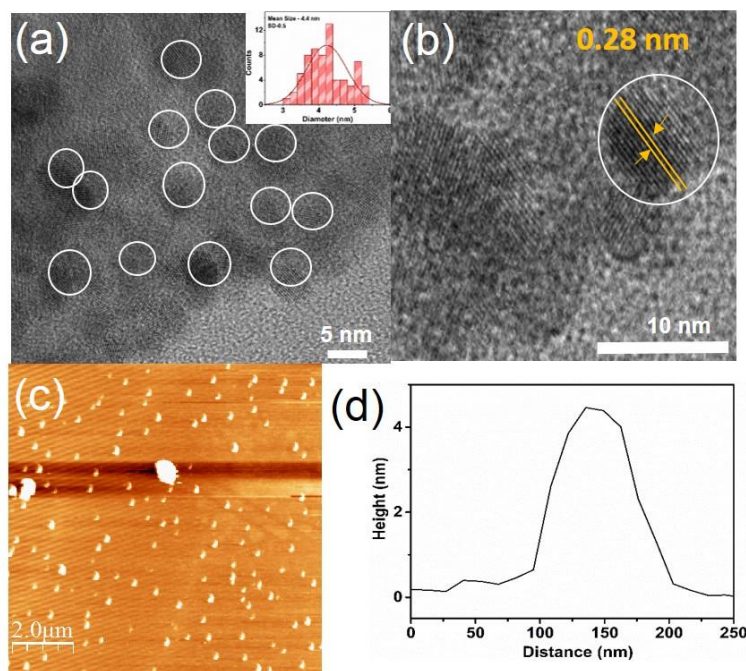


Figure 6.5: (a,b) HR-TEM image of MoS₂ QD (Inset is showing particle size distribution (~4.4 nm). (c,d) AFM image and height profile of MoS₂ QD.

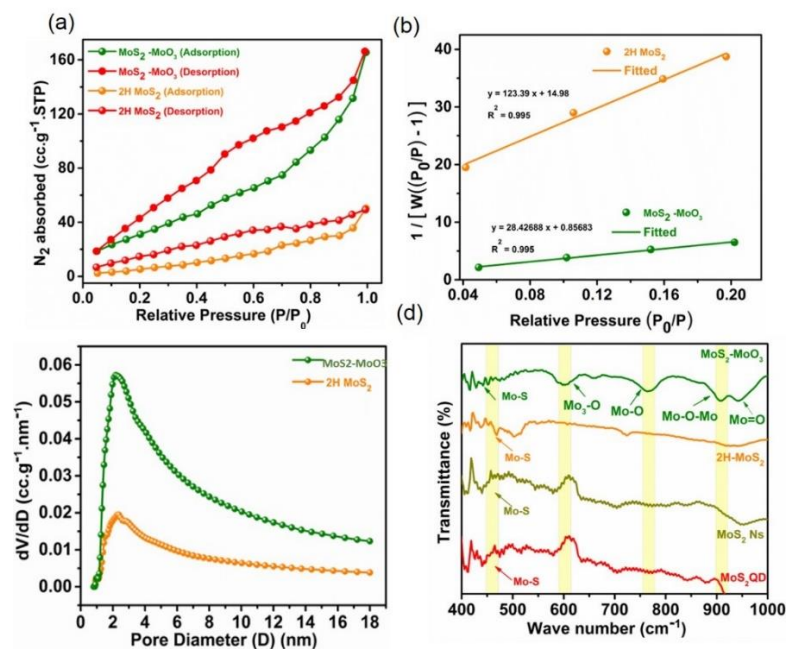


Figure 6.6: N₂ adsorption-desorption isotherm of (a) MoS₂-MoO₃ and 2H-MoS₂ (b,c) pore diameter distribution with relative pressure. (d) FTIR spectra of MoS₂-MoO₃, 2H-MoS₂, MoS₂ Ns and MoS₂ QD.

6.3.2. Band Engineering and surface activity

First, principles based structural optimizations reveal 1T-MoS₂ and 2H-MoS₂ are metallic and semiconducting in their pristine form as shown in Figure 6.7a,b. DFT-based structural modeling indicates that the 1T-MoS₂ and MoO₃ layers interact via van der Waals interaction with the out-of-plane O atoms of the MoO₃ layer pointing inward towards the MoS₂ layer (Figure 6.7c). To correctly model the vacancy-induced MoS₂-MoO₃ (o-MoS₂-MoO₃), the vacancy formation energy is investigated by removing oxygen atoms residing in-plane and out-of-plane of the MoO₃ layer. The vacancy formation energy is calculated to be -1.45 eV and -1.31 eV for O vacancy incorporated in the system by removing one in-plane O atom and one out-of-plane O atom respectively. The higher negative value of the in-plane oxygen vacancy formation energy represents the higher stability of the system and subsequent HER mechanism on the vacancy induced MoS₂-MoO₃ has been studied for the system with in-plane oxygen vacancy (Figure 6.7d).

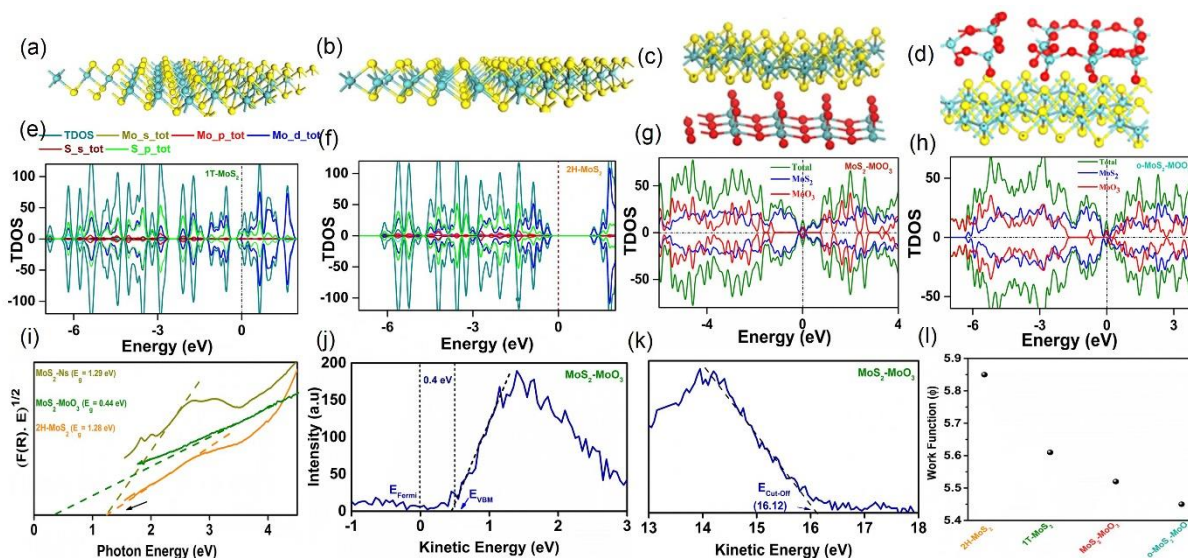


Figure 6.7: Energy optimized structures and total Density of states (TDOS) of (a,e) 1T- MoS₂ and (b,f) 2H-MoS₂ (c,g) MoS₂-MoO₃ and (d,h) o-MoS₂-MoO₃. D band center has been shown in DOS curves. (i) Tauc plot has been calculated from absorbance spectra. (j,k) Ultraviolet photoelectron spectroscopy (UPS) spectrum for MoS₂-MoO₃ (l) DFT-based work function of different MoS₂ based heterostructure.

The metallic phase has no band gap at or near the Fermi level in case of both MoS₂-MoO₃ and o-MoS₂-MoO₃ (Figure 6.7g,h). The optical band gap values calculated for MoS₂-MoO₃, 2H-MoS₂,

MoS₂ Ns, and MoS₂ QD are 0.4 eV, 1.3 eV, 1.8 eV, and 3.8 eV, respectively (Figure 6.7i) [71]. Generally, metal surface contains active sites for hydrogen adsorption due to high accessibility of electron density at the conduction band. From ultraviolet photoelectron spectroscopy (UPS), it has been observed that MoS₂-MoO₃ exhibits work function (ϕ) and valance band maxima at 5.5 eV and 0.4 eV respectively (Figure 6.7j,k). DFT calculation suggests the work function (ϕ) has significantly shrunk for o-MoS₂-MoO₃ to 5.45 eV in comparison with MoS₂-MoO₃ (ϕ - 5.52 eV), 1T-MoS₂ (ϕ - 5.61 eV) and 2H-MoS₂ (ϕ -5.85 eV) which well justifies our experimental analysis (Figure 6.7l and 6.8).

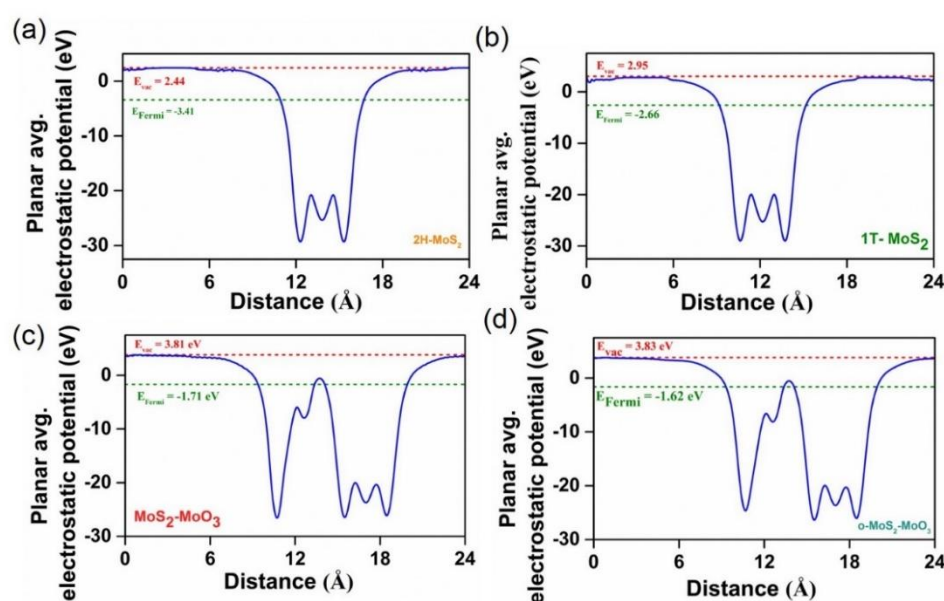


Figure 6.8: Work function of (a) 2H- MoS₂ and (b) 1T-MoS₂ (c) MoS₂-MoO₃ and (d) o-MoS₂-MoO₃ from DFT analyses.

The UV-Vis absorption study reveals a decrease in absorbance with wavelength for MoS₂-MoO₃, mainly due to metal scattering of 1T-MoS₂ (Figure 6.9a). Since the absorbance is much weaker for MoS₂-MoO₃, the optical band gap (E_g) has been calculated from DRS spectra having band gap close to zero, concluding that metallic phase predominantly exists in the composite system (Figure 6.9b). The surface activity of MoS₂-MoO₃ has been measured from zeta potential and contact angle measurements. Generally, the 1T MoS₂ is hydrophilic in comparison with 2H-MoS₂ counterpart. Our study manifests MoS₂-MoO₃ and 2H-MoS₂ exhibit contact angles of $24^\circ \pm 8^\circ$ and $115^\circ \pm$

having highly hydrophilic and hydrophobic properties, respectively (Figure 6.9c). The surface charge is calculated from zeta potential analyses and the values are found to be -4.5 ± 2 mV and $+1 \pm 0.8$ mV for $\text{MoS}_2\text{-MoO}_3$ and 2H-MoS_2 , respectively (Figure 6.9c). The negative zeta potential and hydrophilicity are attributed to higher concentrations of negative surface charge due to S^{2-} and O^{2-} in case of $\text{MoS}_2\text{-MoO}_3$ as compared to 2H-MoS_2 .

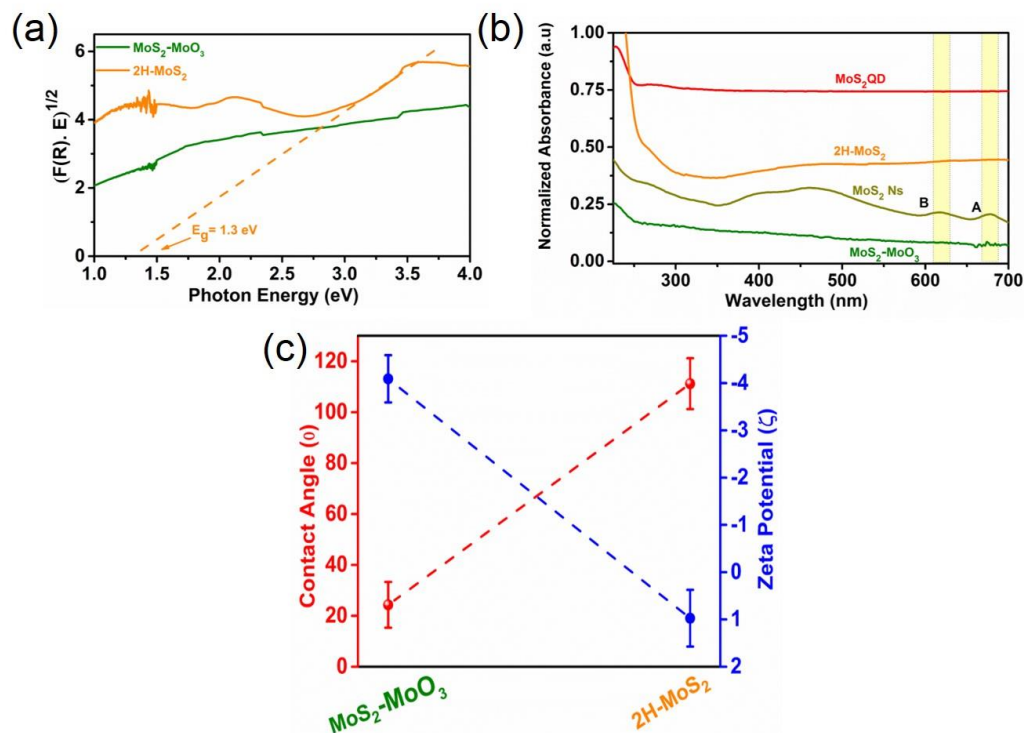


Figure 6.9: (a) Tauc plot from Diffuse Reflectance spectroscopy (DRS) (b) UV-Vis absorbance spectra of $\text{MoS}_2\text{-MoO}_3$ (DI), 2H-MoS_2 (DI), MoS_2 Ns (DMF) and MoS_2 QD (DMF). (c) Comparison of zeta potential (ζ) between $\text{MoS}_2\text{-MoO}_3$ and 2H-MoS_2 .

6.3.3. Acidic HER activity and catalytic mechanism

The HER performance of $\text{MoS}_2\text{-MoO}_3$, 2H-MoS_2 , and MoS_2 QD has been obtained via linear sweep voltammetry (LSV) in N_2 saturated 0.5 M H_2SO_4 . From iR-corrected polarization curve (LSV), the $\text{MoS}_2\text{-MoO}_3$ exhibits superior HER performance in acidic media (pH~1) to an overpotential of (η_{10}) ~114 mV at current density of 10 mA cm^{-2} . The as-synthesized $\text{MoS}_2\text{-MoO}_3$ is a much better electrocatalyst than previously reported crystalline $\text{MoS}_2\text{-MoO}_3$, bare 1T MoS_2 , or composites. In comparison, the 2H-MoS_2 and MoS_2 QD show η_{10} ~331 mV and η_{10} ~475 mV in acidic medium exhibiting poor catalytic performance (Figure 6.10a). The reaction

kinetics and rate-determining step has been obtained from Tafel slope, where MoS₂-MoO₃ shows a 46.18 mV/decade value in 0.5 M H₂SO₄ following Volmer–Heyrovsky mechanism (Figure 6.10b) [72–73]. In contrast, the calculated Tafel slope of 20% Pt/C, 2H-MoS₂ and MoS₂ QD are 39.65 mV/decade, 103 mV/decade, and 161 mV/decade, respectively (Figure 6.10c). Electrochemical impedance spectroscopy further demonstrated faster charge transfer kinetics of MoS₂-MoO₃ with a much lower charge transfer resistance (R_{ct}) \sim 45 Ω as compared to 2H-MoS₂ (R_{ct} \sim 83.9 Ω) and MoS₂ QD (R_{ct} \sim 859 Ω). The lower R_{ct} manifests higher conductivity of the MoS₂-MoO₃ surface, enhancing the HER efficiency (Figure 6.10d & table 6.3).

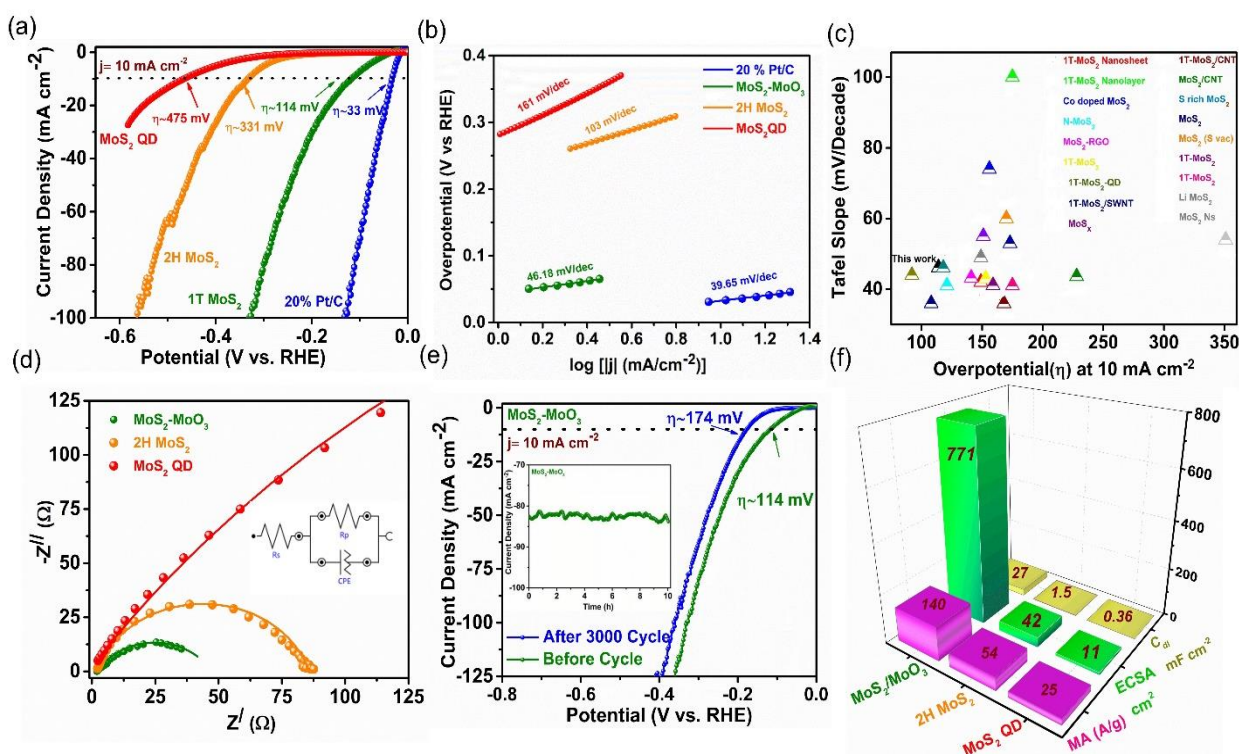


Figure 6.10: HER activity in 0.5 M H₂SO₄ (a) LSV polarization curves (b) Tafel slopes of the as-prepared catalysts (c) Comparison of the HER Kinetics (overpotential and Tafel slope) for MoS₂-MoO₃ with different MoS₂ based catalysts (Table 6.4) [84–101] (d) Nyquist plots for MoS₂-MoO₃, 2H-MoS₂, and MoS₂ QD at potential -0.4 V vs. RHE (Inset showing circuit diagram) (e) Polarization curve of MoS₂-MoO₃ before and after 3000 cycles (50 hours); Inset showing chronoamperometry test for 10 hours (f) Comparison of mass activity (MA) at η -300 mV, electrochemically active surface area (ECSA) and C_{dl} of MoS₂-MoO₃, 2H-MoS₂ and MoS₂ QD.

However, negligible decay of η_{10} up to 174 mV after 3000 cycles (50 hours) manifests superior HER durability of MoS₂-MoO₃ (Figure 6.10e). From chronoamperometry analysis, there is only a minute decrease in relative current density for MoS₂-MoO₃ after 10 hours of continuous tests (Figure 6.10e). To shed light on the active catalytic sites, MoS₂-MoO₃ has been found to exhibit significantly higher capacitive double layer (c_{dl}) $\sim 27 \text{ mF cm}^{-2}$ than 2H-MoS₂ ($c_{dl} \sim 1.5 \text{ mF cm}^{-2}$) and MoS₂ QD ($c_{dl} \sim 0.36 \text{ mF cm}^{-2}$) (Figure 6.10f). Moreover, the magnitude of active surface area (ESCA) for MoS₂-MoO₃ shows a value of 771 cm² which is more significant than 2H-MoS₂ (ESCA $\sim 42 \text{ cm}^2$) and MoS₂ QD (ESCA $\sim 10.3 \text{ cm}^2$) (Figure 6.10f). The mass activity (MA) of MoS₂-MoO₃ is calculated to be 140 A/g which is 2.5 times higher than that of 2H-MoS₂ (Figure 6.10f).

Materials	R _{ct}	R _s	Y _o	n	C _{eff} (mF)	C _{eff} (mF) per cm ⁻²
MoS ₂ -MoO ₃	45 Ω	2.20 Ω	6.72 mMho	0.681	1.63	23.10
2H-MoS ₂	83.9 Ω	11 Ω	55 μ Mho	0.818	0.09	1.27
MoS ₂ -QD	859 Ω	13.4 Ω	62.6 μ Mho	0.628	0.019	0.26

Table 6.3: Fitted parameters of Nyquist plots for MoS₂-MoO₃, 2H-MoS₂, and MoS₂ QD at potential -0.4 V vs.RHE in 0.5 M H₂SO₄.

We further evaluated the number of H₂ produced per second per active site (TOF) of MoS₂-MoO₃ and it is found to be the highest (0.57 H₂ s⁻¹) in comparison to 2H-MoS₂ (0.21 H₂ s⁻¹) and MoS₂ QD (0.29 H₂ s⁻¹) at $\eta \sim 300 \text{ mV}$, shown in Figure 6.11. The in-situ gas chromatographic (GC) technique determines the rate of H₂ production of MoS₂-MoO₃ in the order of $4 \times 10^{-5} \text{ mol h}^{-1}$, which is much higher than 2H-MoS₂ ($0.3 \times 10^{-5} \text{ mol h}^{-1}$) (Figure 6.11).

To evaluate the electronic interaction between adsorbate hydrogen and catalysts, we have assessed the d band energy (E_d) for 1T- MoS₂, 2H-MoS₂, MoS₂-MoO₃, and o-MoS₂-MoO₃ to a value of -3.76 eV, -3.39 eV, -4.46 eV, and -4.71 eV respectively (Figure 6.12a). Generally, the coupling between the adsorbate and MoS₂ d states gives rise to a lower energy bonding state and higher energy antibonding state, which are closer to Fermi level and higher than d states [72,74].

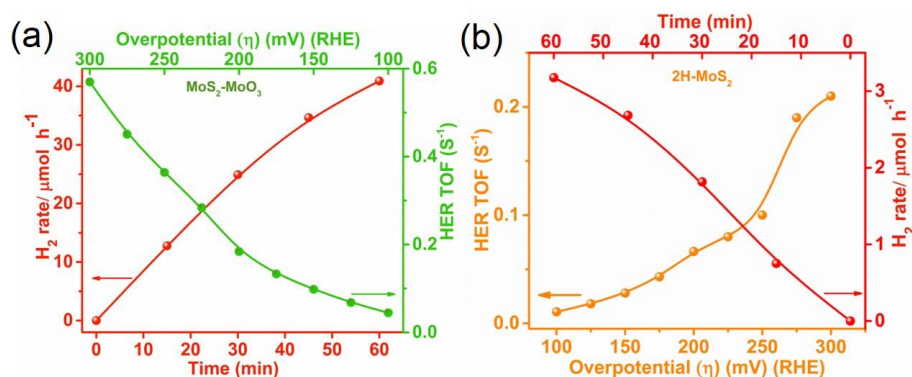


Figure 6.11: (a) HER TOF (s⁻¹) with overpotential (η) and H₂ evolution rate from gas chromatography of MoS₂-MoO₃ and 2H-MoS₂.

The most negative d band center of o-MoS₂-MoO₃ implies antibonding states are stabilized and weakens the bond strength between adsorbate (H^{*}) and catalyst. Such weaker interaction increases the H adsorption energy (adsorption process becomes less exothermic) and facilitates the easy desorption of H from the catalytic interface, which is beneficial for efficient HER catalysis [73]. To understand the band engineering for HER kinetics, the energy level diagram of MoS₂-MoO₃ (difference between vacuum and Fermi level from UPS analyses) has been calculated to be -5.5 eV (1 V vs. RHE), having closer to than reduction potential of H₂O (1.23 V) (Figure 6.12b). Thus, closer zero reduction potential benefits water splitting kinetics [75]. The DFT study has been investigated to understand the detailed fundamental reaction pathways and active sites in MoS₂-MoO₃ and o-MoS₂-MoO₃ (Figure 6.12c). Initially, the free energy (ΔG) of the intermediate adsorbed hydrogen (H^{*}) of different possible sites of both configurations has been estimated w.r.t H⁺/H₂ with $\Delta G=0$ eV (detailed in experimental section). The free energy of H^{*} adsorption at three various sites of MoS₂-MoO₃ shows a value of -0.03 eV (S1 site: O site of MoO₃), 0.87 eV (S2 site: S site of 1T MoS₂), and 1.84 eV (S3 site: Mo site of MoO₃). In comparison, o-MoS₂-MoO₃ exhibits free energy for H^{*} adsorption at -0.10 eV (S4 site: O site of MoO₃), 0.88 eV (S6 site: S site of 1T MoS₂), and 1.70 eV (S8 site: Mo site of MoO₃ far from O vacancy) (Figure 6.12c). The -0.07 eV lower energy suggests proton trapping at the O site becomes more significant in MoS₂-MoO₃ after oxygen vacancy. The negative ΔG values of H^{*} at O site for MoS₂-MoO₃ (-0.03 eV) and o-MoS₂-MoO₃ (-0.10 eV) suggest a preferential hydrogen adsorption site at the intermediate. Comparatively, two most possible configurations

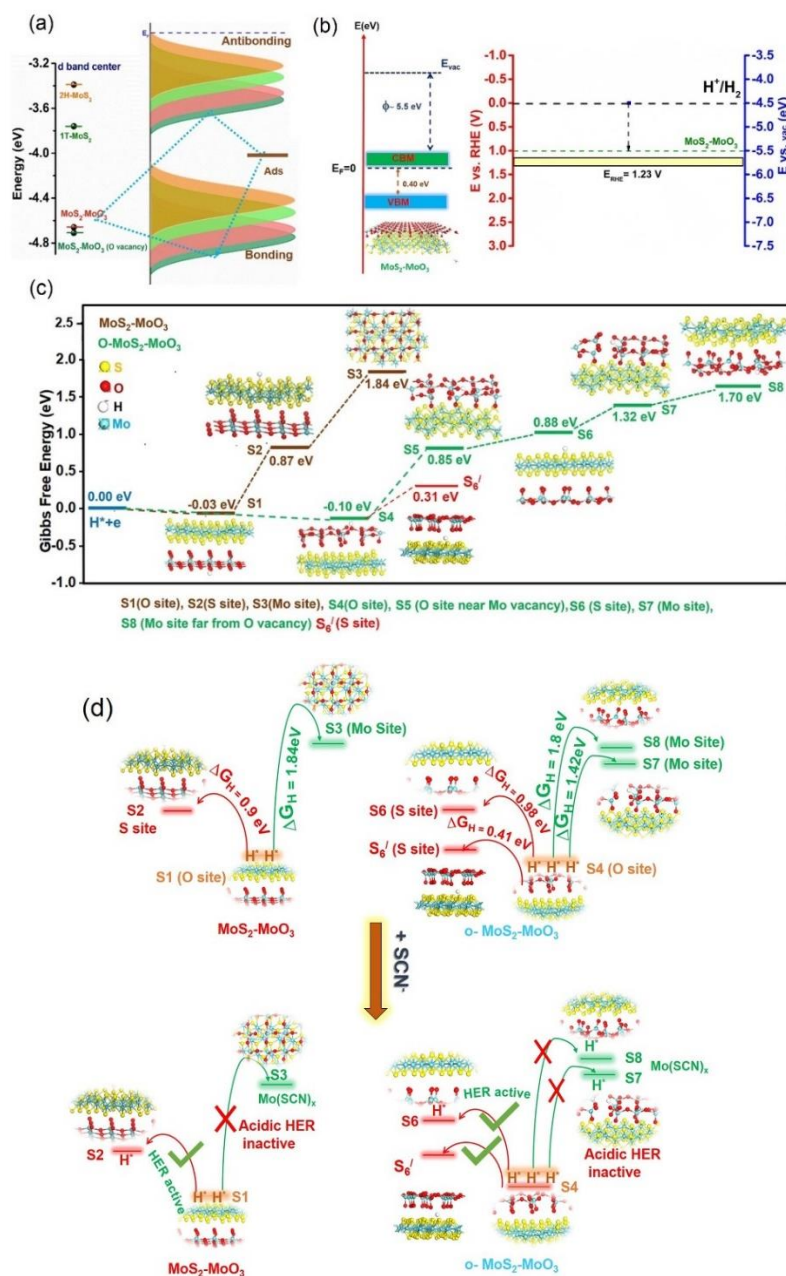


Figure 6.12: (a) Schematic representation of bonding and antibonding state between adsorbate (H*) and catalyst. (b) Experimentally, Band structure and energy level diagram for HER of MoS₂-MoO₃ obtained from UPS spectra (c) DFT analyses of HER process involving adsorption free energy of H* (ΔG_{ads}) at various catalytic sites of MoS₂-MoO₃ without and with oxygen vacancy (d) Schematic illustration of masking mechanism for Mo⁵⁺/Mo⁶⁺ with SCN⁻ and determination of acidic HER active site and H₂ spillover energy.

of hydrogen adsorption at oxygen site near Mo vacancy (S5 site) and Mo site near oxygen vacancy (S7 site) show free energy at 0.85 eV and 1.32 eV respectively. Generally, for binary composite, hydrogen spillover between metal and non-metal surfaces enhances faster H_2 evolution rate, which depends upon the thermodynamic barrier [76-79]. Secondly, favorable adsorption of H^* at the catalytic site (more negative free energy) leads to thermodynamically unfavorable desorption, an essential step in HER kinetics [80-81]. In our scenario, if H^* can migrate from O sites to Sulphur or Mo sites, hydrogen evolution will be faster than single active Mo or S site in 1T/2H-MoS₂. The thermodynamic barrier (free energy difference, ΔG_H) between Mo site (S3 & S8 site) and O site (S1 & S4 site) are 1.84 eV and 1.80 eV for MoS₂-MoO₃ and o-MoS₂-MoO₃ respectively. Conversely, the hydrogen spillover across the interface between O site (S1 & S4 site) to S site (S2 & S6 site) is immensely facilitated due to lower ΔG_H across 0.90 eV and 0.98 eV respectively. Significantly, the barrier is too high to exhibit spillover mechanism and such energy barrier can be reduced when the exothermic and endothermic adsorption sites lie closer to $\Delta G=0$ eV. It should be noted that the H^* adsorption on S atom (S2 & S6 site) is out of the surface from O layer in MoO₃ and the diffusion pathway of H^* is hindered. We try to modify the possible configuration of H^* adsorption on S atom (S6') in o-MoS₂-MoO₃ where S layer of MoS₂ and O layer of MoO₃ occupies a confined space. Notably, the significant change of ΔG from 0.88 eV (S6 site) to 0.31 eV (S6' site) gradually facilitates the H^* adsorption with lower thermodynamic barrier (0.41 eV). In this regard, hydrogen adsorption-desorption is highly favorable in confined Oxygen and sulphur layer and triggers the production of H_2 molecules (Figure 6.12d). Various experimental tools have been employed to understand the theoretically described spillover phenomenon and active sites (S^{2-} and O^{2-}) in acidic HER. Initially, we incorporated thiocyanate (SCN^-) solution as a masking agent during catalysis to evaluate the influence of deactivation on metal centers. While SCN^- has an affinity to bind with Pt based metals with $p(\pi)$ - $d(\pi)$ overlap via synergistic mechanism [81]. The interaction between various metal centers ($Mo^{4+/5+/6+}$) with SCN^-/NCS^- has been confirmed from UV-Vis absorbance and FTIR spectroscopy at three different pH~2, pH~7, and pH~14 solutions [82,83]. From UV-Vis spectroscopy, multiple absorption peaks remain prominent in acidic and alkaline conditions within the range 250-450 nm, which suggests SCN^-/NCS^- occupies the coordination site of Mo leading to $Mo(SCN)_x^- / Mo(SCN)_x$ type complex formation (Figure 6.13) [83]. It should be noted

the intensity of new absorption maxima decreases with time, and the peak remains completely diminished after four days, shown in Figure 6.14. To unravel the specified Mo centers for complexation with SCN^- at different pHs, the UV-Vis spectrum of 2H-MoS₂ with SCN^- has been evaluated. Interestingly, no peaks are obtained over a wide range of absorption wavelengths in any medium, manifesting $\text{Mo}^{5+/6+}$ are preferably bound with SCN^- rather than Mo^{4+} (Figure 6.13d-f). In addition, the C-N stretching frequency significantly reduced from 1663 cm^{-1} to 1644 cm^{-1} after binding with MoS₂-MoO₃ shown in Figure 6.14. Such result elucidates the synergistic mechanism between the $\text{Mo}^{5+/6+}$ with SCN^- via $p(\pi)$ - $d(\pi)$ overlap and shrinks the C-N bond strength (Figure 6.14b,c). However, no degradation of HER polarization curve has been noticed after SCN^- addition (Figure 6.15). As anticipated, the HER LSV profile remains unaltered after 4 hours (240 cycles) which strongly suggests minimal effects of $\text{Mo}^{5+}/\text{Mo}^{6+}$ as an active site in acidic HER (Figure 6.15a). In contrast, the LSV curve remains unaltered for 2H-MoS₂ after adding SCN^- indicating inactive site of Mo^{4+} for acidic HER (Figure 6.15b). Furthermore, post XPS analyses of Mo^{6+} 3d spectra remain unchanged after 3000 cycles in acidic HE

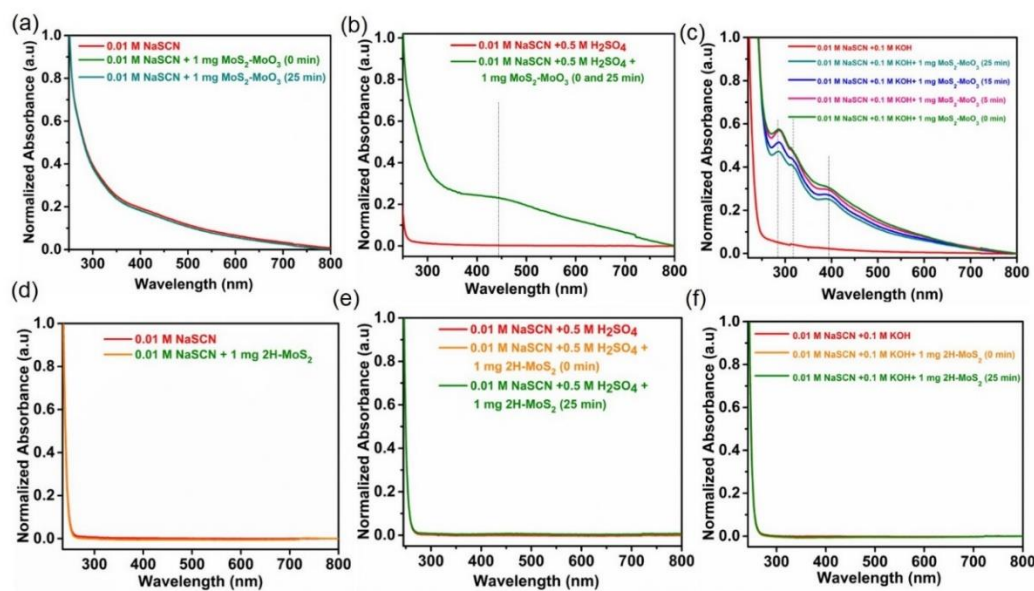


Figure 6.13: Effect of sodium thiocyanate in UV-Vis absorbance of MoS₂-MoO₃. Absorbance profile of 0.01 M NaSCN and MoS₂-MoO₃ at (a) pH~7 (b) pH~2 and (c) pH~14. Absorbance profile of 0.01 M NaSCN and 2H-MoS₂ at (d) pH~7 (e) pH~2 and (f) pH~14.

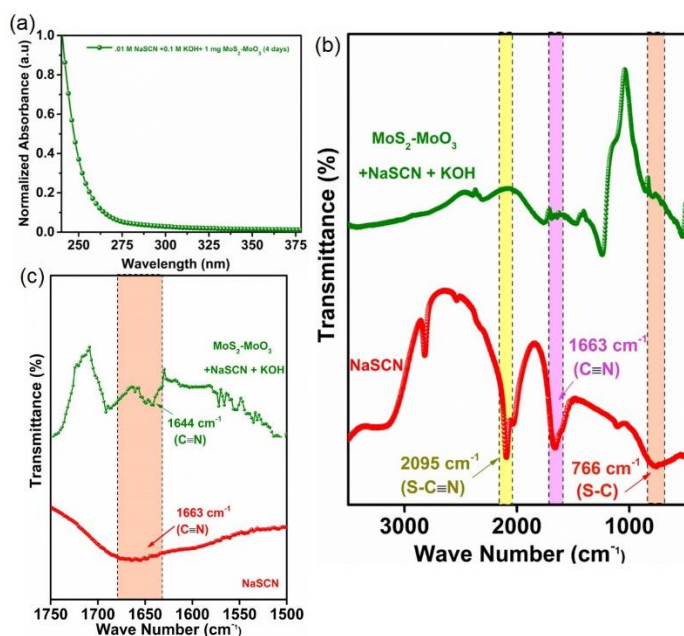


Figure 6.14: Absorbance profile of 0.01 M NaSCN and MoS₂-MoO₃ at pH~14 after four days (b,c) FTIR spectra of (b) NaSCN and MoS₂-MoO₃ + NaSCN at pH-14 (c) Stretching frequency of C≡N bond of NaSCN before and after MoS₂-MoO₃ addition at pH~14.

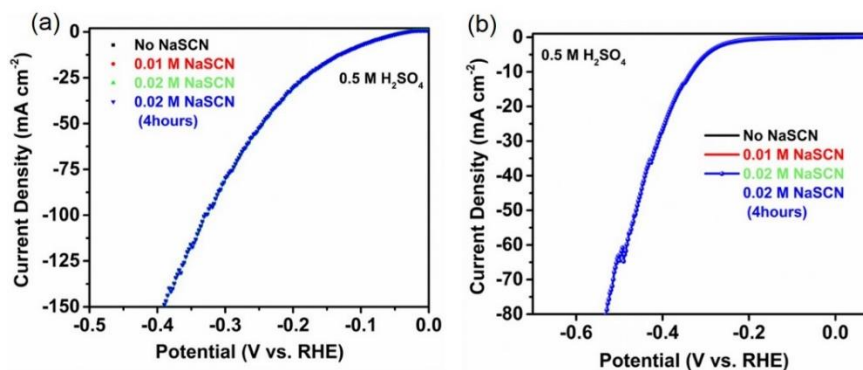


Figure 6.15: Effect of SCN⁻ on catalytic activity of (a) MoS₂-MoO₃ and (b) 2H-MoS₂ towards HER activity in 0.5 M H₂SO₄ solution. Inset showing negligible change in HER profile with SCN⁻ addition for MoS₂-MoO₃ and 2H-MoS₂.

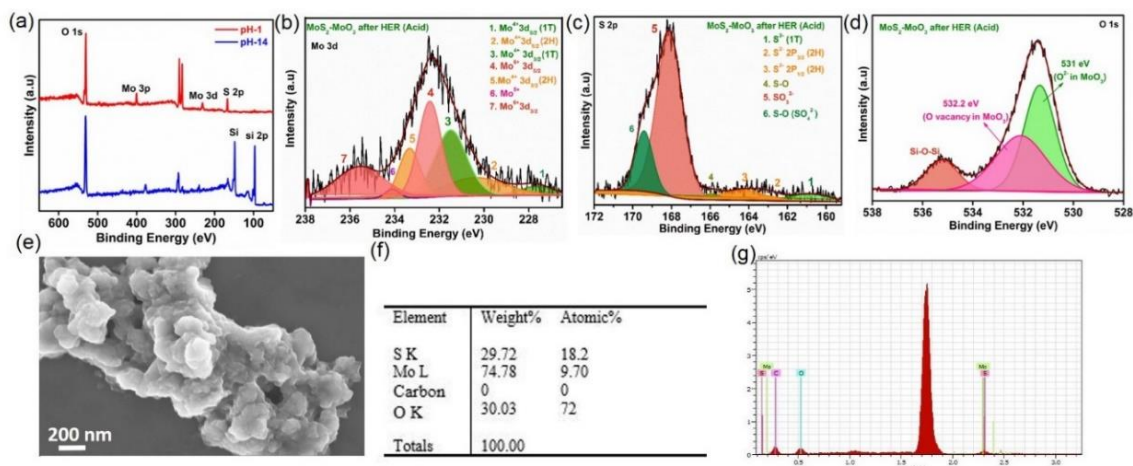


Figure 6.16: (a) Post XPS survey spectra of MoS₂-MoO₃ after 3000 cycles in pH-1 and pH-14 solution. XPS spectra of (b) Mo 3d (c) S 2p and (d) O 1s in 0.5 M H₂SO₄ solution after 3000 cycles. (e-g) FESEM image and EDX analyses of MoS₂-MoO₃ after HER in 0.5 M H₂SO₄.

Catalyst	Overpotential (η) (mV) at 10 mA cm ⁻²	Tafel Slope (mV/Decade)	Stability (Hours or Cycles)	Methods	Ref
1T-2H-MoS ₂ -MoO ₃	114	46.18	3000 cycles	Hydrothermal	Our work
Flower like 2H-MoS ₂	331	103	-	Hydrothermal	Our work
1T' MoS ₂ nano monolayers	149	42	10000 cycles	Colloidal	84
1T' MoS ₂ Nanosheet	175	100	-	CVD	85
Co-doped MoS ₂ foam	156	74	5000 cycles	Wet chemical synthesis	86
N-MoS ₂ nanosheet	121	41	5000 cycles	Sintering method	87
MoS ₂ /rGO	141	43.2	3000 cycles	Microwave assisted solvothermal	88
Porous-1T-MoS ₂	153	43	1000 cycles	Li ⁺ intercalation	89
1T-MoS ₂ QDs	92	44	10000 cycles	Li ⁺ intercalation	90
1T-MoS ₂ /SWNT	108	36	3000 cycles	NH ₄ ⁺ intercalation	91
Amorphous-MoS _x	159	41.1	1000 cycles	Spray Pyrolysis	92
MoS _x /CNTs hybrid	168	36	-	Ultrasonic	93

Defects-MoS₂/CNTs	228	43.6	-	Quasi emulsion assistant strategy	94
Sulfur-rich amorphous MoS₂	118	46	1000 cycles	Aging	95
MoS₂ nanodots	173	53	10000 cycles	Li ⁺ intercalation	96
Strained MoS₂	170	60	-	CVD	97
1T- MoS₂/ carbon	151	55	5000 cycles	Hydrothermal	98
1T-MoS₂	175	41	1000 cycles	Hydrothermal	99
Phenyllithium-MoS₂	351	54	-	Aromatic exfoliated	100
Expanded MoS₂ nanosheets	149	49	3,000 cycles	Microwave-assisted synthesis	101

Table 6.4: Comparison of HER activity of MoS₂-MoO₃ with the reported MoS₂-based composite electrocatalysts in 0.5 M H₂SO₄ electrolyte.

The notable positive shift in binding energy of Mo⁴⁺ 3d (1T) has been determined after HER catalysis. However, the atomic percentage and peak intensity of S²⁻ (1T & 2H) is highly diminished (Figure 6.16). Post FESEM and EDX analyses suggest the agglomeration of the nanosheets after acidic HER catalysis (Figure 6.16). The two experimental tools and theoretically obtained spillover effect provide strong evidence of reactive S²⁻ and O²⁻ sites for efficient acidic HER catalysis. The HER activity has been compared with previously reported catalysts shown in table 6.4.

6.3.4. Alkaline HER activity and catalytic mechanism

To get details of the active sites' role in alkaline HER, we have investigated the overpotential and Tafel slopes of MoS₂-MoO₃, 2H-MoS₂, and MoS₂ QD. From LSV polarization curve, MoS₂-MoO₃ exhibits a low overpotential of (η_{10}) ~244 mV, which is much higher than 2H-MoS₂ (η_{10} ~405 mV) and MoS₂ QD (η_{10} ~ 517 mV) (Figure 6.17a and table 6.5). The Tafel slope has been calculated for 20% Pt/C, MoS₂-MoO₃, 2H-MoS₂ and MoS₂ QD and the corresponding values are found to be 56.85 mV/decade, 89.18 mV/decade, 153 mV/decade, and 233 mV/decade respectively (Figure 6.17b,c). However, MoS₂-MoO₃ shows charge transfer resistance (R_{ct}) ~ 50.8 Ω having a much lower value compared to 2H-MoS₂ (R_{ct} ~ 370 Ω) and MoS₂ QD (2.9 k Ω pH~14) (Figure 6.17d). The LSV curve remains unaltered (η_{10} ~266 mV) after 3000 cycles and chronoamperometry test for 10 hours, as shown in Figure 6.17e. The active site density from double layer capacitance (c_{dl}) and ESCA has been calculated for MoS₂-MoO₃ to 28.7 mF cm⁻²

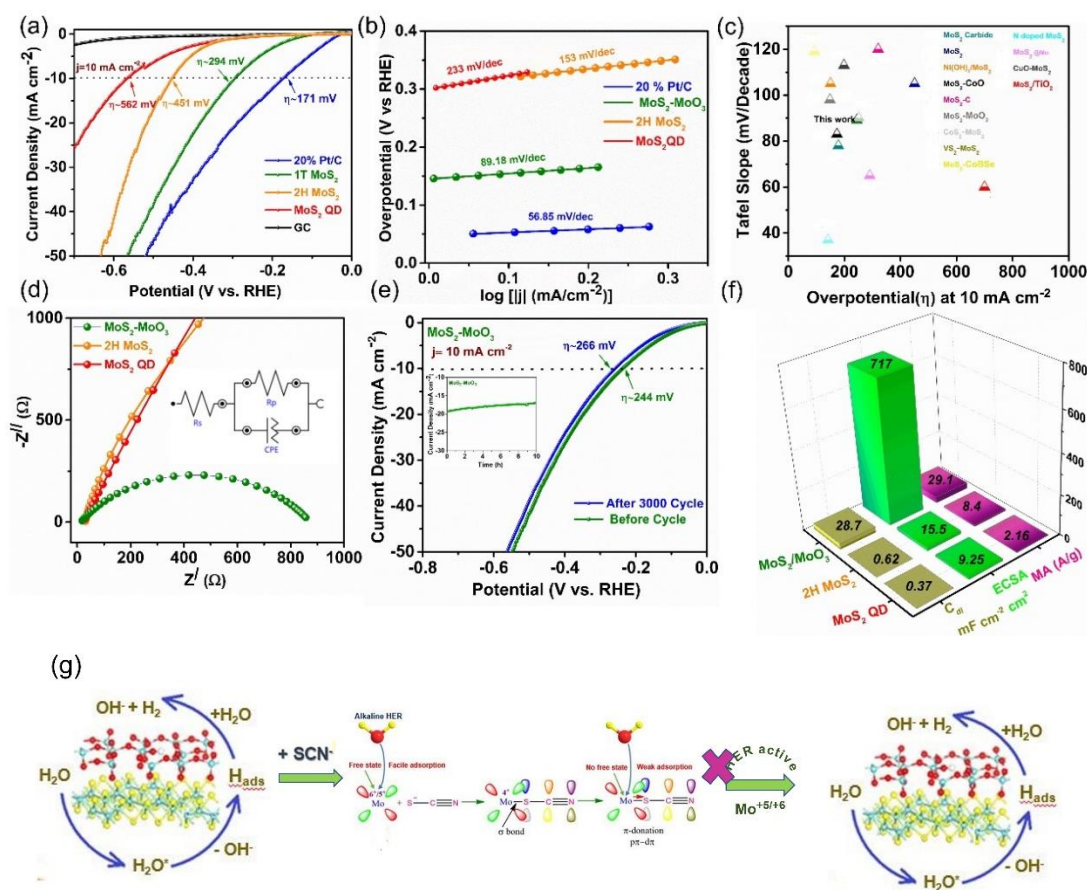


Figure 6.17: HER activity in 1 M KOH (a) LSV polarization curves (b) Tafel slopes of the as-prepared catalysts (c) Comparison of the HER Kinetics (table 6.5) [102-114] (d) Nyquist plots for at potential -0.4 V vs.RHE (Inset showing circuit diagram) (e) Polarization curve of MoS₂-MoO₃ after 3000 cycles; Inset showing chronoamperometry test (f) Comparison of mass activity at η -300 mV (MA), electrochemically active surface area (ESCA) and C_{dl} (g) Schematic illustration of masking mechanism for Mo⁵⁺/Mo⁶⁺ with SCN⁻ and determination of alkaline HER active site.

and 717 cm², which is significantly higher than 2H-MoS₂ (0.62 mF cm⁻², 15.5 cm²) and MoS₂ QD (0.37 mF cm⁻², 9.25 cm²). In addition, the mass activity of MoS₂-MoO₃ shows a value of 29.1 A/g, as shown in Figure 6.17f. The morphology-based pure 2H-MoS₂ cannot exhibit alkaline HER performances due to basal plane inactivity and poor reactive site density. Apart from high active site density and high conducting surfaces, the HER performance of alkaline medium is quite inferior to acidic HER. This can be summarized by two factors. Generally, the poor crystalline decelerates rate the HER kinetics in alkaline than acidic medium. Secondly, in

Volmer–Heyrovsky mechanism, the multiple reaction steps involving dissociation energy of water molecules (H_2O^*) to H^* and desorption of hydrogen (H^*) play a crucial role in faster alkaline HER kinetics (Figure 6.17g). In the previous section, it is well established that the high energy spillover effect of H^* becomes insignificant between Mo and O sites in acidic HER. To further verify the reactive centers, addition of SCN^- significantly reduces HER current density with large overpotential (Figure 6.18a). At 10 mA cm^{-2} current density, the overpotential changes to -0.4 V vs. RHE and -0.5 V vs. RHE with 0.01 M and 0.02 M SCN^- respectively, implying that $\text{Mo}^{5+}/\text{Mo}^{6+}$ has mainly involved for alkaline HER. It is the key to identifying the effect of HER kinetics with SCN^- for 2H-MoS_2 having negligible change in alkaline environment (Figure 6.18b). Post XPS and EDX analyses suggest that the area of Mo 3d spectra has been highly reduced due to involvement as a reactive site in alkaline HER (Figure 6.19). This further confirms the $\text{Mo}^{5+}/\text{Mo}^{6+}$ at the interface increases the active site density and interfacial electron transfer for H_2O^* and H^* adsorption and boosts the intrinsic alkaline HER activity for $\text{MoS}_2\text{-MoO}_3$.

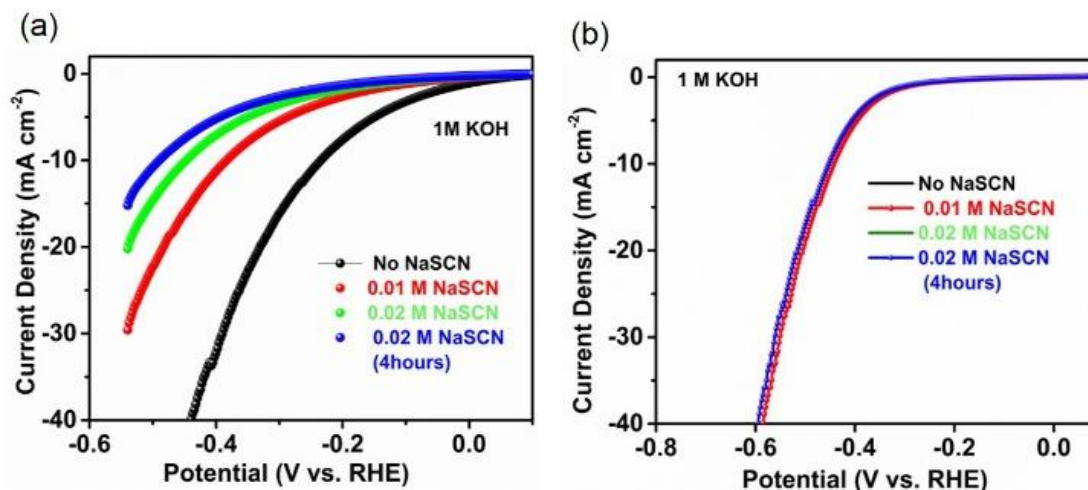


Figure 6.18: Effect of SCN^- on catalytic activity of $\text{MoS}_2\text{-MoO}_3$ and 2H-MoS_2 towards HER activity in 1 M KOH solution. Inset showing negligible change in HER profile with SCN^- addition for $\text{MoS}_2\text{-MoO}_3$ and 2H-MoS_2 .

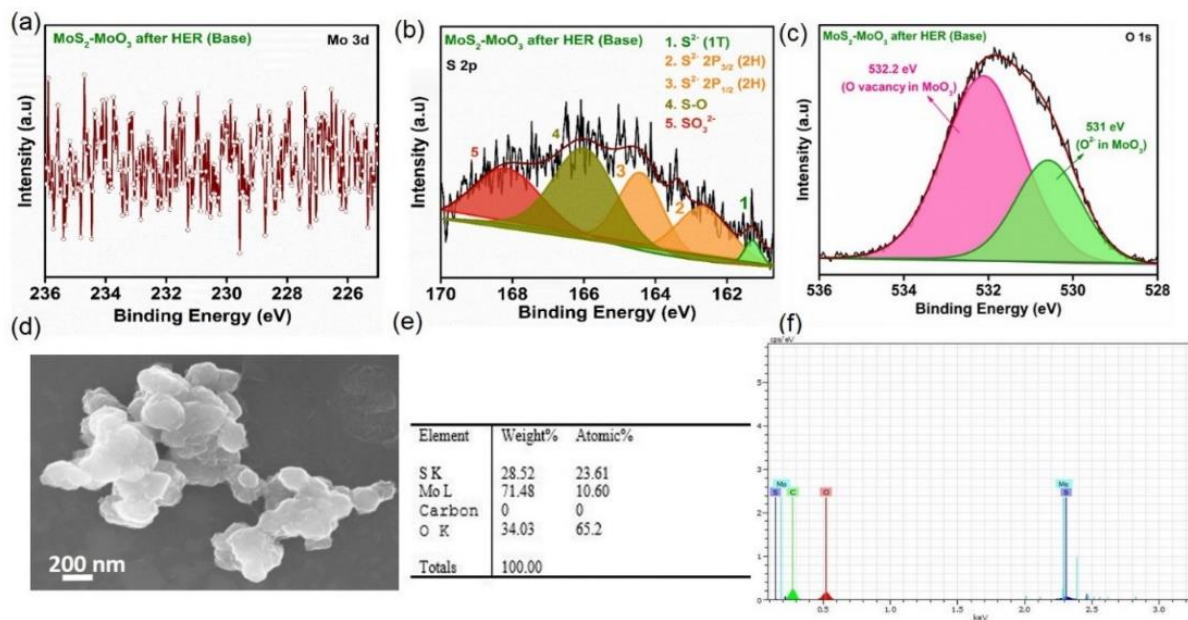


Figure 6.19: Post XPS spectra (3000 cycles) of (a) Mo 3d (b) S 2p and (c) O 1s of MoS₂-MoO₃ in 1 M KOH solution. (d-f) FESEM image and EDX analyses of MoS₂-MoO₃ after HER in 1 M KOH.

Catalyst	Overpotential (mV) (η) at 10 mA cm ⁻²	Tafel Slope (mV/Decade)	Stability (Hours or Cycles)	Methods	Ref
1T-2H-MoS ₂ -MoO ₃	244	89.18	3000 cycles	Hydrothermal	Our work
Molybdenum Carbide@Carbon Sheets	178	78	1000 cycles	Hydrothermal	102
MoS ₂ Nanosheet	450	105	-	Exfoliation	103
Ni(OH) ₂ /MoS ₂	150	105	1000 cycles	Ultrasonication and refluxed	104
MoS ₂ @CoO-coated carbon cloth	173	83	1000 cycles	Hydrothermal	105
MoS ₂ /Carbon	300 at 1 mA cm ⁻²	120	3000 cycles	PVD and annealing	106
MoS ₂ -MoO ₂ @NSC	156	99	-	pyrolysis	107
CoS ₂ - MoS ₂	251	90	-	Hydrothermal	108
VS ₂ - MoS ₂	148	98	-	Annealing	109
MoS ₂ /CoB-Se/CC	93	119	-	Hydrothermal	110
N doped MoS ₂	141	37	1000 cycles	Solvothermal	111

MoS ₂ @Mo-S-C ₃ N ₄	290	65	5000 cycles	Hydrothermal	112
Ru-doped CuO/MoS ₂	198	113	1000 cycles	Hydrothermal	113
MoS ₂ /TiO ₂	700	60	-	Hydrothermal	114

Table 6.5: Comparison of HER activity of MoS₂-MoO₃ with the reported MoS₂-based composite electrocatalysts in 1 M KOH electrolyte.

6.3.5. Catalytic reduction of PNP and K₃[Fe(CN)₆]

Initially, we performed the experiments with minimal O₂ saturation (< 1 mg/ml) at a fixed concentration of MoS₂-MoO₃ (1mg), 0.1 M NaBH₄, and 1.5 mM PNP. The time dependent reduction process has been determined by reducing the absorption maxima of PNP ($\lambda_{\text{max}} \sim 400$ nm) along with enhancing the absorption intensity of para amino phenol (PAP) at $\lambda_{\text{max}} \sim 300$ nm, shown in Figure 6.20a. Two isosbestic points suggest the successful formation of para-aminophenol (PAP) [115]. Notably, the rate of catalytic reduction is facile for MoS₂-MoO₃ (~8 min) than MoS₂ QD (~31 min) and MoS₂ Ns (> 3 days). No noticeable change in PNP maxima suggests that the 2H-MoS₂ and bare NaBH₄ are catalytically inactive for chemical reduction. The rate constant (k) has been estimated for MoS₂-MoO₃ and MoS₂ QD to be 0.43 min⁻¹ and 0.09 min⁻¹, respectively (Figure 6.20b). We further investigated the reduction kinetics by optimizing the NaBH₄ and MoS₂-MoO₃ concentrations and the maximum rate constant is obtained to be k~1.22 min⁻¹. The increase in rate constant is mainly due to higher accessibility of BH₄⁻ ions and catalysts on the catalytic sites (Figure 6.20c). Compared with MoS₂-MoO₃, the rate constant has been estimated to be 0.04 min⁻¹ and 0.09 min⁻¹ for 0.009 mol% and 0.01 mol% of MoS₂ QDs. Temperature-dependent absorbance measurement has been studied to obtain total activation energy (E_a) for the PNP reduction. Figures 6.20d show activation energy (E_a) for MoS₂-MoO₃ having a value of ~12.55 kJ/mol much lower than MoS₂ QDs (E_a ~32.55 kJ/mol). However, the reduction of such catalysts is highly influenced by dissolved oxygen and induction time [116]. We employed O₂ purging into the aliquot before adding the substrate (PNP). The dissolved oxygen concentration is estimated to be 5.5 mg/ml, 7.9 mg/ml and 10.1 mg/ml at different purging times of 5 min, 10 min, and 15 min, (Figure 6.20e). The induction time is enhanced with O₂ purging duration where the interaction or adsorption of dissolved oxygen in MoS₂-MoO₃ hinders the reactive centers for PNP reduction. Secondly, the intermediate 4-nitrophenol undergoes oxidation with excess O₂ to regenerate the PNP and inhibits the 4-AP formation [116]. The appearance of mass spectroscopic signals at 110.04 *m/z* is attributed to amine-protonated PAP

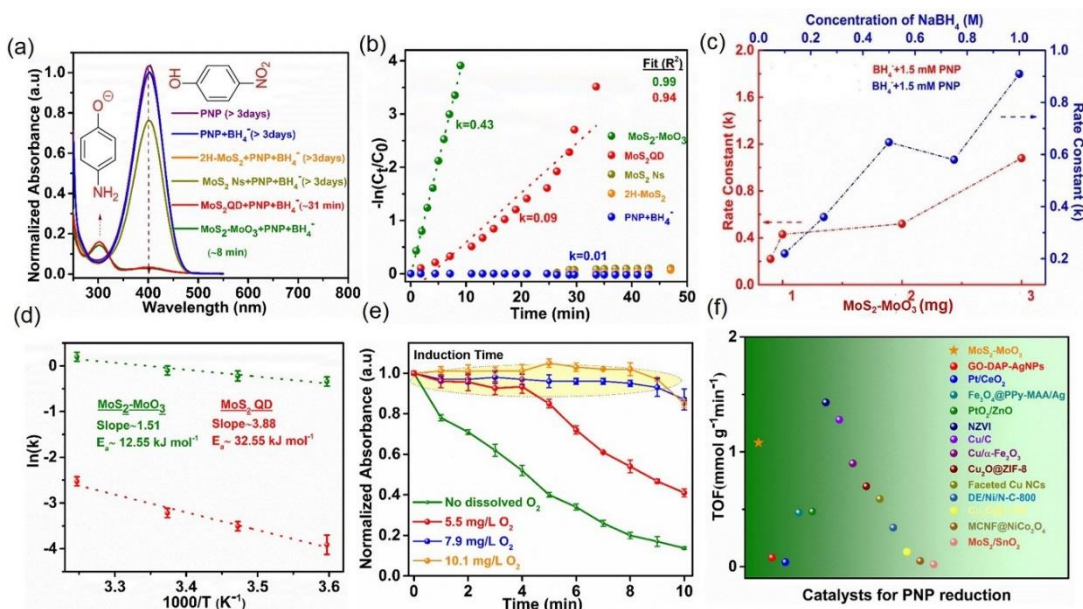


Figure 6.20: (a) MoS₂ based catalytic reduction of PNP (1.5 mM) involves decrease in 4-nitrophenolate absorption at ~ 400 nm with the formation of new peak at ~300 nm in 0.1 M NaBH₄ (b) Determination of rate constant (k) from the linearized data for the first order kinetics of PNP (1.5 mM) reduction with 0.1 M NaBH₄ (c) Variation of the rate constant (k) with various concentration of MoS₂-MoO₃ and NaBH₄ with 1.5 mM PNP solution (d) Plot of $\ln k$ vs. $1/T$ for the PNP reduction with 0.25 M NaBH₄ and 1.5 mM PNP keeping concentration of MoS₂-MoO₃ and MoS₂-QD are 1 mg and 0.01 mol% respectively. Error bars correspond to standard deviation on three experiments (e) Progress of PNP (1.5 mM) reduction catalyzed by MoS₂- MoO₃ (1 mg) and determination of induction time after O₂ purging at different concentrations (5-15 min) (f) Comparison of turnover frequency (TOF) [ref:119-131].

(PAP-H) formation as a major product (Figure 6.21a). Generally, PAP is unstable in alkaline solutions and undergoes oxidation to form different oxidized fragments. Two new peaks at 107.96 and 108.5 m/z are assigned to benzoquinone and 4-amino phenoxide ion (PAP⁻), respectively. The formation of by-products and dissociation of PAP results in non-constantly enhancing peak intensity with time at λ_{\max} ~ 300 nm for all the catalyst systems. Mass spectra suggest that the peak intensity at 110.04 m/z is largely diminished, with an intense peak at 140.02 m/z attributed to protonated PNP (PNP-H). Interestingly, two new intense peaks at 114.05 m/z are mainly assessed for maleic acid formation via ring opening mechanism of PNP (Figure 6.21b) [117]. The high TOF (1.02 mmole g⁻¹ min⁻¹) and activity factor (0.43 min⁻¹ mg⁻¹) of MoS₂-MoO₃

are relatively higher than reported precious-metal and non-precious materials (Figure 6.20f). It is mentioned that positively charged metal nanoparticles (Ag, Au, etc.) with positive zeta potential are prone to participate in the PNP reduction [118]. Our study reveals negative zeta potential (ζ) of MoS₂-MoO₃ than 2H-MoS₂, where the contribution of surface charge for PNP reduction needs to be investigated. We try to modulate the surface charge of MoS₂-MoO₃ and MoS₂ QDs by changing the pH of the medium to acidic. Keeping the concentrations of catalyst (1mg), NaBH₄ (0.1 M), and PNP (1.5 mM) are unchanged, the rate constant in acidic media (pH~2) for both MoS₂-MoO₃ ($k \sim 0.43 \text{ min}^{-1}$) and MoS₂ QD ($k \sim 0.16 \text{ min}^{-1}$) decreases significantly (Figure 6.22). Notably, during experiment, the pH of the solution becomes ~ 9 after PNP addition, suggesting all H⁺ ions have been trapped by negative sites (S²⁻ or O²⁻) of MoS₂-MoO₃ or the oxygen site of PNP. To evaluate further details, the PL profile of MoS₂ QDs before and after PNP reduction has been determined in both pH-2 and pH-7. The intensity of emission maxima for MoS₂ QDs has been reduced to 20% percent at pH-2, manifesting soft center S²⁻ are highly susceptible to binding with H⁺ ions.

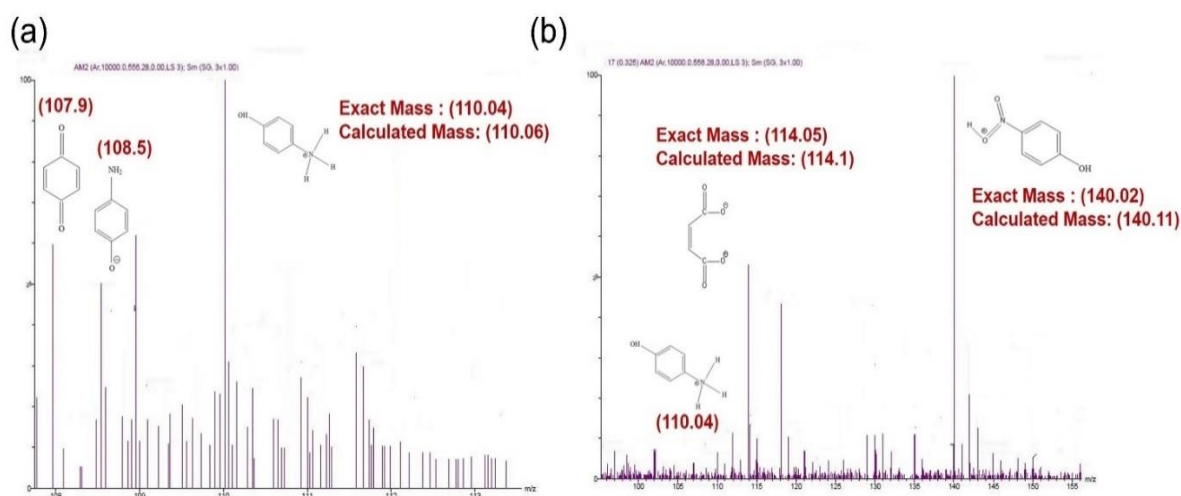


Figure 6.21: (a) GC-MS spectra of p-aminophenol ($m/z \sim 110.04$) with byproduct benzoquinone ($m/z \sim 107.9$) produced by the catalytic reduction of PNP by MoS₂-MoO₃. (b) GC-MS spectra of p-aminophenol ($m/z \sim 110.04$) with protonated PNP (PNP-H) ($m/z \sim 140.02$) and maleic acid ($m/z \sim 114.05$) that are produced by the catalytic reduction of PNP by MoS₂-MoO₃ under O₂ saturation (10.1 mg/ml).

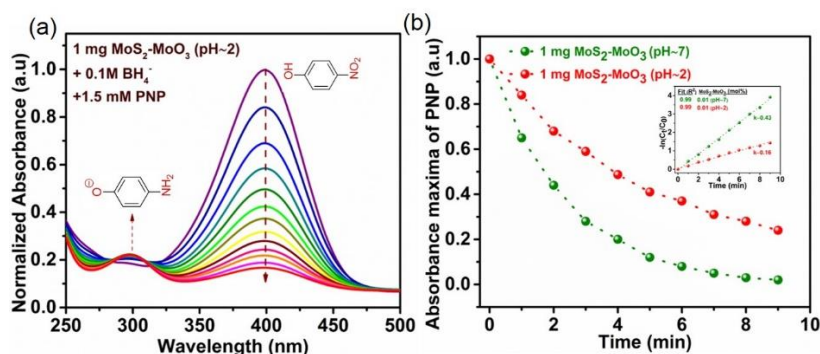


Figure 6.22: Absorbance profile of 1.5 mM PNP at 1 mg $\text{MoS}_2\text{-MoO}_3$ and 0.1 M NaBH_4 under pH-2. (b) Comparison of change in absorption maxima of PNP at two different pH-2 and pH-7. Inset showing linearized data between $-\ln(C_t/C_0)$ with time to determine the rate constant. Note that the pH has been determined before adding the PNP (only $\text{MoS}_2\text{-MoO}_3$ and NaBH_4). After addition of PNP, the pH becomes ~ 9 for all systems.

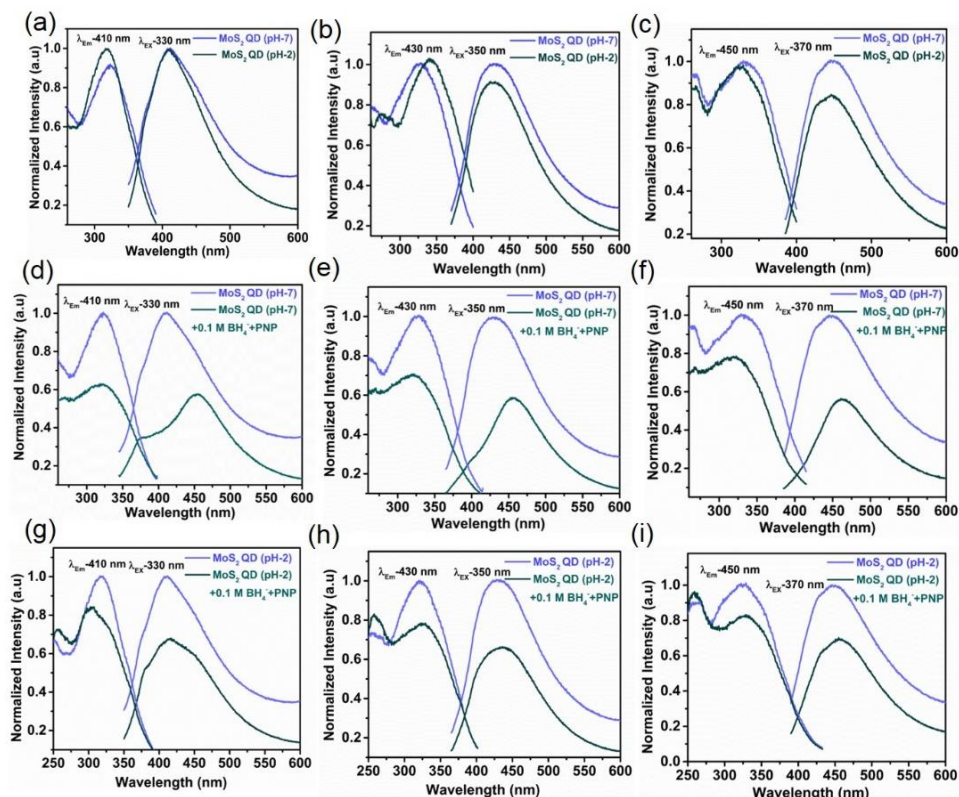


Figure 6.23: (a,b,c) The PLE and PL profile of MoS_2 QD at different pHs under pH-2 and pH-7. PL and PLE profile of MoS_2 QD at (d,e,f) pH-7 and (g,h,i) pH-2 after addition of 0.1 M NaBH_4 and 1.5 mM PNP respectively.

The PL profile is carried out after the PNP reduction in which the emission intensity of MoS₂ QDs at pH~2 is ~1.3 times higher than pH~7 (Figure 6.23). Generally, in acidic environment, the soft center edge active S²⁻ is highly susceptible to binding with H⁺ ions leading to shrinking the PL intensity over a broad excitation of MoS₂ QDs. At three different excitation wavelengths, the intensity of emission maxima has been reduced to 20% percent in acidic environment (Figure 6.23a-c). At pH~7, the normalized emission intensity has been reduced to ~50 % at three excitations (330-370 nm) after PNP addition (Figure 6.23d-f). Interestingly, after addition of PNP and NaBH₄, the intensity at pH~2 is approximately ~1.3 times higher than pH~7, suggesting edge active defect states, i.e., S²⁻ are trapped by PNP (Figure 6.23g-i). The result suggests that the protonation of negative charge centers reduces the active sites in MoS₂ QDs for PNP reduction, resulting in higher peak intensity than pH~7.

Further, post XPS study after reduction of PNP reveals a significant lowering in atomic percentage of Mo⁶⁺ (~17%), Mo⁵⁺ (~1%), and S²⁻ (1T) (~8%) where atomic percentage and peak position remains unaltered for 2H or 1T Mo⁴⁺ sites in MoS₂-MoO₃ (Figure 6.24a-c).

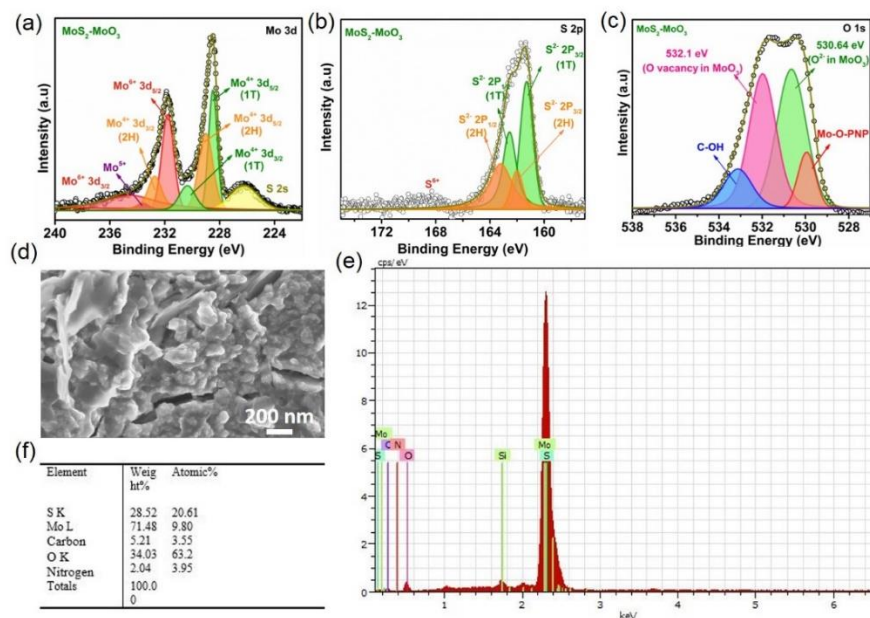


Figure 6.24: Post (a) Mo 3d, (b) S 2p (c) O 1s XPS spectra (d) FESEM image (e,f) EDX and elemental analyses of MoS₂-MoO₃ after PNP reduction.

Indeed, in O 1s spectra, a new peak near ~530 eV reveals that Mo⁶⁺-O-PNP bond formation (metal oxides) occurs after reduction (Figure 6.24c). However, post FESEM and EDX analyses

suggest the morphology of $\text{MoS}_2\text{-MoO}_3$ remains unaltered after PNP reduction with significant amount of nitrogen and carbon present in $\text{MoS}_2\text{-MoO}_3$ moiety (Figure 6.24d-f). To correlate with XPS results, we have incorporated SCN^- solution during catalysis. The rate constant (k) shrinks to a value of 0.07 min^{-1} and 0.06 min^{-1} from 0.21 min^{-1} (no addition of NaSCN), which manifests that the metal centers ($\text{Mo}^{5+/6+}$) are also active catalytic sites for PNP reduction (Figure 6.25). For durability test, the activity of the PNP reduction with $\text{MoS}_2\text{-MoO}_3$ remains unchanged after 5 consecutive cycles, as shown in Figure 6.26a. The decrease in atomic percentage after PNP adsorption and the schematic representation of metal centers ($\text{Mo}^{5+/6+}$) masking is shown in Figure 6.26b,c. Fundamentally, from ultraviolet photoelectron spectroscopy (UPS), the role of band alignment and work function (ϕ) of $\text{MoS}_2\text{-MoO}_3$ before and after PNP reduction has been investigated. Figure 6.26e manifests that $\text{MoS}_2\text{-MoO}_3$ exhibits work function (ϕ) 5.32 eV after catalytic reduction of PNP, which is 0.18 eV lower than pristine $\text{MoS}_2\text{-MoO}_3$. Notably, the valance band maxima (VBM) of $\text{MoS}_2\text{-MoO}_3$ before and after catalysis become 0.4 eV and ~ 0 eV, respectively (w.r.t Fermi level). The shifting of the energy states near the Fermi level implies high electron density, which lowers the work function of $\text{MoS}_2\text{-MoO}_3$ after interaction with PNP (Figure 6.26e,f).

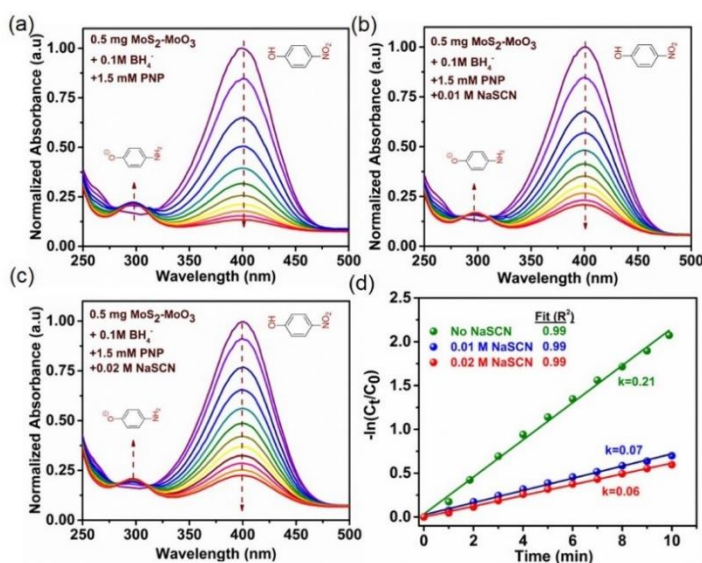


Figure 6.25: (a) Absorbance profile of 1.5 mM PNP with (a) 0.5 M $\text{MoS}_2\text{-MoO}_3$ (b) 0.5 M $\text{MoS}_2\text{-MoO}_3$ + 0.01 M NaSCN and (c) 0.5 M $\text{MoS}_2\text{-MoO}_3$ + 0.02 M NaSCN solution. The concentration of NaBH_4 is constant (0.1 M). (d) The plot of $-\ln(C_t/C_0)$ with time to estimate the decrease in rate constant (min^{-1}) after addition of NaSCN.

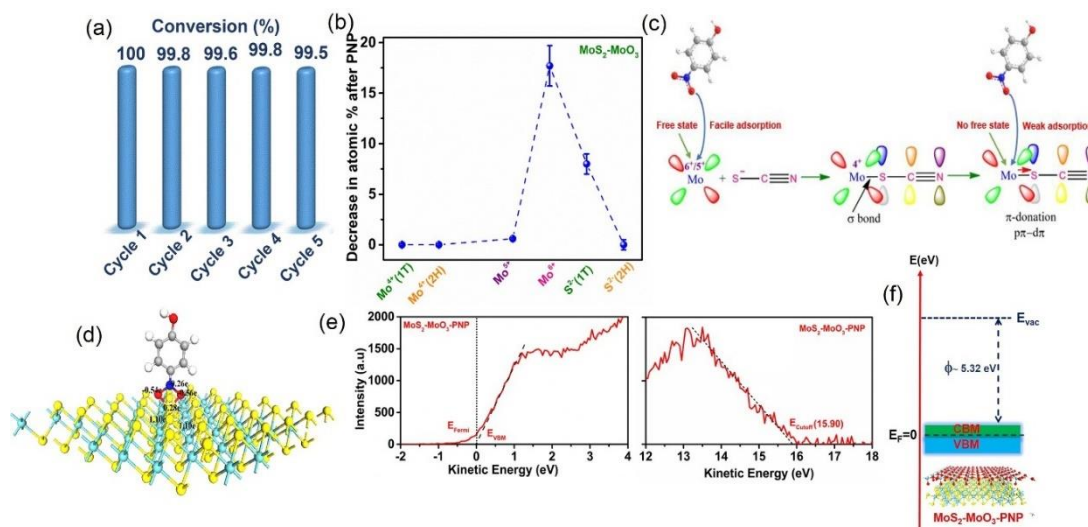


Figure 6.26: (a) Reusability of MoS₂-MoO₃ for the reduction of PNP for 5 cycles (b) Post XPS analyses of MoS₂-MoO₃ after PNP reduction (c) Schematic representation of reactivity towards PNP binding site and masking mechanism with NaSCN (d) Bader charge analysis of PNP with Sulphur sites of 1T-MoS₂ (e,f) Ultraviolet photoelectron spectroscopy (UPS) and experimental work function (φ) analyses for MoS₂-MoO₃ before and after PNP reduction, respectively.

To justify the experimentally obtained reactive sites, DFT analyses have been carried out to suggest the facile adsorption energy of PNP on the S site of 1T-MoS₂ over 2H-MoS₂, as shown in Figure 6.26d. Analysis of the adsorption energy of PNP on both 1T-MoS₂ and 2H-MoS₂ reveals that the PNP adsorbed configuration on 1T-MoS₂ is more stable than the same on 2H-MoS₂ by an energy difference of ~1 eV. First principles based structural optimizations reveal identical PNP adsorbed configurations on both 1T-MoS₂ and 2H-MoS₂ with the PNP bonded to one S atom of MoS₂ surface via the oxygen atoms of the -NO₂ group. 2H-MoS₂, which is semiconducting in its pristine form, shows a sign of being n-doped after PNP adsorption, with the Fermi level shifted within the conduction band states. Still, the gap between the occupied valence band and conduction band states remains. On the other hand, the metallic 1T-MoS₂ remains so with no band gap at or near the Fermi level after PNP adsorption, with the Mo-d states being the major contributor to the occupied valence band states just below the Fermi level. For 1T and 2H-MoS₂, the S atoms accept charges donated by the Mo atoms in pristine configurations. Bader charge analysis revealed that upon PNP adsorption, the adsorbent S atom acts as a donor

of electronic charge to the adsorbed PNP molecules. The O atoms of the $-\text{NO}_2$ group in the PNP molecule are the recipients of the charge released by the S atom. The adsorbent S atom in 2H-MoS₂ donates a larger amount of charge of 0.34e to the O atoms. Compared with 1T-MoS₂, the charge distribution on the O atoms of the $-\text{NO}_2$ group was asymmetric, with one of the O atoms receiving 0.65e amount of charge while the other received 0.55e amount of charge overall for 2H-MoS₂ (Figure 6.27). In the case of PNP adsorption on 1T-MoS₂, the adsorbent S atom donates 0.28e amount of charge to the already electron rich O atoms. During adsorption, the O atoms of the $-\text{NO}_2$ group receive -0.54e and -0.56e amounts of charge respectively (Figure 6.26d).

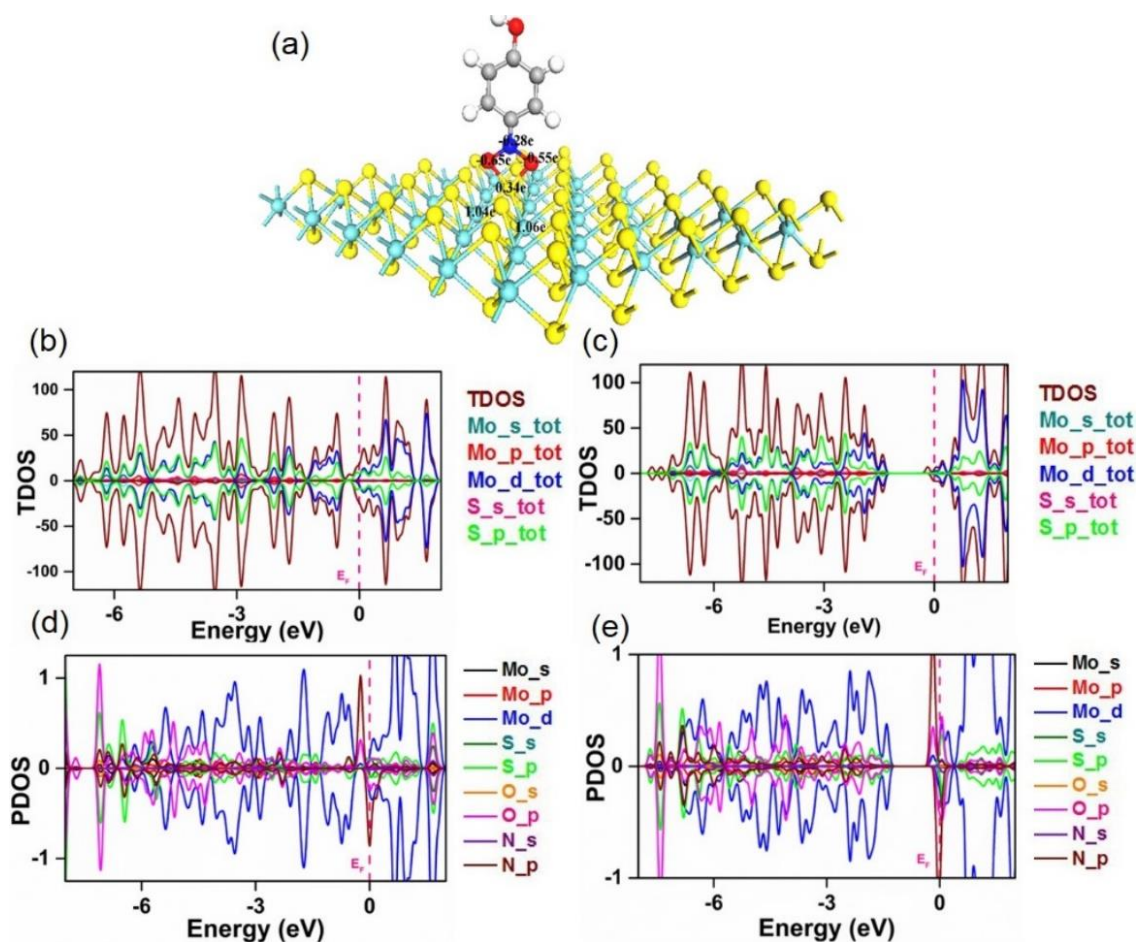


Figure 6.27: (a) Bader charge analysis and adsorption of oxygen site of PNP with Sulphur sites of 2H-MoS₂. Total Density of states (TDOS) and partial Density of states (PDOS) of (b,d) 1T-MoS₂ and (c,e) 2H-MoS₂ after PNP adsorption.

The relatively lower amount of charge transfer to the O atoms from the S atom of 1T-MoS₂ and symmetric charge distribution on the O atoms after adsorption might have played a crucial role in the more stable PNP adsorbed configuration on 1T-MoS₂. The stronger binding of PNP on 1T-MoS₂ along with the metallic nature of 1T-MoS₂ which was unaltered after PNP adsorption is expected to facilitate the transfer of electrons from the electrocatalyst's surface to PNP during the subsequent protonation processes promoting facial degradation of PNP on 1T-MoS₂. In contrast, the direct band gap of MoS₂-QD promotes the electron from valance to conduction band, enhancing the electron density in the conduction band. Likewise, absence of metallic 1T phase in Mo⁵⁺/Mo⁶⁺ and large band gap enhance the activation energy of MoS₂-QD for PNP reduction. In comparison, semiconducting indirect band gap state minimizes the probability of electron transition for PNP adsorption for 2H-MoS₂ and MoS₂ Ns leading to catalytically inert reduction. To further probe the generation of PAP from PNP, we have modeled a reaction pathway and found the possible intermediate generation. Primarily, the reaction has been carried out at very low oxygen saturation and no induction period is observed. Generally, reducing PNP to PAP involves para nitrosophenol as an intermediate product whose reactivity depends upon the critical value of dissolved oxygen. Figure 6.28 represents the possible reaction pathway involving multiple active sites (S²⁻, Mo^{5+/6+}) to enhance the rate constant and TOF in PNP reduction. In the next step, PNP converts to para nitrosophenol where the possibility of the backward reaction to form PAP⁻ can be nullified due to low oxygen saturation (no induction period). Next, the hydride insertion on para nitrosophenol forms para hydroxy-Phenylhydroxylamine. Finally, water removal occurs to form PAP and desorption from the catalytic surfaces.

A similar trend of catalytic performance has been employed to reduce inorganic complex potassium ferricyanides, shown in Figure 6.29. The complete disappearance of absorption maxima at (~420 nm) has been determined to confirm successful reduction of Fe (III) to Fe (II) state. The favorable interaction between [Fe(CN)₆]³⁻ (1.5 mM) with MoS₂-MoO₃ (1 mg) in presence of 0.1 M NaBH₄ shows faster reduction kinetics with rate constant (k) ~1.05 min⁻¹ compared to MoS₂ QD and 2H-MoS₂ (Figure 6.29d).

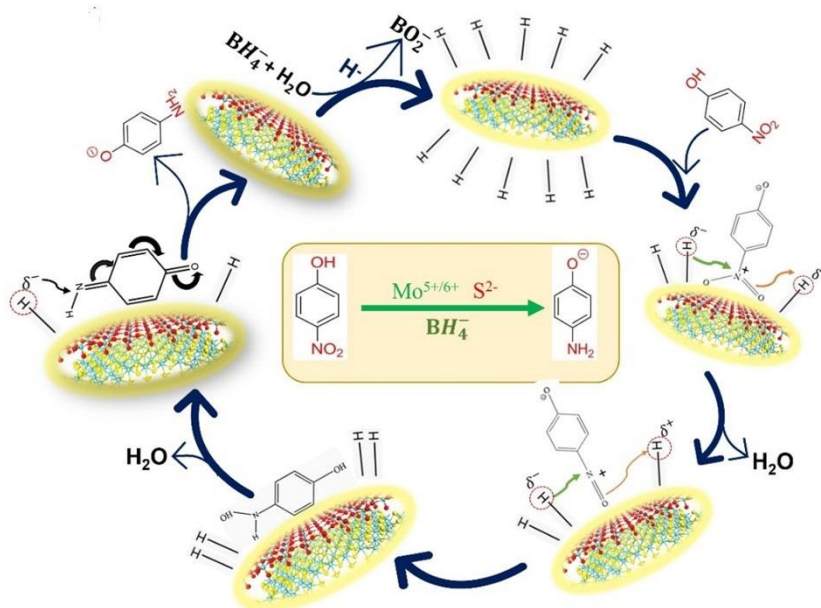


Figure 6.28: Proposed mechanism of PNP reduction.

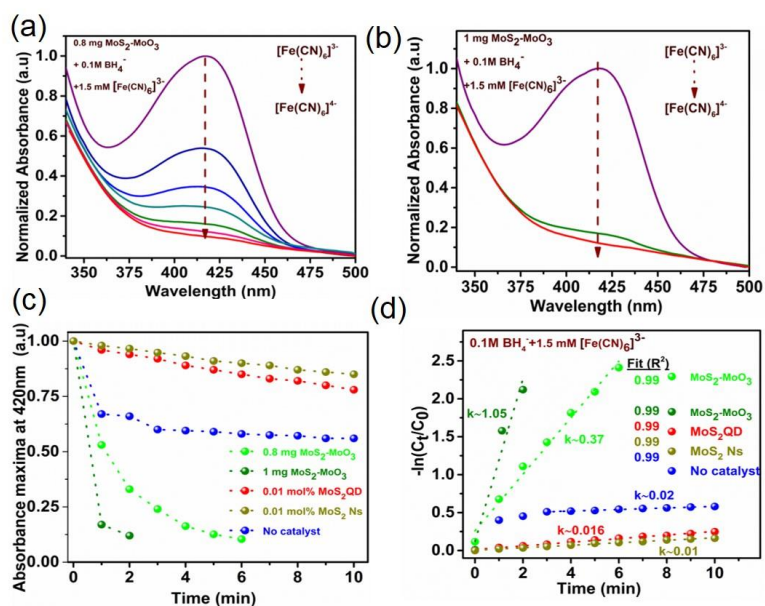


Figure 6.29: Kinetic study of potassium ferricyanide ($[\text{Fe}(\text{CN})_6]^{3-}$) at absorbance maxima (λ_{max}) ~ 420 nm with (a) 0.8 mg and (b) 1 mg $\text{MoS}_2\text{-MoO}_3$ (c) Comparison the performance of different catalysts for the chemical reduction of $\text{Fe}(\text{CN})_6]^{3-}$ by changing the intensity at ~ 420 nm with time. (d) Reduction of ferricyanide to ferrocyanide and linearized data for the first order kinetics for ferricyanide reduction catalyzed by MoS_2 based catal

6.4. Conclusion

In this work, we have theoretically and experimentally investigated multiple active sites and band engineering of oxygen vacancy-induced MoS₂-MoO₃ to exhibit toxic chemical reduction and pH universal HER activity. The oxygen vacancy helps in metal unsaturation and lowering of work function of binary heterostructure. The interfacial electronic structure facilitates hydrogen adsorption of MoO₃ layer and undergoes facile desorption from MoS₂ layer due to low thermodynamic barrier required for H^{*} spillover in acidic HER. The hypothesis is experimentally verified through masking with thiocyanate ion and post XPS analyses. The metallic character and negative d band center having unsaturated metal centers accelerate the hydrogen desorption rate in alkaline HER and the reduction of nitroaromatics. It is convincing that the decrease in work function and equal amount of interfacial charge density at 1T-MoS₂-PNP interface influences the PNP reduction. Thus, the significantly high activity factor, rate constant and turnover frequency for such catalytic performances are better than current state-of-art metal based catalysts. Therefore, this work develops not only design strategy of interfacial mechanism driven by heterogeneous reactive sites but also substantial effect of band alignment on catalysis of metal dichalcogenide based heterostructure.

6.5. References

1. Liu, Z., Nie, K., Qu, X., Li, X., Li, B., Yuan, Y., Chong, S., Liu, P., Li, Y., Yin, Z. and Huang, W., *Journal of the American Chemical Society*, 2022, 144(11), pp.4863-4873.
2. Nardekar, S.S., Krishnamoorthy, K., Manoharan, S., Pazhamalai, P. and Kim, S.J., *ACS nano*, 2022, 16(3), pp.3723-3734.
3. Puente Santiago, A.R., Sanad, M.F., Moreno-Vicente, A., Ahsan, M.A., Cerón, M.R., Yao, Y.R., Sreenivasan, S.T., Rodriguez-Forte, A., Poblet, J.M. and Echegoyen, L., *Journal of the American Chemical Society*, 2021, 143(16), pp.6037-6042.
4. Seh, Z.W., Kibsgaard, J., Dickens, C.F., Chorkendorff, I.B., Nørskov, J.K. and Jaramillo, T.F., *Science*, 2017, 355(6321), p.eaad4998.
5. Gao, Y., Chen, Z., Zhao, Y., Yu, W., Jiang, X., He, M., Li, Z., Ma, T., Wu, Z. and Wang, L., *Applied Catalysis B: Environmental*, 2022, 303, p.120879.
6. Liu, Y., Li, X., Zhang, Q., Li, W., Xie, Y., Liu, H., Shang, L., Liu, Z., Chen, Z., Gu, L. and Tang, Z., *Angewandte Chemie International Edition*, 2020, 59(4), pp.1718-1726.
7. Oh, N.K., Seo, J., Lee, S., Kim, H.J., Kim, U., Lee, J., Han, Y.K. and Park, H., *Nature Communications*, 2021, 12(1), p.4606.
8. Liu, H., Jin, M., Zhan, D., Wang, J., Cai, X., Qiu, Y. and Lai, L., *Applied Catalysis B: Environmental*, 2020, 272, p.118951.

9. Wang, K., Wang, X., Li, Z., Yang, B., Ling, M., Gao, X., Lu, J., Shi, Q., Lei, L., Wu, G. and Hou, Y., *Nano Energy*, 2020, 77, p.105162.
10. Sun, Y., Zhang, T., Li, C., Xu, K. and Li, Y., *Journal of Materials Chemistry A*, 2020, 8(27), pp.13415-13436.
11. Tong, Y., Mao, H., Xu, Y. and Liu, J., *Inorganic Chemistry Frontiers*, 2019, 6(8), pp.2055-2060.
12. Chen, P., Li, K., Ye, Y., Wu, D. and Tong, Y., *Dalton Transactions*, 2023, 52(8), pp.2262-2271.
13. Lin, Z., Li, K., Tong, Y., Wu, W., Cheng, X., Wang, H., Chen, P. and Diao, P. *ChemSusChem*, 2023, 16(2), p.e202201985.
14. Li, K., Tong, Y., Feng, D. and Chen, P., *Journal of Colloid and Interface Science*, 2022, 625, pp.576-584.
15. Tong, Y., Chen, P., Chen, L. and Cui, X., *ChemSusChem*, 2021, 14(12), pp.2576-2584.
16. Eda, G., Yamaguchi, H., Voiry, D., Fujita, T., Chen, M. and Chhowalla, M., *Nano letters*, 2011, 11(12), pp.5111-5116.
17. Yu, Y., Nam, G.H., He, Q., Wu, X.J., Zhang, K., Yang, Z., Chen, J., Ma, Q., Zhao, M., Liu, Z. and Ran, F.R., *Nature chemistry*, 2018, 10(6), pp.638-643.
18. Conley, H.J., Wang, B., Ziegler, J.I., Haglund Jr, R.F., Pantelides, S.T. and Bolotin, K.I., *Nano letters*, 2013, 13(8), pp.3626-3630.
19. Jaramillo, T.F., Jørgensen, K.P., Bonde, J., Nielsen, J.H., Hørch, S. and Chorkendorff, I., *science*, 2007, 317(5834), pp.100-102.
20. Li, Q., Zhao, Y., Ling, C., Yuan, S., Chen, Q. and Wang, J., *Angewandte Chemie International Edition*, 2017, 56(35), pp.10501-10505.
21. Geng, X., Sun, W., Wu, W., Chen, B., Al-Hilo, A., Benamara, M., Zhu, H., Watanabe, F., Cui, J. and Chen, T.P., *Nature communications*, 2016, 7(1), p.10672.
22. He, H., Li, X., Huang, D., Luan, J., Liu, S., Pang, W.K., Sun, D., Tang, Y., Zhou, W., He, L. and Zhang, C., *ACS nano*, 2021, 15(5), pp.8896-8906.
23. Puente Santiago, A.R., He, T., Eraso, O., Ahsan, M.A., Nair, A.N., Chava, V.S., Zheng, T., Pilla, S., Fernandez-Delgado, O., Du, A. and Sreenivasan, S.T., *Journal of the American Chemical Society*, 2020, 142(42), pp.17923-17927.
24. Kochat, V., Apte, A., Hachtel, J.A., Kumazoe, H., Krishnamoorthy, A., Susarla, S., Idrobo, J.C., Shimojo, F., Vashishta, P., Kalia, R. and Nakano, A. *Advanced Materials*, 2017, 29(43), p.1703754.
25. Zhang, K., Feng, S., Wang, J., Azcatl, A., Lu, N., Addou, R., Wang, N., Zhou, C., Lerach, J., Bojan, V. and Kim, M.J., *Nano letters*, 2015, 15(10), pp.6586-6591.
26. Lee, C., Li, Q., Kalb, W., Liu, X.Z., Berger, H., Carpick, R.W. and Hone, J., *science*, 2010, 328(5974), pp.76-80.
27. Chou, S.S., Huang, Y.K., Kim, J., Kaehr, B., Foley, B.M., Lu, P., Dykstra, C., Hopkins, P.E., Brinker, C.J., Huang, J. and Dravid, V.P., *Journal of the American Chemical Society*, 2015, 137(5), pp.1742-1745.
28. Tan, C., Luo, Z., Chaturvedi, A., Cai, Y., Du, Y., Gong, Y., Huang, Y., Lai, Z., Zhang, X., Zheng, L. and Qi, X., *Advanced Materials*, 2018, 30(9), p.1705509.
29. Zeng, Z., Yin, Z., Huang, X., Li, H., He, Q., Lu, G., Boey, F. and Zhang, H., *Angewandte Chemie*, 2011, 123(47), pp.11289-11293.
30. Li, Y., Cao, Y., Xie, J., Jia, D., Qin, H. and Liang, Z., *Catalysis Communications*, 2015, 58, pp.21-25.
31. Menumerov, E., Hughes, R.A. and Neretina, S., *Nano letters*, 2016, 16(12), pp.7791-7797.
32. Neal, R.D., Hughes, R.A., Sapkota, P., Ptasinska, S. and Neretina, S., *ACS Catalysis*, 2020, 10(17), pp.10040-10050.

33. Qiao, X.Q., Zhang, Z.W., Tian, F.Y., Hou, D.F., Tian, Z.F., Li, D.S. and Zhang, Q., *Crystal Growth & Design*, 2017, 17(6), pp.3538-3547.
34. Togano, H., Asai, K., Oda, S., Ikeno, H., Kawaguchi, S., Oka, K., Wada, K., Yagi, S. and Yamada, I., *Materials Chemistry Frontiers*, 2020, 4(5), pp.1519-1529.
35. Xu, S., Li, D. and Wu, P., *Advanced Functional Materials*, 2015, 25(7), pp.1127-1136.
36. Luo, Z., Li, J., Li, Y., Wu, D., Zhang, L., Ren, X., He, C., Zhang, Q., Gu, M. and Sun, X., *Advanced Energy Materials*, 2022, 12(12), pp.2103823.
37. Roy, D., Panigrahi, K., Das, B.K., Ghorui, U.K., Bhattacharjee, S., Samanta, M., Sarkar, S. and Chattopadhyay, K.K., *Nanoscale Advances*, 2021, 3(16), pp.4739-4749.
38. Kibsgaard, J., Jaramillo, T.F. and Besenbacher, F., *Nature chemistry*, 2014, 6(3), pp.248-253.
39. Gharbi, O., Tran, M.T., Tribollet, B., Turmine, M. and Vivier, V., *Electrochimica Acta*, 2020, 343, pp.136109.
40. Zhou, H., Yu, F., Huang, Y., Sun, J., Zhu, Z., Nielsen, R.J., He, R., Bao, J., Goddard III, W.A., Chen, S. and Ren, Z., *Nature Communications*, 2016, 7(1), pp.12765.
41. Zhang, C., Wang, Z., Bhoyate, S., Morey, T., Neria, B.L., Vasiraju, V., Gupta, G., Palchoudhury, S., Kahol, P.K., Mishra, S.R. and Perez, F., *Carbon*, 2017, 3(4), pp.33.
42. Perdew, J.P., Burke, K. and Ernzerhof, M., *Physical review letters*, 1996, 77(18), pp.3865.
43. Blöchl, P.E., Jepsen, O. and Andersen, O.K., *Physical Review B*, 1994, 49(23), pp.16223.
44. Kresse, G. and Hafner, J., *Physical review B*, 1993, 47(1), pp.558.
45. Kresse, G. and Hafner, J., *Physical Review B*, 1994, 49(20), pp.14251.
46. Grimme, S., Antony, J., Ehrlich, S. and Krieg, H., *The Journal of chemical physics*, 2010, 132(15).
47. Tang, W., Sanville, E. and Henkelman, G., *Journal of Physics: Condensed Matter*, 2009, 21(8), p.084204.
48. Nørskov, J.K., Rossmeisl, J., Logadottir, A., Lindqvist, L.R.K.J., Kitchin, J.R., Bligaard, T. and Jonsson, H., *The Journal of Physical Chemistry B*, 2004, 108(46), pp.17886-17892.
49. Baby, M. and Kumar, K.R., In *Journal of Physics: Conference Series* (Vol. 2070, No. 1, p. 012095).2021, IOP Publishing.
50. Mohanty, B., Ghorbani-Asl, M., Kretschmer, S., Ghosh, A., Guha, P., Panda, S.K., Jena, B., Krasheninnikov, A.V. and Jena, B.K., *Acs Catalysis*, 2018, 8(3), pp.1683-1689.
51. Hasani, A., Le, Q.V., Nguyen, T.P., Choi, K.S., Sohn, W., Kim, J.K., Jang, H.W. and Kim, S.Y., *Scientific Reports*, 2017, 7(1), pp.13258.
52. Ding, W., Hu, L., Dai, J., Tang, X., Wei, R., Sheng, Z., Liang, C., Shao, D., Song, W., Liu, Q. and Chen, M., *ACS nano*, 2019, 13(2), pp.1694-1702.
53. Zhang, J., Wang, T., Pohl, D., Rellinghaus, B., Dong, R., Liu, S., Zhuang, X. and Feng, X., *Angewandte Chemie*, 2016, 128(23), pp.6814-6819.
54. Zhou, R., Wang, H., Chang, J., Yu, C., Dai, H., Chen, Q., Zhou, J., Yu, H., Sun, G. and Huang, W., *ACS Applied Materials & Interfaces*, 2021, 13(15), pp.17459-17466.
55. Dai, H., Zhou, J., Qin, G. and Sun, G., *Dalton Transactions*, 2022, 51(2), pp.524-531.
56. Yu, C., Xu, H., Gong, Y., Chen, R., Hui, Z., Zhao, X., Sun, Y., Chen, Q., Zhou, J., Ji, W. and Sun, G., *Res.*, 2021, pp. 6742715.
57. Chen, B., Sun, G., Wang, J., Liu, G., Tan, C., Chen, Y., Cheng, H., Chen, J., Ma, Q., Huang, L. and Chen, P., *Chemical Communications*, 2020, 56(38), pp.5131-5134.
58. Yao, Z., Yu, C., Dai, H., Zhou, J., Liu, X. and Sun, G., *Carbon*, 2022, 187, pp.165-172.
59. Yu, C., Xu, H., Sun, Y., Zhao, X., Hui, Z., Gong, Y., Chen, R., Chen, Q., Zhou, J., Sun, G. and Huang, W., *Carbon*, 2020, 170, pp.543-549.
60. Qin, P., Fang, G., Ke, W., Cheng, F., Zheng, Q., Wan, J., Lei, H. and Zhao, X., *Journal of Materials Chemistry A*, 2014, 2(8), pp.2742-2756.

61. Xu, S., Li, D. and Wu, P., *Advanced Functional Materials*, 2015, 25(7), pp.1127-1136.
62. Singh, S., Deb, J., Sarkar, U. and Sharma, S., *ACS Sustainable Chemistry & Engineering*, 2021, 9(21), pp.7328-7340.
63. Duraisamy, S., Ganguly, A., Sharma, P.K., Benson, J., Davis, J. and Papakonstantinou, P., *ACS Applied Nano Materials*, 2021, 4(3), pp.2642-2656.
64. Roy, R., Thapa, R., Biswas, S., Saha, S., Ghorai, U.K., Sen, D., Kumar, E.M., Kumar, G.S., Mazumder, N., Roy, D. and Chattopadhyay, K.K., *Nanoscale*, 2018, 10(35), pp.16822-16829.
65. Liu, Z., Gao, Z., Liu, Y., Xia, M., Wang, R. and Li, N., *ACS applied materials & interfaces*, 2017, 9(30), pp.25291-25297.
66. Lassalle-Kaiser, B., Merki, D., Vrubel, H., Gul, S., Yachandra, V.K., Hu, X. and Yano, J., *Journal of the American Chemical Society*, 2015, 137(1), pp.314-321.
67. Huang, Y., Sun, Y., Zheng, X., Aoki, T., Pattengale, B., Huang, J., He, X., Bian, W., Younan, S., Williams, N. and Hu, J., *Nature communications*, 2019, 10(1), pp.982.
68. Li, X., Lv, X., Li, N., Wu, J., Zheng, Y.Z. and Tao, X., *Applied Catalysis B: Environmental*, 2019, 243, pp.76-85.
69. Feng, L., Zhang, L., Zhang, S., Chen, X., Li, P., Gao, Y., Xie, S., Zhang, A. and Wang, H., *ACS applied materials & interfaces*, 2020, 12(15), pp.17547-17556.
70. Chiang, T.H. and Yeh, H.C., *Materials*, 2013, 6(10), pp.4609-4625.
71. Ding, X., Peng, F., Zhou, J., Gong, W., Slaven, G., Loh, K.P., Lim, C.T. and Leong, D.T., *Nature Communications*, 2019, 10(1), pp.41.
72. Chen, Z., Song, Y., Cai, J., Zheng, X., Han, D., Wu, Y., Zang, Y., Niu, S., Liu, Y., Zhu, J. and Liu, X., *Angewandte Chemie International Edition*, 2018, 57(18), pp.5076-5080.
73. Sun, S., Zhou, X., Cong, B., Hong, W. and Chen, G., *Acs Catalysis*, 2020, 10(16), pp.9086-9097.
74. Yang, Q., Liu, H., Yuan, P., Jia, Y., Zhuang, L., Zhang, H., Yan, X., Liu, G., Zhao, Y., Liu, J. and Wei, S., *Journal of the American Chemical Society*, 2022, 144(5), pp.2171-2178.
75. Shi, Y., Zhou, Y., Yang, D.R., Xu, W.X., Wang, C., Wang, F.B., Xu, J.J., Xia, X.H. and Chen, H.Y., *Journal of the American Chemical Society*, 2017, 139(43), pp.15479-15485.
76. Wei, Z.W., Wang, H.J., Zhang, C., Xu, K., Lu, X.L. and Lu, T.B., *Angewandte Chemie*, 2021, 133(30), pp.16758-16763.
77. Liu, L., Wang, Y., Zhao, Y., Wang, Y., Zhang, Z., Wu, T., Qin, W., Liu, S., Jia, B., Wu, H. and Zhang, D., *Advanced Functional Materials*, 2022, 32(20), pp.2112207.
78. Sheng, M., Jiang, B., Wu, B., Liao, F., Fan, X., Lin, H., Li, Y., Lifshitz, Y., Lee, S.T. and Shao, M., *ACS nano*, 2019, 13(3), pp.2786-2794.
79. Zhu, L., Lin, H., Li, Y., Liao, F., Lifshitz, Y., Sheng, M., Lee, S.T. and Shao, M., *Nature communications*, 2016, 7(1), p.12272.
80. Li, J., Hu, J., Zhang, M., Gou, W., Zhang, S., Chen, Z., Qu, Y. and Ma, Y., *Nature Communications*, 2021, 12(1), p.3502.
81. Cho, J., Kim, M., Seok, H., Choi, G.H., Yoo, S.S., Sagaya Selvam, N.C., Yoo, P.J. and Kim, T., *ACS Applied Materials & Interfaces*, 2022, 14(20), pp.24008-24019.
82. Suman, S.G., Snæbjörnsson, T., Ragnarsdóttir, O., Polukeev, A.V. and Wendt, O.F., *Polyhedron*, 2021, 209, p.115447.
83. Baranyi, A.D., Makhija, R. and Onyszchuk, M., *Canadian Journal of Chemistry*, 1976, 54(8), pp.1189-1196.
84. Liu, Z., Nie, K., Qu, X., Li, X., Li, B., Yuan, Y., Chong, S., Liu, P., Li, Y., Yin, Z. and Huang, W., *Journal of the American Chemical Society*, 2022, 144(11), pp.4863-4873.
85. Yu, Y., Nam, G.H., He, Q., Wu, X.J., Zhang, K., Yang, Z., Chen, J., Ma, Q., Zhao, M., Liu, Z. and Ran, F.R., *Nature chemistry*, 2018, 10(6), pp.638-643.

86. Deng, J., Li, H., Wang, S., Ding, D., Chen, M., Liu, C., Tian, Z., Novoselov, K.S., Ma, C., Deng, D. and Bao, X., *Nature communications*, 2017, 8(1), pp.14430.
87. Xiao, W., Liu, P., Zhang, J., Song, W., Feng, Y.P., Gao, D. and Ding, J., *Advanced Energy Materials*, 2017, 7(7), pp.1602086.
88. Sun, Y., Alimohammadi, F., Zhang, D. and Guo, G., *Nano letters*, 2017, 17(3), pp.1963-1969.
89. Yin, Y., Han, J., Zhang, Y., Zhang, X., Xu, P., Yuan, Q., Samad, L., Wang, X., Wang, Y., Zhang, Z. and Zhang, P., *Journal of the American Chemical Society*, 2016, 138(25), pp.7965-7972.
90. Chen, W., Gu, J., Liu, Q., Luo, R., Yao, L., Sun, B., Zhang, W., Su, H., Chen, B., Liu, P. and Zhang, D., *ACS nano*, 2018, 12(1), pp.308-316.
91. Liu, Q., Fang, Q., Chu, W., Wan, Y., Li, X., Xu, W., Habib, M., Tao, S., Zhou, Y., Liu, D. and Xiang, T., *Chemistry of Materials*, 2017, 29(11), pp.4738-4744.
92. Park, S.K., Kim, J.K. and Kang, Y.C., *ACS Sustainable Chemistry & Engineering*, 2018, 6(10), pp.12706-12715.
93. Ye, Z., Yang, J., Li, B., Shi, L., Ji, H., Song, L. and Xu, H., *Small*, 2017, 13(21), pp.1700111.
94. Xie, S., Sun, B., Sun, H., Zhan, K., Zhao, B., Yan, Y. and Xia, B.Y., *International Journal of Hydrogen Energy*, 2019, 44(29), pp.15009-15016.
95. Lee, C.H., Lee, S., Kang, G.S., Lee, Y.K., Park, G.G., Lee, D.C. and Joh, H.I., *Applied Catalysis B: Environmental*, 2019, 258, pp.117995.
96. Tan, C., Luo, Z., Chaturvedi, A., Cai, Y., Du, Y., Gong, Y., Huang, Y., Lai, Z., Zhang, X., Zheng, L. and Qi, X., *Advanced Materials*, 2018, 30(9), pp.1705509.
97. Li, H., Tsai, C., Koh, A.L., Cai, L., Contryman, A.W., Fragapane, A.H., Zhao, J., Han, H.S., Manoharan, H.C., Abild-Pedersen, F. and Nørskov, J.K., *Nature materials*, 2016, 15(1), pp.48-53.
98. Liu, Z., Zhao, L., Liu, Y., Gao, Z., Yuan, S., Li, X., Li, N. and Miao, S., *Applied Catalysis B: Environmental*, 2019, 246, pp.296-302.
99. Geng, X., Sun, W., Wu, W., Chen, B., Al-Hilo, A., Benamara, M., Zhu, H., Watanabe, F., Cui, J. and Chen, T.P., *Nature communications*, 2016, 7(1), pp.10672.
100. Tan, S.M., Sofer, Z., Luxa, J. and Pumera, M., *Acs Catalysis*, 2016, 6(7), pp.4594-4607.
101. Gao, M.R., Chan, M.K. and Sun, Y., *Nature communications*, 2015, 6(1), pp.7493.
102. Wang, H., Cao, Y., Sun, C., Zou, G., Huang, J., Kuai, X., Zhao, J. and Gao, L., *ChemSusChem*, 2017, 10(18), pp.3540-3546.
103. Lai, B., Singh, S.C., Bindra, J.K., Saraj, C.S., Shukla, A., Yadav, T.P., Wu, W., McGill, S.A., Dalal, N.S., Srivastava, A. and Guo, C., *Materials Today Chemistry*, 2019, 14, pp.100207.
104. Zhao, G., Lin, Y., Rui, K., Zhou, Q., Chen, Y., Dou, S.X. and Sun, W., *Nanoscale*, 2018, 10(40), pp.19074-19081.
105. Cheng, P., Yuan, C., Zhou, Q., Hu, X., Li, J., Lin, X., Wang, X., Jin, M., Shui, L., Gao, X. and Nötzel, R., *The Journal of Physical Chemistry C*, 2019, 123(10), pp.5833-5839.
106. Nolan, H., Schröder, C., Brunet-Cabré, M., Pota, F., McEvoy, N., McKelvey, K., Perova, T.S. and Colavita, P.E., *Carbon*, 2023, 202, pp.70-80.
107. Huang, S., Cao, Y., Yao, F., Zhang, D., Yang, J., Ye, S., Yao, D., Liu, Y., Li, J., Lei, D. and Wang, X., *Small*, 2023, pp.2207919.
108. Chen, B., Wang, J., He, S., Shen, Y., Huang, S. and Zhou, H., *Journal of Alloys and Compounds*, 2023, 948, pp.169655.
109. Bolar, S., Samanta, P., Jang, W., Yang, C.M., Murmu, N.C. and Kuila, *ACS Applied Energy Materials*, 2022, 5(8), pp.10086-10097.
110. Song, M., Zhao, Y., Wu, Z. and Liu, X., *Sustainable Energy & Fuels*, 2020, 4(10), pp.5036-5041.

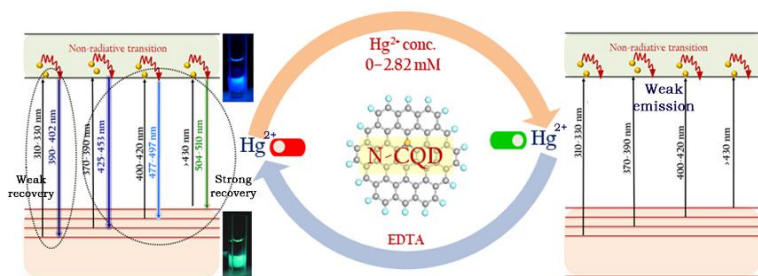
111. Bolar, S., Shit, S., Murmu, N.C. and Kuila, T., *ChemElectroChem*, 2020, 7(1), pp.336-346.
112. Zhang, B., Li, J., Song, Q., Xu, X., Hou, W. and Liu, H., *Inorganic Chemistry*, 2021, 60(4), pp.2604-2613.
113. Maiti, A. and Srivastava, S.K., *ACS Applied Nano Materials*, 2021, 4(8), pp.7675-7685.
114. Tahira, A., Ibupoto, Z.H., Mazzaro, R., You, S., Morandi, V., Natile, M.M., Vagin, M. and Vomiero, A., *ACS Applied Energy Materials*, 2019, 2(3), pp.2053-2062.
115. Liang, J., Song, Q., Wu, J., Lei, Q., Li, J., Zhang, W., Huang, Z., Kang, T., Xu, H., Wang, P. and Zhou, X., *ACS nano*, 2022, 16(3), pp.4152-4161.
116. Strachan, J., Barnett, C., Masters, A.F. and Maschmeyer, T., *ACS Catalysis*, 2020, 10(10), pp.5516-5521.
117. Fang, L., Jiang, R., Zhang, Y., Munthali, R.M., Huang, X., Wu, X. and Liu, Z., *Journal of Solid State Chemistry*, 2021, 303, pp.122461.
118. Roy, S., Rao, A., Devatha, G. and Pillai, P.P., *ACS Catalysis*, 2017, 7(10), pp.7141-7145.
119. Li, B., Ma, J.G. and Cheng, P., *Angewandte Chemie*, 2018, 130(23), pp.6950-6953.
120. Bae, S., Gim, S., Kim, H. and Hanna, K., *Applied Catalysis B: Environmental*, 2016, 182, pp.541-549.
121. Bai, Y., Wang, Q., Du, C., Bu, T., Liu, Y., Sun, X., Luo, W., Li, R., Zhao, Y., Zheng, X. and Wang, L., *Journal of colloid and interface science*, 2019, 553, pp.768-777.
122. Elfiad, A., Galli, F., Boukhobza, L.M., Djadoun, A. and Boffito, D.C., *Journal of Environmental Chemical Engineering*, 2020, 8(5), pp.104214.
123. Huang, C., Ye, W., Liu, Q. and Qiu, X., *ACS applied materials & interfaces*, 2014, 6(16), pp.14469-14476.
124. Zhang, P., Sui, Y., Xiao, G., Wang, Y., Wang, C., Liu, B., Zou, G. and Zou, B., *Journal of Materials Chemistry A*, 2013, 1(5), pp.1632-1638.
125. Jebaranjitham, J.N., Mageshwari, C., Saravanan, R. and Mu, N., *Composites Part B: Engineering*, 2019, 171, pp.302-309.
126. Jiang, D.B., Liu, X., Yuan, Y., Feng, L., Ji, J., Wang, J., Losic, D., Yao, H.C. and Zhang, Y.X., *Chemical Engineering Journal*, 2020, 383, pp.123156.
127. Das, R., Sypu, V.S., Paumo, H.K., Bhaumik, M., Maharaj, V. and Maity, A., *Applied Catalysis B: Environmental*, 2019, 244, pp.546-558.
128. Yang, X., Li, Y., Zhang, P., Zhou, R., Peng, H., Liu, D. and Gui, J., *ACS applied materials & interfaces*, 2018, 10(27), pp.23154-23162.
129. Yang, Y., Zeng, D., Shao, S., Hao, S., Zhu, G. and Liu, B., *Journal of colloid and interface science*, 2019, 538, pp.377-386.
130. Yu, T., Zeng, J., Lim, B. and Xia, Y., *Advanced Materials*, 2010, 22(45), pp.5188-5192.
131. Qiao, X.Q., Zhang, Z.W., Hou, D.F., Li, D.S., Liu, Y., Lan, Y.Q., Zhang, J., Feng, P. and Bu, X., *ACS Sustainable Chemistry & Engineering*, 2018, 6(9), pp.12375-12384.

CHAPTER 7

Probing the emission dynamics in nitrogen doped carbon dots by reversible capping with mercury (II) through surface chemistry

Abstract

In this study, the mechanistic insight and emission dynamics have been explored of size dependent nitrogen doped carbon quantum dots (namely 3A,3B & 3C) with toxic metal Hg^{2+} ions via capping and uncapping mechanism. The excitation and pH dependent emission profile of N-CQDs is assigned to multiple centers involving higher energy aromatic core ($\pi-\pi^*$) and lower energy oxygen and nitrogen based functional groups ($n_{\text{O}2\text{p}}-\pi^*$ and $n_{\text{N}2\text{p}}-\pi^*$). From experimental and theoretical validation, the highly negatively charged surface of 3A is mainly due to high abundance of $-\text{COOH}$ and NH_2 groups promoting weak $(\text{COO}^-)_2\text{-Hg}^{2+}$, $\text{NH}_2\text{-Hg}^{2+}$ bond formation with reduction of sp^2 carbon content with different concentrations of Hg^{2+} ions. Thus, the combined effect shrinks the PL signals (area, and intensity) associated with $\pi-\pi^*$ and $n-\pi^*$ transitions through the static and dynamic quenching pathway (LOD \sim 0.092 μM). Furthermore, the restoration of PLE and PL signals is carried out via uncapping of Hg^{2+} ions where the high recovery percentage (\sim maximum -96%) is mainly governed by COOH and NH_2 groups than the deeply buried core state. Thus, the prominent reversible quenching associated with surface states is well supported by changes in zeta potential measurements. Our investigation demonstrates direct dependency of surface chemistry on the proposed emission dynamics of carbon dots.



7.1. Introduction

Over the years fluorescent graphene quantum dot (GQD) or carbon quantum dot (CQD) have manifested a substantial potential application in charge transfer,[1] solar cells,[2] sensors,[3] drug deliveries, [4] and various optoelectronic devices [5,6] due to its exposed active sites, low toxicity, cost-efficient, and high reactivity [7,8]. However, ascertaining the luminescence mechanism in CQD remains complicated and controversial [9]. Generally, two types of PL phenomena have been established in CQD having excitation independent and excitation dependent emission. Initially, the size modification of CQD tunes the PL emission towards specific wavelength (excitation independent), which restricts its wide applications [10-12]. Secondly, surface chemistry,[13] heteroatom doping,[14] solvents effects[15-18] have a significant impact on controlling the PL properties of CQD involving a different range of broadband emission intensities like red, green, blue, etc. Gao et al. have proposed three types of band-states such as bandgap state, surface defect state, and molecular state are responsible for multi emissions of CQDs [19]. It is worth mentioning that the surface of CQD is highly susceptible to interact with metal ions which can reduce the emission intensity of CQD depending on excitation [20-22]. The binding or adsorption site of quantum dots with different analytes (metal ions, biomolecules, hazardous organic, inorganic molecules) can be tuned by changing the surface states by adding surfactant (surface passivation), size of the quantum dots via controlling reaction time, temperature or medium and different molecular state due to formation of molecular structure which is responsible to exhibit strong fluorescence due to various binding sites and promotes specific metal ion sensor [23]. Apart from surface states, the molecular state has a significant effect to control the PL and quenching efficiency. Since various precursors have been utilized to synthesize carbon dots where reaction medium and type of precursors tend to produce different fluorophore-based N-CQD which is responsible for selective ion sensing [24]. For example, different structures of the monomers or oligomers. citrazinic acid, pyrene based carbon dots are selective sensors of drugs, metal ions, etc [25]. However, the foreign metal and nonmetal doping at the core and surface states also boosts the sensing performance of different metals, carbohydrates i.e. Fe^{3+} , Ga^{3+} , glucose, etc. [26-29]. Hence, the reversible mechanism of active binding site of CQD with metal ions needs to be

investigated before and after PL restoration which can determine individual transition responsible for PL emission.

We report microwave assisted synthesis of differently sized nitrogen doped CQD (N-CQD) using ribose and amino acid arginine (scheme 7.1). The interaction dynamics of different metal ions with the negatively charged surface of N-CQD containing the functional groups are investigated by quenching and subsequent recovery of excitation independent tunable PL emission. The recovery percentage of PL signals associated with core and defect states has been systematically studied and correlated with surface charge. Furthermore, the kinetic stability, the limit of detection of Hg^{2+} have also been evaluated to determine the proficiency of N-CQD towards metal ion detection.

7.2. Experimental Section

7.2.1. Materials

Ethylenediaminetetraacetic acid disodium salt dihydrate (EDTA) having 99% purity is purchased from Sigma-Aldrich. Arginine, Ribose, Dimethylformamide (DMF), cobalt nitrate hexahydrate (98%), nickel nitrate hexahydrate (98%), copper nitrate trihydrate (99%), zinc nitrate hexahydrate (96%), silver nitrate (99%), and mercury nitrate monohydrate (98%), lead nitrate (99%), cadmium nitrate (99%), Dialysis Bags (14 kDa) are purchased from Merck. All the sensing experiments are carried out in deionized water.

7.2.2. Synthesis of N-CQD

N-CQD has been prepared via microwave treatment using a fixed ratio of ribose and arginine. Typically, 50 mg ribose (1mg/ml) and 25 mg arginine (1mg/ml) are dispersed separately in DI and stirred for 10 minutes to get a homogeneous solution. The solutions are then mixed and stirred further for 30 minutes. The resultant solutions are transferred to three separate 30 ml vials respectively and undergo microwave treatment at 120°C for 10 min, 30 min, and 1 hour (under 1000 rpm). The solution is then filtered to 0.22 μM Millipore filter paper up to 5 times. Then the filtrate solution is dialyzed through a dialysis bag (12 kDa) for three days to remove all unreacted particles or byproducts. After dialysis,

pure N-CQDs are stored in a vial. The synthesized three N-CQDs prepared for 10 minutes, 30 min, and 1 hour is designed as 3A, 3B, and 3C, respectively (Scheme 7.1).

7.2.3. PLE and PL study of N-CQD with different metal ions

The as-prepared N-CQD solution has been diluted to make the concentration of each solution 6.25 mg/ml. A fixed concentration ($\sim 50 \mu\text{M}$) of cobalt nitrate hexahydrate (98%), nickel nitrate hexahydrate (98%), copper nitrate trihydrate (99%), zinc nitrate hexahydrate (96%), silver nitrate (99%), and mercury nitrate monohydrate (98%), lead nitrate (99%), cadmium nitrate (99%) are prepared by using an appropriate amount of DI water. Typically, 0.1 ml of sample and 3 ml of each metal stock solution are taken in a quartz tube and keep the solution for 1 min to attain equilibrium. The PL study is carried out at different excitation wavelengths from 330 nm to 430 nm. For ultra-trace level Hg^{2+} detection, different concentration of Hg^{2+} solution is varied ($0.18 \mu\text{M}$ to 2.82 mM) at three different pH ~ 1 , pH ~ 7 , pH ~ 12 . To measure the reversible quenching mechanism of N-CQD with Hg^{2+} ions, EDTA has been utilized as a binder of metal Hg^{2+} ions. Initially, 0.10 gm of EDTA is dissolved in 10 ml DI water. Then fixed concentrations (0.15 ml of the stock solution) of EDTA (0.034M) and N-CQD (6.25 mg/ml) with different concentrations of Hg^{2+} are mixed, and PL studies are carried out at different excitation wavelengths. All the quenching experiments and surface charge analyses have been carried out four times. The relative percentage of PL signals (fwhm (full width at half maximum), area, intensity) of bare N-CQD are considered to be 100 % and all the PL signals have been calculated with respect to bare N-CQD before and after recovery. The quenching efficiency (Q.E) can be calculated from the following Eqn. $\text{Q.E} = 1 - I/I_0$, Where I and I_0 denote PL intensity in the presence and absence of Hg^{2+} . Limit of detection (LOD) for Hg^{2+} can be calculated from the linear portion of S-V equation as follows:

$$\text{LOD} = 3 * (\text{Standard deviation/slope}) \quad (7.1)$$

The recovery percentage of PL signals of N-CQD has been calculated as:

$$(\text{After recovery} - \text{After Quenching}) \times 100 / (\text{Bare N-CQD} - \text{After Quenching}) \quad (7.2)$$

Binding constants are determined from the double-logarithmic equation of fluorescence intensity

data shown as follows [30]:

$$\text{Log} \frac{(F_0 - F)}{F} = \text{Log} K_{bin} + n * \text{Log}[Q] \quad (7.3)$$

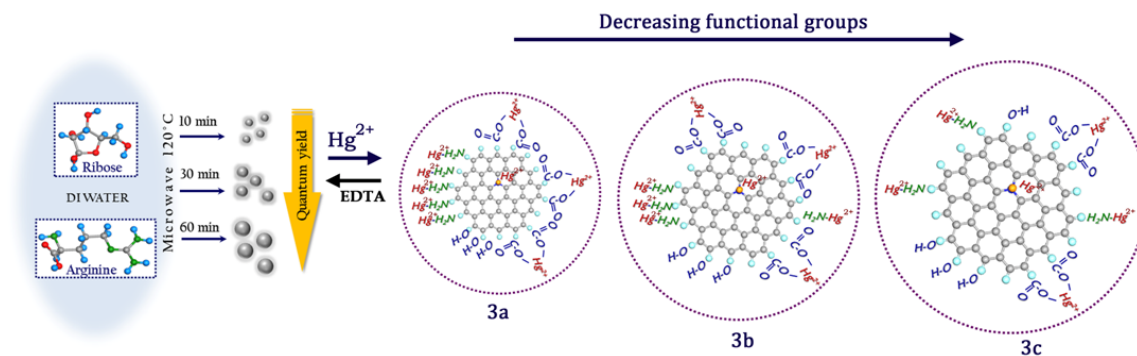
K_{bin} is binding constant, n is the average binding site, and Q is the quencher concentration.

7.2.4. Characterization

A high-resolution transmission electron microscope (HRTEM) is obtained using JEOL 2100 operated at 200 kV using a carbon-film-coated Cu grid. For structural and compositional analyses, X-Ray photoelectron spectroscopy (XPS) is determined using a monochromatic Al K_{α} X-ray source ($h\nu = 1486.6$ eV) and a hemispherical analyzer (SPECS HSA 3500). The survey scans and high-resolution elemental scans for XPS analysis are analyzed with pass energy of 160 at 1.00 eV energy step and of 20 and 0.1 eV energy step, respectively. Fourier transformed infrared spectrophotometer (FTIR) is recorded by Shimadzu FTIR-8400S. Absorption maxima are measured by UV-Vis spectrophotometer (Shimadzu UV-3600). Tauc plots of UV-Vis spectra have been used to determine the band gap where scattering from the samples is very low and thus can be ignored. Zeta potential has been measured by Malvern Zeta sizer Nano-ZS 90 instrument. The photoluminescence excitation (PLE), steady-state, and time-resolved photoluminescence (PL) spectra are carried out on Edinburgh FLSP-980 luminescence spectrometer, with a microsecond flash lamp as the excitation source. The goodness of fit with reduced (χ^2) ~ 1 is achieved for the overall envelope while PLE and PL spectra have been deconvoluted to Gaussian curve profile to obtain peak area, intensity, and fwhm.

7.2.5. Theoretical Methods

We implemented Vienna ab-initio simulation (VASP) package to carry out the first principles calculations [32,33]. Projector-augmented-wave (PAW) approach within the generalized gradient approximation is utilized [34]. The contribution from the exchange correlation terms is taken into account via the Perdew–Burke–Ernzerhof (PBE) functional [35]. The energy cut-off value for all the calculations is set at 500 eV. All the systems are allowed to relax until the energy converges below 10^{-5} eV/ atom. The correction due to dispersive forces is taken into account through the DFT + D2 (Grimme's) method [36].



Scheme 7.1: Schematic diagram of differently sized nitrogen doped carbon quantum dots (N-CQD) from ribose and arginine

7.3. Results and Discussion

7.3.1. Surface chemistry and optical properties of the functional N-CQDs

For N-CQD synthesis, uniform heating from surface to bulk counterparts of the precursors is required to achieve high yield of the product. Herein, the N-CQD has been prepared without any surfactant whether low heating rate undergoes diminution the kinetics (rate), as well as smaller N-CQDs, undergo agglomeration with increasing the time. However, high yield, lower cost, and high reaction rate is required where microwave-assisted technique involves rapid heat generation due to collision with the precursor molecules. Such heating effect polarizes the molecules and enhances the collision frequency between the molecules and subsequently boosts the reaction rate (Scheme 7.1). Figure 7.1a reveals the high-resolution transmission electron microscopy (HRTEM) images of N-CQD (namely as 3A, 3B & 3C) having quasi spherical in nature. The calculated diameter has been measured by taking Gaussian fitted size distribution of 20-30 particles. From Gaussian fitted size distribution, the average diameter of 3A lies between 4.5 ± 0.33 nm where the size increases to 5.13 ± 0.59 nm and 6.40 ± 0.27 nm for 3B and 3C respectively (Figure 7.1a,d,g). The lattice fringes (d) of N-CQDs, are calculated which turn out to be 0.30 nm and correspond to (100) crystal facets of graphitic carbon (Figure 7.1c,f, i) [19,37]. Additionally, no flake like morphology or larger agglomerates were determined in HRTEM analyses of all N-CQDs. Figure 7.1j-o describes the high-resolution X-Ray photoelectron spectroscopy (XPS) spectra of N-CQD (3A, 3B & 3C). The C 1s spectrum corresponds to five components at 284.6 eV, 285.8 eV, 286.4 eV, 287.7 eV, 288.5 eV correspond to C=C, C=N, C-OH, C=O, and O-C=O, bond respectively (Figure 7.1j,l,n) [38,39]. The sp^2 carbon becomes more restored in 3A (% $\text{sp}^2 \sim 38.6\%$) and with increasing the reaction time more oxygenation of basal plane of 3B (% $\text{sp}^2 \sim 36.3\%$) and 3C (% $\text{sp}^2 \sim 34.1\%$) respectively.

$sp^2 \sim 35.5\%$) leading to change in the hybridization of carbon atoms. Strikingly, the percentage of $O-C=O$ remains much higher in 3A (10.32%) in comparison to 3B (8.18 %) and 3C (7.10%), which turns the N-CQD surface more negative. With increasing the time, the agglomeration of smaller particles leads to the loss of functional groups from N-CQD surface. Figure 7.1k,m,o explains N 1s spectrum having peak position at 398.5 eV, 399.8 eV, 400.4 eV, and 402.3 eV denoting the presence of pyridinic, amine, pyrrolic, and graphitic nitrogen respectively of N-CQDs [40,41]. The percentage of graphitic and amine nitrogen predominates for 3A (9.6 % and 36.18%) over 3B (3.6% and 30.6%) and 3C (2.3% and 29.75%) where the lowering in graphitic carbon due to basal plane oxidation of 3C. From the XPS survey spectra, the percentage (%) of nitrogen content decreases from 3A (14.5%) to 3B (14.28%) and 3C (13.67%) (Figure 7.2). Additionally, O 1s spectrum deconvolutes to four distinct peaks at 531.5 eV, 532.2 eV, 532.9 eV, and 534 eV corresponding to $C=O$, $C-O$, $O-H$, $O-C=O$ bonds of N-CQD respectively (Figure 7.2d-f). The atomic percentage of N-CQDs and FTIR analyses are discussed in Figure 7.3.

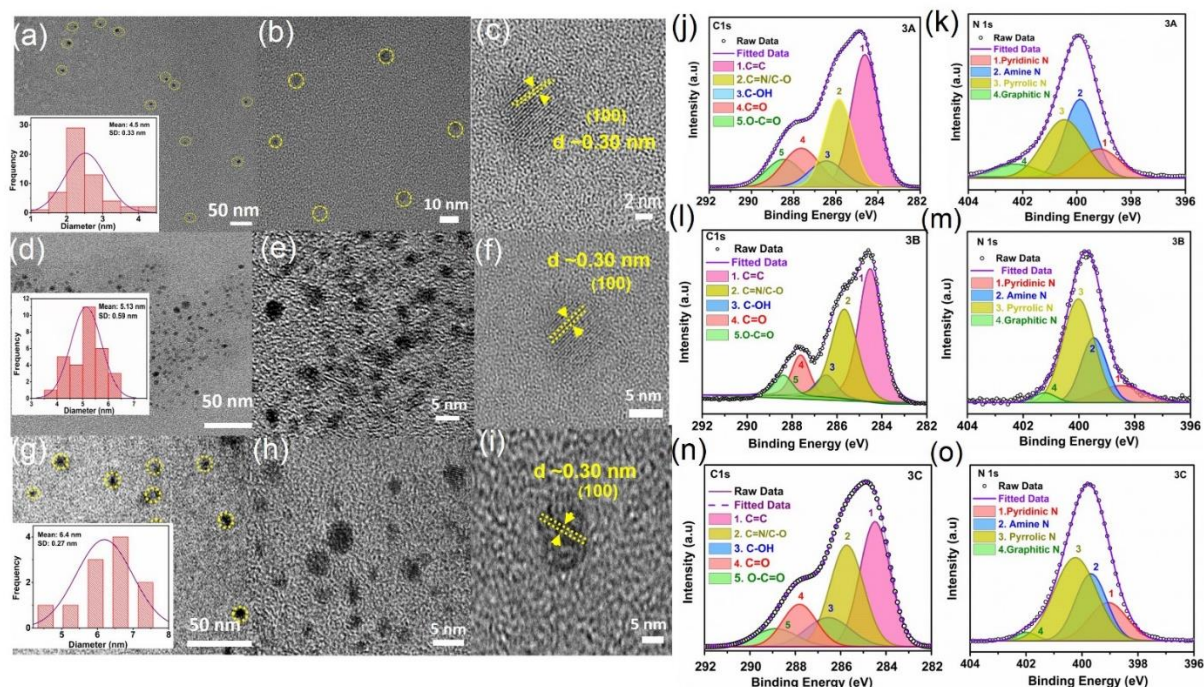


Figure 7.1: High resolution Transmission electron microscope (HRTEM) image of (a,b) 3A (d,e) 3B (g,h) 3C. Inset showing particle size distribution histogram of N-CQD. Lattice fringe pattern of (c) 3A (f) 3B and (i) 3C. High resolution XPS C 1s and N 1s spectra of (j, k) 3A (l,m) 3B and (n,o) 3C respectively.

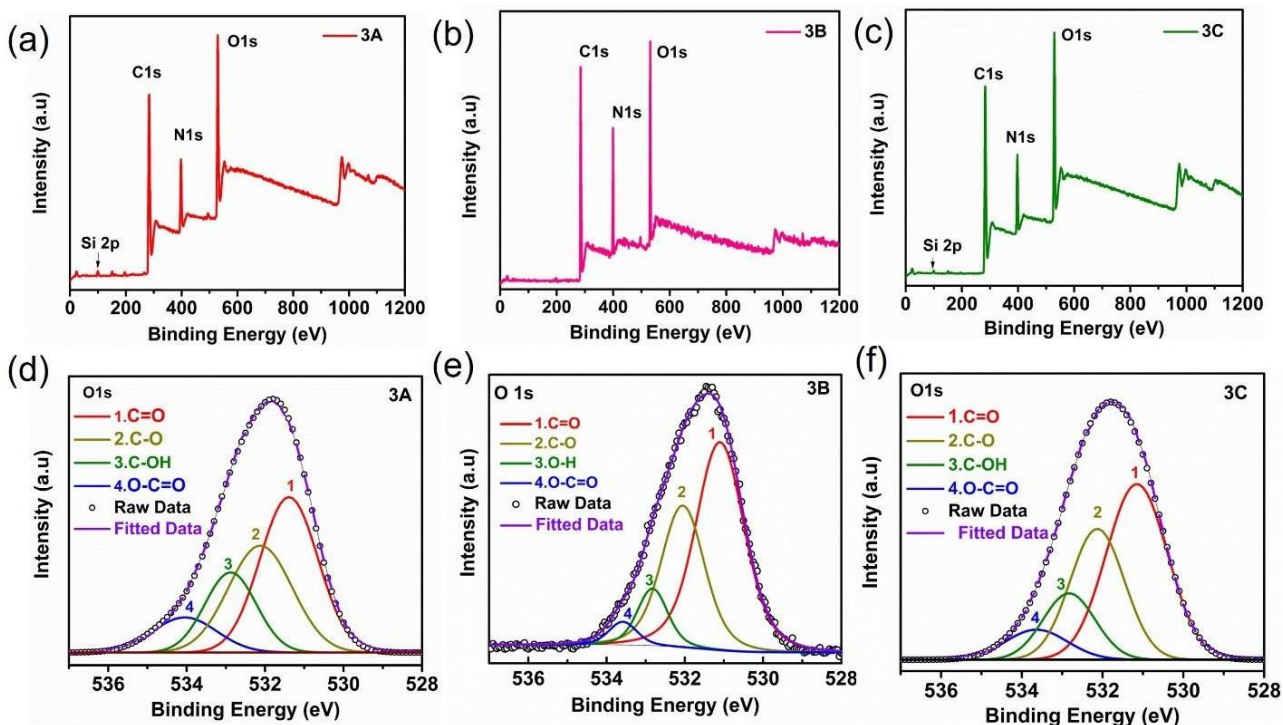


Figure 7.2: XPS survey spectra of (a) 3A (b) 3B and (c) 3C. High resolution XPS O1s spectra of (d) 3A (e) 3B and (f) 3C.

It should be noted the increase in reaction time promotes more oxygenation of basal plane of 3C, leading to decreased sp^2 carbon ($C=C$) content. The -OH percentage gradually increases from 3A (9.4%) to 3C (12%) shown in Figure 7.3a. The chemical environment of functional groups is correlated with FTIR spectra shown in Figure 7.3d. A broad peak around 3450 cm^{-1} and 3200 cm^{-1} attributes to -OH and -NH stretching frequency, respectively of N-CQD. Similarly, a low intense peak at 2900 cm^{-1} and 1620 cm^{-1} implies -C-H and $C=C$ stretching vibrations, respectively [42]. Interestingly, a small peak around $\sim 1300\text{ cm}^{-1}$ and 1580 cm^{-1} is mainly due to C-N and N-H bending vibration modes [43]. The presence of N-H and C-N modes elucidates the nitrogen atom into the surface of N-CQD. Additionally, the occurrence of three distinct peaks at 1720 cm^{-1} , 1100 cm^{-1} , and 1420 cm^{-1} is mainly due to carbonyl ($C=O$), epoxy ($C-O$), and symmetric O-C-O ($-COOH$) vibrations, respectively [44].

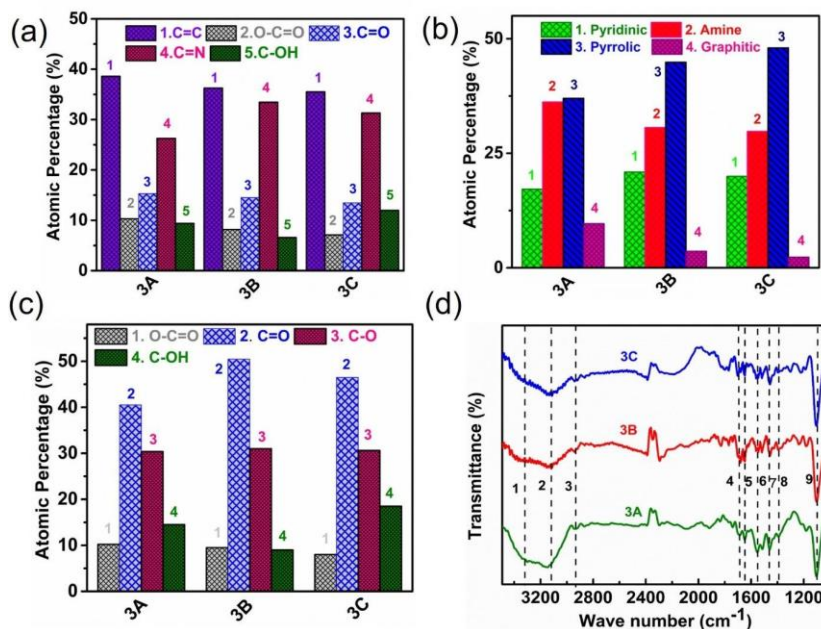


Figure 7.3: Atomic percentage of different functional groups from (a) C1s (b) N1s and (c) O1s spectra of N-CQD (3A,3B,3C). (d) FTIR spectra of 3A,3B, and 3C. (Here 1-9 denotes different functional groups 1)-N-H stretching, 2) O-H stretching, 3) C-H stretching, 4) C=O, 5) C=C, 6) C-N, 7) N-H bending, 8) O-C=O, 9) C-O stretching frequency.

Full Raman spectra of N-CQDs are shown in Figure 7.4. To illustrate the type of defects and sp^2 carbon, the first order spectra are deconvoluted into five components i.e. D^* , D, D^{**} , G, D'' . The phonon-defect bands such as D and D'' are determined by defect-induced Double Resonance (DR) process [45,46]. Generally, the ratio of D and G bands is used to characterize the amount of graphitization into the material. The D band is centered at 1350 cm^{-1} which denotes type of defects (point defect, edge defects) and the G band at 1550 cm^{-1} is the breathing mode of sp^2 graphitic carbon content into Graphene/carbon quantum dots, graphene oxide (Figure 7.4a-d) [39]. The $\text{I}_\text{D}/\text{I}_\text{G}$ ratio decreases from 3A to 3C shown to a value of 0.52, 0.48, and 0.46 (Figure 7.4e). The ratio is less than 1 which signifies low defect density of all N-CQDs where the percentage of defects due to oxygen and nitrogen functional groups are maximum for 3A due to high $\text{I}_\text{D}/\text{I}_\text{G}$ ratio. To correlate the $\text{I}_\text{D}/\text{I}_\text{G}$ ratio with graphitic (sp^2) carbon, the FWHM of the G band follows the inverse relationship with $\text{I}_\text{D}/\text{I}_\text{G}$ ratio. The high FWHM of the G band is mainly due to

disorder of core state due to agglomeration with increasing the time. The FWHM of G band of 3A, 3B and 3C is calculated to be 112 cm^{-1} , 120 cm^{-1} , and 127 cm^{-1} respectively. The broadening i.e. the higher FWHM of G band for 3C is also correlated with A_D/A_G ratio. The lower A_D/A_G ratio of 3C (0.16) also manifests the lower graphitization in comparison with 3A (0.32) and 3B (0.18). Thus, correlation reveals, that the sp^2 percentage is higher for 3A which is well correlated with XPS C 1s spectra.

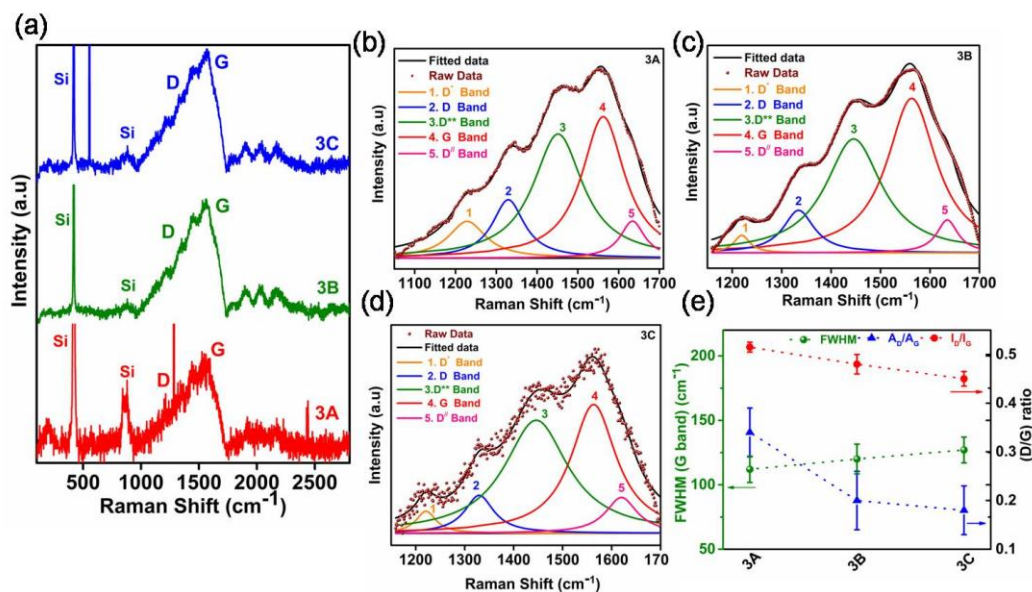


Figure 7.4: (a) Full range Raman spectra for 3A, 3B, and 3C. Deconvoluted Raman spectra consist of first order components for (b) 3A (c) 3B and (c) 3C. Brown lines are the original line shape as obtained from spectrometer and the rest of the colors represent the contributions of different bands. (e) Variation of I_D/I_G , A_D/A_G ratio with FWHM of G band of all N-CQDs.

Figure 7.5 depicts Gaussian fitted photoluminescence excitation spectra (PLE) of N-CQD (3A, 3B & 3C) at different emission wavelengths. At a fixed concentration of N-CQD (6.25 mg/ml), PLE spectrum has recorded three emission maxima (λ_{em}) $\sim 400\text{ nm}$, $\sim 450\text{ nm}$, and $\sim 510\text{ nm}$, respectively where the excitation transition around $\sim 270\text{ nm}$ indicates $n_{2p}-\sigma^*$ transition, which is related to amine or oxygen functional groups. The intense PLE maxima at $\sim 320\text{--}330\text{ nm}$ correspond to $\pi-\pi^*$ transitions of C=C carbon basal plane of N-CQD (Figure 7.5a-c) [47,48]. The PLE maxima at $\sim 370\text{ nm}$, $\geq 400\text{ nm}$, and $\geq 430\text{ nm}$ belong to $n-\pi^*$ transition of functional groups $-\text{COOH}$ ($n_{O2p}-\pi^*$), $-\text{COO}^-$ ($n_{O2p}-\pi^*$) and NH_2 ($n_{N2p}-\pi^*$) respectively [48-51].

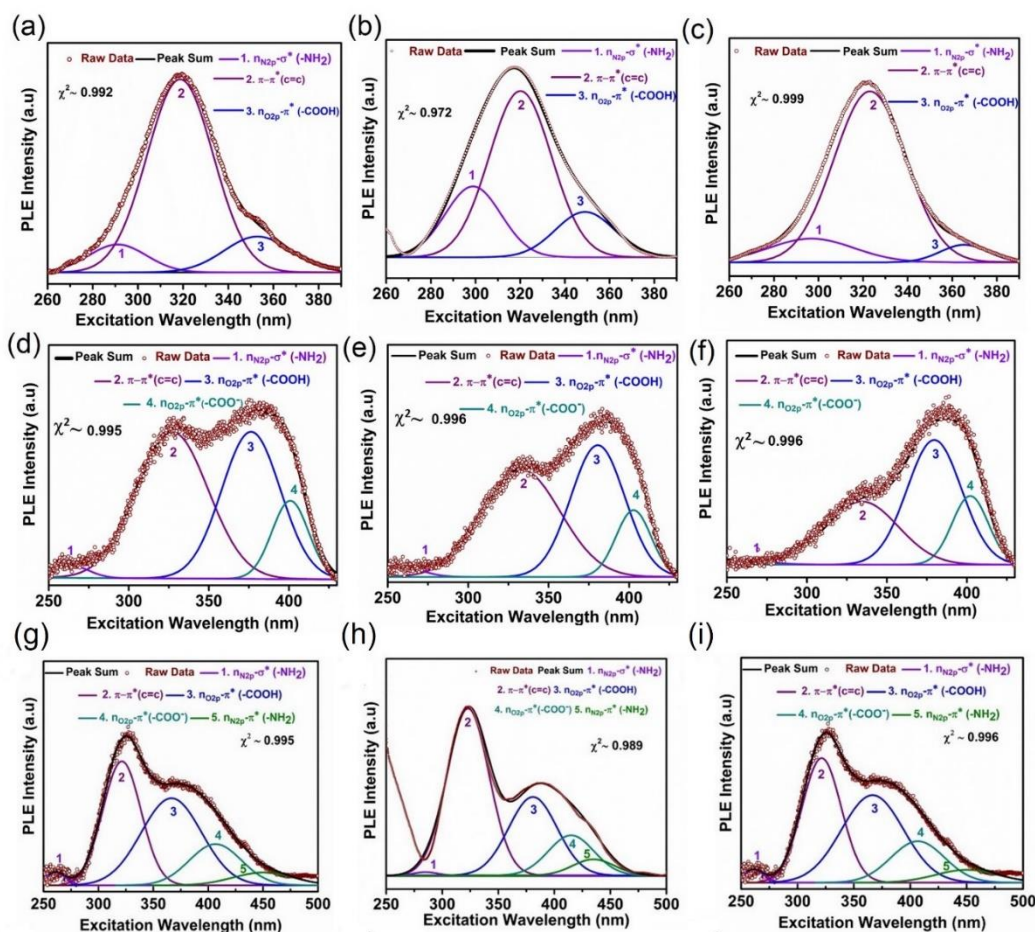


Figure 7.5: Deconvoluted Photoluminescence excitation (PLE) spectra of (a,d,g) 3A (b,e,h) 3B and (c,f,i) 3C at a concentration (6.25 mg/ml) for emission at 410 nm, 445 nm and 510 nm respectively.

As lowering the concentration of 3A from 10 mg/ml to 1.65 mg/ml, the intensity of $n-\pi^*$ absorptions around ~ 370 nm to 420 nm decreases, most likely due to reduction in H-bonding in polar protic solvent (Figure 7.6a-c) [52]. However, a significant lowering of intensity of the $n-\pi^*$ absorptions is observed at lower pH (~ 1) (Figure 7.6d). The protonation of such functional groups hinders the electron transfer toward carbon plane. Figure 7.6f suggests the blue shift of $n-\pi^*$ absorption occurs at lower pH (~ 1) due to the formation of nonradiative groups in a highly acidic environment. In highly basic conditions (~ 12), the formation of carboxylate ion and $p\pi-p\pi$ overlap between NH^- and aromatic sp^2 ring leads to blue shift of $nO_{2p}-\pi^*$ and $nN_{2p}-\pi^*$ transitions[52-55].

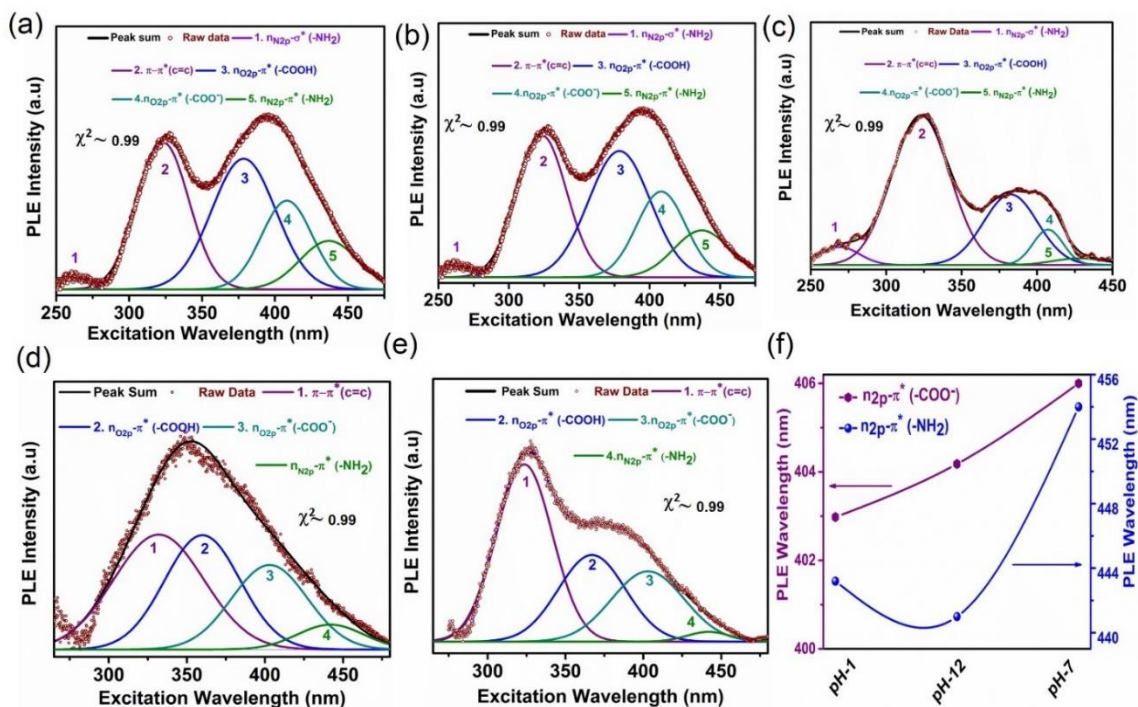


Figure 7.6: Deconvoluted Photoluminescence excitation (PLE) spectra of 3A for the emission at ~506 nm at concentrations (a) 10 mg/ml and (b) 6.25 mg/ml and (c) 1.65 mg/ml. PLE spectra of 3A at (d) pH~1 and (e) pH~12 at ~506 nm emission wavelength. (f) Position of PLE peak maxima of different $n-\pi^*$ transitions of 3A at different pH values.

In Figure 7.7a-c, an intense broadband emission has been observed for all N-CQD under excitation of different wavelengths from 310 nm to 430 nm. At 330 nm excitation wavelength (PLE maxima), the broad PL profile was deconvoluted to two components having high energy emission peak 1 (centered at ~390 nm) due to the $\pi-\pi^*$ transitions and peak 2 (centered at ~450 nm) due to the $n-\pi^*$ transitions from the functional groups (Figure 7.7d). At 370 nm excitation wavelength (PLE maxima), emission maximum (λ_{\max}) occurs at ~445 nm for 3A having two components at peak 1 $n_{O2p}-\pi^*$, (~COOH) (λ_{\max} ~440 nm), and peak 2 $n_{O2p}-\pi^*$ / $n_{N2p}-\pi^*$ (λ_{\max} ~480 nm, COO⁻, NH₂ or amide) (Figure. 7.7e). Generally, the lower energy emission mainly originates from nitrogen type dopants (amine, amides) [56]. The emission at ~510 nm under excitation 430 nm denotes $n_{N2p}-\pi^*$ transitions due to different nitrogen substituents (~NH₂, amide, graphitic nitrogen) [38].

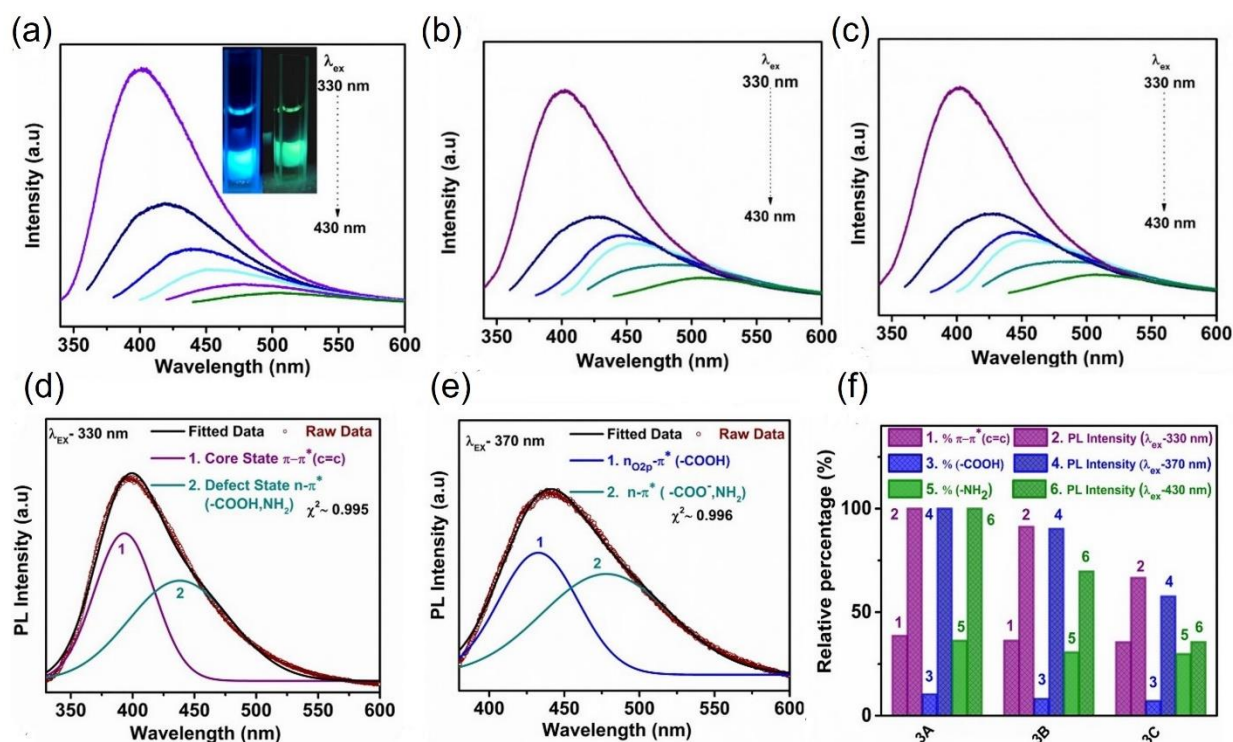


Figure 7.7: Photoluminescence (PL) spectra of (a) 3A (b) 3B and (c) 3C at different excitation wavelengths. Inset showing blue and green emission at 370 nm and 430 nm excitation. Deconvoluted PL spectra of 3A at (d) 330 nm, emission- peak 1 ($\pi-\pi^*$) core and peak 2 (defect state) (e) 370 nm, emission- peak 1 ($n_{\text{O}2\text{p}}-\pi^*$ -COOH) core and peak 2 (COO $^-$, NH_2) excitation. respectively. (f) Relative percentage of atomic composition of (1) sp^2 C=C (3) -COOH (5) -NH $_2$ and PL intensity at excitation wavelength (2) 330 nm ($\pi-\pi^*$) (4) 370 nm ($n_{\text{O}2\text{p}}-\pi^*$ -COOH) and (6) 430 nm ($n_{\text{O}2\text{p}}-\pi^*$ -NH $_2$) of 3A,3B and 3C respectively at a concentration 6.25 mg/ml.

Furthermore, the relative intensity of emissions such as $\pi-\pi^*$, $n_{\text{O}2\text{p}}-\pi^*$ ($\sim\text{COOH}$), and $n_{\text{N}2\text{p}}-\pi^*$ ($\sim\text{NH}_2$ or amide) significantly shrinks from 3A to 3C, which are correlated with atomic compositions of C=C (aromatic sp^2), -COOH, and NH_2 respectively. The higher atomic percentage (estimated from XPS analyses) of the aforementioned functional groups of 3A enhances PL intensity compared to 3B and 3C at a fixed concentration. The calculated relative quantum yield of samples 3A, 3B, and 3C was found to be 49.25%, 44.5%, and 34.5% respectively. Moreover, the maximum percentage of amine, amide, and O-C=O makes the

surface more hydrophilic in nature with a higher negative charge density of 3A (zeta potential (ζ) \sim -15.1 mV), 3B (ζ \sim -14.9 mV) than 3C (ζ \sim -7.57 mV) (Figure 7.8a). The effect of pH on PL spectra has been not significantly changed for N-CQDs. Indeed, the PL intensity diminishes at higher and lower pH under the same concentration, probably due to lesser excited state population by electron donation and protonation of functional group towards graphitic core, respectively (Figure 7.8b-e) [57,58].

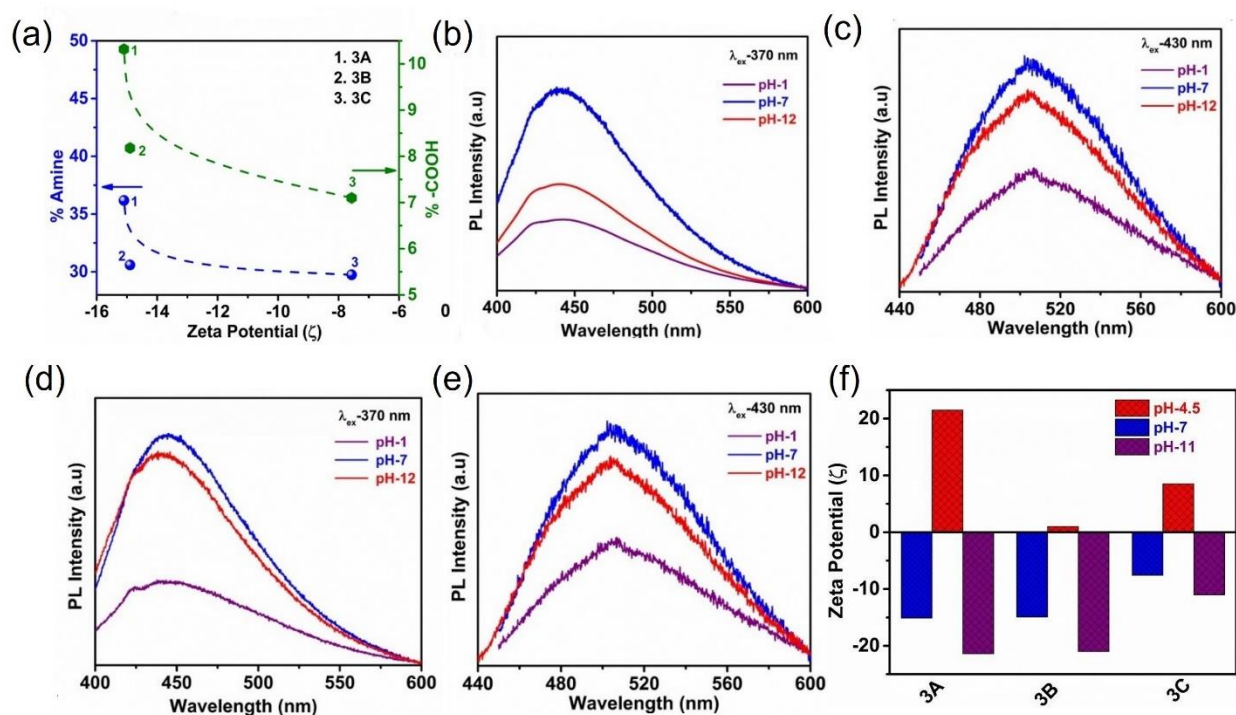


Figure 7.8. (a) Relationship of amine and COOH content of N-CQD (3A, 3B, and 3C) with Zeta Potential (ζ). The pH of all the solutions remains \sim 7. Effect of pH on PL spectra of (b, c) 3A and (d, e) 3B at 370 nm and 430 nm excitation wavelength. (f) Variation of zeta potential (ζ) of N-CQD (3A, 3B, and 3C) at different pH values.

The phenomenon can be established by measuring ζ shown in figure 7.8f. At higher pH (pH \sim 10), the ζ becomes negative to -21.4 mV, -20.9 mV, and -10.9 mV for 3A, 3B & 3C respectively, leading to deprotonation of functional groups which can boost the electron transfer towards graphitic core in comparison with N-CQD at pH \sim 7 (Figure 7.8f). At which, pH \sim 4.5, ζ of 3A, 3B, & 3C becomes positive to +21.5 mV, +1 mV, and +8.60 mV, respectively, which implies deficiency of electrons at the surface via protonation.

7.3.2. Photoluminescence quenching and binding of N-CQDs with metal ions

A model reaction was established to investigate the change of PL signals, including full width at half maximum (fwhm), area, and intensity of deconvoluted PL components of N-CQD via capping with most selective metal ion and subsequently investigate the role of core and surface state towards emission mechanism. Figure 7.9 indicates the quenching of PL signals including fwhm, area, and intensity of 3A under different metal ions (Cd^{2+} , Ni^{2+} , Co^{2+} , Ag^+ , Pb^{2+} , Zn^{2+} , Cu^{2+} , Hg^{2+}) at maximum PLE wavelength, i.e. 330 nm and 370 nm excitation. The lowering of PL signals of all emission maxima is maximum in case of Hg^{2+} which concludes the N-CQD acts as a specific and selective fluorescent metal ion (Hg^{2+}) detector.

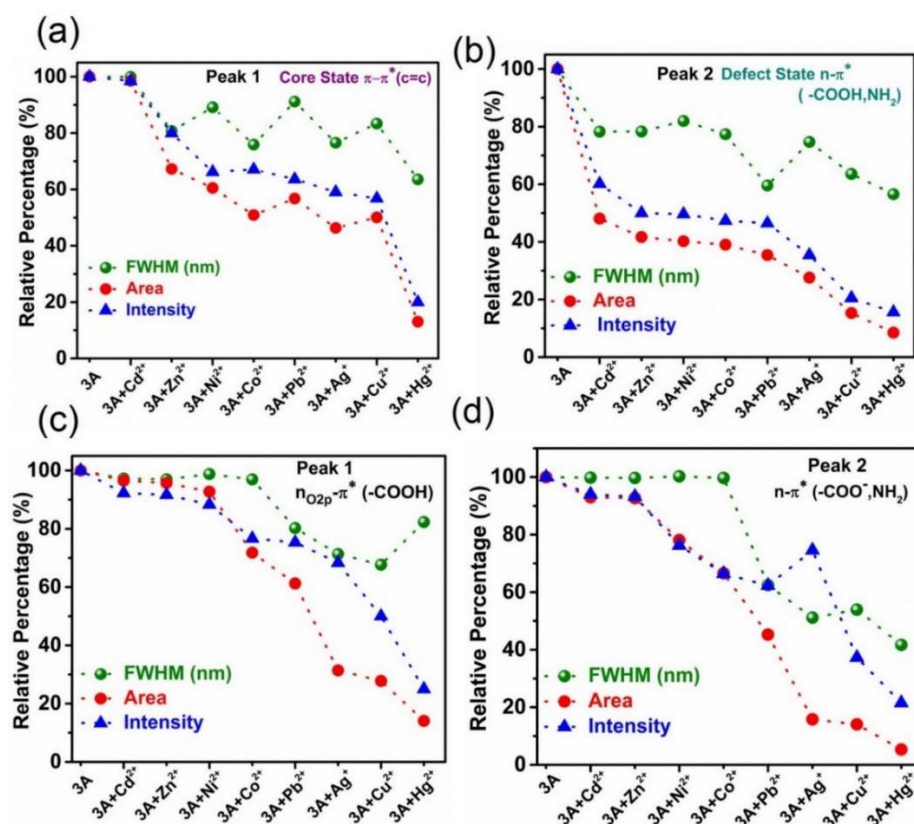


Figure 7.9: Relative percentage of PL fwhm (nm), area and intensity of (a) peak 1 ($\pi-\pi^*$) (b) peak 2 ($n-\pi^*$) (c) peak 1 ($n_{\text{O}2\text{p}}-\pi^*$ $-\text{COOH}$) and (d) peak 2 ($n_{\text{O}2\text{p}}-\pi^*$ $-\text{COO}^-$, NH_2) of 3A after adding metal ions (Cd^{2+} , Zn^{2+} , Ni^{2+} , Co^{2+} , Pb^{2+} , Ag^+ , Cu^{2+} , Hg^{2+}) (Concentrations $\sim 50 \mu\text{M}$).

For better understanding, the concentration of Hg^{2+} varied from 0.18 μM to 2.82 mM with N-CQD and the PL properties has been studied at 370 nm excitation wavelength (Figure 7.10). The steady state Stern-Volmer plots ($(I_0/I)-1$ vs concentration of Hg^{2+}) suggest a nonlinear behavior at a higher concentration of Hg^{2+} . The deviation of linearity at higher concentrations is probably due to steric shielding process or a mixed static and dynamic quenching, which can diminish the accessibility of metal ions towards the active site of all N-CQDs [49,59]. The limit of detection (LOD) for 3A,3B, and 3C has a value of 0.209 μM , 0.27 μM , and 0.41 μM , respectively (comparison table-7.1).

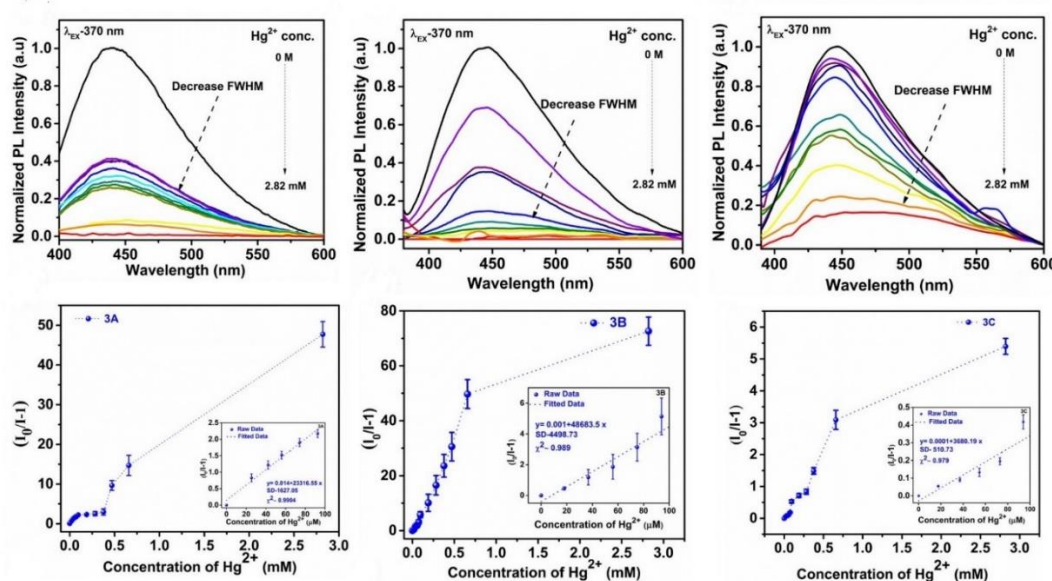


Figure 7.10: PL quenching of (a) 3a (C) 3B and (e) 3C under different Hg^{2+} concentration (0-2.82 mM). Stern-Volmer plots $(I_0/I)-1$ vs concentration of Hg^{2+} of (b) 3A (d) 3B and (f) 3C (Inset showing linear relationship between $(I_0/I)-1$ vs concentration of Hg^{2+}) at 370 nm excitation.

It is worth mentioning, that four different Hg^{2+} concentrations ranging from 56 μM , 94 μM , 376 μM and 658 μM have been utilized for all N-CQDs to study the quenching behavior of PL signals at different excitations. The PL quenching profile at 330 nm excitation of N-CQDs has been depicted in Figure 7.11. At 56 μM Hg^{2+} the peak area and intensity of 3A, 3B and 3C of peak 1 ($\pi-\pi^*$) has diminished to ~18.65%, ~33.2 %, ~51.58 %, ~43.16% and ~99.94%, ~92.59% respectively (Figure 7.11a,e,i & 7.12).

Sensing probes	Application	Medium	Detection Limit	Signal	Q.Y	Ref
CD	Hg ²⁺	Ultrapore Water	0.23 μ M (Range-0-25 μ M)	PL	15.7	60
CD	Hg ²⁺	Phosphate buffer	2.69*10 ³ nmol/ L (Range- 10 ⁻⁷ – 2.69 \times 10 ⁻⁶ M)	PL	-	61
N-CQD	Hg ²⁺	Phosphate buffer	2.3*10 ² nmol/L (Range- 10 ⁻⁷ – 2.69 \times 10 ⁻⁶ M)	PL	-	62
N/C-dots	Hg ²⁺	Ultrapore Water	2 μ M (Range-0-40 μ M)	PL	25.2	63
Graphitized CD	Hg ²⁺	Deionized water	35 nmol/ L (Range- 0-10 ⁻⁶ mol/L)	PL	25	64
FCDs	Hg ²⁺	Deionized water	20 (Range- 0.1– 1.2 μ mol L ⁻¹)	PL	36	65
CD	Hg ²⁺ and Cys	ultrapure water	0.017 μ M (Range- 2 to 22 μ M)	PL	15.3	66
TFIC MNPs	Hg ²⁺	ultrapure water	5.04*10 ⁻⁶ mol/L (Range- 4.0 \times 10 ⁻⁶ to 16 \times 10 ⁻⁶ mol/L)	PL	-	67
CQDs-Tb3+	Hg ²⁺	Water	38.1 nM (Range-1-6 μ M)	PL	-	68
CD	Hg ²⁺	Water	9 nM (Range-0-40 μ M)	PL	-	69
GQD	Hg ²⁺	ultrapure water	0.12 μ M (Range-0.15-20 μ M)	PL	15.1	70
N-CQD	Hg ²⁺	Deionized water	0.209 μ M (Range-0-100 μ M)	PL	54	This Work

*CD: Carbon Dot; #N-CQD: Nitrogen doped Carbon Quantum dot; †FCDs: Fluorescent carbon dots, \$ TFIC MNPs: TSRh6G-b-CD/Fe₃O₄@ SiO₂-nanoparticle, GQD: Graphene quantum dots.

Table 7.1: Comparison of sensing Performance of N-CQD.

The result is congruence with peak 2 ($n-\pi^*$) to quench the peak area and intensity for 3A, 3B and 3C to ~23.4%, ~42.54 %, ~42.90%, ~48.52% and ~99.9%, ~89% respectively (Figure 7.11a,e,i & 7.12). Similarly, the relative percentage of peak area and intensity of peak 1 change to 18%, 27.2% (3A), 37%, 33% (3B) and 30%, 24% (3C) respectively at 94 μ M Hg²⁺ respectively (Figure 7.11b,f,j & 7.12).

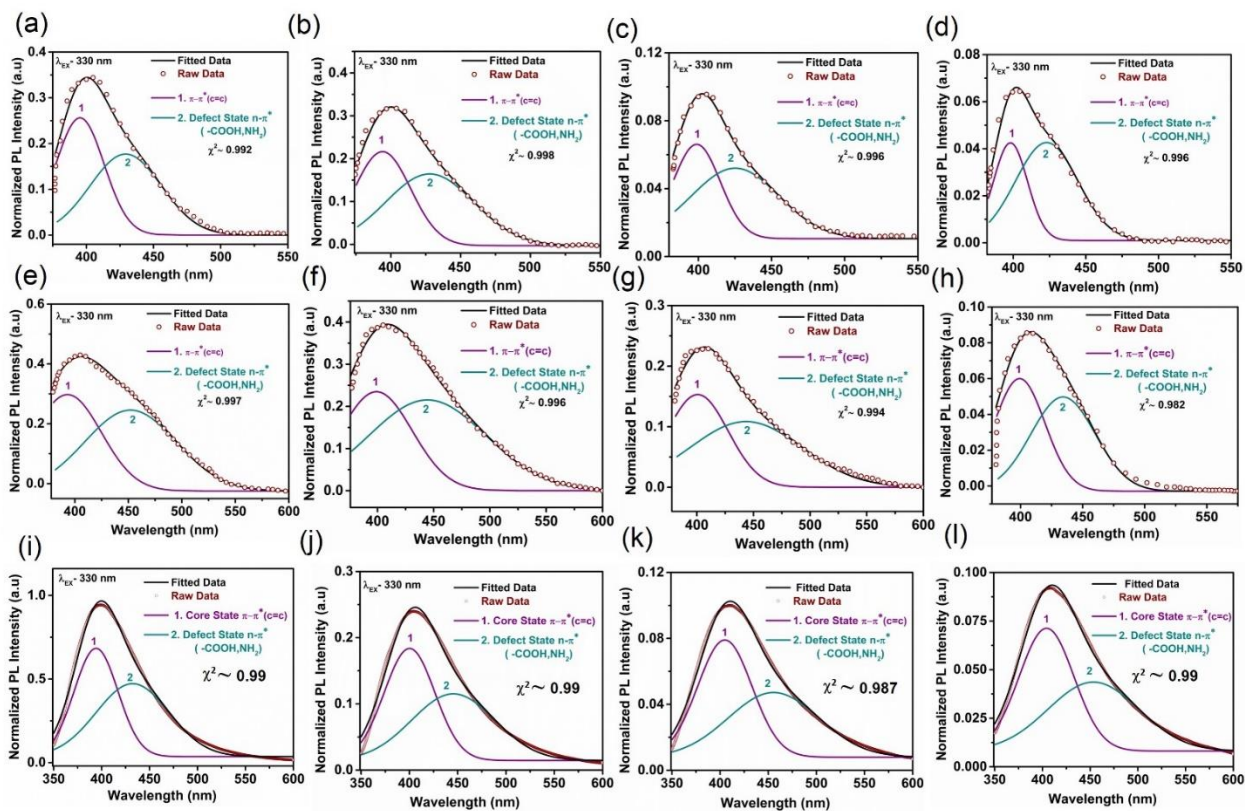


Figure 7.11: Deconvoluted PL profile of 3A, 3B and 3C with (a,e,i) 56 μM (b,f,j) 94 μM (c,g,k) 376 μM and (d,h,l) 658 μM Hg^{2+} respectively at excitation wavelength 330 nm.

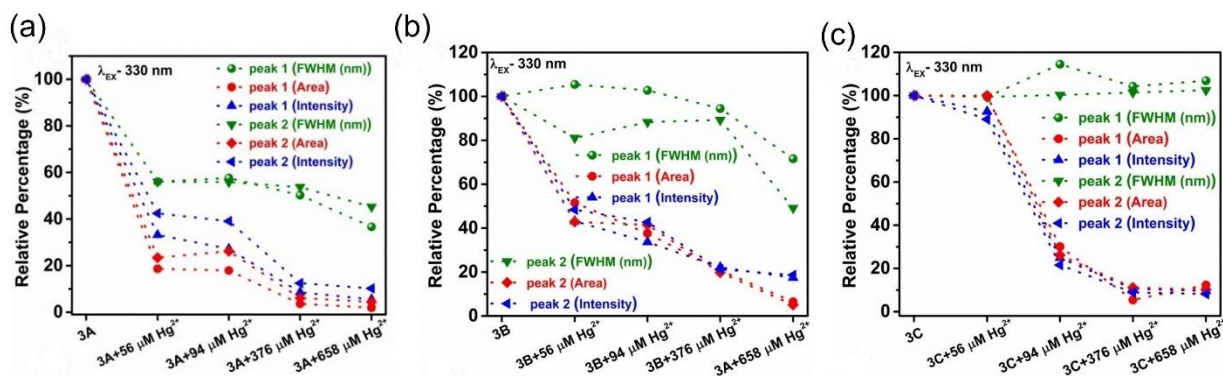


Figure 7.12: Relative percentage of PL fwhm (nm), area and intensity of peak 1 ($\pi\text{-}\pi^*$) and peak 2 ($n\text{-}\pi^*$) at different Hg^{2+} concentrations of (a) 3A (b) 3B and (c) 3C respectively at 330 nm excitation.

The peak area and intensity of peak 2 ($n-\pi^*$) follows the same trend ~26%, ~39% (3A), ~41%, ~42% (3B) and ~26%, ~21% (3C) respectively. Generally, the quenching efficiency follows the trend $3A > 3B > 3C$ at different Hg^{2+} concentrations. At 330 nm excitation, the PL fwhm, area, and intensity of peak 1 ($\pi-\pi^*$) for 3A becomes 36.65 %, 1.97 % and 5.53 % (w.r.t 100%) respectively under 658 μM Hg^{2+} (Figure 7.11a,e,i & 7.12). Similarly, the relative percentage of PL area, and intensity of peak 1 ($\pi-\pi^*$) for 3B and 3C are 6.5 %, 17.41 %, 12.30 %, and 9.6 % respectively under same Hg^{2+} Concentrations (Figure 7.11d,h,i & 7.12). In comparison with peak 1 ($\pi-\pi^*$), relative percentage of PL area, and intensity of peak 2 for 3A, 3B and 3C exhibits 4.4%, 10.3%, 5%, 18.63% and 8.14%, 10.17% respectively at 658 μM Hg^{2+} .

Figure 7.13 and 7.14 reveals the variation of PL signals of peak 1 $n_{O2p}-\pi^*$ (-COOH) and peak 2 $n_{O2p}-\pi^*/n_{N2p}-\pi^*$ (COO^- , NH_2 or amide) with Hg^{2+} concentrations (56 μM , 94 μM , 376 μM and 658 μM) for all N-CQDs. At 56 μM Hg^{2+} the peak area and intensity of peak 1 $n_{O2p}-\pi^*$ (-COOH) has diminished to 37%, 36% (3A), 33%, 36% (3B) and 85%, 90% (3C) respectively (Figure 7.13a,e,i and 7.14). In contrast, the peak area and intensity of peak 2 shrinks to 46%, 44% (3A), 33%, 36% (3B) and 93%, 98% (3C) respectively. Strikingly, the change in relative percentage of PL signals of peak area and intensity follows the same trend at 94 μM Hg^{2+} (for 3A~ (peak 1) 35%, 36% and (peak 2) 44%, 42%), (for 3B (peak 1) ~ 10%, 16% and (peak 2) ~ 13%, 18%) and (for 3C (peak 1) ~ 43%, 60% and (peak 2) ~ 57%, 62%). Nevertheless, the quenching efficiency has been calculated follows the order $3B > 3A > 3C$. The area and intensity of peak 1 $n_{O2p}-\pi^*$ (-COOH) and peak 2 $n_{O2p}-\pi^*/n_{N2p}-\pi^*$ for 3A decreases to ~18 %, 19% and ~ 26%, 24% at 658 μM Hg^{2+} concentration respectively. Additionally, area and intensity of peak 1 $n_{O2p}-\pi^*$ (-COOH) and peak 2 $n_{O2p}-\pi^*/n_{N2p}-\pi^*$ for 3B and 3C follow the same trend to a value 9%, 9.2%, 5.2%, 8% and 35%, 32% ,38%, 49% respectively under same Hg^{2+} (Figure 7.13d,h,i and 7.14). The percentage of quenching with Hg^{2+} is much lower in 3C where the surface functional groups and core state are prone to such lowering of PL signals.

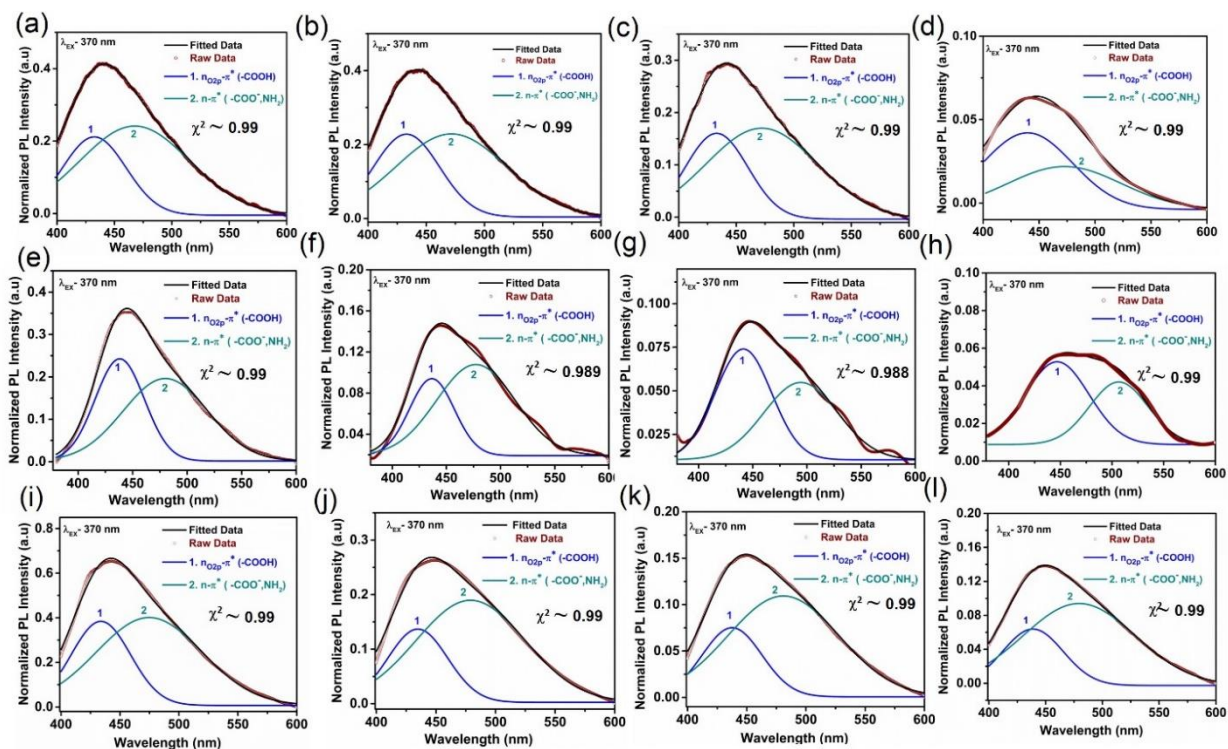


Figure 7.13: Deconvoluted PL profile of 3A,3B and 3C with (a,e,i) 56 μM (b,f,j) 94 μM (c,g,k) 376 μM and (d,h,l) 658 μM Hg^{2+} respectively at excitation wavelength 370 nm.

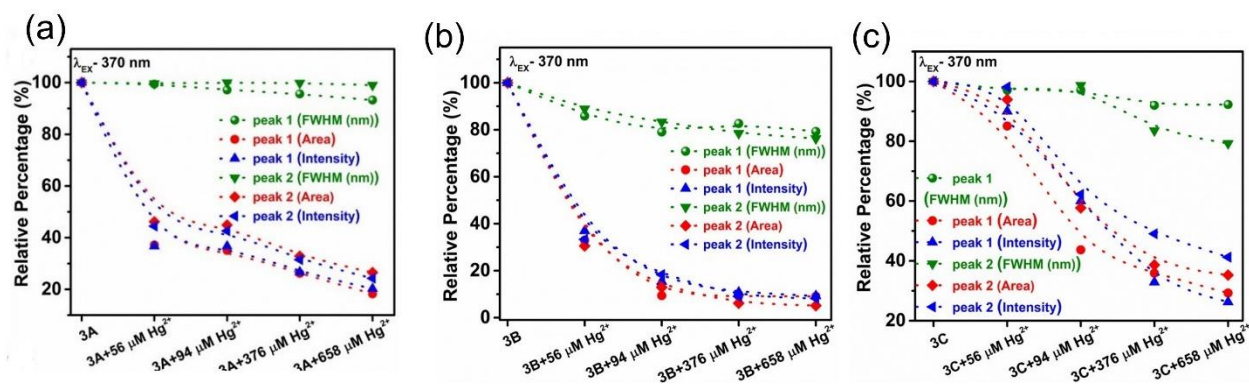


Figure 7.14: Relative percentage of PL fwhm (nm), area and intensity of peak 1 ($\text{nO}_2\text{P}-\pi^*-\text{COOH}$) and (d) peak 2 ($\text{nO}_2\text{P}-\pi^*-\text{COO}^-, \text{NH}_2$) of (a) 3A (b) 3B and (c) 3C with different Hg^{2+} concentrations at 370 nm excitation

7.3.3. Sensing dynamics between N-CQDs and Hg^{2+} ion

we have carried out high resolution XPS to ascertain the structural modification after sensing for sample 3A with the addition of 2.82 mM of Hg^{2+} (maximum Hg^{2+} concentration), as shown in Figure 7.15a. Figure 7.15b explains C 1s spectrum having five deconvoluted peaks at 284.5 eV, 285.2 eV, 286.5 eV, 288.1, and 289.1 eV suggests C=C, C=N, C-OH, C=O, and O-C=O groups, respectively. Interestingly, the atomic percentage of sp^2 (C=C) changes from 38.6% to 32.8% after Hg^{2+} incorporation. The 0.6 eV shift of binding energy of O-C=O groups is probably due to the attachment of carboxyl group with Hg^{2+} . The percentage of O-C=O groups decreases to 5.62% due to binding with Hg^{2+} . N 1s spectrum shows a small shoulder near ~ 398 eV after the addition of 2.82 mM Hg^{2+} (Figure 7.15c). Moreover, N 1s spectrum deconvolutes to five peaks at 398.1 eV, 398.7 eV, 399.5 eV, 400.3 eV, and 401.6 eV having pyridinic, amine, pyrrolic, $\text{NH}_2\text{-Hg}^{2+}$, and graphitic nitrogen, respectively. The new peak at 400.3 eV implies forming a bond with Hg^{2+} with nitrogen donor amide or amine groups, thereby decreasing the percentage of amine significantly to 14.60% [71,72]. Henceforth, we confirm the attachment between carboxyl group with Hg^{2+} from deconvoluted Hg 4f spectrum. Figure 7.15d suggests five deconvoluted peak components at 99.9 eV, 101.1 eV, 101.9 eV, 105.2 eV and 106.3 eV. The XPS binding energy at 103.2 eV corresponds to 2p orbital of SiO_2 [73]. notably, the peak at 99.92 eV and 105.2 eV denotes Hg (0) $4f_{7/2}$ and Hg (0) $4f_{5/2}$, respectively, which concludes the existence of Hg in the system [71]. The peaks positioned at 101.1 eV and 106.3 eV are due to the presence of $\text{Hg}^{2+} 4f_{7/2}$ and $\text{Hg}^{2+} 4f_{5/2}$, respectively [74]. However, the peak at 101.9 eV reveals the binding between $(\text{COO}^-)_2\text{-Hg}^{2+}$ [74,75]. Thus, it can be surmised that the diminution of the percentage of sp^2 (C=C), carboxyl groups, amines, or amides are strongly associated with quenching of PL signals of $\pi\text{-}\pi^*$ and $\text{n-}\pi^*$ at 330 nm, 370 nm, and 430 nm excitation. Figure 7.15e reveals relationship of amine and -COOH functional groups with quenching efficiency at 2.82 mM of Hg^{2+} . The percentage of quenching efficiency decreases from 3A to 3C ($3\text{A} (\sim 0.98) \geq 3\text{B} (\sim 0.97) > 3\text{C} (\sim 0.83)$) at $\lambda_{\text{max}} \sim 445$ nm due to lower atomic percentage of amine or amide and -COOH type functional groups. The above phenomena correlate with surface charge, ζ at five different Hg^{2+} concentrations (56 μM , 94 μM , 376 μM , 658 μM , and 2.82 mM). Figure 3f indicates that the ζ value changes from negative to positive (-15 mV to +15 mV) of 3A, 3B, and 3C, increasing the Hg^{2+}

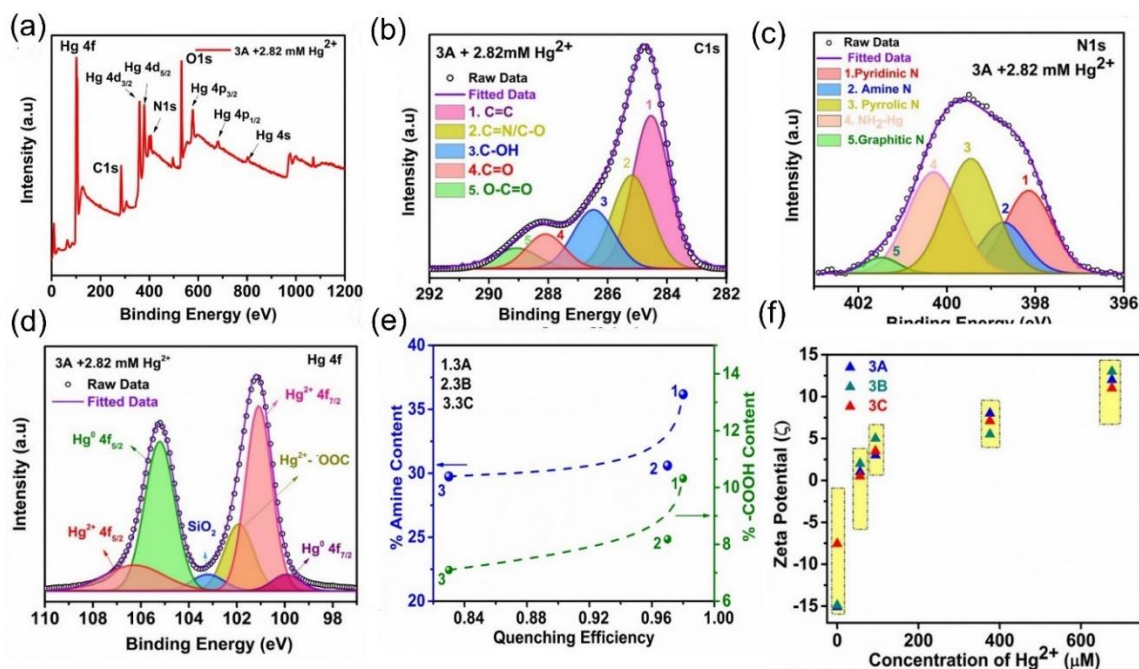


Figure 7.15: XPS survey spectra of (a) 3A with 2.82 mM Hg^{2+} . High resolution XPS spectra of (b) C 1s and (b) N 1s of 3A with 2.82 mM Hg^{2+} . (d) Hg 4f spectra of 3A +2.82 mM Hg^{2+} . (e) Relationship between quenching efficiency of N-CQD (3A,3B, and 3C) towards Hg^{2+} with atomic percentage of amine and COOH functional groups at 370 nm excitation. (f) Variation of Zeta potential (ζ) of N-CQD (3A,3B, and 3C) at 56 μM , 94 μM , 376 μM , 658 μM Hg^{2+} μM concentrate ion.

concentration up to 658 μM (Figure 7.15f). To correlate with XPS studies, the UV-Vis absorption and band gap are determined in all N-CQDs before and after 2.82 mM Hg^{2+} . From, UV-Vis absorption spectroscopy of N-CQD, three different sets of samples have been prepared at pH~1-2, pH~7, and pH~12. It is observed that the position of $n-\pi^*$ (~320 nm) at pH~1-2 and pH~12 of 3A and 3B shows almost similar in nature with respect to pH~7 (Figure 7.16a-c). Figure 7.16d-f shows Tauc plot of all N-CQDs where two linear parts of the spectra are clearly observed. After extrapolating to x-axis, the band gap is calculated for 3A,3B and 3C to a value of 3.3-3.45 eV, 3.8-4.1 eV and 3.5-4.1 eV respectively. At higher concentrations of Hg^{2+} (2.82 mM), the $n-\pi^*$ transition at ~322 nm has completely diminished (Figure 7.17a). In contrast, a broad peak around ~298 nm has been observed, which is the characteristic UV-Vis absorption of $\text{Hg}(\text{NO}_3)_2$. To explain that, UV-Vis absorption of bare $\text{Hg}(\text{NO}_3)_2$ is carried

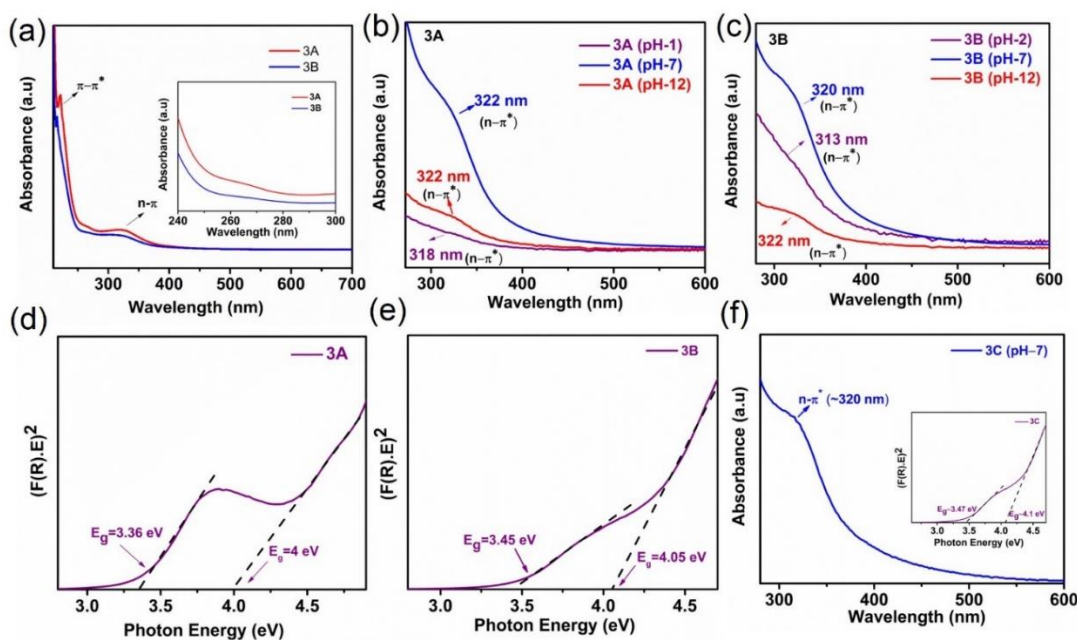


Figure 7.16: UV-Vis absorption spectroscopy of (a,b) 3A and (a,c) 3B. (d,e) Tauc plot of 3A and 3B. (f) UV-Vis absorbance of 3C (Inset is showing Tauc plot of 3C).

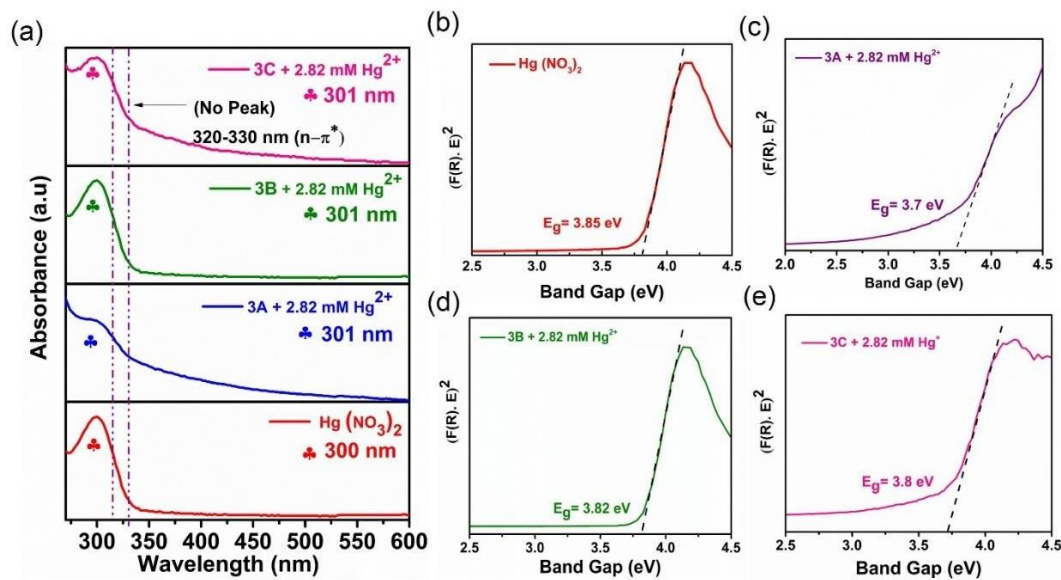


Figure 7.17: UV-Vis absorption spectroscopy of N-CQD (3A,3B,3C) in presence of Hg^{2+} (conc. 2.82 mM). Tauc plot of (b) bare $Hg(NO_3)_2$ (c) 3A (d) 3B and (e) 3C in presence of 2.82 mM Hg^{2+} .

out, showing a broad maximum at ~ 301 nm (Figure 7.17a). Thus, quenching effect on absorbance will also influence the change in band gap of N-CQD significantly. The band gap at 3.34 eV is completely diminished at 2.82 mM Hg^{2+} of 3A, concluding its origin due to the defect states. Interestingly, the band gap of $\text{Hg}(\text{NO}_3)_2$ lies at ~ 3.85 eV, which is almost similar to ~ 3.8 – 4 eV of 3B and 3C (Figure 7.17b–e).

7.3.4. Static and dynamic quenching

The ground state (static) quenching of Hg^{2+} predominates due to weak bond formation between different functional groups, with Hg^{2+} impacting the UV-vis absorbance, band gap, XPS, and PLE profile. Furthermore, the time resolved photoluminescence decay measurement was carried out to confirm the quenching process was fully static or dynamic in nature. In general, the lifetime of CQD is shorter due to the recombination of excitons or coordinate bonds with the functional groups [76,77].

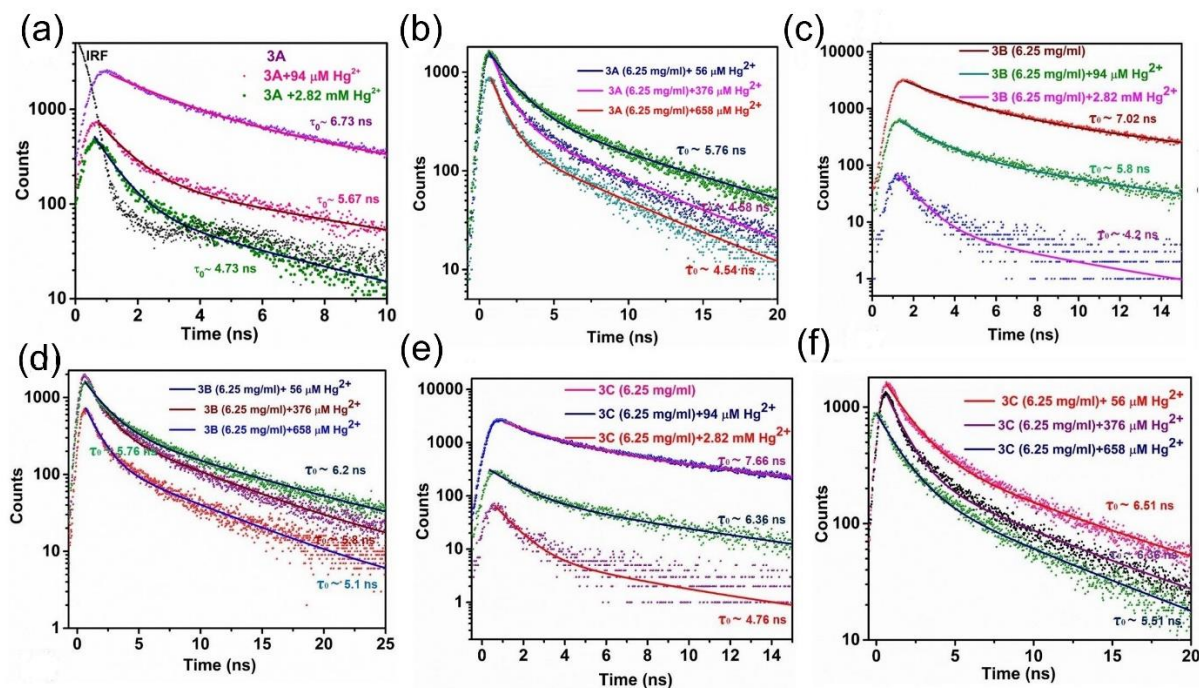


Figure 7.18: Time-resolved PL decay of (a,b) 3A, (c,d) 3B and (e,f) 3C with 56 μM , 94 μM , 376 μM , 658 μM , 2.82 μM Hg^{2+} at emission wavelength.

Sample	Excitation (nm)	Emission (nm)	τ_1 (ns)	A ₁	τ_2 (ns)	A ₂	χ^2	τ_0 (ns)
3A	370	444	2.15	1489	8.78	818	1.2	6.73
3B	370	448	2.17	2004	9.19	1002	1.2	6.94
3C	370	452	2.18	1565	9.84	872	1.2	7.66
3A	430	504	3.86	1383.5	10.84	506.8	1.2	7.40
3B	430	507	3.10	940.4	10.73	282.9	1.2	6.99
3C	430	508	3.06	1039.1	10.70	343.85	1.2	7.16
3A (pH-1)	370	440	1.67	304.3	6.79	212.1	0.88	5.45
3A (pH-12)	370	448	2.84	760	9.63	390	0.94	7.15
3B (pH-1)	370	445	2.17	1039	8.21	409	1.10	5.78
3B (pH-12)	370	452	2.52	737	9.24	365	1.19	6.85
3A + 56 μ M Hg ²⁺	370	445	1.74	343	7.86	146	1.03	5.77
3B + 56 μ M Hg ²⁺	370	450	1.32	381.5	7.95	144	1.05	5.92
3C + 56 μ M Hg ²⁺	370	452	1.6	1183.5 5	8.83	414.22	1.37	6.36
3A +94 μ M Hg ²⁺	370	445	1	540	7.60	173	1.10	5.68
3B +94 μ M Hg ²⁺	370	450	1.23	444.35	7.36	161.3	1.18	5.43
3C +94 μ M Hg ²⁺	370	450	1.1	224.6	8.35	87.6	1.01	6.52
3A + 0.37 mM Hg ²⁺	370	452	1	676.56	6.50	195	1.19	4.58
3B + 0.37 mM Hg ²⁺	370	452	1.08	589.1	6.90	151	1.92	4.69
3C + 0.37 mM Hg ²⁺	370	452	1.1	995.9	7.8	271.08	1.35	5.51
3A + 0.65 mM Hg ²⁺	370	450	1.00	1063.3	6.35	328.3	1.42	4.54
3B + 0.65 mM Hg ²⁺	370	450	1.2	1050.6 4	6.83	378.6	1.41	4.98
3C + 0.65 mM Hg ²⁺	370	450	1.4	674.2	7.79	210.5	1.09	5.45
3A +2.82 mM Hg ²⁺	370	445	0.70	436	5.13	89	1.2	3.35
3B +2.82 mM Hg ²⁺	370	450	1	59.4	5.65	7.9	1.14	2.99
3C +2.82 mM Hg ²⁺	370	450	0.70	77.5	4.70	21.2	1.18	3.29

Table 7.2: Different parameters of N-CQDs with different Hg²⁺ concentrations obtained from PL time decay measurement.

The average lifetime (τ_0) of 3A, 3B, and 3C are estimated to be 6.73 ns, 6.94 ns, and 7.66 ns, respectively (Table-7.2 & Figure 7.18). Interestingly, the average lifetime significantly decreases with increasing concentration of Hg^{2+} . At 2.82 mM Hg^{2+} , the value of τ_1 closely matches the instrument response function (IRF) ~ 1 ns. The disappearance of τ_1 at higher concentration of Hg^{2+} predicts the unavailability of active sites due to the interaction with Hg^{2+} (Figure 7.18). However, the decrease in time decay confirms the process of quenching must be dynamic in nature where collisions with Hg^{2+} at the excited state lower the intensity of radiative transition. In addition, the variation of τ_0/τ vs concentration of Hg^{2+} must be linear to validate whether the quenching mechanism is pure dynamic nature or not. Figure 7.19 suggests the relationship between τ_0/τ vs concentration of Hg^{2+} is quasilinear for N-CQD. The linear relationship was maintained at lower concentrations (below 100 μM of Hg^{2+}), and the curve depicts a non-linear behavior at higher concentrations indicating both static and dynamic quenching [38,72]. Furthermore, the effect and separation of static components have been confirmed by plotting between $(I_0/I)/(\tau_0/\tau)$ vs concentration of Hg^{2+} shown in Figure 7.19. It is seen that the ratio $(I_0/I)/(\tau_0/\tau)$ increases with concentration of Hg^{2+} , which eventually leads to the interface that the static part becomes crucial to predicting the sensing mechanism. The order of static components follows the order 3A \sim 3B $>$ 3C.

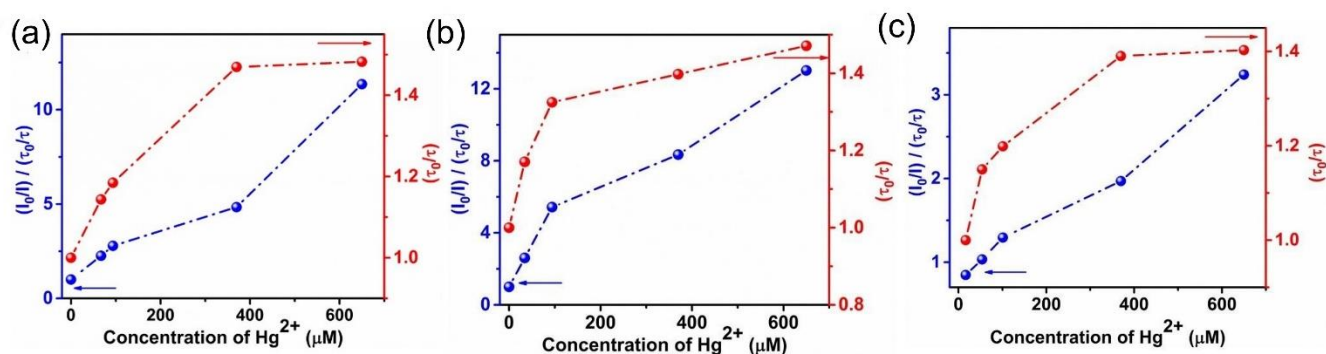


Figure 7.19: (c) Static and dynamic contribution of (a) 3A and (b) 3B and (c) 3C with different concentrations of Hg^{2+} .

The adsorption of Hg, Cd, and Pb atoms was investigated using first principles calculations on $-\text{COOH}$, $-\text{NH}_2$ functionalized CQD, and on pyridinic N doped CQD (Figure 7.20). The adsorption energies of the metal atoms on the functionalized and doped CQDs are represented in table 7.3.

Hg was found to be adsorbed with substantially lower adsorption energy on functionalized and doped CQDs than Cd and Pb indicating stronger binding of the Hg atom on the CQD. No chemical bonding was observed between the adsorbate metal atoms and CQD indicating the physisorption nature of interaction. The metal atoms were found to be interacting with the N atom while adsorption on the -NH_2 functionalized and pyridinic N doped GQDs. In case of adsorption of the metal atoms on the -COOH functionalized CQD, the Hg and Pb atoms were found to be interacting with the O atom in the C-OH bond of the -COOH functional group in the adsorbed configuration whereas Cd was found to be interacting with the O atom of the C=O bond in the adsorbed configuration. The adsorption of Hg is most substantial on carboxylic group functionalized CQD with lowest ground state for absorption energy (ΔE_{Ads} - 0.029 eV) (Figure 7.20a). The calculated adsorption energy (ΔE_{Ads}) for amine and pyridinic sites with Hg is found to be 0.093 eV and 0.102 eV, respectively (Figure 7.20b,c).

COOH-Hg	NH ₂ -Hg	Pyridinic N-Hg	COOH-Cd	NH ₂ -Cd	Pyridinic N-Cd	COOH-Pb	NH ₂ -Pb	Pyridinic N-Pb
0.029 eV	0.093 eV	0.102 eV	1.06 eV	1.14 eV	1.15 eV	2.72 eV	2.85 eV	3.1 eV

Table 7.3: Adsorption energy (eV) of Hg on different active sites (pyridinic, amine, carboxylic group) of N-CQD.

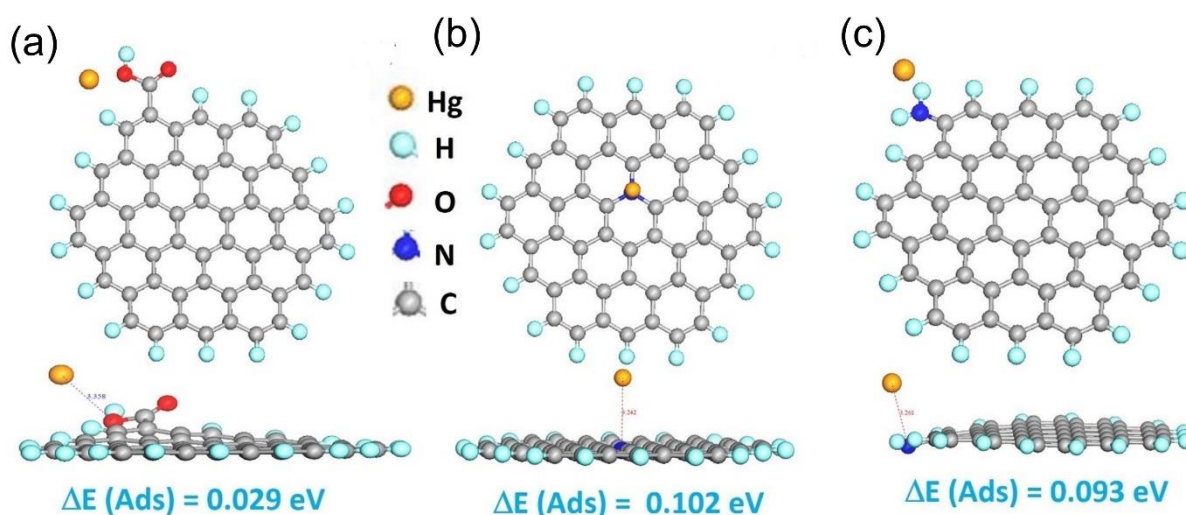


Figure 7.20: DFT study of adsorption of Hg on (a) -COOH , (b) Pyridinic, and (c) amine functionalized N-CQD. The inset ΔE_{Ads} denotes adsorption energy of Hg on N-CQD.

7.3.5. Photoluminescence recovery

In the next section, we try to determine the efficiency of the binding site in N-CQD with Hg^{2+} ions from the context of PL recovery via uncapping of Hg^{2+} with a fixed concentration of EDTA (0.034 M). It should be noted, under 330 nm excitation, the recovery percentage of intensity for peak 1 ($\pi-\pi^*$) are 63.87% (3A), 66.83% (3A), 30.63% (3A), 32.57% (3A), 34.75% (3B), 20.05% (3B), 16.87% (3B), 34% (3B) and 22.22% (3C), 82.97% (3C), 24.8% (3C), 19.8% (3C) at 56 μM , 94 μM , 376 μM , and 658 μM Hg^{2+} respectively (Figure 7.21a,b). The recovery percentage of intensity for peak 2 ($n-\pi^*$) is significantly higher at 96%, 36%, and 87.5% for 3A, 3B, and 3C at 56 μM Hg^{2+} . However, the relative percentage of area of peak1 ($\pi-\pi^*$) and peak 2 ($n-\pi^*$) are enhanced to 47% (3A), 57% (3A), 14% (3B), 15% (3B), 9% (3C), 11% (3C) at 56 μM Hg^{2+} respectively. The result is also consistent with higher Hg^{2+} concentrations (Figure 7.21a,b). At 376 μM Hg^{2+} , the recovery percentage of peak intensity and area of peak 2 ($n-\pi^*$) becomes 37% and 28% (for 3A), 12% and 1.5% (for 3B) and 16% and 2% (for 3C) slightly higher than peak1 ($\pi-\pi^*$). Moreover, the recovery percentage of peak 2 $\text{nO}2\text{p}-\pi^* / \text{nN}2\text{p}-\pi^*$ is much higher than peak 1 $\text{nO}2\text{p}-\pi^* (-\text{COOH})$ at 370 nm excitation (Figure 7.21c,d). Under 56 μM Hg^{2+} concentration, the recovery percentage of PL intensity of peak 1 $\text{nO}2\text{p}-\pi^* (-\text{COOH})$ and peak 2 $\text{nO}2\text{p}-\pi^* / \text{nN}2\text{p}-\pi^*$ are 53.25%, 91.14% (3A), 34.22% (3B), 59% (3B) and 62% (3C), 69.7% (3C) respectively. Subsequently, the recovery of peak area of peak 1 $\text{nO}2\text{p}-\pi^* (-\text{COOH})$ and peak 2 $\text{nO}2\text{p}-\pi^* / \text{nN}2\text{p}-\pi^*$ are 34.69%, 56.2% (3A), 26.22% (3B), 34% (3B) and 61% (3C), 68.7% (3C) respectively. At 94 μM Hg^{2+} , the recovery percentage of peak intensity of peak 1 and peak 2 are 46%, 74% (3A), 57%, 66% (3B) and 31%, 68% (3C) respectively. Under 376 μM and 658 μM Hg^{2+} , the recovery of intensity of peak 1 becomes 50.4% (3A), 68.79% (3B), 22.22% (3C) and 37.77% (3A), 33.5% (3B), 14.89% (3C) respectively. Further, we have carried out the recovery mechanism by adding three times higher concentration of EDTA (0.102 M) with 3A at 94 μM Hg^{2+} . The recovery percentage of emission becomes 90% (at 370 nm excitation) where it changes to 65% for $\pi-\pi^*$ emission (Figure 7.22). The result is correlated with 0.034 M EDTA concentration where in both cases the recovery percentage enhanced especially for $n-\pi^*$ transition. Thus, observation reveals, that EDTA is a good binder with Hg^{2+} due to removal of Hg^{2+} at the edge functionalities where steric hindrance decelerates the recovery rate for $\pi-\pi^*$ emission.

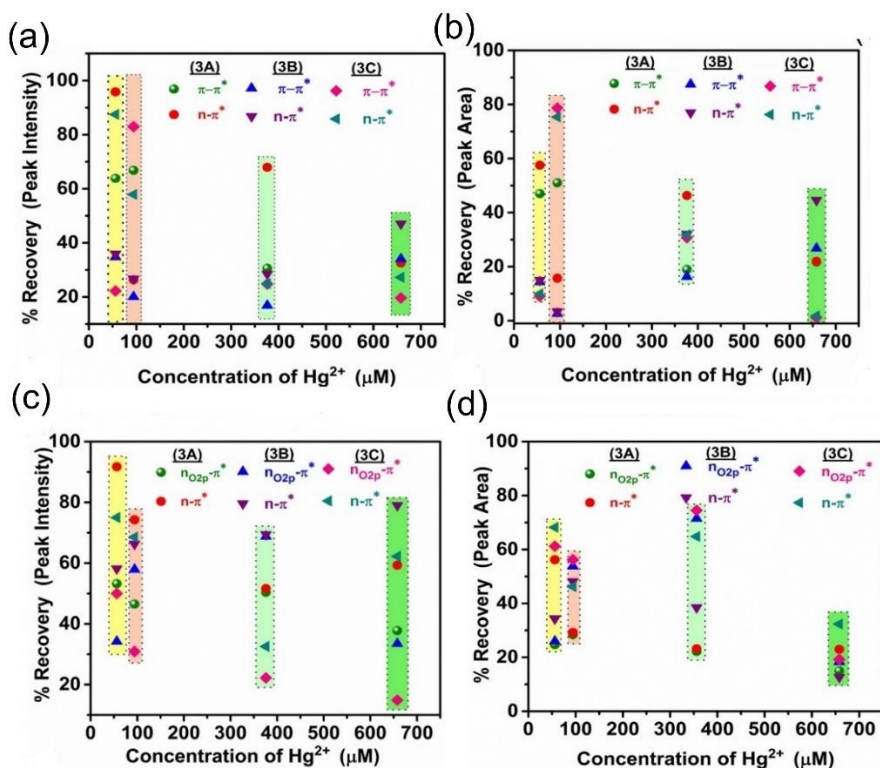


Figure 7.21: Recovery Percentage of (b) intensity and (c) area of peak 1 ($\pi-\pi^*$) and peak 2 ($n-\pi^*$) for N-CQDs (3A,3B & 3C) at different Hg^{2+} concentrations with 0.034 M EDTA (under 330 nm excitation). Recovery Percentage of (d) intensity and (e) area of peak 1 ($n_{\text{O}2\text{p}}-\pi^*$ -COOH) and peak 2 ($n_{\text{O}2\text{p}}-\pi^*$ -COO⁻, NH₂) for N-CQDs (3A,3B & 3C) at different Hg^{2+} concentrations with 0.034 M EDTA (under 370 nm excitation).

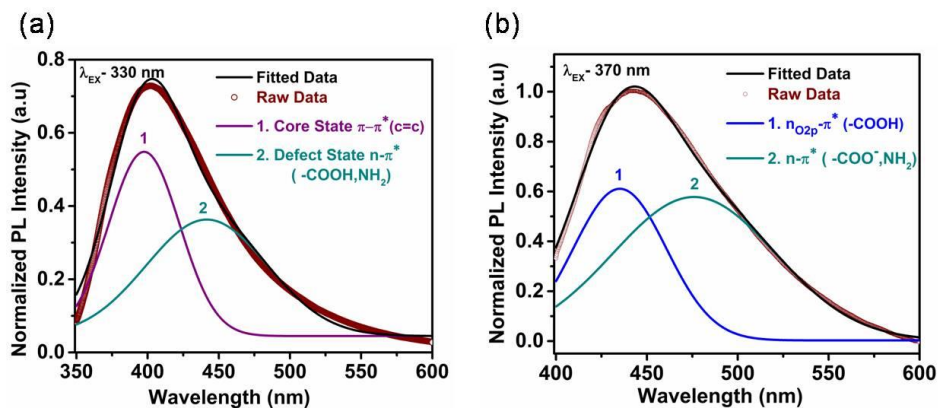


Figure 7.22: Deconvoluted PL profile of 3A with 94 μM Hg^{2+} and 0.102 M EDTA at excitation wavelength (a) 330 nm (b) 370 nm.

The detachment of Hg^{2+} from the binding site ($-\text{COOH}$, COO^- , amine, and amide) makes impact on zeta potential (ζ) and PLE profile. The intensity of the PLE profile at ~ 510 nm emission has been studied with different Hg^{2+} concentrations ($56 \mu\text{M}$, $94 \mu\text{M}$, $376 \mu\text{M}$, and $658 \mu\text{M}$) before and after EDTA incorporation. The intensity of the broad peak (PLE maxima) near ~ 330 nm (core state) remains contracted with increasing the Hg^{2+} . Similarly, the broad shoulder peak between 350 - 450 nm ($n-\pi^*$) has also been decreased and associated with the decrement of the core state. The decrement of such intensity illustrates the possibility of ground state (static) quenching occurring. It is interesting to note at lower concentrations of Hg^{2+} ($56 \mu\text{M}$ and $94 \mu\text{M}$), complete restoration occurs between 350 - 450 nm excitation where the relative intensity near ~ 330 nm becomes 90% and 87% , respectively (Figure. 7.23a,b). Thus, result suggests the efficiency of restoration of PLE for defects states predominates over core states. The lesser possibility of PLE restoring core state at 330 nm reduces the percentage of restoration of PL signals of emission peak $1 \pi-\pi^*$ ($\lambda_{\text{max}} \sim 390$ nm) of N-CQD. At higher concentrations ($376 \mu\text{M}$ and $658 \mu\text{M}$) of Hg^{2+} , the percentage of PLE restoration decreases due to the excess amount of Hg^{2+} at the surface of N-CQD (Figure. 7.23 c,d).

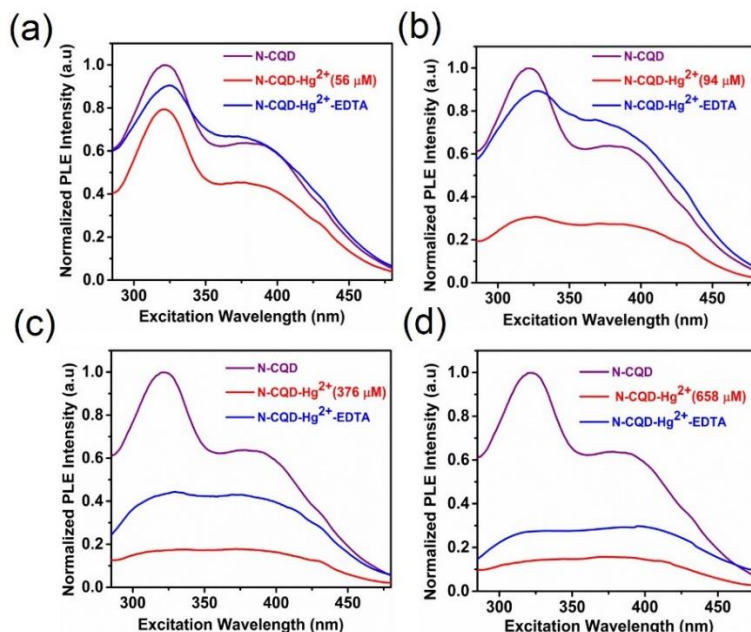


Figure 7.23: PLE profile of N-CQD (3A) with (a) $94 \mu\text{M}$ Hg^{2+} (d) $94 \mu\text{M}$ Hg^{2+} +0.034 M EDTA (b) $376 \mu\text{M}$ Hg^{2+} (e) $376 \mu\text{M}$ Hg^{2+} +0.034 M EDTA (c) $658 \mu\text{M}$ Hg^{2+} and (f) $658 \mu\text{M}$ Hg^{2+} +0.034 M EDTA at emission wavelength ~ 510 nm.

Thus, the higher recovery percentage of $n-\pi^*$ transitions reveals facile removal of Hg^{2+} ions from edge surface defects-based $-\text{COOH}$ and NH_2 - type functional groups than core sp^2 ($\text{C}=\text{C}$). Moreover, the addition of EDTA influences some steric hindrance to bind with Hg^{2+} due to deeply buried pyridyl or pyridinic nitrogen groups towards basal plane leading to shrinks in the recovery percentage of $\pi-\pi^*$ emission [38].

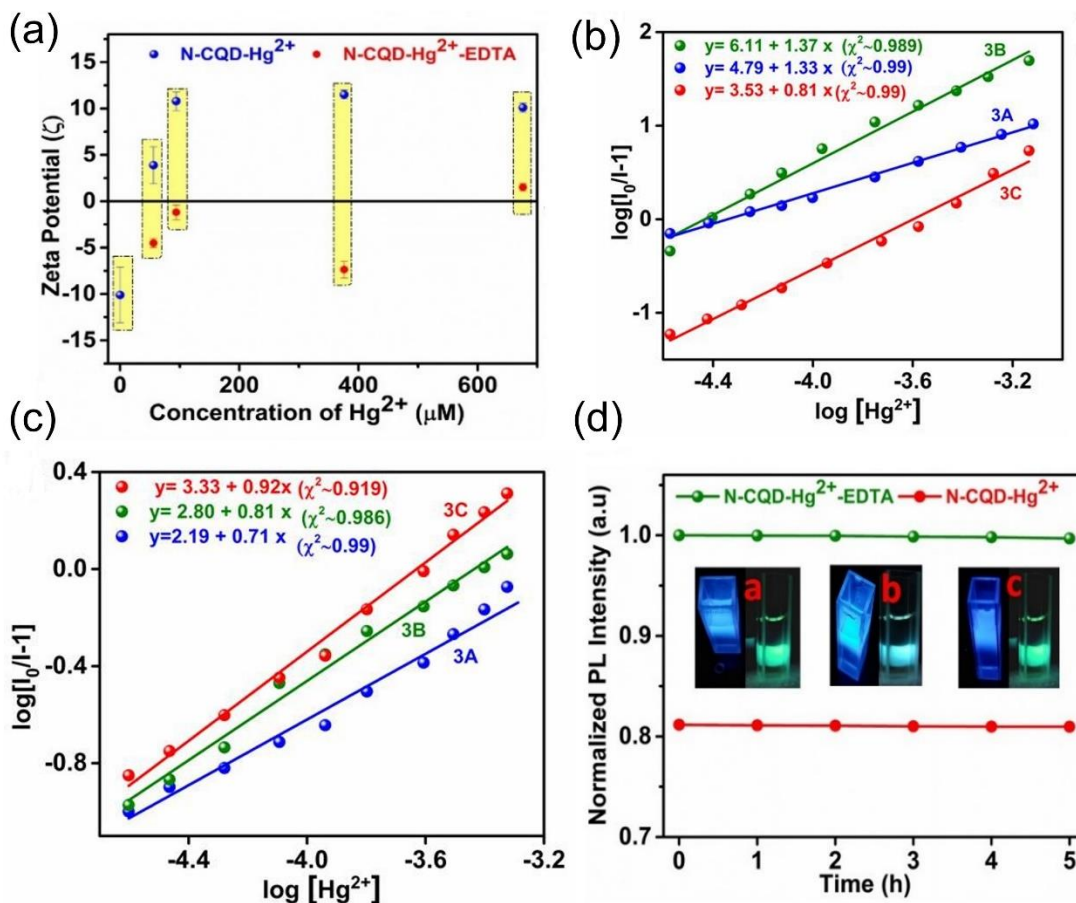
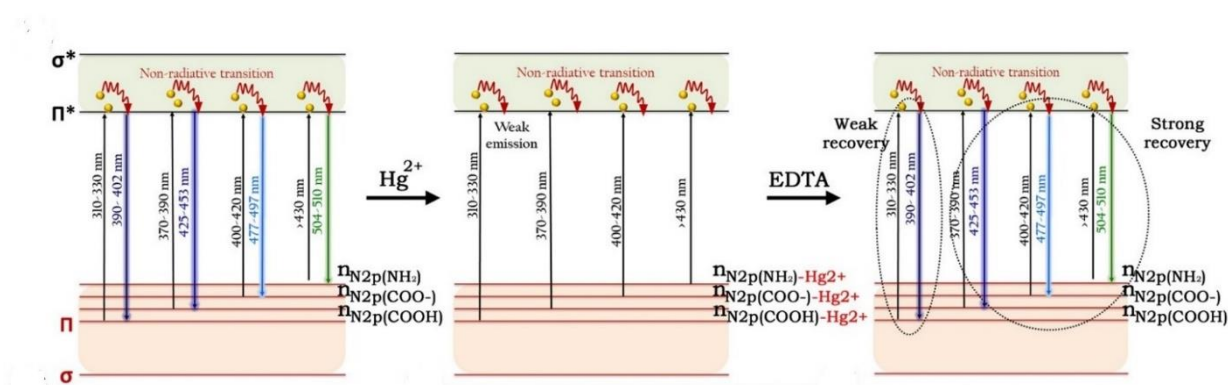


Figure 7.24: (a) Variation of zeta potential (ζ) with different concentrations of Hg^{2+} in presence and absence of 0.034 M EDTA for 3A. Plot of $\log [I_0/I-1]$ vs. $\log [\text{Hg}^{2+}]$ for the determination of binding constant and binding site for N-CQD (b) before (c) after PL recovery with EDTA. (d) Kinetic Stability test before and after PL recovery of 3A. Inset showing the digital photograph of blue and green emission of bare (a)3A with (b) Hg^{2+} (56 μM) and (c) EDTA addition.

The detachments of Hg^{2+} can also make the positive surface shift to negative, implying restoration of functional groups (amine, COOH groups). At 56 μM , 94 μM , 376 μM and 658 μM Hg^{2+} , the ζ value of 3A tends to be positive to $+3.89 \pm 2$ mV, $+10.8 \pm 1$ mV, $+11.5 \pm 0.5$ mV and $+11.1 \pm 0.5$ mV respectively. After surface modification with EDTA, the surface turns to negative -5 ± 0.5 mV, -1.19 ± 0.8 mV, -7.37 ± 0.9 mV and $+1.51 \pm 0.4$ mV at 56 μM , 94 μM , 376 μM and 658 μM Hg^{2+} respectively. It should be noted, the measured ζ value for free EDTA was -9.2 ± 0.1 mV. Meanwhile, no excess EDTA is present due to binding with excess Hg^{2+} ions leading to partial recovery of various PL signals. The measured ζ value after recovery originates mainly from N-CQD with an excess of Hg^{2+} ions. Thus, the highest restoration of PL signals of peak 1 $\text{nO}_{2\text{p}}-\pi^*$, ($\sim\text{COOH}$) ($\lambda_{\text{max}} \sim 440$ nm), and peak 2 $\text{nO}_{2\text{p}}-\pi^*/\text{nN}_{2\text{p}}-\pi^*$ are directly associated with surface chemistry i.e. zeta potential of N-CQDs (Figure 7.24a). From the slope and intercept (eqn. 7.6), we can determine the binding sites and bind constant. Obtained values for K_{bin} and n at 298K are 6.1×10^4 L mol^{-1} and 1.33 for 3A. The value decreases for 3C to 3.38×10^3 L mol^{-1} and 0.81 shown in Figure 7.24b. The value of $n \sim 1$ implies single binding sites or 1:1 stoichiometry of the binding site [78]. However, the low binding constant of 3A in comparison with 3B ($K_{\text{bin}} \sim 1.28 \times 10^6$ L mol^{-1}) is possible due to agglomeration of smaller particles during Hg amalgam formation which allows to hinders the Hg^{2+} . Most importantly, the K_{bin} has remarkably decreased to 154.88 L mol^{-1} , 630.5 L mol^{-1} , and 2137.96 L mol^{-1} for 3A, 3B, and 3C respectively after EDTA addition (0.034 M) (Figure 7.24c). The lower K_{bin} signifies maximum uncapping of Hg^{2+} from the N-CQD surface. Our investigation suggests the modified K_{bin} value after EDTA incorporation follows the same order as the recovery percentage ($3\text{A} > 3\text{B} > 3\text{C}$). Moreover, the kinetic stability of N-CQD with Hg^{2+} and EDTA has been illustrated in Figure 7.24d. The kinetic stability of N-CQD (3A) at 56 μM Hg^{2+} before and after recovery with EDTA is carried out for 5 hours. The PL intensity becomes unaltered after 5 hours suggests the systems are quite stable in Hg^{2+} and EDTA environments. The PL mechanism before and after masking has been schematically represented in scheme 7.2. Thus, our result suggests the role of core and defect states towards emission maxima with mercury ions depending on the surface chemistry of N-CQDs.



Scheme 7.2: Schematic energy diagram of different multi color emissions of bare N-CQD before and after recovery with Hg^{2+} .

7.4. Conclusion

In summary, microwave-assisted N-CQD has been prepared successfully from low cost, biomolecule carbohydrate ribose, and amino acid arginine. The weak bond formation between $(\text{COO}^-)_2\text{-Hg}^{2+}$, $\text{NH}_2\text{-Hg}^{2+}$, and reduction of decay parameters with Hg^{2+} concentration elucidate both the static and dynamic nature of quenching. Thus, the interactive effect between the COOH and amines with Hg^{2+} and reduction in sp^2 percentage diminishes the PL signals of $\pi\text{-}\pi^*$, $\text{nO}_2\text{p-}\pi^*$ (-COOH), and $\text{nN}_2\text{p-}\pi^*$ (amines and amides) transition. Additionally, zeta potential of N-CQD becomes positive upon enhancement of Hg^{2+} concentration, including diminution of band gap (3.4 eV) and deconvoluted PLE profile manifests the defects states are mainly responsible for higher wavelength emission. The high atomic percentage of COOH, amines, amides, and sp^2 C=C content as well as smaller size of 3A exhibits higher PL intensity and quantum yield at respective excitation wavelengths (330 nm to 430 nm) than 3B and 3C. Such a high atomic percentage enhances the surface charge of 3A with a trend of $3\text{A}>3\text{B}>3\text{C}$ and is well reflected in quenching efficiency ($3\text{A}>3\text{B}>3\text{C}$) at 330 nm ($\pi\text{-}\pi^*$) and 370 nm ($\text{nO}_2\text{p-}\pi^*$) excitation. Furthermore, restoring functional groups associated with PL signals and PLE intensity is carried out by incorporating EDTA, which undergoes chelation with Hg^{2+} . The high recovery percentage of PL signals of defect states ($\text{nO}_2\text{p-}\pi^*$, $\text{nN}_2\text{p-}\pi^*$) than core state ($\pi\text{-}\pi^*$) has been studied at different Hg^{2+} concentrations. The observations are well reflected in the post zeta potential analyses. The lower recovery percentage of core state and negative surface charge generation due to functional group restoration is commensurate with the aforementioned emission dynamics of N-CQD.

7.5. References

1. Behera, R.K., Mishra, L., Mondal, S., Kumar, S., Panigrahi, A., Singha, S., Basu, S. and Sarangi, M.K., *The Journal of Physical Chemistry C*, 2021, 125(31), pp.17418-17427.
2. Mirtchev, P., Henderson, E.J., Soheilnia, N., Yip, C.M. and Ozin, G.A., *Journal of Materials Chemistry*, 2012, 22(4), pp.1265-1269.
3. Gong, N., Wang, H., Li, S., Deng, Y., Chen, X.A., Ye, L. and Gu, W., *Langmuir*, 2014, 30(36), pp.10933-10939.
4. Wang, Z., Liao, H., Wu, H., Wang, B., Zhao, H. and Tan, M., *Analytical Methods*, 2015, 7(20), pp.8911-8917.
5. Yuan, F., Wang, Z., Li, X., Li, Y., Tan, Z.A., Fan, L. and Yang, S., *Advanced materials*, 2017, 29(3), pp.1604436.
6. Sarkar, S., Ray, U., Roy, D., Banerjee, D. and Chattopadhyay, K.K., *Materials Letters*, 2021, 303, p.130493.
7. Roy, R., Thapa, R., Biswas, S., Saha, S., Ghorai, U.K., Sen, D., Kumar, E.M., Kumar, G.S., Mazumder, N., Roy, D. and Chattopadhyay, K.K., *Nanoscale*, 2018, 10(35), pp.16822-16829.
8. Nguyen, H.A., Srivastava, I., Pan, D. and Gruebele, M., *Acs Nano*, 2020, 14(5), pp.6127-6137.
9. Liu, C., Zhang, F., Hu, J., Gao, W. and Zhang, M., *Frontiers in chemistry*, 2021, 8, p.605028.
10. Mei, Q., Chen, J., Zhao, J., Yang, L., Liu, B., Liu, R. and Zhang, Z., *ACS Applied Materials & Interfaces*, 2016, 8(11), pp.7390-7395.
11. Zheng, K., Li, X., Chen, M., Gong, Y., Tang, A., Wang, Z., Wei, Z., Guan, L. and Teng, F., *Chemical Engineering Journal*, 2020, 380, pp.122503.
12. Park, C.H., Yang, H., Lee, J., Cho, H.H., Kim, D., Lee, D.C. and Kim, B.J., *Chemistry of Materials*, 2015, 27(15), pp.5288-5294.
13. Ren, S., Liu, B., Han, G., Zhao, H. and Zhang, Y., *Nanoscale*, 2021, 13(28), pp.12149-12156.
14. Yang, S., Sun, J., He, P., Deng, X., Wang, Z., Hu, C., Ding, G. and Xie, X., *Chemistry of Materials*, 2015, 27(6), pp.2004-2011.
15. Zhan, J., Geng, B., Wu, K., Xu, G., Wang, L., Guo, R., Lei, B., Zheng, F., Pan, D. and Wu, M., *Carbon*, 2018, 130, pp.153-163.
16. Wang, Y., Wang, K., Han, Z., Yin, Z., Zhou, C., Du, F., Zhou, S., Chen, P. and Xie, Z., *Journal of Materials Chemistry C*, 2017, 5(37), pp.9629-9637.
17. Zhu, Q., Zhang, L., Van Vliet, K., Miserez, A. and Holten-Andersen, N., *ACS applied materials & interfaces*, 2018, 10(12), pp.10409-10418.
18. Zhang, W., Liu, Y., Meng, X., Ding, T., Xu, Y., Xu, H., Ren, Y., Liu, B., Huang, J., Yang, J. and Fang, X., *Physical Chemistry Chemical Physics*, 2015, 17(34), pp.22361-22366.
19. Zhu, P., Tan, K., Chen, Q., Xiong, J. and Gao, L., *Chemistry of Materials*, 2019, 31(13), pp.4732-4742.
20. Han, Y., Tang, B., Wang, L., Bao, H., Lu, Y., Guan, C., Zhang, L., Le, M., Liu, Z. and Wu, M., *ACS nano*, 2020, 14(11), pp.14761-14768.
21. Venkatesan, M., Veeramuthu, L., Liang, F.C., Chen, W.C., Cho, C.J., Chen, C.W., Chen, J.Y., Yan, Y., Chang, S.H. and Kuo, C.C., *Chemical Engineering Journal*, 2020, 397, pp.125431.
22. Liang, F.C., Kuo, C.C., Chen, B.Y., Cho, C.J., Hung, C.C., Chen, W.C. and Borsali, R., *ACS Applied Materials & Interfaces*, 2017, 9(19), pp.16381-16396.

23. Gharat, P.M., Chethodil, J.M., Srivastava, A.P., Praseetha, P.K., Pal, H. and Choudhury, S.D., *Photochemical & Photobiological Sciences*, 2019, 18, pp.110-119.
24. Wang, T.Y., Chen, C.Y., Wang, C.M., Tan, Y.Z. and Liao, W.S., *ACS sensors*, 2017, 2(3), pp.354-363.
25. Lan, M., Zhao, S., Wei, X., Zhang, K., Zhang, Z., Wu, S., Wang, P. and Zhang, W., *Dyes and Pigments*, 2019, 170, pp.107574.
26. Murugan, N. and Sundramoorthy, A.K., *New Journal of Chemistry*, 2018, 42(16), pp.13297-13307.
27. Veeramuthu, L., Venkatesan, M., Liang, F.C., Benas, J.S., Cho, C.J., Chen, C.W., Zhou, Y., Lee, R.H. and Kuo, C.C., *Polymers*, 2020, 12(3), pp.587.
28. Liu, Y., Wang, H., Guo, X., Xing, Y., Wei, K., Kang, M., Yang, X., Pei, M. and Zhang, G., *New Journal of Chemistry*, 2022, 46(21), pp.10386-10393.
29. Duan, Y., Huang, Y., Chen, S., Zuo, W. and Shi, B., *ACS omega*, 2019, 4(6), pp.9911-9917.
30. Mei, Q., Zhang, K., Guan, G., Liu, B., Wang, S. and Zhang, Z., *Chemical communications*, 2010, 46(39), pp.7319-7321.
31. Karami, K., Lighvan, Z.M., Barzani, S.A., Faal, A.Y., Poshteh-Shirani, M., Khayamian, T., Eigner, V. and Dušek, M., *New Journal of Chemistry*, 2015, 39(11), pp.8708-8719.
32. Kresse, G. and Hafner, J., *Physical review B*, 1993, 47(1), pp.558.
33. Kresse, G., Furthmüller, J. and Hafner, J.J.P.R.B., *Physical Review B*, 1994, 50(18), pp.13181.
34. Blöchl, P.E., *Physical review B*, 1994, 50(24), pp.17953.
35. Perdew, J.P., Burke, K. and Ernzerhof, M., *Physical review letters*, 1996, 77(18), pp.3865.
36. Grimme, S., *Journal of computational chemistry*, 2006, 27(15), pp.1787-1799.
37. Ding, Y., Zheng, J., Wang, J., Yang, Y. and Liu, X., *Journal of Materials Chemistry C*, 2019, 7(6), pp.1502-1509.
38. Bhattacharya, D., Mishra, M.K. and De, G., *The Journal of Physical Chemistry C*, 2017, 121(50), pp.28106-28116.
39. Roy, D., Sarkar, S., Bhattacharjee, K., Panigrahi, K., Das, B.K., Sardar, K., Sarkar, S. and Chattopadhyay, K.K., *Carbon*, 2020, 166, pp.361-373.
40. Yin, H., Niu, J., Ren, Y., Cong, J., Zhang, X., Fan, F., Xiao, Y., Zhang, X., Deng, J., Xie, M. and He, Z. *Sci Rep*, 2015, 5 (1): 1–12.
41. Kundu, A., Park, B., Oh, J., Sankar, K.V., Ray, C., Kim, W.S. and Jun, S.C., *Carbon*, 2020, 156, pp.110-118.
42. Luo, X., Bai, P., Wang, X., Zhao, G., Feng, J. and Ren, H., *New Journal of Chemistry*, 2019, 43(14), pp.5488-5494.
43. Tan, J., Zou, R., Zhang, J., Li, W., Zhang, L. and Yue, D., *Nanoscale*, 2016, 8(8), pp.4742-4747.
44. Muthulingam, S., Bae, K.B., Khan, R., Lee, I.H. and Uthirakumar, P., *RSC advances*, 2015, 5(57), pp.46247-46251.
45. Yoon, D., Son, Y.W. and Cheong, H., *Physical review letters*, 2011, 106(15), pp.155502.
46. Ferrari, A.C. and Basko, D.M., *Nature nanotechnology*, 2013, 8(4), pp.235-246.
47. Behzadi, F., Saievar-Iranizad, E. and Pakizeh, E., *Journal of Photochemistry and Photobiology A: Chemistry*, 2018, 364, pp.595-601.
48. Lai, S., Jin, Y., Shi, L., Zhou, R., Zhou, Y. and An, D., *Nanoscale*, 2020, 12(2), pp.591-601.
49. Pal, A., Srivastava, S., Saini, P., Raina, S., Ingole, P.P., Gupta, R. and Sapra, S., *The Journal of Physical Chemistry C*, 2015, 119(39), pp.22690-22699.
50. Han, Y., Huang, H., Zhang, H., Liu, Y., Han, X., Liu, R., Li, H. and Kang, Z., *Acs Catalysis*, 2014, 4(3), pp.781-787.

51. Ma, C.B., Zhu, Z.T., Wang, H.X., Huang, X., Zhang, X., Qi, X., Zhang, H.L., Zhu, Y., Deng, X., Peng, Y. and Han, Y., *Nanoscale*, 2015, 7(22), pp.10162-10169.
52. Xie, S., Su, H., Wei, W., Li, M., Tong, Y. and Mao, Z., *Journal of Materials Chemistry A*, 2014, 2(39), pp.16365-16368.
53. Lai, S., Jin, Y., Shi, L., Zhou, R., Zhou, Y. and An, D., *Nanoscale*, 2020, 12(2), pp.591-601.
54. Ma, C.B., Zhu, Z.T., Wang, H.X., Huang, X., Zhang, X., Qi, X., Zhang, H.L., Zhu, Y., Deng, X., Peng, Y. and Han, Y., *Nanoscale*, 2015, 7(22), pp.10162-10169.
55. Zhan, Y., Geng, T., Liu, Y., Hu, C., Zhang, X., Lei, B., Zhuang, J., Wu, X., Huang, D., Xiao, G. and Zou, B., *ACS applied materials & interfaces*, 2018, 10(33), pp.27920-27927.
56. Teng, C.Y., Nguyen, B.S., Yeh, T.F., Lee, Y.L., Chen, S.J. and Teng, H., *Nanoscale*, 2017, 9(24), pp.8256-8265.
57. Schneider, J., Reckmeier, C.J., Xiong, Y., von Seckendorff, M., Susha, A.S., Kasák, P. and Rogach, A.L., *The Journal of Physical Chemistry C*, 2017, 121(3), pp.2014-2022.
58. Dutta Choudhury, S., Chethodil, J.M., Gharat, P.M., PK, P. and Pal, H., *The journal of physical chemistry letters*, 2017, 8(7), pp.1389-1395.
59. Das, A., Roy, D., Mandal, M., Jaiswal, C., Ta, M. and Mandal, P.K., *The Journal of Physical Chemistry Letters*, 2018, 9(17), pp.5092-5099.
60. Zhang, R. and Chen, W., *Biosensors and Bioelectronics*, 2014, 55, pp.83-90.
61. Gonçalves, H.M., Duarte, A.J. and da Silva, J.C.E., *Biosensors and Bioelectronics*, 2010, 26(4), pp.1302-1306.
62. Gonçalves, H., Jorge, P.A., Fernandes, J.R.A. and da Silva, J.C.E., *Sensors and Actuators B: Chemical*, 2010, 145(2), pp.702-707.
63. Li, L., Yu, B. and You, T., *Biosensors and Bioelectronics*, 2015, 74, pp.263-269.
64. Liu, Y., Liu, C.Y. and Zhang, Z.Y., *Applied Surface Science*, 2012, 263, pp.481-485.
65. Gao, Z.H., Lin, Z.Z., Chen, X.M., Lai, Z.Z. and Huang, Z.Y., *Sensors and Actuators B: Chemical*, 2016, 222, pp.965-971.
66. Yan, F., Shi, D., Zheng, T., Yun, K., Zhou, X. and Chen, L., *Sensors and Actuators B: Chemical*, 2016, 224, pp.926-935.
67. Wang, W., Zhang, Y., Yang, Q., Sun, M., Fei, X., Song, Y., Zhang, Y. and Li, Y., *Nanoscale*, 2013, 5(11), pp.4958-4965.
68. Wu, H. and Tong, C., *Analytical Chemistry*, 2020, 92(13), pp.8859-8866.
69. Zhao, J., Huang, M., Zhang, L., Zou, M., Chen, D., Huang, Y. and Zhao, S., *Analytical chemistry*, 2017, 89(15), pp.8044-8049.
70. Yang, P., Su, J., Guo, R., Yao, F. and Yuan, C., *Analytical Methods*, 2019, 11(14), pp.1879-1883.
71. Li, N., Bai, R. and Liu, C., *Langmuir*, 2005, 21(25), pp.11780-11787.
72. Huang, L., Zhu, Q., Zhu, J., Luo, L., Pu, S., Zhang, W., Zhu, W., Sun, J. and Wang, J., *Inorganic chemistry*, 2019, 58(2), pp.1638-1646.
73. Fatema, K.N., Liu, Y., Cho, K.Y. and Oh, W.C., *ACS omega*, 2020, 5(36), pp.22719-22730.
74. Guo, X., Li, M., Liu, A., Jiang, M., Niu, X. and Liu, X., *Water*, 2020, 12(8), pp.2105.
75. Bond, A.M., Miao, W. and Raston, C.L., *Langmuir*, 2000, 16(14), pp.6004-6012.
76. Song, Y., Zhu, S., Xiang, S., Zhao, X., Zhang, J., Zhang, H., Fu, Y. and Yang, B., *Nanoscale*, 2014, 6(9), pp.4676-4682.
77. Zhu, S., Shao, J., Song, Y., Zhao, X., Du, J., Wang, L., Wang, H., Zhang, K., Zhang, J. and Yang, B., *Nanoscale*, 2015, 7(17), pp.7927-7933.
78. Tong, J.Q., Tian, F.F., Liu, Y. and Jiang, F.L., *RSC Advances*, 2014, 4(104), pp.59686-59696.

CHAPTER 8

Grand Conclusion and Future Scope

8.1. Research Outcomes

The development of green technology is a sustainable approach to overcoming the potential barriers to energy and environmental crisis. Advancement of heterogeneous catalysts can overcome the problem where high prices, scarcity, and low durability are essential drawbacks to developing advanced catalytic materials. The thesis is focused on new cost effective synthesis routes of low dimensional material and enhance the catalytic activity in energy related applications such as oxygen reduction reaction, hydrogen evolution reaction, charge storage supercapacitive performances. The fundamental understating of structural and catalytic mechanism has been widely studied with different experimental tools and DFT analyses. The optical properties are also employed to detect toxic metal ions, organic pollutants. All work mentioned in the previous chapters are summarized as follows:

1. In summary, a novel inexpensive and non-hazardous reducing agent imidazole (part of histidine amino acid in the human body) has been employed for the conversion of graphene oxide (GO) to reduced graphene oxide (rGO) and simultaneous introduction of nitrogen functionalities in the resultant rGO sheet, both at moderate reaction conditions circumventing the requirement of inert gas protection and high-temperature annealing. The synthesis route is simple, one-pot, and reproducible with the high atomic percentage of incorporated nitrogen, hence, overcomes various practical bottlenecks and makes the product a superior candidate for the oxygen reduction reaction in point of use. Additionally, moderate surface area and porosity provide the material with high charge storage capacity. Such dual proficiency of efficient ORR activity and high

charge storage property is rarely been achieved so far by means of simple solution chemistry. From XPS and DFT analyses the pyridinic and amine nitrogen on NrGO-90 exhibits four electron pathways rather than two electron pathways. The conversion of pyridinic to graphitic nitrogen i.e. more in plane nitrogen doping at higher temperatures and higher probability of layer stacking decelerates the oxygen adsorption for NrGO-400. Such effect sheds light on lowering of BET surface area and supercapacitive performances of NrGO. The superior performance of NrGO-90 has been compared with nitrogen-free rGO which follows two electron transfer processes followed by hydrogen peroxide production.

2. To further aiming efficient catalyst towards oxygen reduction reaction, hBN & 2H-MoS₂ composite (HBPS) has been designed as a ORR catalyst. Hexagonal boron nitride (hBN) exhibits poor ORR execution owing to its inherent large bandgap. MoS₂ nanosheets also show poor catalytic activity towards ORR involving a two-electron transfer process owing to its indirect band gap and inactive basal plane. Theoretically, defect free hBN-MoS₂ composite system involves peroxide (HO₂⁻) formation which is energetically more efficient for two electron pathways. The peroxide formation is mainly attributed to weak adsorption (endothermic) of oxygen and first protonation. The enhanced reactivity of the basal plane of 2D-hBN can be carried out via functionalization with OH group. In probe sonication method, the O-H incorporation weakenes B-N double bond and longer exposure of sonication tends to remove B-OH group and create boron vacancy. The oxygen adsorption at boron vacancy site is quite facile which enhances the limiting current density of ORR kinetics. However, the ORR process still follows the two electron process. The exfoliation in presence of few layer MoS₂ leads to inter-sheet van der Waals interaction and charge transfer which shrinks the B-N bond strength and enhances the rate of B-vacancy formation (atomic percentage ~ 28%). The high concentration of B-vacancy has been confirmed experimentally with XPS analyses and Rietveld refinement. The stronger adsorption of oxygen on the vacancy site and lower free energy difference of the intermediate steps follow four electron transfer processes. The vacancy induces lowering of bandgap of HBPS enabling a rapid electron transfer from the valance band to the conduction band. This leads to electron enriched conduction band which plays a prime role in enhanced ORR activity. The HBPS's

electrocatalytic performance is highly comparable with the precious and nonprecious catalysts and superior over other previously hBN and MoS₂ reports.

3. In hydrogen economy, the advancement of electrocatalyst becomes crucial for sustainable development. This work approaches the development of an advanced low-cost catalyst MoS₂-MoO₃ with multiple active sites showing para-nitro phenol (PNP), ferricyanide reduction, and pH universal hydrogen evolution (HER) reaction. The drastically improved reaction kinetics was compared well with sulphur vacancy induced 2H-MoS₂, 2H-MoS₂-nanosheet, quantum dots and different metal and non metal based catalysts. Generally, the insulating MoO₃ is HER inactive and we have designed a binary composite of MoS₂-MoO₃ with high oxygen vacancy. Such oxygen vacancy induces metal unsaturation Mo^{5+/6+}, which is a reactive site for alkaline HER and PNP reduction. Theoretical analyses suggest low thermodynamic barrier ($\Delta G_H = 0.41$ eV) enhances the hydrogen (H^{*}) spillover from exothermic O²⁻ site ($\Delta G = -0.1$ eV) to endothermic S²⁻ ($\Delta G = 0.3$ eV) site than Mo site ($\Delta G = 1.42$ eV) of MoO₃. The spillover effect in confined space accelerates the desorption of adsorbed hydrogen (H^{*}) from the endothermic S site, combines with another H^{*} for H₂ production and enhances the rate in acidic HER. The low charge transfer resistance high durability, high electrochemically active surface area and mass activity provide MoS₂-MoO₃ acts as an efficient HER catalysts. The correlation of band engineering and surface activity has been determined from DFT and UPS analyses. Oxygen vacancy reduces work function (ϕ), d band energy and valance band maxima (VBM) shifting near Fermi level. Such optimization influences the availability of the electron density near conduction band and is beneficial for intermediate H^{*}, H₂O^{*} and PNP adsorption. The determination of active sites predicted from theoretical analyses has been well described with post XPS analyses and masking with SCN⁻. The p(π)-d(π) overlap between Mo^{5+/6+} with SCN⁻ and Mo(SCN)₆ type complex formation in alkaline solution tends to reduce the rate of PNP and alkaline HER kinetics where acidic HER kinetics remain unaltered. The result is correlated with sulphur vacancy induced MoS₂ which shows negligible effect with SCN⁻ in both acidic and alkaline media, manifesting the role of various Mo oxidation states during catalysis. However, temperature, concentration, pH,

and oxygen concentration variations have been carried out in PNP reduction of $\text{MoS}_2\text{-MoO}_3$ to determine the rate constant and activation energy. The low activation energy and high active site density enhance the reaction rate with high turnover frequency. This study suggests oxygen vacancy induced $\text{MoS}_2\text{-MoO}_3$ is an effective catalyst to show facile reduction of various organic and inorganic pollutants with pH universal hydrogen evolution.

4. Addressing the environmental pollution, cost effective and efficient detection of pollutants is measured using optical spectroscopy. Sensing and emission dynamics of low dimensional materials like quantum dots depend on types of functionalization, dopants, dielectric medium and surface charges. This work has explored a new approach to establish the emission dynamics of differently sized N-CQD (3A,3B & 3C) through surface chemistry via capping and uncapping of Hg^{2+} ions. The pH and excitation dependent emission spectra of N-CQD involve various centers involving core and surface states. The PL signals (Fwhm, Area, and Intensity) of each center shrinks after capping with Hg^{2+} ions and the mixture was identified with different experimental protocols and theoretical validation. After capping with Hg^{2+} , the weak bond between $(\text{COO}^-)_2\text{-Hg}^{2+}$, $\text{NH}_2\text{-Hg}^{2+}$ occurs along with reduction of sp^2 carbon which manifests the involvement of aforementioned groups towards emission dynamics. The dual static and dynamic based quenching has been developed where quenching efficiency decreases gradually from 3A to 3C N-CQDs. Furthermore, after uncapping of Hg^{2+} , the recovery percentage of PL signals associated with $n_{\text{O}2\text{p}}\text{-}\pi^*$ and $n_{\text{N}2\text{p}}\text{-}\pi^*$ ($-\text{COOH}$ and NH_2) are higher than the aromatic core ($\pi\text{-}\pi^*$). The result has been correlated with zeta potential (ζ) analyses which leads to an interface that the surface chemistry dependency towards our proposed emission dynamics of N-CQDs.

8.2. Future scope of the work

The author has investigated the active sites and catalytic mechanisms of various low dimensional materials on different energy and optical based applications. The fundamental understanding and correlation between stepwise mechanism, interfacial chemistry and

band engineering play a pivotal role on design a catalyst. However, perquisite upgradation of structural and chemical properties of new 2D materials like MXene, Janus, 2D covalent organic framework, hybrid organic-inorganic perovskite is required. The understanding of chemical properties like crystal structure, morphology, surface energy, surface charge, types of metals and ligands as well as band alignment can modify different biomedical, energy, optoelectronic, sensing applications. The 2D based materials can be a good energy storage devices in next generation sodium, sulphur and aluminum battery applications, carbon dio oxide reduction and methanol oxidation.

However, large scale production of catalysts and application in industry becomes a challenging factor. Also the temperature, piezoelectric or photo induced water splitting, toxic gas reduction, fuel cell reactions need to be improved by changing the physical and chemical properties of the catalysts. Interestingly, nitrogen reduction reaction (NRR) is important to produce different nitrogen based products like urea, ammonia, hydrazine. In NRR mechanism, HER is a side reaction due to high activation of protons to produce hydrogen. However, the reduction potential of N_2 becomes higher than H_2 and to suppress the HER, the band alignment of the catalyst should be optimized. The rational design of catalysts, charge transfer, energy or atom spillover technique can overcome the sluggish kinetics rate and activation energy.

PhD Thesis

ORIGINALITY REPORT

6%

SIMILARITY INDEX

PRIMARY SOURCES

- | | | |
|---|--|-----------------|
| <div style="background-color: red; color: white; padding: 2px 5px; display: inline-block;">1</div> | www.rsc.org
<small>Internet</small> | 2793 words — 5% |
| <hr/> | | |
| <div style="background-color: purple; color: white; padding: 2px 5px; display: inline-block;">2</div> | Arnab Das, Dipayan Roy, Bikram Kumar Das, Md Imran Ansari, Kalyan Kumar Chattopadhyay, Sourav Sarkar. "Zinc doping induced WS2 accelerating the HER and ORR kinetics: A theoretical and experimental validation", Catalysis Today, 2022
<small>Crossref</small> | 457 words — 1% |
| <hr/> | | |
| <div style="background-color: purple; color: white; padding: 2px 5px; display: inline-block;">3</div> | eprints.lse.ac.uk
<small>Internet</small> | 316 words — 1% |
-